SPECT beeldvorming met roterende-vlakkencollimatie

SPECT Imaging with Rotating Slat Collimation

Roel Van Holen

Promotoren: prof. dr. S. Vandenberghe, prof. dr. ir. S. Staelens
Proefschrift ingediend tot het behalen van de graad van
Doctor in de Ingenieurswetenschappen: Biomedische Ingenieurstechnieken

Vakgroep Elektronica en Informatiesystemen
Voorzitter: prof. dr. ir. J. Van Campenhout
Faculteit Ingenieurswetenschappen
Academiejaar 2008 - 2009

UNIVERSITEIT
GENT

ISBN 978-90-8578-275-9
NUR 954
Wettelijk depot: D/2009/10.500/34

Universiteit Gent
Faculteit Ingenieurswetenschappen
Vakgroep Electronica en Informatiesystemen

Promotoren:

Prof. dr. Stefaan Vandenberghe
Prof. dr. ir. Steven Staelens

Leden van de examencommissie:

Prof. dr. ir. Rik Van de Walle (Universiteit Gent, voorzitter)
Prof. dr. Ignace Lemahieu (Universiteit Gent, secretaris)
Prof. dr. Stefaan Vandenberghe (Universiteit Gent)
Prof. dr. ir. Steven Staelens (Universiteit Gent)
Prof. dr. ir. Aleksandra Pizurica (Universiteit Gent)
Prof. dr. ir. Christian Vanhove (Vrije Universiteit Brussel)
Wenli Wang, PhD (Memorial Sloan-Kettering Cancer Center, New York, VS)
Daniel Gagnon, PhD (TOSHIBA Medical Research Institute, Vernon Hills, VS)

Universiteit Gent
Faculteit Ingenieuswetenschappen
Vakgroep Elektronica en Informatiesystemen (ELIS)
Instituut voor Biomedische Techniek (IBITECH)
MEDISIP
Campus Heymans
De Pintelaan 185
9000 Gent
België

Dit werk is tot stand gekomen in het kader van een specialisatiebeurs van het instituut voor de aanmoediging van Innovatie door Wetenschap en Technologie in Vlaanderen (IWT-Vlaanderen).

Acknowledgements

Unless you consider your Personal Computer as your best friend, the preparation of a PhD dissertation is a rather individual activity. Nevertheless, in a research lab, one can not escape the obligatory social contacts from time to time. Luckilly! This work would simply not have been possible without the involvement of many of you. I would like to take the opportunity here to thank all the people who gave me chances, learned me skill, guided me and gave me insights. This work would never have been possible without the help and support of friends, colleagues and family.

In the first place, I would like to thank Prof. Dr. Ignace Lemahieu who, at the time he was promotor of my Master's thesis, gave me the opportunity to start a PhD at MEDISIP. Prof. Dr. Ir. Steven Staelens, at that time doing his PhD research, deserves a very big thank you because he was the driving force for the onset of my work. Not only did he convince me in the very beginning that I was suited for research, he also motivated and guided me throughout the whole period of my thesis. Thanks to Steven, I could manage. After my first year of research, Prof. Dr. Stefaan Vandenberghe rejoined our lab. Always constructive, Stefaan showed me how to reconstruct images, how to calculate sensitivities and resolutions, how to treat artifacts. Endless is the list of novel ideas he came up with and many were the scientific talks which were and still are a mental revitalization.

I would like to thank some of my former colleagues. Yves D'Asseler for the never ending and fascinating stories. Eric Nolf for his IT assistance. Jeroen Verhaeghe, Mahir Ozdemir and Els Fieremans simply for willing to share the office with me. I know it is difficult! Of all of my current colleagues, Hans Hallez is the most enthusiastic. Hans is always kind, eager to help, cooperative and constructive. I would like to thank Jan De Beenhouwer, besides for his professional input, for the stay in Africa. Long Zhang for the scientific discussions. Erwann Rault for sharing the

bed with me during short conference nights. Tom Ghekiere for waking me up after long conference days, not only in the morning. Steven Deleye for showing me how to dance. Vincent Keereman for learning me some methods for guaranteed - not always scientific - success. Sarah Assecondi for sharing her cooking experience. I also appreciate the new people that recently enriched our team: Enrico for his 'dry' humor, Eva for her funny laugh, Pieter for separating the sheep from the goats, Karel for his high-end motivation and Tom Nollet for his interest. Furthermore I would like to thank the administrative force, Rita, Ayfer and Anne-Marie who arranged things I could not manage.

Furthermore, a word of gratitude goes to the people of VUB and KUL under guidance of Prof. Defrise and Prof. Nuyts, for insights provided in the framework of our national collaboration, financially supported by the 'Fonds Wetenschappelijk Onderzoek - Vlaanderen'. From the many people involved in international collaborations, I especially would like to thank Daniel Gagnon, Wenli Wang and Jerry Griesmer, at that time working for Philips Medical Systems, for their support and training on the prototype Solstice camera.

I would especially like to thank Marainne and Bobonne, voor de mooie jeugd die jullie me gaven, voor alles wat jullie mijn hele leven voor me deden. From my father I inherited creativity, my mother gave me my resoluteness while without Erik I would never have been so curious about technology and research. I would like to thank my brother Gorik, for doing the household and my little brothers Raoul and Cyril for showing me the world through different eyes.

I finally wish to thank the Institute for the Promotion of Innovation by Science and Technology in Flanders (IWT-Vlaanderen), who financially supported my work through a postgraduate grant.

Thank you all!!

Table of Contents

List of Figures

List of Tables

List of Acronyms

A

AoR	Axis of Rotation
APD	Avalanche PhotoDiode
ART	Algebraic Reconstruction Technique

B

BOLD	Blood Oxygen Level Dependent
BP	BackProjection

C

C-C	Continuous-Continuous
CB	ConeBeam
CCD	Charge-Coupled Device
CF	Correction Factor
CFD	Convolution based Forced Detection
CG	Conjagate Gradient
CNR	Contrast-to-Noise Ratio
CoR	Center of Rotation
CRC	Contrast Recovery Coefficient
CRI	Contrast Recovery Increase
CS	Compton Scattering

CT	Computed Tomography
CZT	Cadmium Zinc Telluride

D

D-D	Discrete-Discrete
DE	Detection Efficiency
DEW	Dual Energy Window
DOI	Depth Of Interaction

E

EEG	ElectroEncephaloGraphy
EM	Expectation Maximization
EM-CCD	Electron-Multiplying Charge-Coupled Device
ET	Emission Tomography

F

F3D	Fully 3 Dimensional
FB	FanBeam
FBP	Filtered BackProjection
FDF	Frequency-Distance Filtering
FDG	Fluor-DeoxyGlucose
FDR	Frequency-Distance Relation
FFT	Fast Fourier Transform
FOV	Field-Of-View
FP	Forward Projection
FWHM	Full Width at Half Maximum
FWTM	Full Width at Tenth Maximum

G

GAP	General All Purpose
GATE	Geant4 Application fro Tomographic Emission
Geant4	Geometry And Tracking 4
GR-MLEM	Gaussian Rotator based MLEM

H

HE	High Energy
HR	High Resolution

I

IEC	Iterations at Equal Contrast
IGain	Iteration Gain
ILST	Iterative Least-Squares Technique
ISM	Integrated Split Matrix

L

LE	Low Energy
LEHR	Low Energy High Resolution
LLIR	Localized Linear Impulse Response
LS	Least-Squares

M

MAE	Mean Absolute Error
MAP	Maximum A Posteriori
MART	Multiplicative Algebraic Reconstruction Technique
MBR	Metastasis to Background Ratio

MC	Monte Carlo
MC-MLEM	Monte Carlo based MLEM
MCAT	Mathematical Cardiac Torso
MDP	Methyl DiPhosphonate
ME	Medium Energy
MEG	MagnetoEncephaloGraphy
MIBI	MethoxyIsoButyl Isonitrile
ML	Maximum Likelihood
MLEM	Maximum Likelihood Expectation Maximization
MRI	Magnetic Resonance Imaging
MRS	Magnetic Resonance Spectroscopy
MU	Memory Usage

N

NC	Noise Coefficient
NCAT	Nurbs-based Cardiac-Torso
NL	Noise Level
NMR	Nuclear Magnetic Resonance
NRMSE	Normalized Root Mean Square Error

O

OSEM	Ordered Subsets Expectation Maximization

P

PDE	Photon Detection Efficiency
PE	Photo-Electric
PET	Positron Emission Tomography
PFOV	Partial Field-Of-View
PH	Parallel Hole
PiH	PinHole

PMT	PhotoMultiplier Tube
PRF	Point Response Function
PS-PMT	Position Sensitive PhotoMultiplier Tube
PSF	Point Spread Function

Q

QE	Quantum Efficiency

R

RAMLA	Row-Action Maximum Likelihood Algorithm
RBI-EM	Rescaled Block Iterative Expectation Maximization
RCNR	Relative Contrast-to-Noise Ratio
RF	Radio Frequency
RIT	Relative Imaging Time
RM	Resolution Modeling
RMSE	Root Mean Square Error
ROI	Region Of Interest
RS	Rotating Slat
RSM	Resolution and Sensitivity Modeling
RX	Radiography

S

SD	Steepest Descent
sIEC	sub-Iterations at Equal Contrast
SiPM	Silicon PhotoMultipliers
SIRT	Simultaneous Iterative Reconstruction Technique
SM	Split Matrix
SNR	Signal-to-Noise Ratio
SOLSTICE	SOLid State Imager with Compact Electronics

SPECT	Single Photon Emission Computed Tomography

T

TEW	Triple Energy Window
TF	Transmitted Fraction
TGain	Time Gain
TPI	Time Per Iteration
TT	Total Time
TTG	Total Time Gain

U

UHE	Ultra High Energy
UHR	Ultra High Resolution
US	UltraSound

W

WLS	Weighted Least-Squares

English Summary

Nederlandstalige Samenvatting

English summary

Single Photon Emission Computed Tomography (SPECT) is a frequently used biomedical imaging technique which visualizes functional processes in-vivo, based on the emission of γ-rays from within the body. The most important difference with other imaging modalities is that SPECT is based on the tracer principle, discovered by de Hevesy in the early 1900s. This principle originates from the insight that an atom in a molecule which takes part in the metabolism of an organism can be replaced by one of its radioactive isotopes. With the detection of photons emitted by the radioactive element, the pathways followed in the metabolism can be tracked.

SPECT uses a device known as a gamma camera to produce images. A gamma camera consists of two main functional components, the collimator and the radiation detector. A radiation detector is essential to absorb and measure the γ-rays that escape the body. Once the detector can record incoming photons, spatial information on their origin is needed to form projection images or tomographic images which are reconstructed from projections. Therefore, a collimator is used. Traditional SPECT imaging uses a parallel hole collimator which is a lead slab perforated with small parallel holes. These holes define a possible line of origin, perpendicular to the place of interaction on the detector. All holes together define a parallel beam through which photons are detected. This translates in direct projection images (planar imaging) or in 3 dimensional images, reconstructed from projections under different angles.

This dissertation investigates SPECT imaging with another type of collimation, namely the rotating slat collimator. This collimator differs from a parallel hole collimator in the sense that the possible origin of the photons is restricted to a plane perpendicular to the detector. This allows for a lot more photons to be measured within the same period of time, possibly resulting in an enhanced image quality. This immediately states the necessity of underlying research: is it advantageous to use a rotating slat collimator over a parallel hole collimator?

An important drawback of rotating slat collimators is that every measured photon contains less information. Where with parallel hole collimated data, one can immediately see a projection image, rotating slat collimated data always need image reconstruction, even for obtaining planar images.

Underlying dissertation contains two main accents, namely planar imag-

ing and tomographic imaging. For both main components, the same categories are treated: image reconstruction, correction techniques, image quality comparison and possible applications.
Before starting the part of planar image quality, the most important properties of the collimator, sensitivity and resolution, were investigated. In a first phase, an analytic model of the rotating slat collimator, based on the calculation of sensitivity and resolution, was derived. Furthermore, an accurate Monte Carlo model has been built. Both models were validated using measurements on a prototype system. The development of these validated models in a first phase was important for all further research steps. On one hand, the analytic model was applied to improve image reconstruction. On the other hand, the Monte Carlo model served as an important tool for both the planar and tomographic comparisons. Subsequently, the importance of the system modeling during image reconstruction was pointed out. A contrast improvement of about 10% was found at equal noise in the images by applying a system model during planar image reconstruction. An important source of artifacts, affecting planar imaging with rotating slat collimators is the partial field-of-view activity This cause of image errors was investigated and a correction method was proposed. By applying the correction method based on Fourier techniques, the error in the images was reduced, in the worse case, from 119% to 17%. These measurements confirmed the potential of the proposed correction method. Consequently, the image quality obtained with a rotating slat collimator was compared to the image quality obtained with a parallel hole collimator. The most important findings from this comparison were an improved image quality with a factor 3 to 10 for a standard image quality phantom. The smaller the total activity, the larger the lesion and the higher the contrast, the larger the improvement in image quality will be with respect to a parallel hole collimator. Even for low positive (hot) contrast in a background as large as the field-of-view, an improved image quality was found. For imaging of cold lesions, there was no improved image quality.

Planar image reconstruction of data from a rotating slat collimated acquisition (plane integral data) is as complex as tomographic image reconstruction of data from a parallel hole collimator. The number of calculations, needed for reconstructing tomographic plane integral is even an order of magnitude larger. Furthermore, for plane integral data, iterative reconstruction techniques require more iterations to reach convergence

compared to parallel hole collimated data. One says the algorithm converges slowly. The combination of these speed limiting factors makes it very difficult to reconstruct tomographic images. Therefore, tomographic image reconstruction of plane integral data was investigated in depth. By splitting the reconstruction problem in two separate problems, the problem of complex calculations was reduced. This however does not solve the problem of slow convergence. Therefore, a fast converging method was developed, based upon two updates per iteration instead of only one. The proposed method was then investigated on the basis of speed and accuracy. Results show a 20 times faster calculation with the proposed technique compared to existing techniques. Thanks to this method it is now possible to reconstruct tomographic images within half an hour on a single CPU. Furthermore the extra update step did not influence image quality.

Typical image degrading factors in SPECT are caused by photons interacting in the body of the patient, before leaving it. When an emitted photon undergoes a Compton-scatter interaction, it deviates from its original path and it causes the photon to be detected at a wrong location or to be not detected at all. On the other hand, when a photon is completely absorbed by a photo-electric interaction, it can not be detected anymore. The detection of photons at the wrong location due to scatter requires scatter correction while not detecting a photon due to absorption or scatter when it should otherwise have been detected, needs attenuation correction. Both correction methods, scatter and attenuation correction, are well described for classical SPECT imaging. For SPECT with rotating slat collimators, no common correction methods have been described so far. In the framework of tomographic image reconstruction, the influence of scatter was investigated. A scatter correction method, similar to a correction method used for classical SPECT, was implemented and validated. For attenuation correction, there was no correction method that could be borrowed from classical SPECT. Therefore, a new method for attenuation correction of plane integral data was developed and validated with Monte Carlo simulations, where the exact number of attenuated photons is known.

With an efficient reconstruction algorithm and the appropriate correction methods available, tomographic image quality was investigated with respect to a parallel hole collimator. For a standard image quality phantom, an improvement in image quality with a factor of 4 to 5 was found for cold lesions and a factor 2 to 3 was found for hot lesions. However, this improvement is subject to the distribution of the source in the field-

of-view of the camera. For instance, a larger SPECT rotation radius and high uptake in the neighborhood of the area of interest can cause lower performance of the rotating slat collimator. This was illustrated with a realistic phantom setup where a heart defect was simulated. The larger rotation radius and the hot liver activity in the neighborhood of the heart caused the image quality of the rotating slat collimator to be slightly worse at higher noise levels.

Finally, image quality was investigated for isotopes with high-energy emissions. Parallel hole SPECT with these isotopes, I-123 and I-131, suffers from penetration of the high-energy photons through the collimator. This shows up in the images as a degradation of contrast. Due to the relatively higher sensitivity of the rotating slat collimator for 'wanted' photons which did not penetrate the collimator, the latter will be less affected by penetrated photons. It was shown that for planar imaging with I-123, a contrast gain of 25% could be obtained. For tomographic I-131 imaging, a 10% contrast gain was found at equal noise in the images compared to parallel hole.

The research was performed in the MEDical Image and SIgnal Processing research group (MEDISIP). MEDISIP is a research group of the ELIS department of the faculty of engineering of the Gent University. The work resulted in 3 journal publications as a first author [169, 173, 172] and 3 journal publications as a co-author [177, 134, 36] in international A1 journals. Many parts of underlying work have been presented at national and international conferences [160, 161, 167, 165, 162, 164, 166, 170, 175, 163, 159, 174].

Nederlandstalige Samenvatting

Single Photon Emission Computed Tomography (SPECT) is een veel gebruikte biomedische beelvormingstechniek die functionele processen in vivo in beeld brengt en is gebaseerd op de emissie van γ-straling vanuit het lichaam. Het belangrijkste onderscheid met andere beeldvormingstechnieken is dat SPECT gebaseerd is op het speurstofprincipe, voor het eerst toegepast door de Hevesy aan het begin van de vorige eeuw. Dit principe omvat het inzicht dat een atoom in een molecule, dewelke deelneemt aan het metabolisme, kan vervangen worden door een van zijn radioactieve isotopen. Aan de hand van de detectie van de bij het radioactief verval vrijgekomen fotonen kan een beeld gevormd worden van de verdeling van de beschouwde molecule in het lichaam.
SPECT maakt gebruik van een toestel dat de gammacamera genoemd wordt. De gammacamera bestaat uit twee belangrijke functionele componenten, namelijk de stralingsdetector en de collimator. De stralingsdetector is een essentiëel onderdeel dat zorgt voor de absorptie en meting van de γ-stralen die het lichaam verlaten. Van zodra de detector straling kan opmeten is het noodzakelijk om de oorsprong van elk invallend foton te achterhalen. Voor dit doel wordt een collimator gebruikt. In traditionele SPECT beeldvorming maakt men gebruik van een parallelle-gatencollimator. Deze loden plaat geperforeerd met parallelle gaatjes zorgt ervoor dat de mogelijke invalsrichting van de fotonen beperkt is tot een lijn loodrecht op de plaats van detectie op de detector. Samen definiëren alle gaten een parallele stralenbundel volgens dewelke fotonen gedetecteerd worden. Dit zorg ervoor dat directe projectiebeelden kunnen gevormd worden (planaire beeldvorming) of dat er na beeldreconstructie 3 dimensionele beelden verkregen worden (tomografische beeldvorming).

Dit proefschrift onderzoekt SPECT beeldvorming met een ander type collimator, de roterende-vlakkencollimator. Deze verschilt van een parallelle-gatencollimator in die zin dat de mogelijke oorsprong van de opgemeten fotonen wordt beperkt tot een vlak loodrecht op het punt van detectie. Hierdoor is het mogelijk om meer fotonen te meten in eenzelfde tijdsspanne hetgeen zich vertaalt in een mogelijk verbeterde beeldkwaliteit. Dit geeft meteen het belang aan van onderliggend onderzoek: is het voordelig om een roterende-vlakkencollimator te gebruiken als alternatief voor de parallelle-gatencollimator?
Het belangrijkste nadeel van een roterende-vlakkencollimator is dat er minder informatie bevat is in de gemeten fotonen. Waar we met een

parallelle-gatencollimator onmiddellijk projectiebeelden kunnen vormen is het nodig om bij een roterende-vlakkencollimator altijd beeldreconstructie toe te passen, zelfs voor het verkrijgen van planaire beelden.
Het proefschrift omvat twee hoofdbestanddelen, namelijk planaire beeldvorming en tomografische beeldvorming. Voor beide hoofdbestanddelen komen dezelfde onderdelen aan bod: beeldreconstructie, correctietechnieken, beeldkwaliteit en toepassingsgebied.
Vooraleer te beginnen aan het onderdeel planaire beeldreconstructie, werden de belangrijkste eigenschappen, namelijk de sensitiviteit en resolutie, van een roterende-vlakkencollimator onderzocht. In een eerste fase werd aan de hand van de berekening van sensitiviteit en resolutie een analytisch model opgesteld voor de roterende-vlakkencollimator. Verder werd ook een accuraat Monte Carlo model van de collimator opgesteld. Beide werden vervolgens gevalideerd aan de hand van metingen met een prototype camera. De ontwikkeling van deze gevalideerde modellen in een eerste fase van het onderzoek was van belang voor het verdere goede verloop. Enerzijds werd het analytisch model toegepast om de beeldreconstructie te verbeteren en anderzijds is het Monte Carlo model een groot hulpmiddel gebleken voor zowel de planaire als tomografische verdere vergelijkingsstudies.
Het belang van de modellering van de collimator tijdens planaire beeldreconstructie werd vervolgens aangetoond. Een contrastverbetering van bijna 10% bij gelijke ruis in de beelden werd vastgesteld door gebruik te maken van modellering tijdens de reconstructie. Een belangrijk beelddegraderend effect bij planaire beeldvorming, namelijk de partiële activiteit, werd bestudeerd en een correctiemethode werd voorgesteld om voor deze bron van artefacten te corrigeren. Door de op Fourier-technieken gebaseerde correctie werd de fout in het beeld in het slechtste geval gereduceerd van 119% naar 17%. Deze metingen bevestigden de goede werking van de voorgestelde correctiemethode. De vergelijking van de beeldkwaliteit met een parallelle-gatencollimator kwam vervolgens aan bod. De belangrijkste bevindingen bij deze vergelijkende studie waren een verbeterde beeldkwaliteit met een factor 3 tot 10 voor een klassiek fantoom bedoeld voor het bepalen van de beeldkwaliteit. Deze verbeterde beeldkwaliteit is onderhevig aan grootte van het object, grootte van de lesie en het contrast van de lesie. Hoe kleiner de totale activiteit, hoe groter de lesie en hoe groter het contrast, hoe groter de verbetering in beeldkwaliteit zal zijn ten opzichte van een paralelle-gatencollimator. Zelfs voor een laag positief contrast (warme lesies) in een grote achtergrond is er een verbeterde beeldkwaliteit. Voor

koude lesies is er geen verbetering van de beeldkwaliteit.

Beeldreconstructie van planaire beelden uit data afkomstig van een roterende-vlakkencollimator is even complex als een tomografische beeldreconstructie van data afkomstig van parallelle-gatencollimatie. Het aantal berekeningen, nodig voor de reconstructie van tomografische roterende-vlakken-data (of vlak-integraal-data) is nog een grootte-orde groter. Daarenboven zijn er voor iteratieve beeldreconstructie, waarvan hier gebuik gemaakt werd, meer iteraties nodig vooraleer een oplossing gevonden wordt. Men spreekt van trage convergentie van het reconstructie-algoritme. De combinatie van deze beide snelheidsbeperkende factoren maakt het zeer lastig om tomografische beelden te reconstrueren. Daarom werd de tomografische beeldreconstructie voor roterende-vlakkencollimatie nader onderzocht. Door de reconstructie op te splitsen in twee afzonderlijke delen wordt het aantal berekeningen terug gereduceerd. Dit verhelpt echter niets aan het probleem van trage convergentie. Daarom werd een methode ontwikkeld die snel convergeert op basis van een dubbele update-stap in elke iteratie van het gebruikte iteratief reconstructie-algoritme. De voorgestelde reconstructiemethode werd onderzocht op snelheid en accuraatheid. De resultaten wijzen op een 20 keer snellere berekening met de hier voorgestelde methode. Hierdoor is het mogelijk om tomografische data afkomstig van SPECT beeldvorming met een roterende-vlakkencollimator uit te voeren in minder dan een half uur op 1 enkele CPU. Bovendien werd aangetoond dat de beeldkwaliteit niet beïnvloed wordt.
Typische beelddegraderende effecten bij SPECT worden veroorzaakt door foton interacties in het lichaam van de patiënt. Wanneer een uitgezonden foton een Compton-scatter interactie ondergaat, wijkt het van zijn oorspronkelijke baan af en wordt het ofwel foutief ofwel helemaal niet gedetecteerd. Anderzijds, wanneer een foton volledig geabsorbeerd wordt door een foto-elektrische interactie, zal het foton ook niet gedetecteerd kunnen worden. De foutieve detectie van fotonen na scatter vereist scattercorrectie, terwijl het niet detecteren van fotonen terwijl deze wel worden verwacht, attenuatiecorrectie vereist. Beide correctiemethoden, scattercorrectie en attenuatiecorrectie, zijn goed beschreven voor klassieke SPECT beeldvorming. Voor SPECT aan de hand van roterende-vlakkencollimatie bestaan er echter nog geen correctie-technieken. In het kader van tomografische beeldvorming met roterende-vlakkencollimatie werd de invloed van scatter op de beelden nagegaan. Gelijkaardige correctiemethoden, gebruikt voor de correctie van klassieke SPECT beelden,

werden geïmplementeerd en hun goede werking werd gevalideerd. Voor het doel van attenuatiecorrectie waren de gekende technieken niet langer toepasbaar. Een nieuwe methode voor attenuatiecorrectie van tomografische vlak-integraal-data werd ontwikkeld en gevalideerd aan de hand van Monte Carlo simulaties, waar het exact aantal geattenueerde fotonen gekend is.
Met een efficiënte reconstructiemethode en gevalideerde correctiemethoden voorhanden werd de tomografische beeldkwaliteit bestudeerd in vergelijking met een parallelle-gatencollimator. Voor een standaard fantoom voor meting van beeldkwaliteit werd een verbetering met een factor 4 tot 5 gevonden voor koude lesies en een factor 2 tot 3 voor warme lesies. Deze verbetering is echter, zoals bij planaire beeldvorming, afhankelijk van de bronverdeling in het gezichtsveld van de camera. Een grotere rotatie-radius en hoge activiteit in de buurt van de beoogde lesie kunnen zorgen voor een afname van de beeldkwaliteit van een roterende vlakken-collimatie. Dit werd aangetoond aan de hand van een realistische patiëntenscan waar een hartdefect gesimuleerd werd. Voor deze simulatie werd geen verbetering van de beeldkwaliteit aangetroffen. Dit door een gecombineerd effect van grotere rotatie-radius en hoge opname van de lever in de buurt van het hart. Verder onderzoek is echter nodig om de exacte randvoorwaarden te omschrijven voor dewelke een roterende-vlakkencollimator beter scoort.
Finaal werd de beeldkwaliteit onderzocht voor isotopen dewelke fotonemissie hebben bij hogere energieën. Beeldvorming met deze isotopen, I-123 en I-131, en een parallelle-gatencollimator wordt beïnvloed door de penetratie van hoge-energie fotonen doorheen de collimator. Dit komt in de beelden tot uiting als een gereduceerd contrast. Door de relatief hogere gevoeligheid van de roterende-vlakkencollimator voor gewenste fotonen dewelke de collimator niet penetreren, geeft de ze laatste mogelijk een verbeterde beeldkwaliteit. Het werd aangetoond dat voor planaire beeldvorming met I-123 een winst in contrast van 25% kan behaald worden. Voor de tomografische beeldvorming met I-131 was de winst in contrast 10% bij gelijke ruis in de beelden.
Dit ondezoek werd verricht in de onderzoeksgroep MEDical Image and SIgnal Processing (MEDISIP). MEDISIP is een onderzoeksgroep van de vakgroep ELIS van de faculteit ingenieurswetenschappen. Het voorgestelde werk resulteerde in 3 publicaties als eerste auteur [169, 173, 172] en 3 publicaties als co-auteur [177, 134, 36] in internationale A1 tijdschriften. De resultaten van onderliggend werkwerden gepresenteerd op tal van nationale en internationale conferenties [160, 161, 167, 165, 162,

164, 166, 170, 175, 163, 159, 174].

Chapter 1

Introduction

1.1 Situation

The subject of this dissertation is situated in the world of Single Photon Emission Computed Tomography (SPECT), which is a frequently used medical imaging technique. Contrary to radiological imaging techniques which use an external X-ray source for visualizing the anatomy, Single Photon Emission Computed Tomography (SPECT) is used to study functional processes in-vivo, based on γ-ray emission from within the body. The administration of a radiopharmaceutical to the patient provides us with a photon emitting source. Since this photon source (Tc-99m, I-123, In-111, Tl-201) is bound to a radiopharmaceutical, we can follow where it distributes in the body by detecting the γ-rays emitted by the isotope.
SPECT uses a device known as a gamma camera to produce images. A gamma camera consists of two main functional components, the collimator and the radiation detector. A radiation detector is essential to absorb and measure the γ-rays that escape the body. Once the detector can record incoming photons, spatial information on their origin is needed to form projection images or tomographic images which are reconstructed from projections. Therefore, a collimator is used.
A parallel hole collimator is a slab of heavy metal like lead or tungsten with densely packed small holes and is placed just in front of the photon detector. Each hole will define a small solid angle through which photons can reach the detector. By approximating the small solid angle by a line, the origin of the photon detected through a hole is located somewhere along this line. In this way projection images of the isotope distribution

are formed. The amount of photons that reach the detector through the collimator defines image quality in terms of noise. The more photons detected, the higher the sensitivity and the lower the noise in the projections. A second, equally important measure of image quality is the spatial resolution. This measure defines how well two neighboring points of activity can be discriminated by the gamma camera. In a classical gamma camera, it is mainly the collimator that defines sensitivity and spatial resolution. The size of the holes not only determines the amount of photons that reach the detector (sensitivity) but also the extent to which two neighboring points can be distinguished: decreasing the hole size with a factor of two for better spatial resolution would however decrease the sensitivity with a factor of 4 and vice versa. This trade-off between spatial resolution and sensitivity limits the optimization of SPECT scanners for more than 30 years. Attempts to obtain better image quality with mechanical collimation are two-fold. On one hand, better image quality is achieved through image reconstruction. By use of accurate models for image degradations such as attenuation, scatter and depth dependent resolution, quantitative content of reconstructed images can greatly be improved. On the other hand, a lot of effort is put into new collimator design, aiming at a better sensitivity-resolution balance. In most of these designs, focusing collimators such as pinhole, fanbeam or slit-slat collimators are used. The price paid here is always a reduced field of view, resulting in dedicated scanners for e.g. brain imaging or imaging of the heart.
This dissertation investigates rotating slat collimators, which exist of a set of equally spaced parallel lead slats placed in front of the detector. Rotating slat collimators offer a better sensitivity versus resolution trade-off without decreasing the field of view. They fundamentally differ from parallel hole collimators in the sense that instead of line integrals, they measure plane integrals. The better sensitivity for equal resolution does however not readily imply better image quality, since the photons originating from a plane contain less spatial information compared to photons originating from a line.

1.2 Outline

In chapter 2, SPECT will first be revised in its historical context. The gamma camera, used for SPECT imaging is explained later and a detailed overview of the main components of a gamma camera, the detector

and collimator, will be reviewed. The most frequent techniques used for mechanical collimation are described with respect to their spatial resolution, sensitivity and field of view. Also some insights are given in the choice of an optimal collimator by comparing all classically available collimators. Photon integrating detectors which are traditionally used for SPECT are reviewed with a look upon novel detector concepts which are still in a research phase. Once the components of a gamma camera are understood, an introductory review of iterative reconstruction techniques is given with special attention to corrections for different image degrading effects. Finally, the importance of Monte Carlo simulations, which will be extensively used, is explained.
Chapter 3 first explains why rotating slat collimators are investigated here. Subsequently, analytical expressions for sensitivity and spatial resolution are derived with special attention to the large photon incident angles and points close to the collimator. Furthermore, a Monte Carlo model will be implemented to verify the analytic expressions. This Monte Carlo model will be validated with measurements on our prototype rotating slat system. Finally, the importance of a validated description of the rotating slat collimator system is pointed out: a study of the image quality that can be obtained with two possible planar image reconstruction methods, one without and one with system modeling, is performed.
Chapter 4 deals with the problem of partial field-of-view artifacts. These kind of artifacts which only affect rotating slat collimators are caused by sources of activity which are situated outside the area in front of the collimator. In a patient study, activity accumulated in the bladder will for instance affect a scan of the brain. To overcome this problem, we developed a method to separate the partial field-of-view activity from the data. Therefore, we will base ourselves on Fourier techniques. It will be shown that the filtering method works adequately by performing different phantom scans on the prototype system.
The validated Monte Carlo model of chapter 3 will be extrapolated to a rotating slat collimated system with dimensions of a conventional gamma camera for the purpose of fair image quality comparison. In chapter 5, planar image quality that can be obtained with rotating slats is presented in comparison with a parallel hole collimator. Parameters like object size, contrast and lesion size are influencing the image quality in the case of a rotating slat collimator. Therefore, they are taken into account while investigating image quality. A case study which simulates a planar bone scan, points out the clinical relevance of using rotating slat collimators for planar scintigraphy.

Before investigating the tomographic image quality in chapter 7, chapter 6 deals with the tomographic reconstruction of plane integral data. Since iterative reconstruction of plane integrals is characterized by slow convergence and computational complexity, a fast reconstruction method is proposed. This method is compared to existing reconstruction methods in terms of computational load, convergence speed and conservation of image quality.
Chapter 7 compares tomographic image quality. Therefore, an attenuation correction technique has to be implemented in the previously developed reconstruction method first. Once the attenuation correction method is validated, image quality is compared to parallel hole SPECT imaging for a typical image quality phantom. A clinically relevant case, simulating a myocardial infarction, is studied in order to have an idea of imaging performance of the rotating slat collimator in a clinical setting.
Chapter 8 investigates an interesting application of rotating slat collimators. Isotopes like I-123 and I-131 suffer from image degradations due to photon penetration of high energy photons through the collimator. Since the rotating slat has a higher geometrical sensitivity compared to other mechanical collimators, the relative influence of the contamination will be lower. The influence of using a rotating slat collimator on the energy spectrum, on the resolution and on image quality in general will be studied. It is pointed out that in clinical cases where these isotopes are used, the rotating slat collimator could have an additional advantage over classical collimation techniques.
In the final chapter, chapter 9, a general conclusion is drawn and some possible future research directions are given.

Chapter 2

Single Photon Emission Computed Tomography

2.1 Medical imaging

Medical imaging comprises a wide variety of methods and systems used in clinics to aid diagnosis of disease and planning of disease treatment. Non-invasive imaging techniques based on ionizing radiation found in radiology are Computed Tomography (CT) and planar X-ray Radiography (RX). Next, UltraSound (US) and Magnetic Resonance Imaging (MRI), which do not use ionizing radiation, are classified in radiology. Nuclear medicine is the clinical specialty which uses Single Photon Emission Computed Tomography (SPECT) and Positron Emission Tomography (PET). ElectroEncefaloGraphy (EEG), MagnetoEncefaloGraphy (MEG) and Magnetic Resonance Spectroscopy (MRS) can also be seen as medical imaging techniques since they provide physiological information which can be mapped to a 3 dimensional (3D) volume and thus also provide - although limited - spatial information. Autoradiography and electron microscopy are invasive techniques used in anatomic pathology while photo-acoustic imaging and optical imaging are promising new techniques for future non-invasive imaging.
All of these imaging modalities have their own advantages and disadvantages. This makes them quite complementary and often patients are scanned on different imaging modalities. For example, today, radiological imaging is often combined in hybrid systems with nuclear medicine imaging modalities. We will limit ourselves to give a short description

of the imaging modalities which can or will be found in the near future in hybrid scanners with nuclear medicine imaging modalities.

2.1.1 Anatomical imaging

The X-ray discovery in 1895 by Wilhelm Conrad Röntgen and the observation that X-rays were able to penetrate the body made it first possible to non-invasively image the interior of the body. Next to ordinary X-ray images or radiographs, which are 2 dimensional (2D) projection images, technologically advanced Computed Tomography (CT) is routinely used in all modern hospitals. A CT scanner provides 3 dimensional (3D) information by combining the data of radiographs taken from different angles around the body. The theory of CT was developed in the 1960's independently by Cormack and Houndsfield. The latter, at that time working for EMI, built the first CT scanner in the early 1970's. Tomographic reconstruction methods based on the inversion of the Radon transform, soon became available. A CT scanner basically consists of an X-ray source and a detector, which is positioned at the opposite side of the patient. Depending on the density of the different tissues, a fraction of the X-rays emitted by the source will be absorbed in the body. This results in a different projection image at each rotation angle of the source-detector pair. By re-projecting the projection images to the image space, a reconstruction of the patient's tissue density can be formed. X-ray and CT images display the anatomy or structure of the body's interior. Functional or physiological information can only be extracted in an indirect way by looking at morphological changes or by the use of certain contrast agents.

In 1980, MRI became clinically available as a tool for structural imaging. MRI is used complementary to CT when high contrast in soft tissue is mandatory and is based on the scientific principles of Nuclear Magnetic Resonance (NMR). The principle of NMR is to polarize a fraction of the protons in the human body by applying a strong magnetic field of typically several Tesla. Once the protons are polarized, they are de-polarized by a Radio Frequency (RF) pulse. The speed at which the protons repolarize to their initial state and the signal strength give information on the number of protons and on the kind of protons. Since proton density depends on the tissue we are looking at, different tissue can be distinguished. Thanks to the work of Paul Lauterbur in the 1970's, who was able to extract spatial information from the NMR data by applying gradients in the magnetic fields, MRI was born. Functional MRI

(fMRI) is able to locate neuronal activity in the brain by measurement of the oxygen level through the so-called Blood Oxygen Level Dependent (BOLD) signal. However, this is also an indirect and semi-quantitative measurement of the physiology.

2.1.2 Molecular imaging

Direct quantitative functional imaging therefore relies on imaging modalities other than CT and MRI. The functional imaging modalities have been developed concurrently with the medical specialty of nuclear medicine and are grouped under the name 'emission tomography'. Based upon the physical properties of the isotopes used in this discipline, we differentiate between Positron Emission Tomography (PET) and Single Photon Computed Tomography (SPECT).

Two major milestones characterize the development of emission tomography: the tracer principle and the development of the Anger camera, while a more detailed timeline of important developments can be found in figure 2.1. The roots of nuclear medicine date back from the early 1900s when the tracer principle was invented by de Hevesy. This principle is based upon the insight that an atom in a molecule which takes part in the metabolism of an organism can be replaced by one of its radioactive isotopes. With the detection of photons emitted by the radioactive element, the pathways followed in the metabolism can be tracked.

The second milestone is the development of the Anger camera in 1957 by Hal Anger. Although numerous developments regarding scanner optimization have been made, today's commercial gamma cameras are still based on the same components composing the Anger camera. Both a modern camera and Anger's camera consist of collimator, photon detector, light sensing Photo-Multiplier Tubes (PMTs) and electronic circuitry. Availability of transverse reconstruction techniques made it possible to perform SPECT scans with the gamma camera. Careful collimator design, digital electronics and iterative reconstruction techniques have indeed optimized the gamma camera throughout the past fifty years, but the main factor - the trade-off between sensitivity and spatial resolution - limiting the performance of a gamma camera remains unchanged in current camera designs.

In 1956, positron emitters were first used in clinic but it was only in the 1970's that transverse slices were imaged, mainly due to the development of the Filtered Back Projection (FBP) reconstruction technique

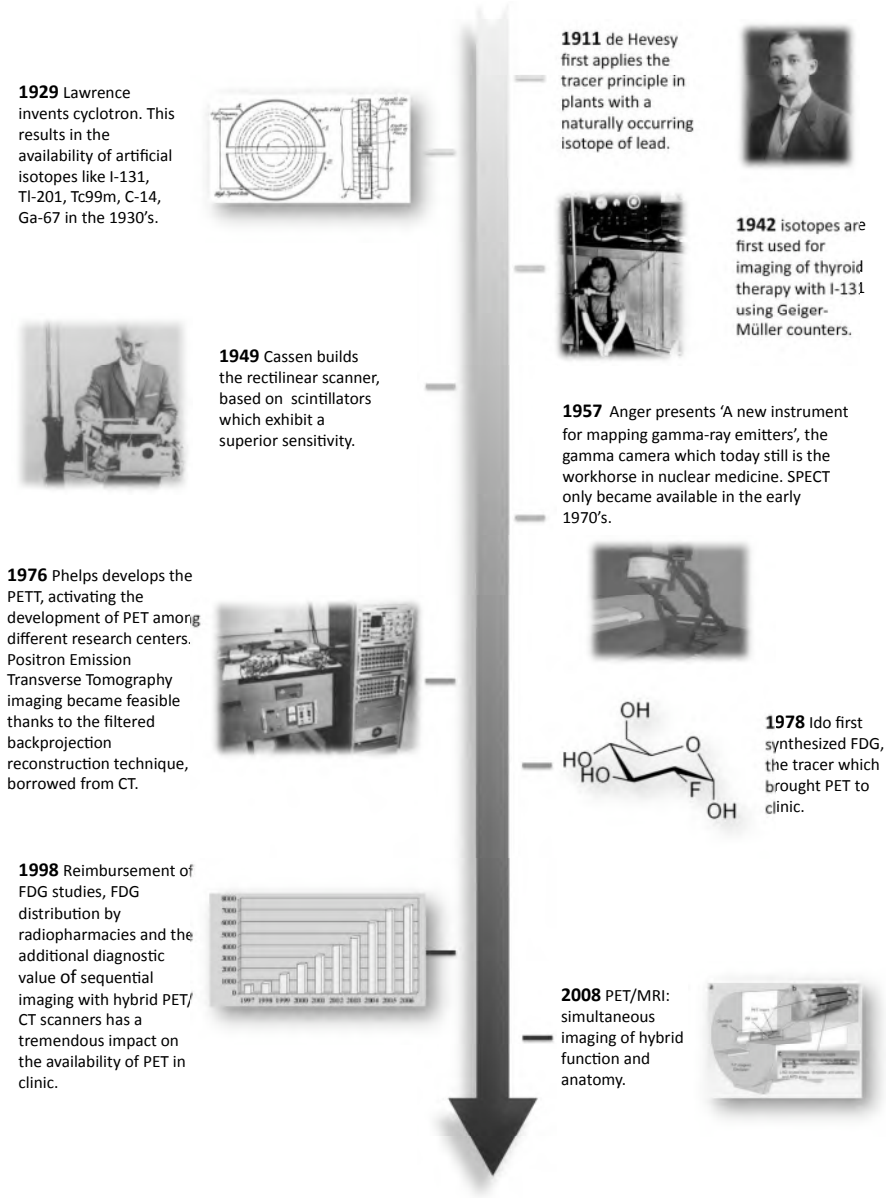

Figure 2.1: Timeline showing the most important developments in the history of nuclear medicine. Pictures and graphs from [19, 131, 73].

borrowed from CT. PET became of interest in many research institutes and made it to clinic thanks to the development of the tracer FDG, which is able to monitor the glucose metabolism of the body and more specifically of the brain. The more recent and increasingly important imaging modality is based on the physical properties of positron annihilation, which is characterized by the emission of two back-to-back gamma rays. The simultaneous emission of these two 511 keV photons allows determination of the line of origin of annihilation - and thus of the tracer - presuming that detection of the back-to-back photons happens in a finite coincidence time frame of typically several nanoseconds. In contrast to SPECT imaging, this coincidence sorting - named electronic collimation - happens after photon detection and results in a lot more photon pairs to be recorded. Mechanical collimation in front of the detector in a SPECT scanner leads to a detection efficiency of about 0.01%. PET systems typically offer a 2 to 4% sensitivity. This effects in a shortening of the scan time, dose reduction and less noisy images. Drawbacks of PET systems are the higher cost with respect to the scanner electronics and detectors, the limited amount of available tracers and the expensive cyclotron produced F-18, which is the most commonly used isotope for PET. Consequentially, it was only in the late 1990's that PET became available on a routinely basis thanks to a combination of commercial, economical and technical aspects among which the availability of cheap coincidence systems, the reimbursement of FDG studies, better scintillators, lower cost of the electronics, iterative reconstruction techniques and the added value of hybrid PET/CT. During recent years, there is an evolution in medical imaging from single imaging modalities toward combinations of structural and functional imaging modalities. Most PET and quite some SPECT scanners sold commercially nowadays are shipped with a CT while there is also a trend toward PET/MRI, SPECT/PET/MRI and SPECT/PET/CT.

2.2 Gamma camera imaging

Both planar scintigraphy and SPECT are performed with gamma cameras. Planar imaging is done with the camera 'looking' at the patient from only one direction, resulting in a 2 dimensional (2D) image where the activity of different layers is stacked. The advantage of planar imaging is that it can be performed relatively fast (typically five minutes). When information in the third dimension is mandatory, a SPECT scan

is needed, which typically combines 60 to 120 planar projections to reconstruct a 3D volume. A description of the different parts of a gamma camera is given before the different isotopes and clinical applications will be introduced.

2.2.1 A patient SPECT scan

For a patient SPECT investigation, the radiopharmaceutical has to be prepared first. Therefore, the radioactive isotope has to be available. For obtaining for instance Tc-99m in the hospital, so-called generators are used (figure 2.2). These generators contain the long living mother-isotope Mo-99, with a half life of 66 hours, from which the decay results in Tc-99m. By simply eluting the Tc-99m from the generator, the isotope is available for radiochemistry. By the radio-pharmacy, the isotope is bound to the tracer. Once the radio-labeled tracer is ready, the syringes

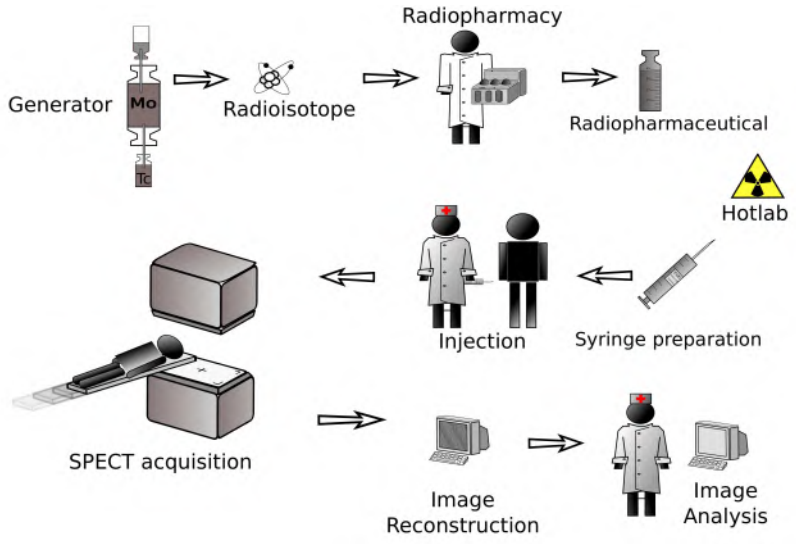

Figure 2.2: The different steps involved in a normal SPECT scan.

are prepared for injection. This all happens in the hot-lab. Once the patient is ready, he can be injected with the tracer. Typically, the patient has to wait a pre-defined period in order to let the radiopharmaceutical take part in the metabolism. After this waiting time, the patient is taken to the SPECT camera and projection images are taken for typically 20 to 30 minutes. After the scan, the patient can go home and once the

images are reconstructed and the medical physicist has examined them, a diagnosis can be made.

2.2.2 The Anger camera

The gamma camera was invented in 1957 by Hal Anger [6, 7, 9, 8, 10]. His developments were preceded by the rectilinear scanner of Cassen [28, 29] which for the first time employed a scintillator ($CdWO_4$) instead of low sensitivity Geiger-Müller counters for the detection of gamma rays. The rectilinear scanner consisted of a small disc of scintillator coupled to a single PhotoMultiplier Tube (PMT). When moving the scanner over the body surface, a 2D image could be made with a single hole collimator. The scintillator was quickly replaced by NaI(Tl) in commercial systems. At that time, Newell [123] pointed out the advantage of magnification by using focussed collimators. Previous developments in the field thus already applied scintillation detectors and different types of collimators but Anger was the first to build a large detector which was able to discriminate the two dimensional position of an incident photon using multiple PMTs coupled to one large continuous crystal. By distributing the light among neighboring PMTs with a light-guide, position discrimination was done by applying the so-called Anger logic. The scintillation position is obtained by linear interpolation of the signal strengths measured at the output of the different PMTs.
Before a photon can be detected by the gamma camera, several conditions should be met. First of all, the photons generated as a result of radioactive decay of the radiotracer have a certain probability to be reabsorbed or scattered in the patient's body before leaving it. Photons which are capable of leaving the body of the patient and travel in the direction of the gamma camera are mechanically selected by the collimator (figure 2.3). In the case of a parallel hole collimator, the collimator only selects those photons which travel perpendicular to the detector or within a small solid angle subtended by a collimator hole seen from the source. When a photon arrives through a collimator hole at the detector surface, it will likely be stopped by the scintillation crystal, which converts the photon energy to a visible light flash. The light-guide will distribute the light among neighboring PMTs which in turn will respond by providing electrical signals at their outputs. The electronics behind the PMTs will integrate these electrical signals and determine energy and position of the photon which struck the detector. Finally, a computer stores the number of detections per (discretized) detector position,

resulting in a projection image. For tomography, a finite number of such images, stacked for different detector angles, are stored in a sinogram which can be reconstructed to a 3D volume.

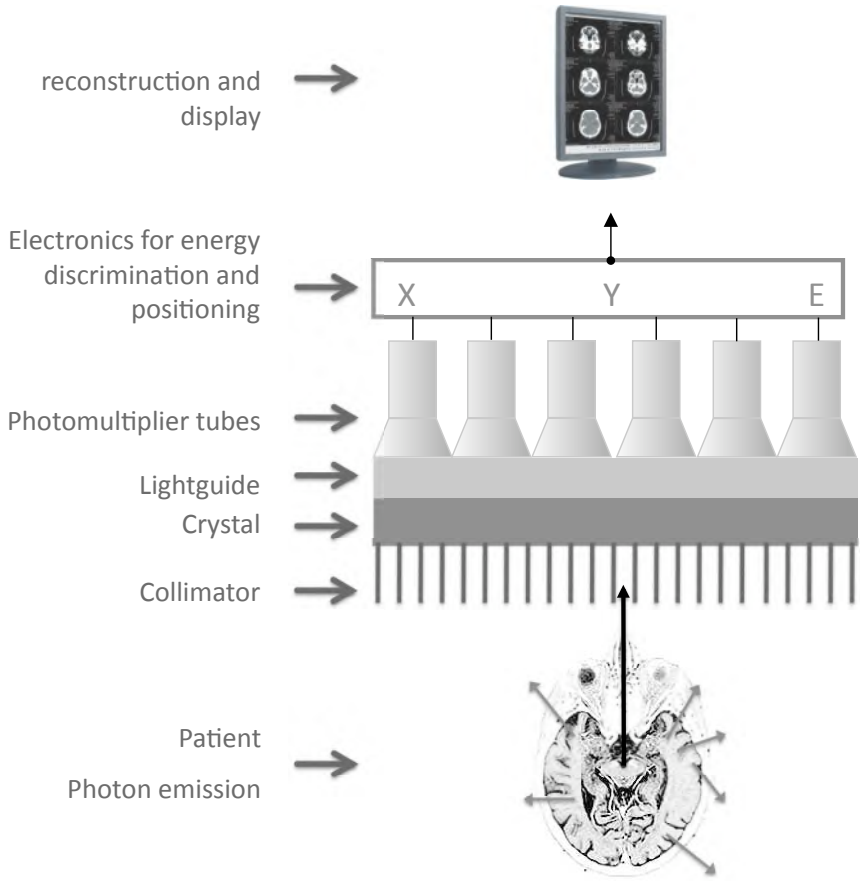

Figure 2.3: Basic components of the Anger camera. Most modern gamma cameras still consist of collimator, scintillator (crystal), light-guide, photomultiplier tubes, energy calculating and positioning electronics, computer for data processing and display.

2.2.3 Important gamma camera characteristics

Several parameters characterize the performance of a gamma camera. The sensitivity and the accuracy on the determination of the energy (en-

ergy resolution) and position (spatial resolution) of detected photons are the most important characteristics of a gamma camera.

Sensitivity

The sensitivity or efficiency of a gamma camera is a measure of the number of counts that are recorded in a certain period of time for a given activity. Activity is expressed in Bq (1 Bq = 1 disintegration per second) or in mCi (1 mCi = 37 MBq). Sensitivity is most often expressed in cps/MBq or cpm/mCi or as a percentage of the emitted photons. Sensitivity is determined by three factors: (a) the solid angle subtended by the detector(s), (b) the geometric properties of the collimator and (c) the material properties of the photon detector(s). Furthermore, sensitivity depends on the system dead time. However, at low count rates encountered in SPECT, the effect of dead time can be ignored.

The probability of a photon to be detected when it leaves the body is primarily determined by the joint solid angle subtended by the detectors. The more detectors or the larger the detectors, the higher the probability of interaction. Ideally, when a point would be imaged inside a sphere of surrounding detector material without the presence of a collimator, the geometrical sensitivity would be one. However, the detectors of a gamma camera usually are rectangular and the dimensions are limited regarding economical and practical considerations. A typical gamma camera has one to three detector heads of about 40 by 50 cm. Once the dimensions are fixed, the geometrical sensitivity only depends on the square of radius r, being the distance from the source to the detector surface:

$$\text{geometric sensitivity} \sim \frac{1}{r^2}. \tag{2.1}$$

This dependency can be understood when considering the constant photon flux through the surface of a sphere with radius r. Next, system sensitivity is determined by the collimator. For a parallel hole collimator, the collimator sensitivity is a function of the square of the hole diameter g, the collimator height h and the number of holes seen by the source:

$$\text{collimator sensitivity} \sim \frac{g^2}{h^2} \times \#\text{ holes seen}. \tag{2.2}$$

Since the number of holes seen by the source increases proportional to the square of the radius and thus compensates for the geometric sensitivity loss at larger radius, the total sensitivity is independent on the detector

radius:

$$\text{geometric} \times \text{collimator sensitivity} \sim \frac{g^2}{h^2}\frac{r^2}{r^2} \tag{2.3}$$

$$\sim \frac{g^2}{h^2}. \tag{2.4}$$

This interesting property of uniform sensitivity throughout the Field Of View (FOV) of a parallel hole collimated SPECT camera does not hold for other types of collimation which will be discussed in more detail in paragraph 2.3.
Finally, the probability of a photon, impinging on the detector, to be stopped by the detection material, also called the intrinsic detection efficiency will determine the complete system sensitivity. The intrinsic detection efficiency $\epsilon_{int}$is defined as [85]:

$$\epsilon_{int} = \frac{\text{number of events recorded}}{\text{number of photons incident on detector}}, \tag{2.5}$$

is dependent on the attenuation coefficient μ of the detection material and the detector thickness. For energies, relevant to gamma camera imaging, the attenuation coefficient is determined by two effects: the effect of Compton Scattering (CS) and the PhotoElectric (PE) effect. A PE interaction completely converts the photon energy into electron energy, the CS effect only deviates the photon from it's original pathway and only converts part of the photon's energy. The latter effect is undesirable but the relative probability of both effects is thus important when selecting a detection material. A 1 cm thick NaI detector stops 93% of the photons with a relative probability distribution at 140 keV of five PE interactions to one CS interaction.

Energy resolution

The sum of the electrical signals measured at the output of the PMTs in the neighborhood of the interaction is proportional to the energy of the incoming γ-ray. On one hand, the error on this energy measurement is related to the spatially varying light generation in a scintillator. To minimize this effect, an energy calibration procedure is performed. The other source of error can not be corrected for and is directly related to the error on the local energy determination, which - in the case of scintillator based detectors - is Poisson distributed and dominated by the standard deviation $\sqrt{N}$ of the minimal number of information carriers

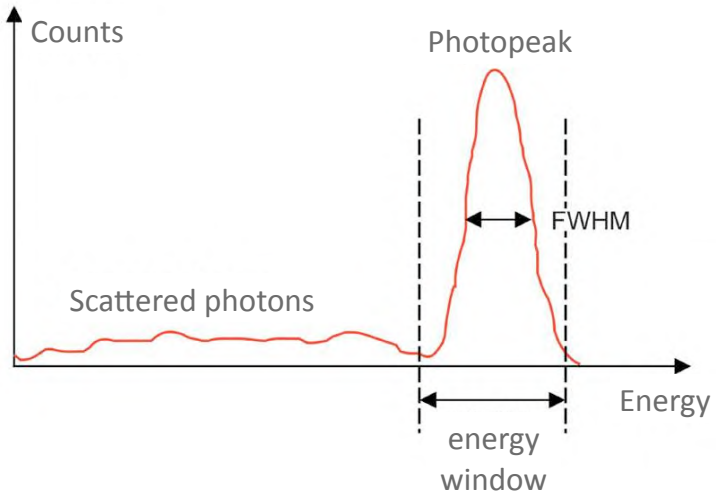

Figure 2.4: A typical energy spectrum measured by a gamma camera. The energy resolution is expressed as the FWHM of the photopeak.

N in the cascade of events leading to the detection of a photon. In a traditional gamma camera, this number N is the number of electrons leaving the photocathode of the PMT. The ratio of N and the number of photons striking the photocathode is expressed in the quantum efficiency of a PMT and is the most important characteristic determining the energy resolution. Energy resolution is expressed as a percentage of the γ-energy and is measured as the Full Width at Half Maximum (FWHM) of the photopeak (figure 2.4). A NaI detector, coupled to PMTs has a typical energy resolution of 11 keV or 8% at 140 keV. A better energy resolution is characterized by a smaller FWHM and will result in an improved image quality since the scattered photons, which contribute to a bias in the image, can be better separated from non-scattered photons which contain the useful information on the tracer distribution. A better energy resolution also allows to better separate two or more photo-peaks in the case of imaging with multiple isotopes.

Spatial resolution

Due to the finite thickness of the crystal and the light-guide, the light will be distributed over several PMTs. A PMT close to the interaction point will measure a high signal while a far-away PMT will measure only

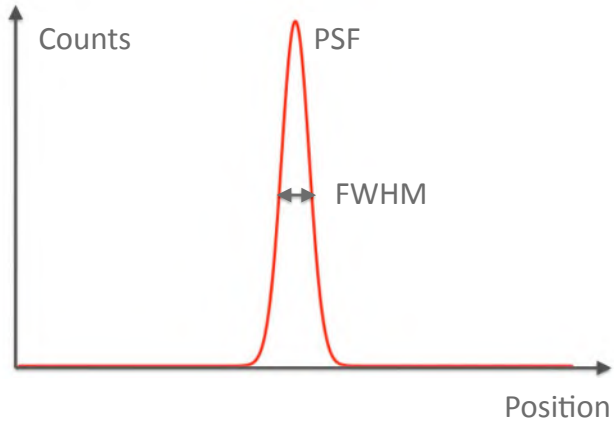

Figure 2.5: A typical point spread function. This is the function which models the acquisition process of a gamma camera. Spatial resolution is expressed as the FWHM of the point spread function.

little light. Event positioning is performed by combining the output of all the PMTs in a given decoding scheme. The most elementary way to decode the position is by applying so-called Anger logic where all PMT positions are weighted by the signal measured at their respective outputs. The precision on the positioning is characterized by the intrinsic spatial resolution and depends on the material and thickness of the scintillator and light-guide, on the size and number of PMTs. Besides the Anger logic weighting scheme for event positioning, a number of other positioning algorithms are applied to more accurately determine the interaction position of the photon [33, 60, 72]. This is especially important for small animal imaging where better intrinsic resolution is mandatory. Also, the Anger logic scheme fails at the edge of a detector. For a continuous crystal, this only affects a small portion of the detector. For pixelated detectors however, a lot more detector area would be lost. A classical NaI detector in combination with PMTs typically offers an intrinsic spatial resolution of 3 mm, defined as the FWHM of the point spread function (PSF) (figure 2.5).

2.3 Collimator Design

In order to extract directional information from light photons for e.g. photography, one relies on the focussing properties of optical lenses. High energy gamma rays can however not be focussed by lenses. Therefore, in order to extract directional information out of a beam of incoming gamma rays, collimators are used. Their task is to absorb all photons, not traveling according to the collimator-imposed direction. As a result, only photons traveling in the required direction will pass the collimator and consequently be detected. In the rectilinear scanner, a single hole collimator was first employed to only accept photons from the region in front of the scanner. Soon, the advantage of magnification induced by a pinhole collimator for imaging of small organs like the thyroid, was appreciated. In the Anger camera, single hole collimation was replaced by parallel hole collimation while the sensitivity gain by using multiple pinholes became clear in the early 1970s [195]. Focussed collimators, first used by Anger in the tomoscanner are now used in the form of fanbeam and conebeam collimators, mainly for brain imaging. All the aforementioned types of collimation suffer from the same trade-off between sensitivity, spatial resolution and FOV. A comparison of the most common collimators with respect to these three criteria will be discussed. For the derivation of the analytical formulas that will be used, the reader is referred to the overview papers by Wieczorek [192], Accorsi [1] and Moore [119].

2.3.1 Parallel hole collimators

A parallel hole collimator can be regarded upon as a numerous amount of closely packed long, parallel holes through a slab of highly attenuating material such as lead or tungsten. Traditionally, it is fabricated by sheets of lead foil, folded in half-hexagonal holes which precisely stacked together form a honey-grate structure. Next to folded collimators, casted collimators based on precise molding techniques exist. The latter type of collimator is more precise and also can be fabricated with smaller thickness of the septa t. Besides the septal thickness, the most important design parameters of a parallel hole collimator are its height h and hole size g (figure 2.6). A parallel hole collimator makes direct 1 to 1 projection images of the source on the detector. Therefore, the FOV of a parallel hole collimator is equal to the size of the detectors which makes this type of collimator generally applicable for all types of nu-

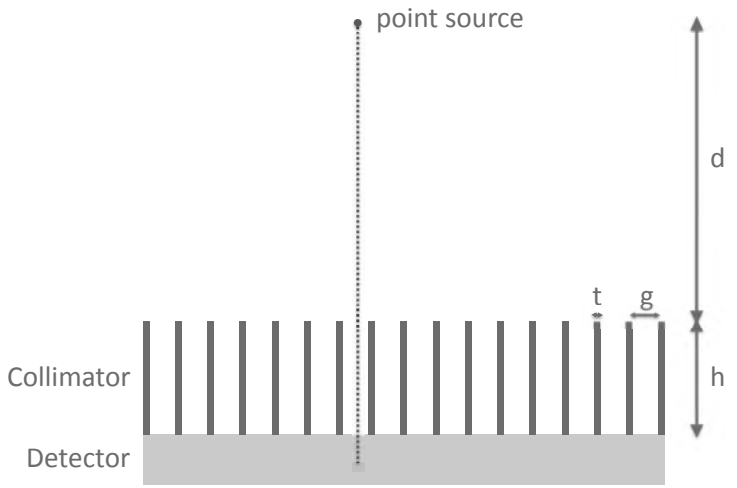

Figure 2.6: Section through a parallel hole collimator with the indication of the notation. This schematic also represents an axial cut through a fanbeam collimator

clear medicine examinations. A critical parameter which determines the collimator design is the energy of the photons that need to be stopped. The septal thickness and the attenuation coefficient μ of the collimator material at the photon energy will determine the amount of septal penetration. This effect can be taken into account by defining an effective collimator height h_{eff}:

$$h_{eff} = h - \frac{2}{\mu}. \tag{2.6}$$

Next, the desired sensitivity and resolution are the parameters determining the design of a collimator. A number of typical collimators, together with their most important geometric parameters and properties can be found in table 2.1. In the next paragraphs, it will become clear that it is wise to use a different type of collimator when a large FOV is not required.

The most important property of a collimator is the trade-off between sensitivity and spatial resolution. The sensitivity of a parallel hole collimator can be generally expressed as:

$$S_{paho} = \frac{g^2}{4\pi h^2}. \tag{2.7}$$

Table 2.1: Properties of some typical collimators. Data from PRISM 3000XP SPECT camera (Philips Medical Systems^{TM}).

	FOV@10cm (mm × mm)	g (mm)	h (mm)	t (mm)	R_{sys}@10cm[b] (mm)	S (cps/MBq)
Parallel Hole (PH)						
General All Purpose (GAP)	240× 400	1.57	25.4	0.24	8.3	229
High Resolution (HR)	240× 400	1.40	27.0	0.18	7.2	168
Ultra High Resolution (UHR)	240× 400	1.40	34.9	0.15	6.2	104
Medium Energy (ME)	240× 400	3.40	58.4	0.86	9.7	172
High Energy (HE)	240× 400	3.81	58.4	1.73	10.8	160
Fanbeam[a] (FB)						
General All Purpose (GAP)	240× 320	1.57	25.4	0.24	8.1	286
High Resolution (HR)	240× 320	1.40	27.0	0.18	7.0	210
Ultra High Resolution (UHR)	240× 320	1.40	34.9	0.15	5.9	131
Conebeam[a] (CB)						
General All Purpose (GAP)	192× 320	1.57	25.4	0.24	8.1	357
High Resolution (HR)	192× 320	1.40	27.0	0.18	7.0	262
Ultra High Resolution (UHR)	192× 320	1.40	34.9	0.15	5.9	163
PinHole (PiH)						
General All Purpose (GAP)	218× 364	3.0	110		6.4	56
High Resolution (HR)	218× 364	2.0	110		5.0	25
Ultra High Resolution (UHR)	218× 364	1.5	110		4.2	14

[a] focus=50 cm

[b] Transaxial, calculated with $R_{int} = 3\ mm$

Collimator resolution is given by:

$$R_{c,paho} = g\frac{h+d}{h}. \tag{2.8}$$

Here, g is the hole size, h is the height of the collimator and d is the distance from the collimator to the point where the sensitivity is evaluated. The complete system resolution of a gamma camera R_s is however not only determined by the collimator. The detector resolution or intrinsic resolution R_i, arising from the finite pulse discriminating capabilities of the detector also contributes to the system resolution. This is important to mention here because the extent to which this intrinsic resolution contributes to the total resolution is determined by the type of collimator. For a parallel hole collimators, assuming both collimator and detector PSFs are 2D Gaussians with respective FWHM R_c and R_i, the total system PSF is a 2D convolution of both PSFs resulting in a system FWHM of:

$$R_{s,paho} = \sqrt{R_{c,paho}^2 + R_i^2}. \tag{2.9}$$

Since the intrinsic resolution is usually small and collimator resolution degrades with increasing collimator distance, it will be important only at small collimator distances where it becomes the dominant factor in the system resolution. From the above formulas it can be read that for a better spatial resolution (smaller R_c), a smaller hole size g or a larger collimator height h should be chosen. However, regarding the sensitivity, a linear change in g or h will result in a quadratically decreased sensitivity. The following far field ($d >> h$) relation between sensitivity and resolution shows the main limitation of a gamma camera, namely that resolution can not be optimized without compromising sensitivity and vice versa:

$$S \sim R_c^2. \tag{2.10}$$

This relation can also be observed from table 2.1: while the resolution improves with a factor 1.4, going from the GAP to the UHR collimator, sensitivity degrades by a factor 2.16. The trade-off is thus not exactly quadratic since parameters such as septal thickness also play a (limited) role in the above equations. More detailed expressions of sensitivity and resolution which take these effects into account can be found in [192].

2.3.2 Fanbeam and conebeam collimators

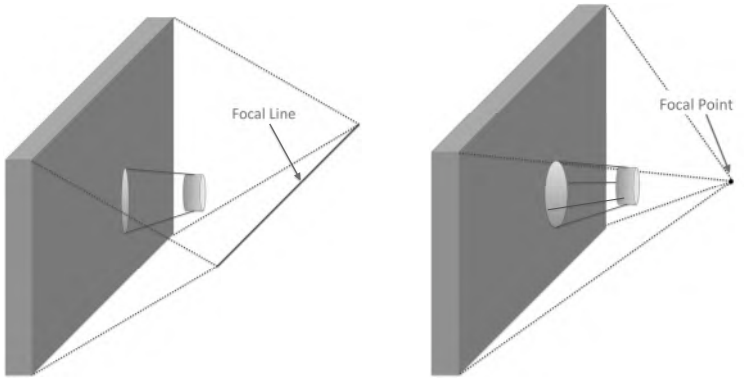

(a) (b)

Figure 2.7: (a) In fanbeam collimators, all holes are directed to a line parallel to the axis of rotation of the scanner. (b) Conebeam collimators have all their holes directed to one single point.

In fanbeam collimators the holes are tilted toward a focal line (figure 2.7(a)) while conebeam collimators have their holes focussed to a point (figure 2.7(b)). Because the focal line of a fanbeam collimator is parallel to the axis of rotation of the camera, we only have a magnification effect in the transaxial direction and no magnification in axial direction. On the other hand, projections made with a conebeam collimator are magnified both in axial and transaxial direction. The focal locus is usually chosen to lie at the opposite side of the patient or object under investigation in order to have magnification in the whole FOV. It has been shown however that in certain imaging conditions it can be better to choose the focal length inside the FOV, e.g. for brain imaging [129]. Also for cardiac imaging, asymmetric focussing collimators have been used.
Compared to parallel hole collimators, an extra parameter is introduced in the sensitivity formula of converging hole collimators, namely f. f is a design parameter representing the distance between the collimator surface and the focal locus of the collimators (figure 2.8). The sensitivity of a fanbeam collimator is, compared to parallel hole sensitivity, increased with a factor $(\frac{f}{f-d})$. For a conebeam collimator sensitivity is additionally increased with $(\frac{f}{f-d})$. This results in the general sensitivity

expression:

$$S = \frac{g^2}{4\pi h^2}\left(\frac{f}{f-d}\right)^n, \tag{2.11}$$

where n respectively equals 1 and 2 for fanbeam and conebeam collimators and d is the distance of the point in the FOV where the sensitivity is considered to the collimator surface. It is thus the ratio of f and the distance from the point to the focal locus (f-d) which determines the gain in sensitivity. There is no gain at the collimator surface ($d = 0$) while sensitivity gain increases the more the focal locus is approached. The sensitivity formula for parallel hole collimators (equation (2.7)) can be derived from equation (2.23) by assuming $n = 0$, but can also be obtained by the insight that a parallel hole collimator is a converging collimator with focal distance f equal to infinity. Collimator magnification m is

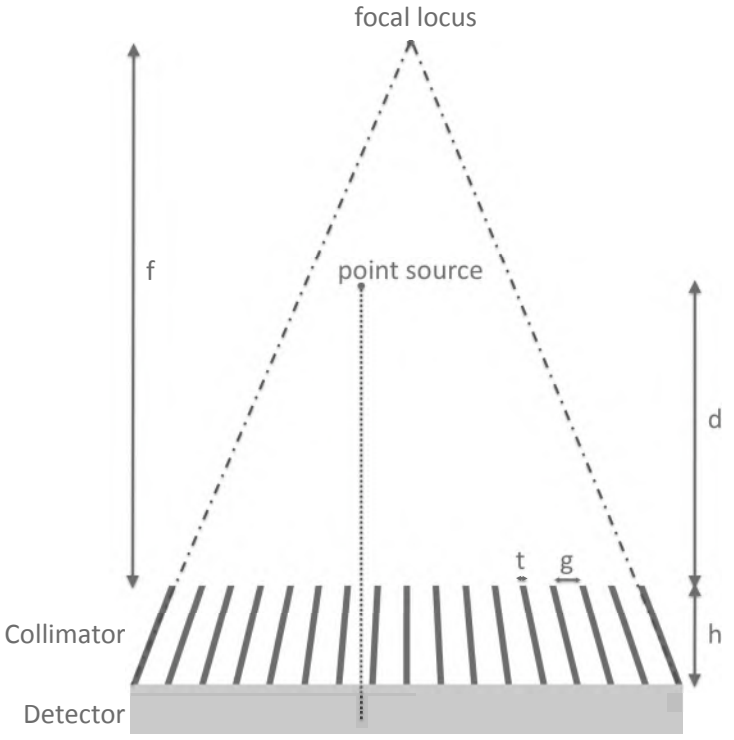

Figure 2.8: Transaxial cut through a fanbeam collimator or conebeam collimator. This schematic also represents the axial cut through a cone beam collimator.

defined as:

$$m = \left|\frac{f+h}{f-d}\right|. \tag{2.12}$$

The collimator resolution of equation 2.8 has to be multiplied by a factor $f/(f+h)$ for the directions where there is focussing. The converging beam collimator resolution $R_{c,cb}$ becomes:

$$R_{c,cb} = g\frac{h+d}{h}\frac{f}{f+h}. \tag{2.13}$$

The intrinsic resolution gets compromised by the magnification effect and thus the system resolution becomes:

$$R_{s,cb} = \sqrt{R_{c,cb}^2 + \left(\frac{R_i}{m}\right)^2}. \tag{2.14}$$

Therefore, a slightly better resolution is obtained with converging collimators. The price paid for the better sensitivity and slightly better resolution is the smaller FOV_t which reduces to:

$$FOV = \frac{D}{m}, \tag{2.15}$$

with D the FOV of a parallel hole collimator or, in other words, the size of the detector. The axial FOV of a fanbeam collimator remains unchanged compared to a parallel hole collimator. A more detailed investigation of converging collimator characteristics can be found in [70], [32], [87], [128], [129] while the problem of singularity at the focal locus ($S \to \infty$) of converging collimators is solved in [2] and [3]. A review on convergent beam collimation, including pinhole collimation, was provided by Gullberg [64].

2.3.3 Pinhole collimators

A pinhole is, like applied in the camera obscura, a very natural way of projecting (and mirroring) a large object (e.g. the outside world) to a small surface (e.g. a wall in a dark room). In nuclear medicine, pinhole collimators were used from the very beginning to make projections of small regions of interest to a larger detector surface. As opposed to the camera obscura, where objects are mapped to a minified projection

image, a pinhole collimator exhibits the magnification effect by placing the object close to the pinhole. This magnification effect will again - like with converging hole collimators - minimize the effect of intrinsic detector resolution. This property, together with the high sensitivity in the near field make collimation with pinholes an attractive alternative when imaging small organs like the thyroid [81], parathyroids [149], joints [13] or kidneys [11]. The magnification m of a pinhole collimator is defined

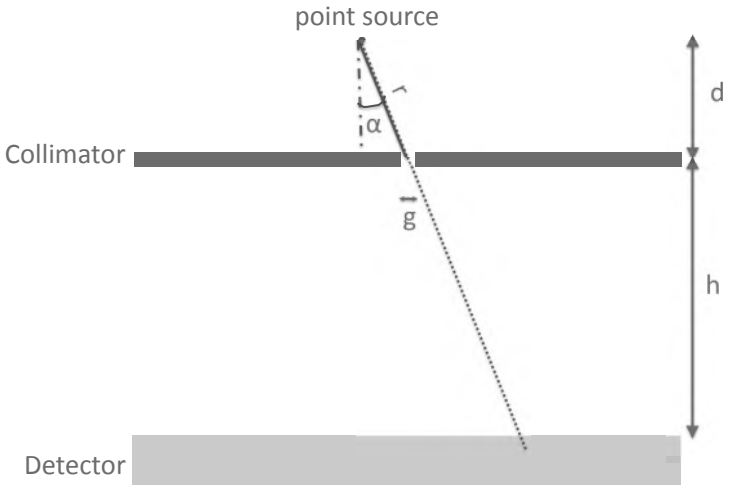

Figure 2.9: Cut through a pinhole collimator.

as:

$$m = \frac{h}{d}, \tag{2.16}$$

with h the detector pinhole distance and d the distance from the object to the pinhole plane (figure 2.9). The sensitivity of a pinhole collimator is equal to the normalized solid angle subtended by the pinhole. For a round pinhole, sensitivity equals:

$$S = \frac{\pi \frac{g^2}{4} \cos\alpha}{4\pi r^2} \tag{2.17}$$

$$= \frac{g^2}{16 d^2} \cos^3\alpha, \tag{2.18}$$

with $r = d/\cos\alpha$. A square pinhole has sensitivity equal to:

$$S = \frac{g^2 \cos\alpha}{4\pi r^2} \tag{2.19}$$

$$= \frac{g^2}{4\pi d^2} \cos^3\alpha, \tag{2.20}$$

Collimator resolution is equal to the resolution of a parallel hole collimator:

$$R_{c,ph} = g\frac{h+d}{h}. \tag{2.21}$$

For pinholes, h however represents the detector-pinhole distance which is usually larger compared to the height of a parallel hole collimator. Therefore, collimator resolution of a pinhole will be better. Total system resolution is given by:

$$R_{s,ph} = \sqrt{R_{c,ph}^2 + \left(\frac{R_i}{m}\right)^2}. \tag{2.22}$$

The FOV of a pinhole collimator gets smaller by a factor m. Thus, the closer to the pinhole, the smaller the FOV. Here the trade-off between sensitivity, spatial resolution and FOV again plays an important role. From sensitivity and resolution point of view, we would like to image as close as possible to the pinhole. However, the FOV reduces to zero when $d = 0$ (in reality, the FOV reduces to the size of the pinhole). In principle, when d would be larger than h, a FOV larger than the detector could be scanned. This is however never done in practice because the sensitivity decreases proportional to d^2 and already is too low at $d = h$.

2.3.3.1 Multi-pinhole collimators

Pinhole collimators are mostly applied when a better spatial resolution is desired. When the object is small and when the pinhole can physically be brought near the object, better resolution at equal sensitivity is possible. From the formulas it is clear that again, with better resolution (smaller pinhole diameter g), sensitivity is quadratically decreased. Thus, when even higher resolution is desired, such as in preclinical imaging, sensitivity can be increased by directing multiple pinholes in the direction of the object. This approach was first introduced in nuclear medicine in

the early 1970s by Wouters [195]. Multi-pinhole systems have had limited applications in clinics but are still under active investigation and are promising for imaging of the heart [180][53][153], brain [130] kidneys [46] and bone [127]. On the other hand, multi-pinhole collimation has become the standard in small animal SPECT imaging. Pre-clinical multi-pinhole systems can be classified according to their number of pinholes, but also as stationary or non-stationary. Also the degree of overlap of projections from different pinholes, called multiplexing is an important area of research. With these systems, resolutions down to 150 μm have been reported. Numerous different systems exist from which the most important have been developed by McElroy [111] (A-SPECT), Schramm [141] (HiSPECT), Beekman [17] (U-SPECT), Lackas [90] (T-SPECT) and Kim [83] (SemiSPECT). An overview of multi-pinhole collimation for pre-clinical imaging can be found in [14] .

2.3.3.2 Sampling completeness

One of the major problems in collimation with pinholes is the sampling completeness. Complete data are only recorded in the transaxial plane of the pinhole (which we will assume to be the central slice). Other transaxial slices suffer from incomplete data which results in artifacts after image reconstruction. Typically, these artifacts become more pronounced, the further we move away from the central slice. The extent of these artifacts are usually visualized by scanning a Defrise disk phantom (Data Spectrum Corp.) which is a stack of axially repeated cold and hot slices. Typically, for a pinhole collimators, the more a slice is axially off-center, the more artifacts it will show after reconstruction.
The first to address the issue of data completeness for parallel hole collimation was Orlov [126]. For a point in the FOV of the camera, each possible photon detection path to the detector is intersected with a unit sphere, centered at the point considered. The union of points formed by the intersection of the projection lines and unit sphere defines a region Ω on the Orlov sphere. Orlov's condition for data completeness is fulfilled when any circle on the Orlov sphere intersects Ω. Sampling incompleteness becomes more severe if more great circles can be drawn without intersecting Ω. For a parallel hole collimator, Orlov's condition holds for all points in the FOV, when the detector is rotated for at least 180°. For points in the central slice in the FOV of a pinhole collimator, Ω is also a great circle or equator and thus data are complete (figure 2.10 (a)). The more one moves axially off-center, the more the circle formed

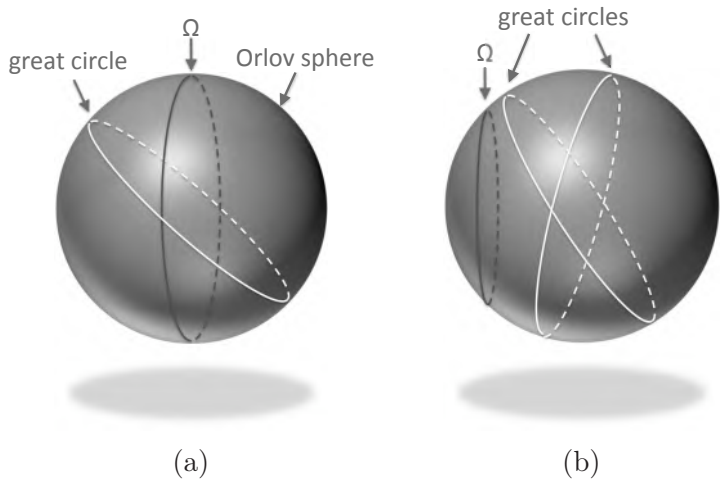

Figure 2.10: (a) Projections on the Orlov sphere for (a) all points in the FOV of a parallel hole collimator and the central transaxial slice in the FOV of a pinhole collimator. No great circle can be found that does not intersect Ω while in (b), showing the projections for an off center point in the pinhole FOV, a lot of great circles can be drawn that do not intersect Ω.

by the points Ω shifts toward the poles and more great circles can be found that do not intersect Ω (figure 2.10 (b)). Thus, the more we move off-center, the less complete the data will be. Also conebeam collimators suffer from data incompleteness toward the edge of the FOV, but there the effect is usually less pronounced since, in most cases, the focal distance is relatively large. Solutions for the problem of sampling incompleteness consist of scanning orbits different from circular ones (e.g. helical scans) [21],[116] or using multi-pinhole collimators [43].

2.3.4 Slit-slat collimators

Slit-slat collimators are based on a number of parallel slats which are placed on the detector (figure 2.11). This slat collimation results in one-directional collimation as opposed to two-directional collimation in a parallel hole collimation. However, in the direction perpendicular to the slats, photon selection is the same as with a parallel hole collimator. Most commonly, the slats are oriented perpendicular to the axis of rotation (AoR), resulting in an axial collimation equal to parallel hole collimation. To get information from the transaxial direction, a slit is

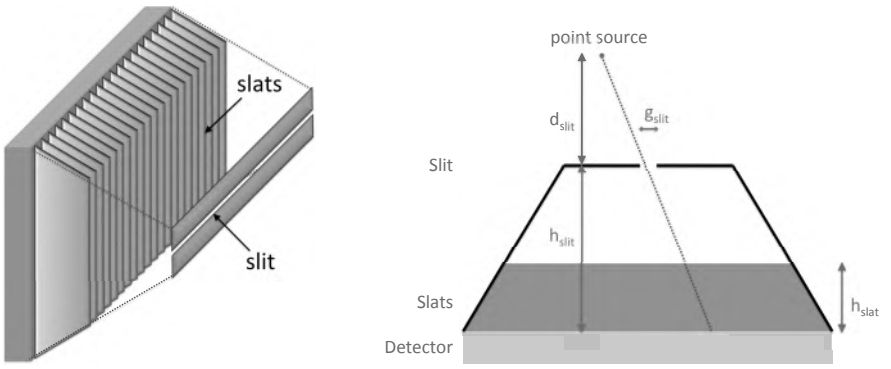

(a) (b)

Figure 2.11: (a) A slit-slat collimator combines properties of a parallel hole collimator in axial direction while exhibiting the high sensitivity properties of a pinhole collimator in transaxial direction. The transaxial geometry is clarified in (b).

placed above the slats, parallel to the AoR. This results in pinhole collimation in the transaxial direction. Slit-slat collimation is thus nothing more than parallel hole collimation in axial and pinhole collimation in transaxial direction. The advantage of this collimator is that there will be no artifacts in the reconstructed image when axially moving away from the center and that a higher sensitivity can be obtained for equal (transaxial) resolution compared to a pinhole collimator. Resolution formulas can be borrowed from parallel hole collimators for the axial direction and from pinhole collimation for the transaxial direction. Sensitivity calculation is however more complicated and for on-axis points has been shown to be equal to the geometrical mean of pinhole and parallel hole sensitivity [115]. A more general expression of the sensitivity which is correct for all points in the FOV is given by Accorsi [4]:

$$S = \frac{g_{slit} g_{slat}}{4\pi d_{slit} h_{slat}} \cos^3 \alpha, \tag{2.23}$$

with g_{slit} and g_{slat} respectively the slit width and the slat spacing. d_{slit} is the perpendicular distance between the slit and the point where sensitivity is evaluated while h_{slat} is the slat height. When a smaller transaxial FOV is allowed, a slit-slat collimator can be used as an alternative which is situated in between pinhole collimation and parallel hole or fanbeam collimation. In transaxial direction, the slit-slat collimator inheres the

resolution properties of a pinhole collimator - which is usually better due to larger h - while sensitivity is still high. Also sensitivity does not drop as fast with collimator distance d compared to a pinhole collimator. Furthermore, sampling completeness is fulfilled for an orbital scan in all points of the FOV. Axial resolution is equal to parallel hole resolution. However, in most designs, the object can not be placed near to the slats because of the presence of the slit, causing an offset in axial resolution (figure 2.13(b)). Slit-slat collimators were first applied in the SPRINT brain SPECT camera design by Rogers [139, 140] and have been applied in cardiac studies [31] as well as in small animal imagers [185].

2.3.5 Optimal choice of collimator and collimator optimization

To answer the question of which collimator type to use for which study, sensitivity, spatial resolution and FOV are the main characteristics to look at. In figure 2.12, a comparison of the sensitivity of the previously described collimators is made. It can be respected that pinhole or slit-slat collimation should be used when the object is small and can be placed close to the detector. Further away, fanbeam and conebeam have higher sensitivity, at the cost of smaller FOV. In figure 2.13 and figure 2.14, collimators can be compared on basis of respectively spatial resolution and relative size of the FOV. Resolution is generally better with pinhole collimators. Slit-slat collimators offer better transaxial resolution while axial resolution is worse. This is due to the fact that the object can not be placed close to the slats due to the slit which usually is situated higher than the slats. The design parameters are based on clinically used collimators (table 2.1). As a summary one could state that parallel hole collimation is the best choice for whole body imaging which requires a large FOV for a reasonable scan time. Fanbeam and cone beam collimators are only advantageous when smaller organs are imaged at relatively large distance because their sensitivity increases with the collimator distance. When the organ of interest is small and can be placed close to the detector (small animal imaging), pinhole or multi pinhole collimation is preferable because for equal sensitivity, much better spatial resolution can be obtained. The slit-slat collimator should be situated in between parallel or fanbeam collimation and pinhole collimation. It combines the advantages of superior transaxial resolution and high sensitivity close to the slit. Furthermore, extended axial FOV and extended axial sampling completeness with respect to pinhole collimation is traded for axial

resolution.

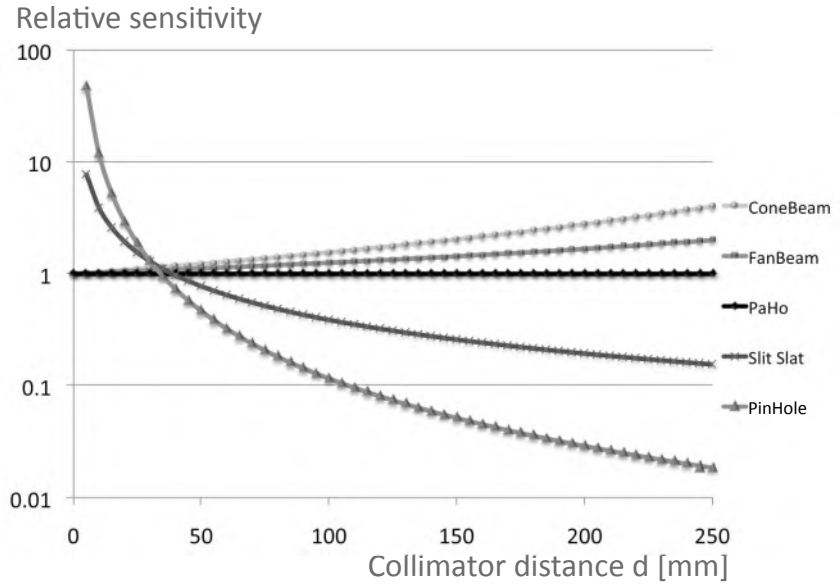

Figure 2.12: In this plot, the on-axis sensitivity is compared relative to the sensitivity of a parallel hole collimator. Closer than 3 cm to the collimator, it is advantageous to use a pinhole or slit-slat collimator while for the converging hole collimators, sensitivity increases while moving further from the collimator. Design parameters for drawing these plots can be found in table 2.1

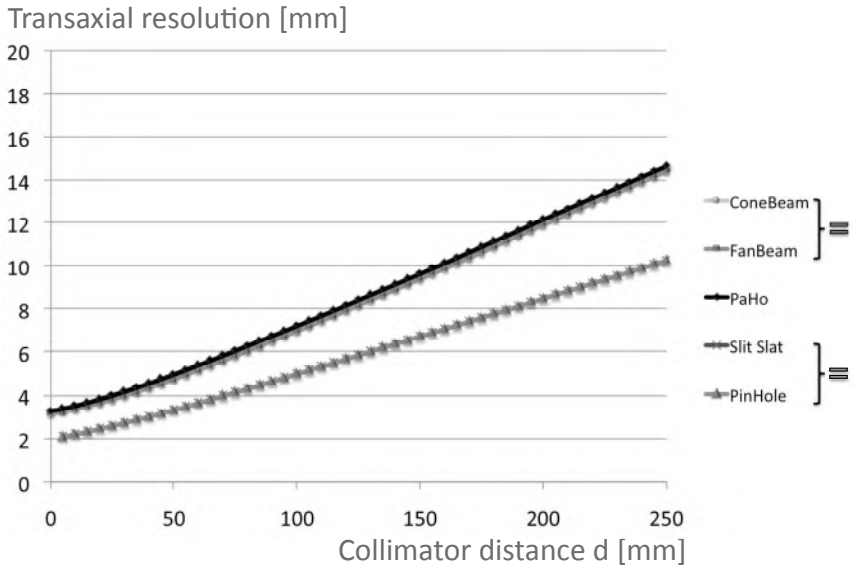

(a)

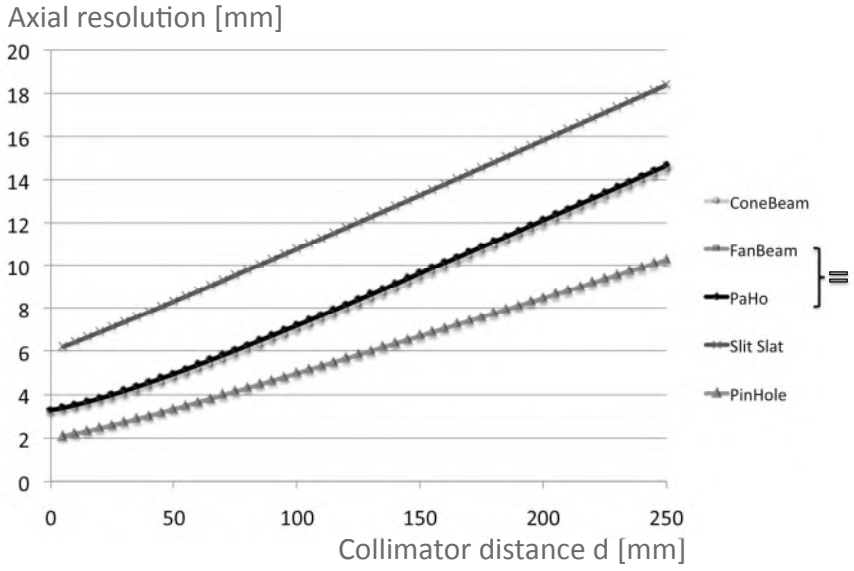

(b)

Figure 2.13: Plot (a) and (b) respectively compare the transaxial an axial resolution that can be obtained with the different collimators. Transaxial resolution is equal for fanbeam and conebeam and also for pinhole and slit-slat collimation. Axial resolution is equal for parallel hole and fanbeam collimators. The axial resolution of a slit-slat is worse compared to parallel hole because zero collimator distance is defined by the slit height h_{slit} and not by the slat height h_{slat}. The design parameters used can be found in table 2.1

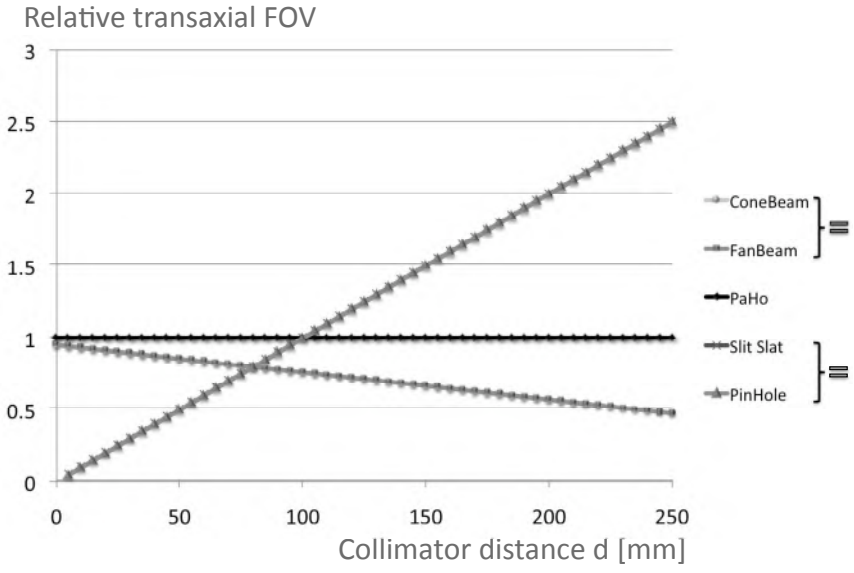

(a)

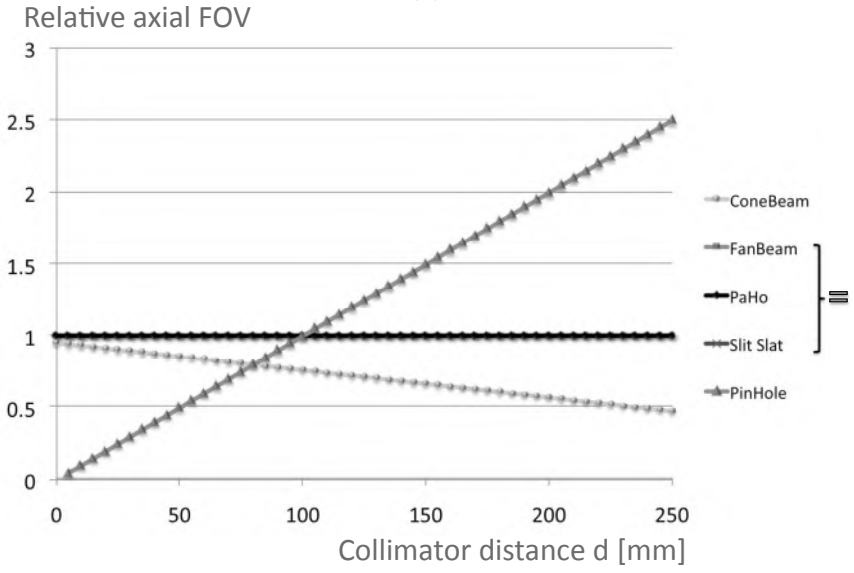

(b)

Figure 2.14: Plot (a) and (b) respectively compare the transaxial and axial FOV, relative to the FOV of a parallel hole collimator. Transaxial FOV is equal for fanbeam and conebeam and also for pinhole and slit-slat collimation. Axial FOV is equal for parallel hole, fanbeam and slit-slat collimators. The design parameters used can be found in table 2.1

For a long time, there was only an optimization of collimators with respect to the allowable fraction of penetration of Tc-99m photons and with respect to the desired resolution at a certain distance [79]. This ad-hoc approach does not take into account photon noise, nor background or lesions variability which influence both lesion detection and activity estimation. An optimization of parallel hole collimators based on projection images has been made by Moore [117] and more specifically with respect to optimal detection and estimation for the special case of Ga-67 imaging in [118]. For tomographic imaging, an optimization of the collimator has been proposed by Zeng [201]. This study and a study by Kamphuis [76]. suggest that for SPECT, one should use larger collimator holes at the expense of spatial resolution, which can be recovered using an accurate system model during image reconstruction. Collimator optimization is especially important for isotopes which are not mono-energetic emitters. For instance, optimal collimator choice for I-123 imaging, hampered by the down-scatter and collimator penetration of high energy photons, has been the subject of a large number of studies [35, 55, 69].
Optimization of pinhole and especially multi-pinhole collimation is especially important for preclinical molecular imaging. A simulation study by Cao [27] finds the optimal number of pinholes to be used for a fixed geometry and the specific application of mouse brain imaging. An analytic technique proposed by Rentmeester [136] finds the optimal tradeoff between sensitivity and spatial resolution through a feedback loop which varies the pinhole diameter for a fixed field of view. Yet another study proposes a theoretical method to optimize multi-pinhole imaging for the special case of post-smoothed MLEM image reconstruction [182]. The parameters to be optimized in this study were hole size, collimator distance, collimator height, acceptance angle, position and number of pinholes.

2.3.6 Rotating slat collimators

Rotating slat collimators, which are the subject of this dissertation, break with the traditional collimators described above. They fundamentally differ in the sense that instead of line integrals, they measure plane integrals. Furthermore, rotating slat collimators exhibit a different resolution/sensitivity relationship which will be studied in the next chapter of this dissertation. This type of collimation has been used in combination with solid state detectors in the SOLSTICE (SOLid STate Imager with Compact Electronics) design proposed by Gagnon [54, 63]. Due to the ro-

tating slat design, only a limited number of detector elements is required to fill a strip area which reduces the cost. A similar design has been published by Entine [48] about 20 years ago combining a CdTe detector with a parallel plate collimator. Before this the design of a linear detector has been proposed independently by Keyes [82] and Tosswill [154]. Traditional rectangular SPECT detectors have been studied in combination with rotating slat collimators by Webb, who found an increased sensitivity of about a factor of 40 for the rotating slat concept [190]. Due to the different nature of the data measured by this collimator, other reconstruction techniques have to be used to reconstruct images. Analytic reconstruction methods for planar and tomographic acquisitions have been derived by Lodge [102, 103]. The conclusions drawn from these studies was that regarding signal-to-noise in the images, it is advantageous to use rotating slat collimators instead of parallel hole collimators in the cases of hot spot imaging in small objects. A 3D iterative reconstruction algorithm for the data from the SOLSTICE camera has been proposed by Wang [187] and by Zeng [200]. In [187], next to better hot spot contrast, also an increased contrast was found for cold lesions.

2.4 Photon integrating detectors for SPECT

2.4.1 Scintillator based detectors

Scintillator based detectors still work according to the principle of the classical gamma camera. Gamma rays are converted by the crystal into light photons which are converted in a second step to an electrical signal (section 2.2.2). Evolutions in performance of these types of detectors are found on one hand in the search for new scintillation crystals with higher density and better light yield. On the other hand, there is an evolution in the readout technology for converting light photons into electrical current from the original PMTs to some other devices which mainly are aiming for smaller dimensions, better spatial resolution and insensitivity to magnetic fields.

2.4.1.1 Scintillators: conversion of high energy photons to visible light photons

The most important scintillator, which is still used in most commercially available systems today, is NaI(Tl). Other scintillators, used in research

SPECT scanners are CsI(Tl) and $LaBr_3$(Ce). Their main properties are summarized in table 2.2.

	Density [g/cm^3]	**Light yield [photons/keV]**	**Light wavelength [nm]**
NaI(Tl)	3.67	38	415
CsI(Tl)	4.51	54	550-565
$LaBr_3$(Ce)	5.08	63	380
$LaCl_3$(Ce)	3.85	49	350

Table 2.2: Properties of the most important scintillators for SPECT (data from Saint-Gobain Crystals).

The density of the scintillation material is related to the stopping power. The higher the density, the smaller the required thickness of the crystal. Intrinsic resolution of a thin detector will be better compared to a thick detector because there will be less spreading of the secondary emitted light photons. However, when the detector is pixelated, the light will usually only spread within the pixel. The intrinsic resolution is then defined by the crystal pixel size. Furthermore, CsI(Tl) can be grown in a structure of fine needles with diameters as small as 10 μm. This results in a very good intrinsic detector resolution and is used nowadays in digital RX systems. For SPECT however, the requirements on the light conversion step are more demanding. Where an RX detector is photon counting, a SPECT detector has to be photon integrating in order to measure the energy of each individual gamma quantum. This results in a more frequent read-out and thus less light per channel or lower Signal to Noise Ratio (SNR). Additionally, pixelated crystals and columnar structures in particular have lower light yield due to absorption at the edges of each pixel or column. In comparison with continuous crystals, this results in even higher requirements with respect to the light convertors. From this point of view, $LaBr_3$(Ce) is a promising scintillator because it has high density and excellent light yield. As explained previously, the latter is especially important to obtain a better SNR at the read-out pixel level which finally reflects in a better energy resolution. Energy resolution is thus not only defined by the incoming gamma ray energy but also by the light yield of the scintillator.

2.4.1.2 Light conversion into an electrical signal

The PMT will also play an important role in the energy resolution. A PMT basically consists of a photocathode and a number of dynodes, which amplify the electrons in order to have a measurable current at the output. Although the dynodes occupy the largest space in a PMT, they are not important for the energy resolution. The key component of a PMT is the photocathode which converts the light photons to electrons through the photo-electric effect. The design of the photocathode has to be such that enough light photons are stopped and enough secondary generated electrons should be able to escape. The thicker the cathode, the more light photons are stopped, but the less electrons will escape. Once the optimal thickness is determined, the Quantum Efficiency (QE) of the photocathode - the number of electrons generated per number of incoming light photons - defines the quality of a PMT [85]:

$$QE = \frac{\text{number of secondary electrons}}{\text{number of incoming light photons}}. \tag{2.24}$$

The QE of a PMT dependent on the wavelength. A maximum of typically 30%, optimized for the wavelength - and thus scintillator - of interest. Furthermore, it is important that a measurable electrical pulse is created. In this context, 'measurable' means that the signal amplitude needs to be large enough compared to the noise in the front-end electronics. The amplitude of the signal provided at the output of a PMT is defined by the gain, which typically is in the order of 10^5 for a PMT. The higher the gain will be, the lower the requirements - and thus cost - of the detector electronics.

2.4.1.3 Example of energy resolution calculation

The energy resolution is besides the intrinsic spatial resolution (section 2.2.3) the most important characteristic of a gamma camera detector. A simple example of a NaI(Tl) detector in combination with a typical PMT will give insight in the mechanisms of photon detection and the influence of the cascade of detection steps on the energy resolution. For NaI(Tl), we typically need 20 eV to create a 420 nm light photon. For the energy of a gamma emitted by Tc-99m (140 keV), a complete absorption would result in 7000 light photons. Due to phosphorescence

and quenching (respectively a slow light response and radiationless de-excitations), this number is reduced by 20% to a mean of 5600 light photons. Light loss at the edges of the scintillator and between the PMTs is typically 25% resulting in 4200 light photons reaching the light detector. A QE of 30% results in 1260 secondary electrons which are multiplied by the dynodes by a factor of 10^5, resulting in a measurable voltage. The statistical fluctuations on the lowest number of information carriers will determine the energy resolution. In this example, the lowest number is the number of secondary electrons escaping the photocathode. Statistical fluctuations are defined by a Poisson process where the standard deviation is equal to the square root of the mean number:

$$\begin{aligned}
\text{Energy resolution} &= \frac{FWHM}{E_0} && (2.25)\\
&= \frac{2.35\sigma}{E_0} && (2.26)\\
&= \frac{2.35\mathrm{k}\sqrt{\mu}}{\mathrm{k}\mu} && (2.27)\\
&= \frac{2.35}{\sqrt{1260}} && (2.28)\\
&= 6.6\%@140\text{ keV}, && (2.29)
\end{aligned}$$

where σ and μ are respectively the standard deviation and mean number of secondary electrons. In Gaussian approximation, the fixed ratio between FWHM and standard deviation is 2.35. E_0 is the gamma ray energy which is assumed to be in linear relation to the mean number of information carriers with k as a proportionality constant. This numerical example results in an energy resolution of 6.6% which is an underestimation compared to the typical gamma camera energy resolution which is around 10%. This can be explained by crystal non-uniformities and varying reflection conditions when considering a complete system instead of just one part of a crystal and one PMT. Also, there are differences in the photo-electron collection efficiency for the different PMTs. All these factors lead to a further spreading of the energy resolution of a complete gamma camera.

2.4.1.4 Alternatives for PMTs

Alternatives for PMTs have been developed during recent years. Several types are described below and characteristics of some typical devices are

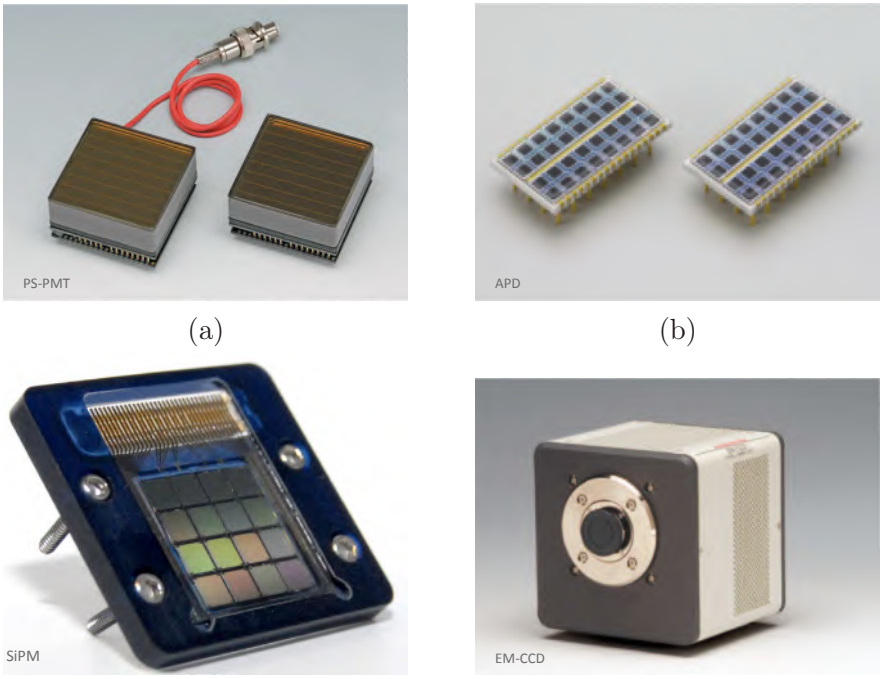

(a) (b)

(c) (d)

Figure 2.15: Alternatives for PMTs: (a) The Hamamatsu H-8500 PS-PMT, (b) Hamamatsu S-8550 APD, (c) SensL SPM array SiPM and (d) Hamamatsu C9100-02 EM-CCD camera.

given in table 2.3:

- Position sensitive PMTs:
  Where a detector with classical PMTs determines the position by applying Anger logic, a position sensitive PMT (PS-PMT) intrinsically offers the ability to discriminate position. Next to the measured signal, a PS-PMT also presents the 2D position at its output by segmenting the anode [188] [121]. PS-PMTs are more expensive and are usually much smaller compared to single PMTs. Furthermore, where single PMTs are round, PS-PMTs are square and therefore have lower dead space when packed together (figure 2.15 (a)). This makes them ideally suited for readout of pixelated crystals. PS-PMTs therefore can be found in systems where higher spatial resolution is obtained by pixelization of the crystal. Examples are microPET [120, 155, 189] and microSPECT

systems [142, 106, 185]. Mainly due to their smaller footprint, PS-PMTs are also used in human scintimammography scanners [193].

- Avalanche photodiodes:
  Avalanche PhotoDiodes (APDs) are silicon devices which convert incident light photons to electron-hole pairs. By applying a reverse voltage over the device, the electron-hole pairs are multiplied by the avalanche effect resulting in a measurable electric signal on the electrodes [144], [39]. Advantages of the APD include resistivity to magnetic fields for use in an MRI scanner and smaller dimension. The APD can also be position sensitive and is therefore, like the PS-PMT, also used in combination with pixelated crystals. Unlike the PMTs, APDs were developed for use in hybrid imaging in combination with MR imaging.

- Silicon photomultipliers:
  In recent years, SiPMs have become of interest and can now already be found in a lot of research centers, serving as a replacement for the APD, especially for PET applications. Like APDs, SiPMs are immune to magnetic fields but they offer the advantage of very high gain which reduces the cost of the front-end electronics. The functional building block of a SiPM is an APD, which is operated in Geiger mode (bias above breakdown voltage). A lot of small 20 to 50 μm APDs are connected in parallel to form one pixel of e.g. 3 mm^2. The output of a single SiPM pixel is thus the sum of the outputs of all individual APDs. Since the APDs measure individual light photons, the pixel output will be proportional to the energy of the incoming gamma ray. Operating the APDs in Geiger mode offers excellent gain but the main drawback of this approach is that their are dead zones in between the small APD cells, resulting in a smaller Photon Detection Efficiency (PDE), which is the QE multiplied by the fill factor. The fill factor is dependent on the cell size and varies from 30 to 80% for respectively 25 to 100 μm cell size. Instead of specifying the QE, one should thus specify the PDE for a SiPM. Furthermore, current SiPMs still have low QE for the light wavelength of SPECT scintillators like NaI and CsI. To make SiPMs more suitable for SPECT, attempts are ongoing to make them more sensitive to blue light.

- Electron-Multiplying Charge-Coupled Device (EM-CCD):
  Electron-Multiplying Charge-Coupled Devices (EM-CCDs) have

Table 2.3: Main characteristics of light converters used in nuclear medicine (data from Hamamatsu).

Hamamatsu	PMT R1307	PS-PMT H5800	APD S8550	SiPM S10362-33-100C	EM-CCD C9100-02
QE (PDE for SiPM)	30	30	70	56	60
Gain (%)	2.7×10^5	1.5×10^6	50	2.4×10^6	2000
Pixel size	76 mm[a]	5.8 mm^2	1.6 mm^2	3 mm^2	8 μm^2
Packing fraction (%)	67	89	78	82	fiber optic taper[b]
MR compatible	N	N	Y	Y	N

[a] PMT diameter. Positioning is done with a positioning scheme such as Anger logic.

[b] The pixel size of these devices is so small that there is usually a taper of a factor 2 to 4 from scintillator to EM-CCD.

been experimentally used by de Vree [38] in combination with columnar CsI(Tl). SPECT images with exquisite spatial resolution of 60 μm were reported. Ordinary CCDs can be found in every digital camera and consists of a lot of individual pixels. Their main property is the very small cell size that can be obtained. In these silicon cells, charge is built up as a response to light photons which are incident on them. The readout of the many small charges happens in a serial way by shifting the charges from one cell to another. An EM-CCD differs from a CCD in the sense that much more charge is built up by the cells. This is necessary because in nuclear medicine applications, the light output of a scintillator is much lower compared to the light present when making a photograph with a regular CCD. In radiography, CCDs have been used for a long time to read the light photons of a CsI crystal. However, in a SPECT exam, the energy of every individual photon has to be determined which translates in a much more frequent readout, which would again results in a charge built-up which is too low to be measurable. For these reasons, EM-CCDs, with an internal gain of typically 500 should be used for gamma camera applications. EM-CCDs are expensive and additionally require cryogenic cooling down to -50° C.

2.4.2 Solid-state detectors

Semiconductor detectors or solid-state detectors fundamentally differ from scintillator based detectors in the sense that a direct conversion from gamma quantum to electrical signal is achieved. Each incident gamma ray creates a number of electron-hole pairs, typically several ten-thousands. By applying a voltage over the semiconductor, the holes and electrons will start drifting toward their corresponding electrode, hereby inducing an electric charge on these electrodes (figure 2.16(a)). The main advantage of a solid state detector is the large number of information carriers because more information carriers are formed per unit energy and there is no extra conversion which would result in a lot of information carriers to be lost. This results in a superior energy resolution which will be dominated by noise in the front-end electronics. Furthermore, the statistical variation on the electron-hole pair creation is not defined by a Poisson process. The variance on the electron-hole pair generation is typically only about 10% of the variance in a pure Poisson process. This deviation is expressed in the so-called Fano factor. The most de-

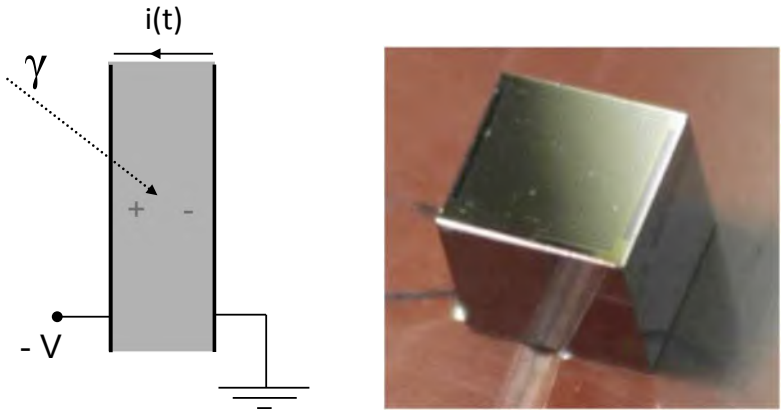

(a) (b)

Figure 2.16: (a) In a solid state detector, incoming gamma ray energy is converted into charge, induced by the movements of electrons and holes. In (b) a typical CZT detector is shown (image courtesy of University of Dortmund, Germany).

veloped solid state detectors for gamma ray spectroscopy are Si and Ge. While both offer exquisite energy resolutions, Si has the disadvantage of low stopping power and Ge has a small band-gap energy, requiring cryo-

genic cooling. The most frequently used solid-state detector in nuclear medicine is therefore CdZnTe (figure 2.16(b)), which has a high stopping power, is room temperature operable and has a theoretical energy resolution of 0.4% at 140keV. In practice, the energy resolution is degraded by hole trapping and noise in the read-out electronics to values of 1 to 3% at 140keV [112]. In a semiconductor detector, anode pixelization makes it possible to discriminate position. Each anode is then read by individual amplifiers, which have to be very low noise in order to maintain energy resolution. These demands on the amplifiers in combination with the large number of amplifiers required makes a solid-state still an expensive alternative compared to a classical scintillator based detector.

2.5 Iterative image reconstruction

The physical image formation process in a gamma camera can be generally expressed as:

$$s_i = \iiint_{FOV} f(x,y,z) h_i(x,y,z) dxdydz. \tag{2.30}$$

This process maps a continuous function $f(x,y,z)$, which is the tracer distribution in the body of the patient, to a discrete function $\mathbf{s} = (s_1, ..., s_i, ..., s_I)^T$, with I the number of measurements. The measurement is discrete due to the subdivision of the detector in a limited number of pixels and the finite number of rotation angles. The discrete measurement is typically stored in a so called sinogram where the detections are histogrammed according to detector position and rotation angle.In the above formula, the operator $h_i(x,y,z)$ expresses the probability that a photon, generated at position (x,y,z) is detected in sinogram bin i. This weighting function typically has a tube-like support and therefore limits the integration to the domain where $h_i(x,y,z)$ is non-zero. For SPECT, the effect of collimator resolution appears in $h_i(x,y,z)$ as a broadening of the integration kernel while moving away from the collimator. Also effects like attenuation, scatter and collimator penetration can be included in the kernel.
The problem of image reconstruction is to find back the tracer distribution $f(x,y,z)$ from the measured sinogram s_i and the approximate model of the imaging process $h_i(x,y,z)$. One of the main factors influencing the quality of a certain image reconstruction method is the accuracy with which $h_i(x,y,z)$ can be defined. The more effects modeled and the

more realistic their description, the more accurate the reconstruction will be. To derive a reconstruction method, one can proceed with the continuous-discrete model, which is natural to the image formation process. In this model, the continuous function $f(x, y, z)$ is represented as the superposition of the integration kernels $h_i(x, y, z)$, so-called natural pixels [178, 25]:

$$f(x, y, z) = \sum_{i=1}^{I} q_i h_i(x, y, z). \tag{2.31}$$

The reconstruction problem is now solved by finding the coefficients q_i. On the other hand, one might interpret the measurement $\mathbf{s}$ as samples of a continuous function, resulting in a continuous-continuous (C-C) imaging model. A well known image reconstruction technique derived according to this model is Filtered BackProjection (FBP), based on the inversion of the Radon transform. The main limitation of this approach is that the Radon transform replaces each tube-shaped integration kernel by a simple line of integration. Therefore it is not possible to model the imaging physics. Also, no model of the data statistics is included, resulting in noisy reconstructions. Finally, streak artifacts appear in the images due to discretization errors with respect to the finite number of detector elements and rotation angles [68]. Despite all these limitations, FBP has for a long time been the standard reconstruction method in nuclear medicine thanks to its short reconstruction time. The last and nowadays most frequently used image reconstruction methods are based on the discrete-discrete (D-D) model, where the continuous tracer distribution function is represented by a set of discrete basis functions. These basis functions are usually nothing more than non-overlapping unitary functions with cubic support, also called voxels. Nevertheless, more complicated basis functions have been proven to better represent the continuous tracer distribution. Entry points to literature on iterative reconstruction can be found in [99, 95, 176, 92].

2.5.1 Reconstruction based on the D-D model

In the D-D model, the continuous image distribution $f(x, y, z)$ is replaced by the superposition of discrete basis functions $b_k(x, y, z)$, related to each-other by:

$$f(x, y, z) = \sum_{k=1}^{K} f_k b_k(x, y, z), \tag{2.32}$$

where K represents the number of basis functions and $\mathbf{f}=(f_1, ..., f_k, ...f_K)^T$ represents the basis function coefficient or intensity. The best example of a basis function is a voxel which has unit value inside a small cube and is zero elsewhere. Next to voxels, blobs have been studied intensively [97, 109]. Blobs are also localized, but have a smoother shape such that they are band limited. This property will lead to conservation of smoothness in the reconstructed image and thus provides less noisy results compared to voxels. Also, in some cases, the use of blobs can lead to a more efficient calculation of the system matrix elements. Basis functions which adapt to the image content have been investigated [22].
In the D-D model, the reconstruction problem translates into finding the right coefficients $\mathbf{f}$ and equation 2.30 now becomes:

$$s_i = \sum_{k=1}^{K} a_{ik} f_k, \tag{2.33}$$

with

$$a_{i,k} = \iiint_{FOV} h_i(x,y,z) b_k(x,y,z) dxdydz. \tag{2.34}$$

$a_{i,k}$ represents the probability of having a detection in sinogram bin i resulting from an emission in basis function k. Matrix $\mathbf{A}$, containing all elements $a_{i,k}$ is often referred to as the probability matrix or system matrix. Equation 2.33 represents a set of linear equations

$$\mathbf{s} = \mathbf{A}\mathbf{f}, \tag{2.35}$$

which should be solved for $\mathbf{f}$ given measurement $\mathbf{s}$ and system matrix $\mathbf{A}$. Direct inversion methods are difficult not only due to the large number of elements of the system matrix but mainly due to the bad condition number of $\mathbf{A}$. Therefore, a solution is typically derived in an iterative way, meaning that a better estimate of the true image distribution is derived in successive iterations. The two basic components of an iterative reconstruction algorithm are (i) the criterion that is used to decide which estimate is currently the best estimate and (ii) the algorithm used for calculating the best estimate, specified by the criterion.

2.5.1.1 The objective function

The criterion is expressed in the objective function $\Phi(\mathbf{f}, \mathbf{s})$ and can be generally described by a data fitting term and an image property term.

In the case of penalized log-likelihood, the objective function is:

$$\Phi(\mathbf{f},\mathbf{s}) = L(\mathbf{f},\mathbf{s}) - \beta R(\mathbf{f}), \tag{2.36}$$

where $L(\mathbf{f},\mathbf{s})$ expresses how well the data fit the current estimate and $R(\mathbf{f})$ is the image property term. This term is referred to as the regularization and can for instance include constraints on local smoothness. The balance between the data fitting criterion and the pre-imposed regularization term is controlled by β. Other criteria are constraint satisfaction, which assumes there is a unique solution on the intersection of all hyper-planes defined by each equation $s_i = a_{ik} f_k$. Maximum Likelihood (ML) supposes that there exists a law describing the probability $p(\mathbf{s}|\mathbf{f})$ of measuring $\mathbf{s}$ given a certain $\mathbf{f}$ and is thus a statistical estimation criterion [93]. In the context of emission tomography, $p(\mathbf{s}|\mathbf{f})$ is referred to as the likelihood function. When the likelihood function is unknown, one can use the Least-Squares (LS) or Weighted-LS (WLS) criterion which simply projects an image using system matrix $\mathbf{A}$ and, in terms of Euclidean distance, looks how well the result fits the measured data [78]. The Maximum A Posteriori (MAP) criterion seeks to maximize $p(\mathbf{f}|\mathbf{s})$ as opposed to $p(\mathbf{s}|\mathbf{f})$ for the ML criterion [62, 132]. Since

$$p(\mathbf{f}|\mathbf{s}) = \frac{p(\mathbf{s}|\mathbf{f})p(\mathbf{f})}{p(\mathbf{s})}, \tag{2.37}$$

next to the likelihood function, also the prior $p(\mathbf{f})$ will be present in the objective function. Assuming a Gibbs smoothing prior $p(\mathbf{f}) = \exp[-\beta R(\mathbf{f})]$, one finds back equation 2.36, where $L(\mathbf{f},\mathbf{s})$ denotes the log-likelihood function. When no preference is given to any $\mathbf{f}$ or, in other words, assuming a uniform prior, the MAP solution reduces to the ML solution. Also, one could device a penalized least-squares or penalized weighted-least-squares objective function by replacing $L(\mathbf{f},\mathbf{s})$ by the LS or WLS objective function respectively [49].

2.5.1.2 The algorithm

Every iterative algorithm does basically the same: it forward projects an initial estimate of the source distribution to the data space, using system matrix $\mathbf{A}$. The forward projected data estimate is then compared to the measured data. Based on the discrepancy between the measured and estimated data, a correction term is derived. After mapping this correction term from projection space to image space in the backprojection

step, the initial estimate is corrected, yielding a next image estimate.
One of the earliest used iterative algorithms in emission tomography is the Algebraic Reconstruction Technique (ART) [59, 67], based on the constraint satisfaction criterion. Here, the algorithm finds the intersection of all hyperplanes, each defined by one of the linear equations, by consecutively projecting an image estimate from one hyper-plane to another. This method does not take into account the statistical nature of the data but it allows for modeling of the geometric system response. ART uses an additive update step and therefore, negative pixel values can be encountered. These types of reconstruction algorithms are called algebraic reconstruction methods. Next to ART, Multiplicative ART (MART) [108] which implicitly enforces non-negativity, Simultaneous Iterative Reconstruction Technique (SIRT) [56] and Iterative Least-Squares Technique (ILST) [58] are other examples of algebraic iterative reconstruction techniques.
Algorithms to find the LS or WLS solution have been widely studied. This resulted in a number of algorithms which differ mainly in the way the stepping direction is chosen. The first algorithm is the Steepest Descent (SD) algorithm [50], which determines the update direction by choosing it according to the most decreasing side of the objective function. The Conjugate Gradient (CG) algorithm [158, 91] is more efficient in the sense that it is devised such that every new update is unable to counteract a previous update [133]. The Expectation Maximization (EM) [94] algorithm has been used both in combination with the ML [145] and the MAP [96] objective function and basically consists of two steps: the expectation step which calculates the expectation of the likelihood function of the complete data and the maximization step which maximizes this likelihood function.

2.5.1.3 MLEM

The combination of the EM algorithm with the ML criterion has lead to the best known iterative reconstruction technique in nuclear medicine: MLEM [145]. MLEM takes into account the randomness in the data, therefore equation 2.35 should be rewritten as:

$$E[\mathbf{s}] = \mathbf{A}\mathbf{f}, \tag{2.38}$$

where $E[\cdot]$ represents expected value. As explained previously, the ML criterion is based on a law describing $p(\mathbf{s}|\mathbf{f})$. Since the data measured on

a SPECT scanner are distributed according to a Poisson model, MLEM is based on a Poisson description of this probability law:

$$p(\mathbf{s}|\mathbf{f}) = \prod_{i=1}^{I} \frac{\bar{s}_i^{s_i} \exp(-\bar{s}_i)}{s_i!}, \tag{2.39}$$

with $\bar{s}_i$ the i-th element of $E[\mathbf{s}] = \mathbf{Af}$:

$$\bar{s}_i = \sum_{k=1}^{K} a_{ik} f_k \tag{2.40}$$

The EM algorithm first derives the surrogate function, which is the expectation of the log-likelihood of the complete data (the E-step). This surrogate function is maximized during one iteration of the MLEM algorithm (the M-step):

$$f_k^{t+1} = \frac{f_k^t}{\sum_i a_{ik}} \sum_i a_{ik} \frac{s_i}{\bar{s}_i^t}, \tag{2.41}$$

which finds the maximum of the measured data log-likelihood function at convergence. This formula is quite simple to implement and it follows the general description of an iterative algorithm with the update being a multiplication. The multiplication factor is the ratio of the data and the estimated data, serving as a measure of error. Since it is multiplicative, the estimates produced by MLEM can never be negative. MLEM has two main shortcomings, namely the slow convergence and the very noisy images at high iteration number. To solve the latter problem, three different approaches can be used. One can adapt the objective function to include some image based constraints such as in the MAP-EM algorithm. Other approaches consist of post-smoothing the reconstructed image or filter the image after each iteration. To solve the first problem of slow convergence, Hudson and Larkin devised the OSEM algorithm, which updates the image before processing all the data. OSEM splits the data in so-called subsets and updates the image after each subset is processed. Despite the lack of proof of convergence, it has been shown that comparable image quality is obtained in the same number of iterations as MLEM. However, the computational cost to process only one subset is much less compared to MLEM. Other speed-up versions of the MLEM algorithm are the RBI-EM [26] and RAMLA algorithm [24]. Also, some speedup versions of the MAP-EM algorithm have been developed.

2.5.2 Corrections for image degrading effects

2.5.2.1 Resolution modeling

A model for the depth dependent spatial resolution of a SPECT system can be included in the system matrix of an iterative algorithm. Various approaches exist: one can pre-calculate or pre-simulate the system matrix by Monte Carlo techniques, but more often, the system response is calculated on the fly given the PSFs at different depths. Resolution is then modeled in the forward projector after rotating the current estimate $\hat{f}^t$ according to the appropriate SPECT angle θ. A blurring kernel with FWHM dependent on the collimator distance is then used to convolve the rotated image. 3D-SPECT reconstruction is characterized by a 2D convolution which can be separated in a 2 times 1D convolution when approximating system response by Gaussian kernels. Once the convolution is performed, adding along the depth direction yields the forward projection. One can adopt the same strategy while creating the update image during backprojection to have both resolution modeling in the forward and backward projection. This procedure of rotating and convolution is time consuming and can be faster when implemented as a multiplication in frequency space. Another fast implementation exhibits the fact that Gaussian kernels are separable and starts by convolving the parallel plane which is most distant to the collimator with a small kernel, adds it to the parallel plane just below and convolves again. Repeating this procedure until the last plane will result in faster convolution because of the smaller convolution kernel [198]. Another, even faster way of dealing with resolution modeling is pre-correcting the data. This technique has been successfully applied to analytic reconstruction methods but can also be used in combination with iterative reconstruction. The pre-correction method exhibits the property that there exists a relation between the Fourier transform of the data and the distance of a point in image space to the center of rotation (CoR), which is known as the frequency-distance relation [47]. By restoration filtering of the sinogram with the appropriate filter (based on the CoR distance), one can make an approximate pre-correction of the sinogram [57].

2.5.2.2 Attenuation correction

In order to do attenuation correction, one needs information on the attenuation of the patient at the energy of reference. This attenuation

map has historically been derived in different ways. One can register an attenuation map, originating from another imaging modality such as a CT scanner with the emission tomography (ET) image. Some SPECT scanners are accommodated for transmission tomography by use of an external isotope line or point source attached to one of the heads. Finally, the attenuation map is sometimes deduced from the emission data. Nowadays, some SPECT scanners sold are combined SPECT-CT scanners which provide immediate registration of the CT with the ET image. Once the attenuation map is known, several strategies can be followed to do attenuation correction. The best known method is Chang's method which is a post-correction technique applied after image reconstruction [30]. Chang's method relies on the calculation of the fraction of photons which is transmitted from a certain voxel to a certain sinogram bin:

$$\mathrm{TF}_{\theta,k} = exp(-\int_L \mu(l)dl), \tag{2.42}$$

where L represents the collimator defined line piece connecting voxel k with the detector at angle θ and l is the coordinate along this line. Averaging this TF over all SPECT angles results in a single correction factor CF for each voxel:

$$\mathrm{CF}_k = \frac{1}{\frac{1}{\Theta}\sum_{\theta=1}^{\Theta} \mathrm{TF}_{\theta_i,k}}, \tag{2.43}$$

Applying these correction factors to a reconstructed image results in a zeroth-order Chang estimate, while an iterative procedure can be used to make higher order Chang corrections. Besides with Chang's method, attenuation correction is often applied in the forward projector of the MLEM algorithm. The forward projection

$$\sum_k a_{ik} f_k^t \tag{2.44}$$

is then modified as:

$$\sum_k a_{ik} \mathrm{TF}_{\theta,k} f_k^t. \tag{2.45}$$

The transmission factors TF can be pre-computed, but most often they are calculated on the fly by rotating the attenuation map according to the appropriate SPECT angle and simply summing the needed attenuation values for each voxel [84]. Another approach could be to calculate

the intersection lengths of each detection line with the attenuation map and to multiply each intersection length with the attenuation value at that location. The method based on the integration in the forward projector leads to better performance because no approximations are made regarding equal attenuation for all SPECT angles.

2.5.2.3 Scatter correction

In reconstructed SPECT images, scatter shows up as a bias and affects image contrast and thus hinders correct quantitation. A large variety of methods exist to compensate for scatter. Generally, they can be split into two sub-classes: the compensation techniques that (i) estimate the scatter based on the measured projections and the methods which (ii) compensate for scatter during image reconstruction.
The best known methods that rely on estimation are energy window based. By choosing an energy window below the photopeak, one can correct for scatter as follows [88]:

$$s_{SC} = s_{MW} - k\left(s_{LW}\frac{w_{MW}}{w_{LW}}\right). \tag{2.46}$$

Here, s_{SC}, s_{MW} and s_{LW} respectively represent the scatter corrected data, the data measured in the main energy window and the data measured in the lower-energy window. For Tc-99m the width of the main window w_{MW} is typically chosen to be twice the energy resolution at 140 keV While w_{SW}, the width of the scatter window, is chosen smaller and at lower energy. k is a constant relating the amount of scatter in the main window to the scatter in the scatter window and is usually derived from calibration phantom studies. Variations on this dual-energy window scatter compensation technique include triple energy window scatter compensation [125] and multiple energy window compensation techniques [89], which are clinically useful for isotopes other than Tc-99m. The main drawback of these methods is that they increase the noise in the data due to the subtraction of the scatter estimate. Other estimation techniques base themselves on the spatial distribution of the photopeak measurement rather than on the energy distribution. By modeling the spread of scatter from the source into the scatter distribution, one can approximate the scatter distribution such as in [186]. Another example of this method is the convolution-subtraction method proposed by Axelsson [12]. Other techniques using a spatial variant scatter response model include Monte Carlo methods which generate a set of scatter response

functions which are then interpolated to estimate the spatial scatter distribution from the photopeak measurements [100].
Modeling of the scatter behavior during image reconstruction can also be done in different approaches. Methods that model the scatter in the PSF are implemented in the same manner as collimator blurring is modeled [74, 52, 16]. However, the reconstruction time will be prolonged enormously and it is assumed that scatter response is the same in every point in the FOV. Different ways to take into account non-uniform attenuating objects are to calculate the scatter response by Monte Carlo [51, 20] or analytically based on the Klein-Nishina equations [137] and including it in the projector and/or backprojector of an iterative reconstruction. These approaches have been considered for a long time as being too slow for clinical use but are now more feasible due to the increased available computation power. However, Beekman [15] has developed fast method for image reconstruction which takes into account the patient specific scatter and attenuation by using a fast Monte Carlo simulation of the photon transport in the forward projector. Furthermore, collimator blurring is taken into account by depth dependent convolution. This mixed Monte Carlo/analytic method is referred to as CFD or convolution based forced detection [37] and is promising for quantitative image reconstruction.

2.5.2.4 Collimator photon penetration

As previously discussed in section 2.3.5, collimators are optimized for Tc-99m imaging. This means that the septal thickness is chosen in order to stop e.g. 99% of all 140 keV photons, hitting the septa. Being the most used isotope in SPECT, Tc-99m is however not the only photon emitter used in SPECT. Next to Tc-99m, one can use isotopes like I-123, Tl-201, I-131, In-111 for the purpose of diagnostic imaging. Drawback of these isotopes is that they often have high energy photon emissions which will more likely penetrate the collimator. The measurement of such high energy photons which penetrated the collimator contains almost no spatial information and therefore appear in the image as an artifactual background in the same manner that scatter affects the images. However, one can not always rely on energy subtraction methods to correct for photon penetration, because the spectral distribution is dependent on factors such as patient size and activity distribution. Therefore, different methods have been developed which most of the time are specific for a certain clinical application [148, 75, 42, 45, 150].

2.6 Importance of Monte Carlo simulations

Monte Carlo (MC) simulations are indispensable in many fields of research. Also in the field of nuclear medicine, they become increasingly important. On one hand, MC is used as a tool to gain insight in the chain of events taking place from photon generation to photon detection. Since the history of every photon can be recorded we gain understanding not only in the processes that lead to a correct detection but more importantly, also in the mechanisms which cause distortion or artifacts in the measurements due to blurring, attenuation, scatter and collimator penetration. On the other hand, MC methods are used for simulating processes which are that complex that they can not be simulated analytically. An excellent overview paper about the relevance of Monte Carlo simulations in nuclear medicine is given by Zaidi [196]. A first important application of MC simulations is the characterization of gamma ray detectors. Monte Carlo methods can be used to investigate for instance:

- the optimal dimensions of a crystal and PMTs;
- crystal scatter for different detector geometries;
- the best method to couple a scintillator to the further readout;
- the performance of count positioning algorithms such as the Anger logic scheme;
- depth of interaction (DOI) measurement performance.

This enables one to choose among lots of different materials, geometries and setups and to design application specific detectors. Often, investigating all the different possibilities in practice would be economically not achievable.
MC techniques offer the possibility to study a SPECT system as a whole and to tune parameters like the number of detector heads, their placement and motion relative to each other. Furthermore, MC simulations have been extensively used for the optimization of collimator design. Parameters which are often tuned by MC are hole size, septal thickness, collimator height but also the type of collimator to be used can also be investigated. MC simulations will be especially important in this dissertation to compare rotating slat collimators to parallel hole collimators.
Recording the history of all detected events enables the investigation of image degrading effects. Thanks to MC, we can derive the extent of

blurring undergone by each detected event. Furthermore, we can exactly know the amount of attenuated photons, the amount of scattered photons and whether a photon penetrated the collimator or not. All this information enables us to optimize correction strategies and benchmark them to a gold standard which can otherwise not be derived. In chapter 8 of this book, MC simulations have been used to investigate the relative amounts of contamination for different collimator types. Finally, MC starts to be increasingly used for image reconstruction purposes directly. Since the source position of every event is known, the probability of detecting in a certain detection bin a photon originating from a certain source location can be simulated. In other words, one can derive the whole system matrix in a very accurate way using MC simulations. To get good statistics however, simulating the complete system matrix would require too much time. Often, approximations like using a coarse grid to sample detector and source can already lead to very good results. Also, simulation of the collimator response function, scatter response function and penetration response function with MC is often more accurate than analytical calculations. As already mentioned in section 2.5, MC based iterative reconstruction where the forward projector is replaced by a fast MC simulation is promising and will most likely become the standard in future clinical SPECT scanners.
Throughout this dissertation, Geant4 Application for Tomographic Emission (GATE) has been used as a Monte Carlo simulator. Among other very useful Monte Carlo programs designed for nuclear medicine applications, GATE was chosen since it is flexible due to its modular structure and accurately models the photon behavior at energies relevant in SPECT. Also, a lot of experience with GATE exists in our research group [152, 18]. GATE is built as an upper layer on the well validated Geant4 high-energy physics code [5]. Basically, it extracts the physics needed for simulating SPECT and PET from the Geant4 library and supplies a scripting language to enable easy simulation setup. Furthermore, since it is written in C++, it ensures a high degree of modularity and understandability. This makes the GATE code continuously evolving and extending, answering the needs of the users.

2.7 Conclusion

In this introductory chapter the historical framework is drawn from which nuclear medicine was born. More specifically, the gamma cam-

era used for SPECT imaging, is explained and a detailed overview of the different collimation techniques is given with a description of how to optimize their geometry. Also some insights are given in the choice of optimal collimator by comparing all classically available collimators. Next, photon integrating detectors which are traditionally used for SPECT are reviewed. Also, a look upon novel detector concepts which are still in a research phase gives insight in future possibilities. Once the components of a gamma camera are understood, an introductory review of iterative reconstruction techniques is given with special attention to corrections for different image degrading effects. Finally the importance of Monte Carlo simulations, which will be extensively used in underlying work, is touched upon.

Chapter 3

Analytic description of the rotating slat collimator

In SPECT imaging, image quality is limited by the spatial resolution versus sensitivity trade-off resulting from the geometric properties of parallel hole collimators (chapter 2). While maintaining the same field-of-view (FOV), rotating slat collimators provide a better spatial resolution versus sensitivity compromise [192]. For equal spatial resolution, this results in a 5 times higher sensitivity for a strip detector [54] and a 30-40 times higher photon collection efficiency for a conventional SPECT detector [191].

On the other hand, since photons originate from planes perpendicular to the detector surface, the information that each photon provides about the activity distribution will be lower in the case of a rotating slat collimator. Furthermore, while a parallel hole collimator provides direct parallel projection images of a 2D activity distribution, a stationary rotating slat collimator does not yield directly interpretable images since it measures plane integrals which result in 1D projections. These 1D projections can be mathematically described by the 3D Radon transform when the 1D detector is rotated around its axis at every regular camera SPECT angle. A point source in a 2D plane parallel to the detector would project to an impulse in our 1D detector and consequently, we lose information on one of both coordinates in the original 2D plane. In order to recover information on the second coordinate, the detector has to be spun around its own axis, similar to the gantry rotation a SPECT camera needs to make to recover the second coordinate (depth) in a transverse slice of a 3D object. In combination with image re-

construction similar to SPECT reconstruction, planar images can be recovered with the rotating slat collimator. This extra reconstruction step introduces extra noise compared to a parallel hole collimator since during acquisition, noise from a whole plane - instead of just a line - is superimposed in a detection bin and will accumulate in every point of the plane seen by the detection bin during image reconstruction. This noise accumulation compromises the geometric sensitivity gain to a certain extent, dependent on the image reconstruction method used, the object size and position in the FOV and thus results in a lower effective sensitivity for the rotating slat collimator. It is the purpose of this dissertation to closely study the resolution and sensitivity behavior of a rotating slat collimator and to use this information in iterative reconstruction algorithms. We believe that thanks to an accurate model, the noise accumulation during image reconstruction can be reduced with iterative reconstruction, an extra benefit can be obtained with rotating slat collimators versus parallel hole collimators.
This chapter contains the derivation of analytical expressions for sensitivity and spatial resolution of a rotating slat collimator with special attention to the close field behavior. Furthermore, a Monte Carlo model is implemented to verify the analytic expressions. This Monte Carlo model is then validated with measurements on a prototype rotating slat system. Finally, the planar image quality of the prototype system is investigated for two possible planar image reconstruction methods, making clear the added value of an available system description.

3.1 Introduction

In classical SPECT with parallel hole collimation, the sensitivity is constant over the FOV. This is no longer the case if a rotating slat collimator with planar photon collection is used: there will be a significant variation of the sensitivity within the FOV. On the other hand, the spatial resolution versus distance dependency remains unaltered compared to parallel hole collimation. An accurate description of these system characteristics is not only mandatory for comparison with other types of collimation, it is also needed for quantitative image reconstruction.
There exist a number of previous analytic descriptions of a rotating slat system. In a paper by Entine [48], there is a very good discussion about the photon flux at the detector of these systems. Previous sensitivity

calculations [191] were done for a systems with a rotating slat collimator on a fixed detector. The prototype system we investigate in this chapter [54] is different because it is composed of a rotating slat collimator and strip detector pair and because it has collimator slats of equal length. Staelens [151] extended the method of Metz [114] and Tsui [156] in order to obtain a closed analytical expression for resolution and sensitivity of a rotating collimator on strip detector. This model is a far field model (i.e. 10 cm and more to the collimator). Here, the sensitivity is calculated for all points in the FOV with special importance to points close to the detector and large incident angles.
Analytic results will be compared to Monte Carlo results. The development of a Monte Carlo model will provide us with a practical tool for rotating slat system design. Once the model is validated with measurements on the prototype, it will be extrapolated to different designs which are more general. In chapter 5, we will use this more general model to make a fair comparison of the image quality with respect to a parallel hole collimator. Finally, we investigate image quality with the prototype. Using two different reconstruction approaches, one with and one without accurate system model, the need for the here presented system description is clarified. An ad-hoc comparison with a standard parallel hole system, available in our lab, is made. A general and more detailed comparison of image quality that can be obtained with both types of collimation will be presented in chapter 5.

3.2 The rotating slat collimator system

The geometry of the collimation system is shown in figure 3.1 while the prototype SOLSTICE (SOLid STate Imager with Compact Electronics) camera, available in the Gent University Hospital, is depicted in figure 3.2. The collimator dimensions for the system are based on this prototype design which was proposed in [54]: collimator height $h = 40$ mm, gap size $g = 1.5$ mm and slat thickness $t = 0.3$ mm. The width of the slats is 155 mm and the underlying detector's width $W = 56$ mm while its thickness is 5 mm.

3.3 Analytic description of the sensitivity

For deriving the sensitivity, different factors have to be taken into account: the first and most important factor concerns the collimator and

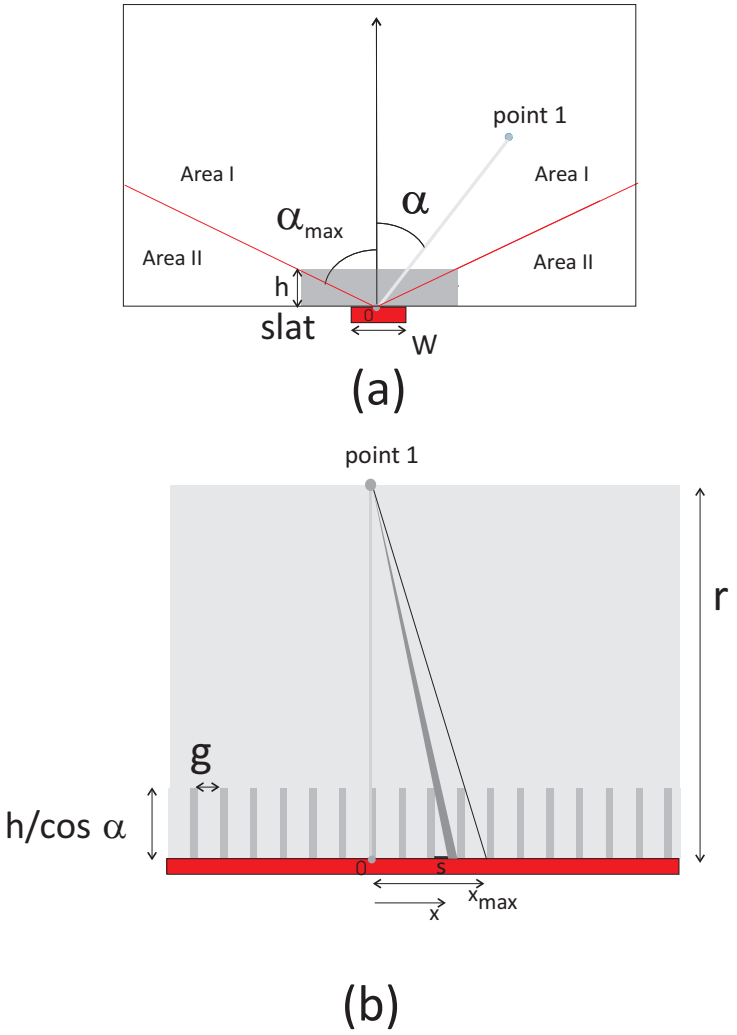

Figure 3.1: Geometry used to calculate the sensitivity. In the upper figure (a) the plane parallel with the slats is shown. In the lower figure (b) the plane perpendicular on the slats and going through point 1 is shown.

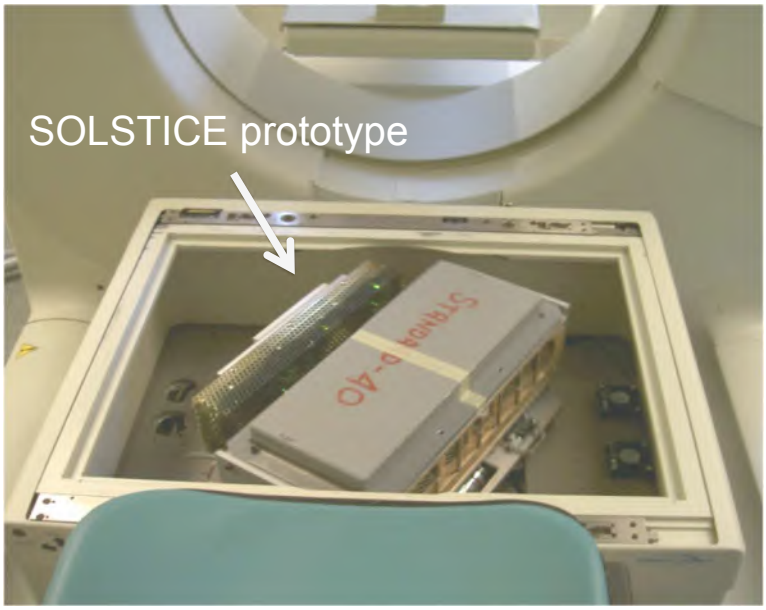

Figure 3.2: The SOLSTICE rotating slat collimator prototype.

detector geometry, upon which the calculations are based. A second, less pronounced factor, is related to intrinsic detector properties and will be incorporated into the calculations as a detection efficiency term which depends on the incident angle. Several assumptions will be made for the calculation of the sensitivity formulas and it will be proven that these calculations deliver a correct prediction of the sensitivity in points far enough from the collimator. To calculate the sensitivity, we have to consider different areas (figure 3.1) which all require a slightly different calculation method. For emissions coming from area I the septa are crossed in a different way than for photons originating from area II. For area III (not shown in the figure), consisting of area I and area II at small collimator distance (less than 2 collimator heights), the assumption of being at large distance from the collimator face would result in a wrong estimate of the incident angle. Therefore, to derive a close field model which also accounts for points close to the collimator surface, a modified calculation method is needed.

3.3.1 Area I

Here we use a similar derivation as in [124]. Only points with $|\alpha| < \alpha_{max}$ are considered. Given h the height of the septa, x the gap position and g the spacing between the septa, we can calculate the sensitivity for a point at a distance r and at an angle α (fig. 3.1). Due to the non perpendicular incidence the effective collimator height is $h_e = \frac{h}{cos\alpha}$. The shadow s is calculated from equivalent triangles:

$$\frac{s\cos\alpha}{h} = \frac{x}{r} \longrightarrow s = \frac{hx}{r\cos\alpha}. \tag{3.1}$$

From this shadow we can calculate the fraction of detected radiation at x, relative to the amount of photons that would be detected if there were no septa:

$$\frac{g-s}{g} = 1 - \frac{xh}{gr\cos\alpha}. \tag{3.2}$$

The maximal distance, x_{max}, where there still can be an incidence on the detector is also calculated from similar triangles:

$$\frac{x_{max}}{r} = \frac{g\cos\alpha}{h} \longrightarrow x_{max} = \frac{gr\cos\alpha}{h}. \tag{3.3}$$

The radiation at a distance r from the point source is proportional with $\frac{1}{4\pi r^2}$. Due to the non-perpendicular incidence, the detected radiation (assuming a perfect detector) is proportional with $W\cos\alpha$. Integration of the detected fraction of that photon flux with x varying from 0 to x_{max} (factor 2 accounts for negative x) gives the following expression for the sensitivity $s(r,\alpha)$:

$$\begin{aligned} s(r,\alpha) &= \frac{W\cos\alpha}{4\pi r^2} 2\int_0^{x_{max}} \Big(1 - \frac{xh}{gr\cos(\alpha)}\Big)dx \\ &= \frac{W\cos\alpha}{4\pi r^2} 2\int_0^{x_{max}} \Big(1 - \frac{x}{x_{max}}\Big)dx \\ &= \frac{W\cos\alpha}{4\pi r^2} x_{max} = \frac{W\cos^2\alpha}{4\pi r}\frac{g}{h}. \end{aligned} \tag{3.4}$$

The septal thickness was ignored in the previous approach so this equation is only valid if the septa are infinitely thin. The aforementioned calculation of the sensitivity will be referred to as analytic calculation method 1.

3.3.2 Area II

Below the lines from the detector strip towards the corners of the slats (see figure 3.1) the effective collimator height h_e is given by the following expression:

$$h_e = \frac{h \tan \alpha_{max}}{\sin \alpha}. \tag{3.5}$$

Here the maximal distance x_{max} becomes larger with increasing angle:

$$\frac{x_{max}}{r} = \frac{g \sin \alpha}{h \tan \alpha_{max}} \longrightarrow x_{max} = \frac{gr \sin \alpha}{h \tan \alpha_{max}}. \tag{3.6}$$

The same calculation as for points in area I (also ignoring the septal thickness) results in the following expression:

$$s(r, \alpha) = \frac{W \cos \alpha \sin \alpha}{4\pi r} \frac{g}{h \tan \alpha_{max}}. \tag{3.7}$$

Sensitivity calculations with equations 3.4 for $\alpha < \alpha_{max}$ and equation 3.7 for $\alpha > \alpha_{max}$ will be referred to as calculation method 2.

3.3.3 Area III

The previous calculations are based on three assumptions which are shortly described below and are shown in figure 3.3. It is demonstrated that equations 3.4 and 3.7 only hold for points far away from the detector and that an extra correction close to the detector is needed. Firstly, the septal thickness and septal penetration were not taken into account (figure 3.3 (a)). A good design of the septa should minimize the penetration so the second factor can be ignored.

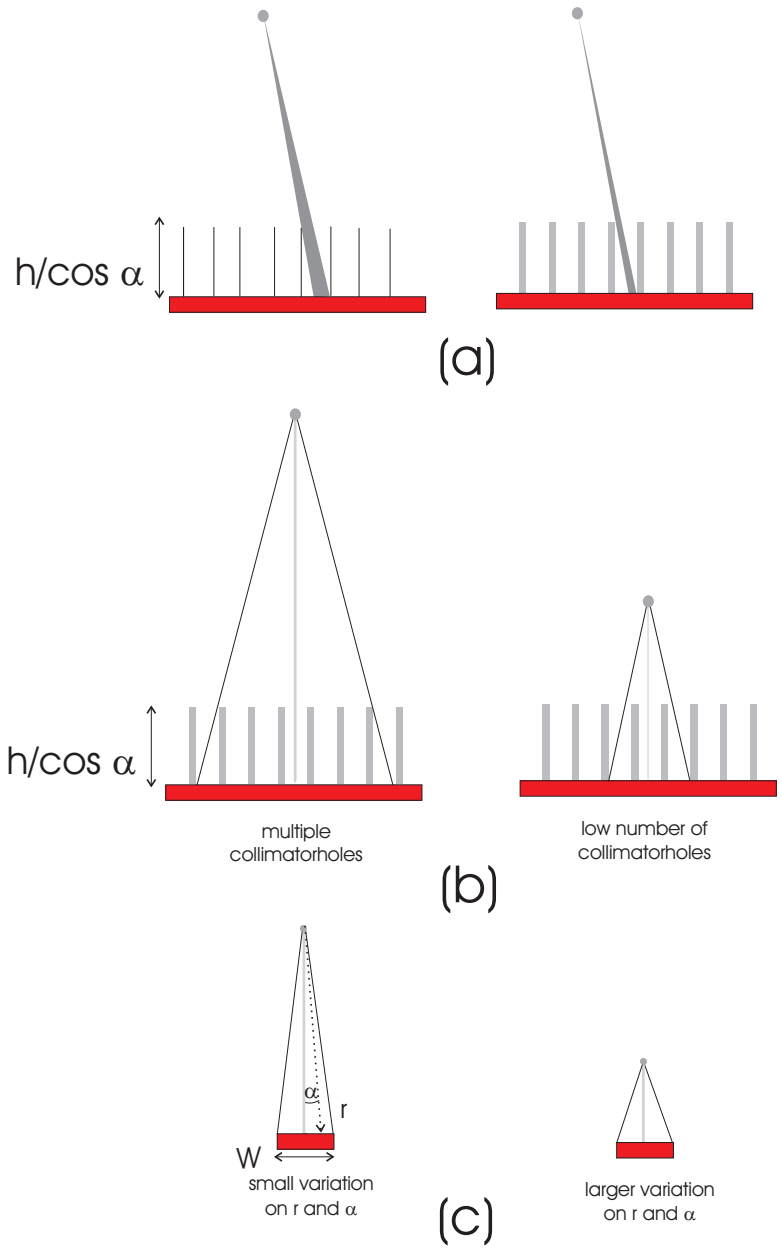

Figure 3.3: Different approximations in the calculation of the sensitivity. In the upper figure (a) the effect of finite septa thickness is illustrated. In the middle figure (b) it is shown that the ratio of distance to collimator height determines the number of gaps seen. In the bottom figure (c) it is shown that incident angle and distance vary significantly over the detector width when the point is close to the detector.

A second assumption (figure 3.3 (b)) is concerning the ratio between the collimator height and spacing, and between the distance and height. The gaps g between the septa are also assumed to be small compared to h. The distance y should be large compared to the height h of the septa. When the point is far enough from the detector, this approximation is valid. When the point comes close (less than 2 x septa height e.g., 80 mm) there will be a variation of the real sensitivity on the position versus the slats. The equations 3.4 and 3.7 above will still give a good estimate of the average sensitivity and are comparable to the far field models derived in (Metz *et al* 1980) and (Staelens *et al* 2005). Thirdly, the width W of the detector should also be small compared to the distance x_{max} (figure 3.3 (c)). If this is not fulfilled the incident angle α and the distance r will vary significantly over the width of the detector. It is especially this assumption which makes equations 3.4 and 3.7 invalid for points close to the detector. Using these equations for e.g. points on the central axis ($\alpha = 0$), would lead to a systematic overestimation of the geometric sensitivity. The use of $\alpha = 0$ in equation 3.6 is far from reality close to the detector where the incident angle α on the detector varies significantly over the width of the detector. In the SOLSTICE device there are 16 small detector elements between two slats. Therefore we propose to use a modified equation taking the pixellated detector into account in order to give a good estimate of the close field sensitivity:

$$s(r, \alpha) = \frac{g}{h} \sum_{e=1}^{16} \frac{W_e \cos^2 \alpha_e}{4\pi r_e}. \tag{3.8}$$

Using this equation for the sensitivity calculation will be referred to as method 3. Accordingly, three approaches were used to calculate the sensitivity of the SOLSTICE system. In the first calculation the method of equation 3.4 was implemented. For the calculations a continuous perfect detector of width 56 mm was used. In the second method, the effect of a different equation for large angles (equation 3.7) was taken into account. In the third method we calculated the sensitivity in the FOV for each detector pixel (taking into account the variation of r and α). The total sensitivity was obtained by summing the sensitivity for each detector pixel (equation 3.8). The dimensions of each pixel are equal to those given in (Griesmer *et al* 2002).

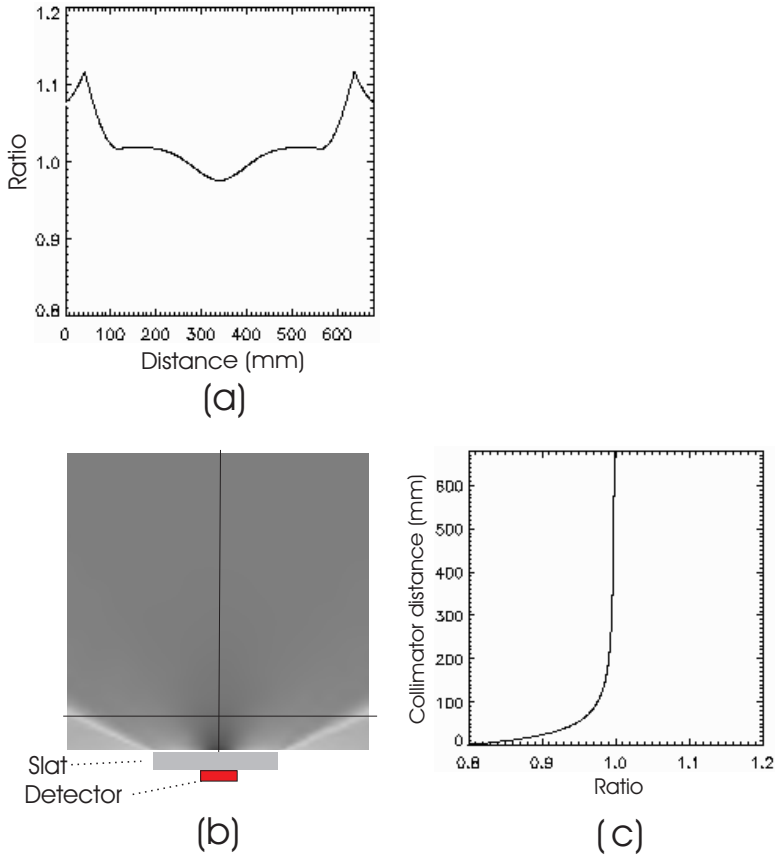

Figure 3.4: Ratio between sensitivities obtained by method 1 and method 3. (a) shows a profile in a plane (at 10 cm distance) parallel to the detector, (b) shows the 2D plot of the ratio, (c) shows a profile on the central axis perpendicular to the detector.

3.3.4 Comparison of the different calculation methods

By taking the ratio between the sensitivity calculated with method 1 and method 3 (figure 3.4), the difference between both calculations can be seen. There are non-uniformities along the lines towards the corner of the collimator (around α_{max}). The reason for this is that method 3 also takes the change in effective collimation height in area II into account. Far away from the detector the ratio is 1 which means both methods are similar. Also close to the detector ($< 10cm$) (figure 3.3(c)) the difference becomes more pronounced. According to this comparison the corrections based on method 1 will give systematic errors for distances below 10 cm and for angles larger than α_{max}.

3.3.5 Tomographic sensitivity calculation

Once an accurate planar sensitivity is obtained, the sensitivity of a point in a tomographic system can be calculated. This is done by rotating the sensitivity map for the different spin angles. The sum of all spin angles will give the sensitivity for one SPECT angle. By repeatedly summing over all SPECT camera angles, the tomographic sensitivity of all points is obtained. An area with a low sensitivity will have a lower signal-to-noise ratio. The tomographic sensitivity was calculated for a system with a radius of SPECT-rotation of 340 mm. Figure 3.5 gives a view of the different sensitivities. The top view shows the planar sensitivity. After spin rotation one obtains the sensitivity for one camera position. After SPECT rotation, the 3D sensitivity is obtained. The profiles through the central plane of the 3D sensitivity are shown in figure 3.6. Less than 20 percent variation (percentage of maximum) is present in the sensitivity map. The variation in the transverse plane is limited. In the axial direction there is clearly more variation visible.

3.4 Validation of the analytic sensitivity model

3.4.1 Monte Carlo model

To check the accuracy of the calculation methods, these are compared to sensitivity and resolution values obtained by Monte Carlo simulations. The SOLSTICE detector system (assuming a perfect and pixellated detector) was modeled in the GATE (Geant4 Application for Tomographic

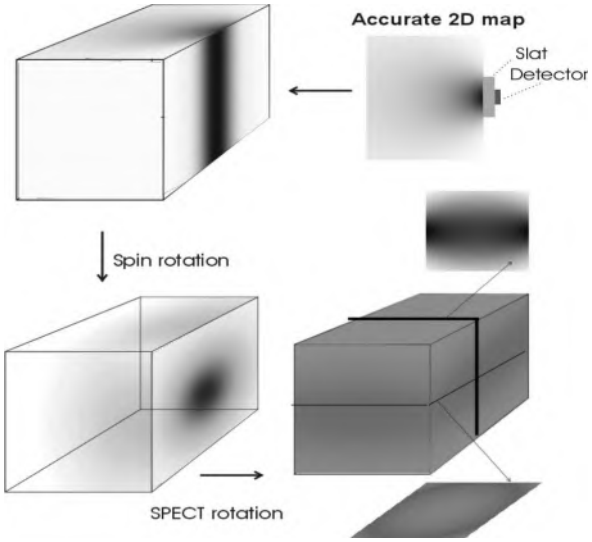

Figure 3.5: Illustration of the tomographic sensitivity after spin and SPECT rotation.

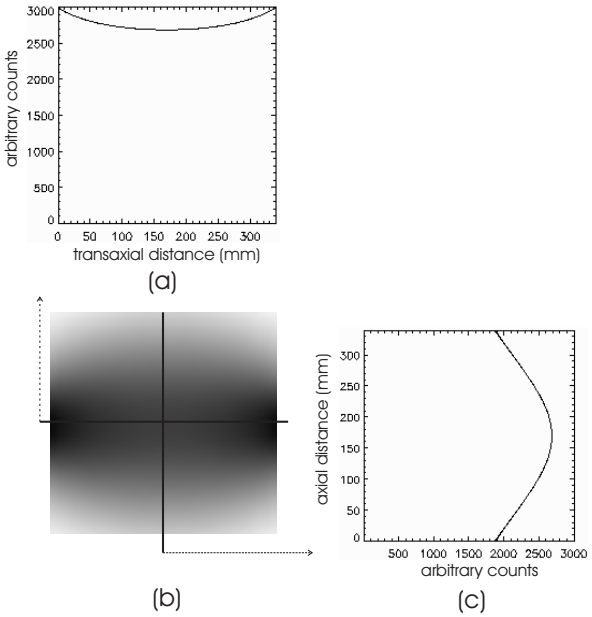

Figure 3.6: Profiles through the central plane of the 3D sensitivity. Figure (a) shows a profile in the transverse plane. Figure (b) shows the 2D plot of the 3D sensitivity, (c) shows a profile in the axial direction.

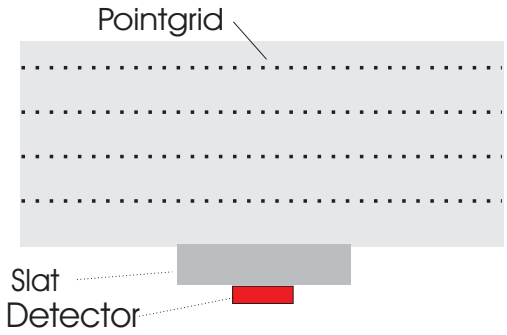

Figure 3.7: Placement of the simulated point sources relative to the detector.

Emission) environment (Santin *et al* 2002) using the geometry and dimensions described in section 3.2. The collimator was modeled to have the same material as in the real system while the CZT was modeled as a real detector (density = 5.68 g/cm^3) with perfect characteristics.

3.4.2 Monte Carlo results compared to analytic calculations

To calculate the relative error of the different calculation methods, a low count simulation was performed. A point-grid (figure 3.7) was placed close to the collimator (at 25 mm, 50 mm, 75 mm and 100 mm depth, and from -340 mm to 340 mm with 10 mm spacing in the other direction). 2.35 million emissions were simulated for each point in front of a fixed strip detector with planar collimation. The sensitivity values are obtained by counting the number of detected emissions from each simulated point source. The average number of detected emissions was 650 per simulated point source (minimum was 33, maximum 5175). The three calculations and the simulation were first normalized on the total counts. Comparison was done for different planes parallel to the detector/collimator pair. The sensitivity values obtained by Monte Carlo simulation were compared to the three calculation methods described above. At each depth, the relative deviation from the simulated sensitivity value was calculated for all points. The average over all points for this depth resulted in an average error. To quantify the accuracy of the calculation methods, the average error along the point-grid of figure 3.7 is plotted at different depths in figure 3.9. The inclusion of the different equation of the sensitivity for large angles in method 2 gives a reduc-

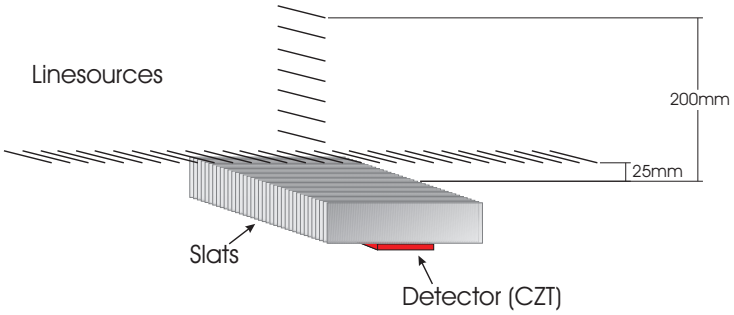

Figure 3.8: Placement of the simulated line sources relative to the detector.

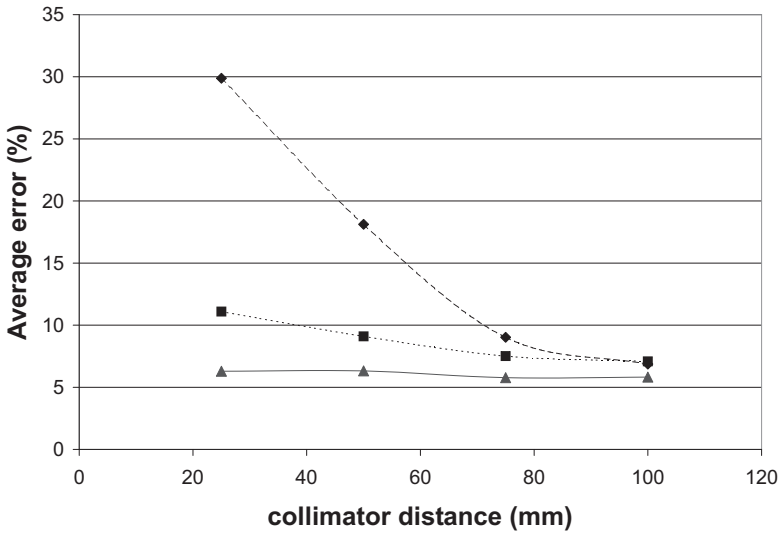

Figure 3.9: Average error (in comparison with GATE simulated data) of three different calculation methods of the sensitivity. Method 3 (▲) clearly shows a small and contineous average error. Method 1 (♦) and method 2 (■) show a higher average error, especially close to the collimator face.

tion in the error. It is clear that the third method (which also takes the discrete detector elements into account) further improves the accuracy and gives a small and almost constant error (less than 7 percent). Most of this remaining error is due to the Poisson noise on the Monte Carlo simulation.

To get an idea of the absolute error of the calculation methods, a high count study was performed. A set of 31 line sources (figure 3.8) was placed in a plane parallel to the collimator face at 25 mm depth with 20 mm spacing. To determine the variation of the sensitivity with source depth, another set of 7 line sources was placed along the spin axis of the detector. Each line had a length of 10 times the slat pitch (i.e. 18 mm) and was placed centrally above the middle slat. 20 million emissions were simulated per line in front of the fixed collimator/detector pair. The sensitivity values are obtained by counting the number of detected emissions from each simulated line source. Detections were accepted within a 20% energy window around 140 keV. The estimated standard deviation (due to Poisson noise) for these data was between 0.3 percent and 0.6 percent of the obtained value. Due to this small statistical deviation resulting from the high count level, an accurate error could be determined for the different methods. The results of the three different

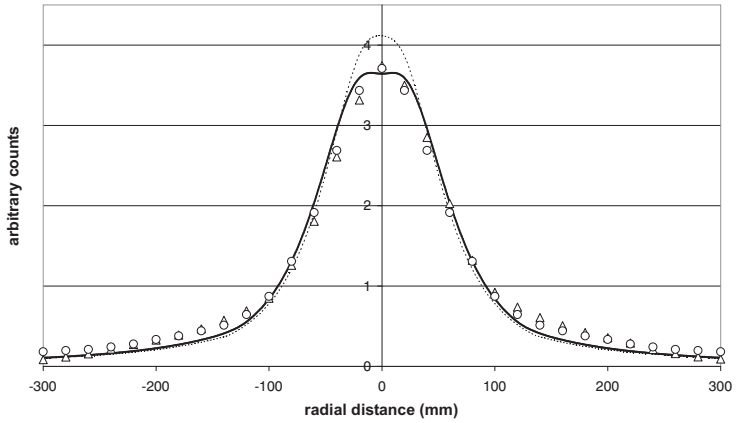

Figure 3.10: Profiles (in a plane at 25 mm from collimator) obtained by calculation method 2 (dashed line) and method 3 (solid line). The discrete data points (○) and (△) are the results obtained by Monte Carlo simulation and by measurements respectively. On the abscissa is the distance from the strip detector to the projection of a point source (in the detector plane parallel to the rotation axis).

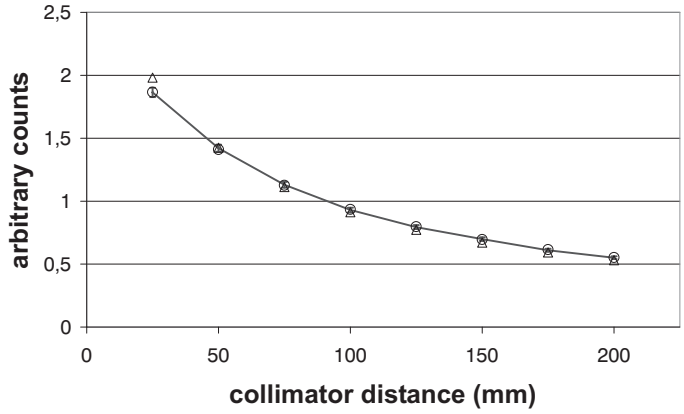

Figure 3.11: The sensitivity of points on the central axis was calculated by method 2(△) and method 3 (○). High count Monte Carlo data (solid line) were used as a gold standard. The error bars are at 2 percent of the gold standard. The curve obtained by method 1 is not shown because on the central axis it is exactly the same as method 2.

methods and the high count Monte Carlo simulation are compared in figure 3.10. Profiles (at 25 mm depth) of the different calculation methods are shown together with the points obtained by the simulation. For reasons of clarity, the results of method 1 are not shown. Although, they are comparable to the results obtained by method 2 with a larger deviation from the simulated values for larger transaxial distances. Best agreement (between simulation and calculation) is clearly obtained by the third method. In figure 3.11 the calculated values along the central axis are shown together with the points obtained by the high count simulations. The third method lies clearly in between the 2 percent error bars, the average error was 1.1 percent. The second method (and also method 1) resulted in an average error of 3.6 percent.

3.4.3 Influence of detection efficiency

Because a real detector will not stop all photons, there is a variation on the absolute sensitivity. The detection efficiency will be higher if the photons hit the detector at a larger oblique incident angle (more detection material on its path). Therefore an extra correction was implemented to correct for this effect. The incident angle is given by α. The detector

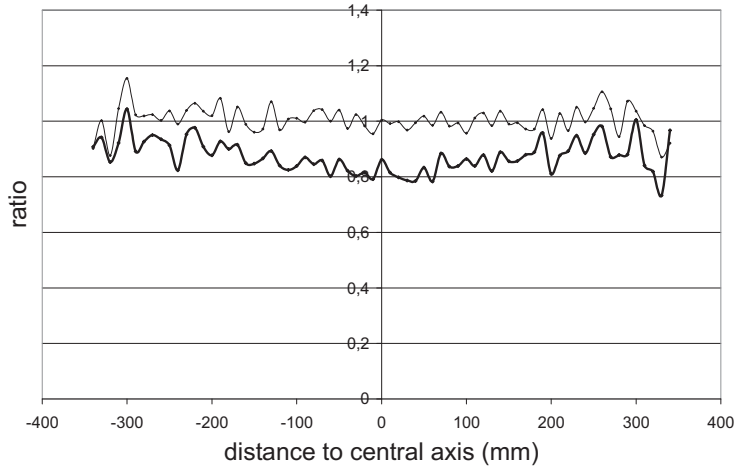

Figure 3.12: Ratio between simulated (simulation with realistic CZT parameters) and calculated values (lower curve is ratio with method 3, upper curve contains correction for detection efficiency).

thickness for this incident angle is $t_e = t/cos\alpha$. The detection efficiency DE is then calculated from the linear attenuation coefficient μ:

$$DE = 1 - exp(-\mu t_e). \tag{3.9}$$

By putting this term into equation 3.8, one obtains a correction for the detection efficiency of CZT. The μ value of 3.505 cm^{-1} was obtained from the NIST website. The profiles shown in figure 3.12 are obtained by taking the ratio between the simulated and calculated sensitivity values for a profile at a distance of 20 cm from the collimator. The profile that has a minimum around the central axis is obtained by dividing the simulated values by values obtained by method 3. The other profile is obtained in the same way, but method 3 is now scaled by the detection efficiency. It is clear that this profile is more uniform and closer to 1 than the other profile.

3.4.4 Validation through prototype measurements

For sensitivity measurements, a line source filled with 58 MBq of Tc-99m and of length 18 mm was placed in the same positions as described for the simulations (figure 3.8). The energy window was set to 20% at 140 keV. As a measure of sensitivity, the count rate was averaged over

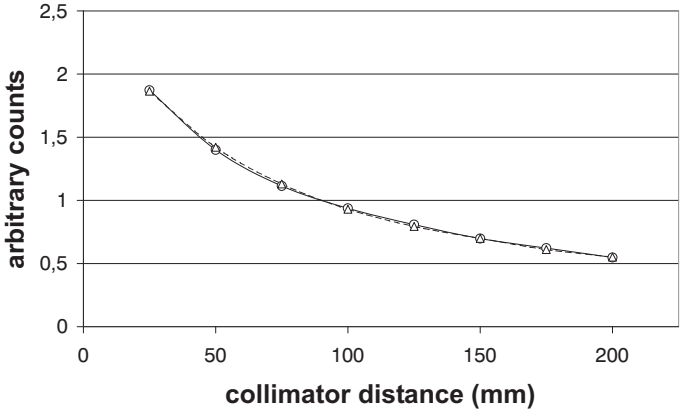

Figure 3.13: The measured sensitivity (△) of points on the central axis were compared to Monte Carlo data (○).

a period of 10 seconds. Normalized profiles are measured along both sampled directions and compared to the simulated sensitivity values. In figure 3.10 and figure 3.13, sensitivity values of real measurements are plotted against simulated values. It is clear that both show good agreement.

3.5 Analytic model for the spatial resolution

Equation 3.2 gives the fraction of detected radiation at x. Knowing that the sensitivity per unit area is equal to $\frac{1}{4\pi r^2}$, the Point Spread Function (PSF) can easily be derived:

$$PSF(x) = \frac{1}{4\pi r^2}(1 - \frac{xh}{gr\cos\alpha}). \tag{3.10}$$

When the term in parentheses is $\frac{1}{2}$ this gives x_{HWHM} and the FWHM is given by:

$$FWHM = 2x_{HWHM} = \frac{gr\cos\alpha}{h}. \tag{3.11}$$

r is equal to $\frac{d+h}{\cos\alpha}$ for planes at distance d parallel with the collimator/detector system. This results in a depth dependent FWHM that is constant in a plane at fixed detector distance and yields an identical

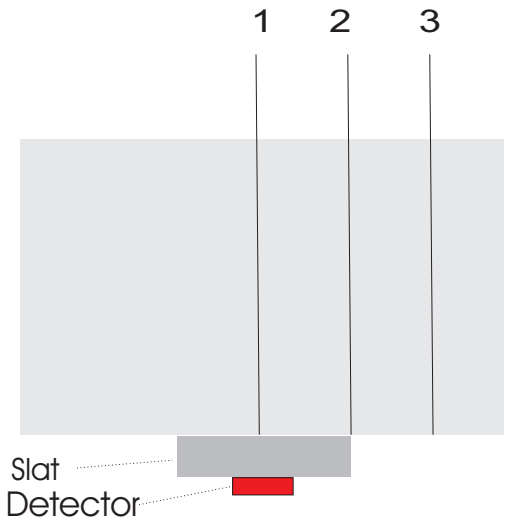

Figure 3.14: Location of the lines for simulation and measurement of resolution.

equation as for a parallel hole collimation system (Nuyts 2001):

$$FWHM = \frac{g(d+h)}{h}. \tag{3.12}$$

On the contrary, if non-rectangular slats were used (e.g., circular slats like shown in figures of (Zeng *et al* 2001)) this will not result in equal resolution in a plane parallel to the detection/collimator system. The resolution was calculated along three different lines perpendicular to the detector/collimator system (see figure 3.14). For comparison, the resolution was also calculated for the parallel hole AXIS ^{TM} (Philips Medical Systems, Cleveland OH, USA) system along the same three lines. The parameters of this system are in accordance with (Staelens *et al* 2003).

3.6 Validation of the analytic resolution model

For determination of the resolution, the detected count profiles, originating from simulated point sources along the three lines of figure 3.14 were fitted to a Gaussian function. To compare these results to the parallel hole AXIS ^{TM} system's resolution, the same method was used. To check the spatial resolution of the prototype rotating slat camera, count

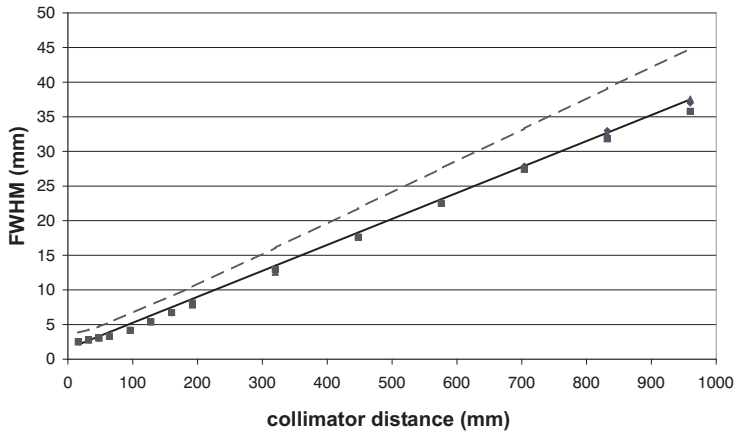

Figure 3.15: Resolution values obtained by calculation from equation 3.12 for SOLSTICE (solid line) and AXIS camera (dashed line). The discrete points show the simulated resolution values along line 1 (♦), line 2 (■) and line 3 (▲)from figure 3.14.

profiles originating from measured point sources along the three lines of figure 3.14 were evaluated. 512 spin angles were measured resulting in 512 count profiles per point. The FWHM of these profiles was taken and the average was calculated for each point. The obtained averages were then compared to the values derived from the calculations. The simulated and calculated values for the SOLSTICE device are shown in figure 3.15. The closest point in the simulations is at 16 mm distance and gives a FWHM = 2.51 mm. Linear extrapolation between the two points closest to detector gives an estimated FWHM at 0 mm of 1.8 mm. The calculations were also done for the AXIS camera. In figure 3.15 it can be seen that the resolution of the SOLSTICE camera is superior compared to the AXIS camera. This is due to the smaller spacing between the slats. Figure 3.16 shows that the resolution, measured on the prototype camera are in accordance with the values expected from simulations and calculations. It is clear from the figures that the resolution is constant in a plane parallel to the detector plane.

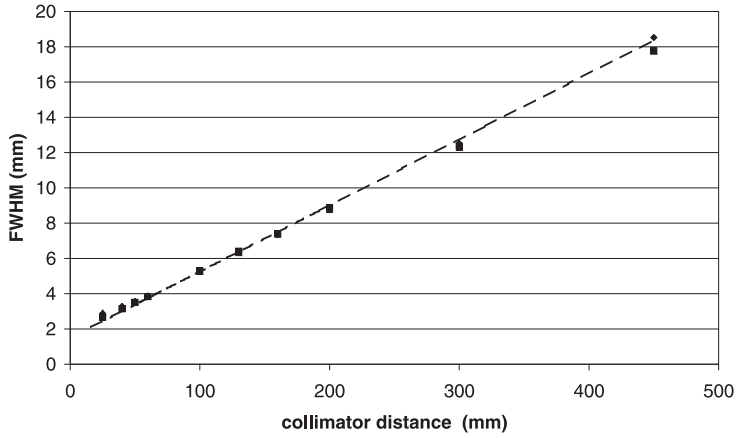

Figure 3.16: Resolution values obtained by calculation from equation 3.12 for SOLSTICE (dashed line). The discrete points show the measured resolution values along line 1 (♦), line 2 (■) and line 3 (▲)from figure 3.14.

3.7 Relevance of system modeling in the reconstruction

A planar image quality phantom was used in order to asses the influence of using the above derived system description in an iterative reconstruction. Furthermore, planar image quality of the prototype RS collimated gamma camera will be compared to a standard low-energy high-resolution (LEHR) parallel hole collimator. The system model will be derived using the Monte Carlo model, validated in previous sections.

3.7.1 Acquisition setup

The image quality phantom consisted of a warm circular background with a diameter of 170 mm, printed on a sheet of paper together with 12 hot lesions of varying diameter, ranging from 4 mm to 20 mm (figure 3.17). The Tc-99m on the paper had an activity of 15 MBq while the contrast was set to be 7:1. The sheet of paper was centered in the FOV parallel to the detector surface at 10 cm collimator distance. The detector/collimator prototype of figure 3.2 was spun 360° around its axis and the measurements were binned in 512 discrete spin angles during the 120 second acquisition. The acquisition was repeated ten times for the purpose of noise calculation. The same measurements were performed

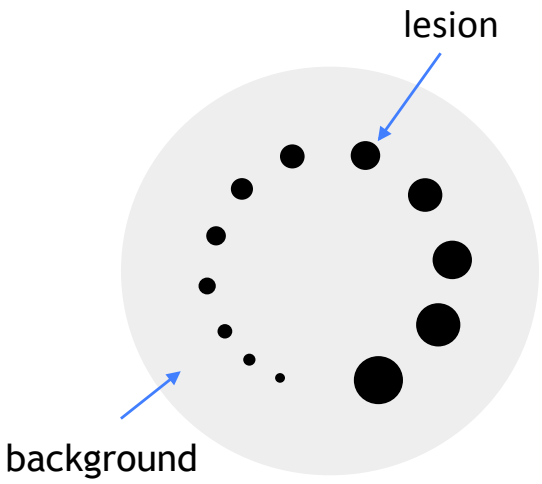

Figure 3.17: The printed image quality phantom with 12 hot lesions and a 17 cm background. Lesion to background contrast is 7:1.

on a traditional system equipped with a LEHR collimator, in order to compare to a classical gamma camera. Since both systems not only have different types of collimator, but also differ in collimator resolution (section 3.6) and detection material (CZT versus NaI(Tl)), it is not clear which factor has the largest influence on image quality.

3.7.2 Image reconstruction

Since the planar integral measurements reduce to line integrals in the case of planar imaging, the RS data can be reconstructed to projections using classical SPECT reconstruction techniques such as MLEM [145]. Our reference reconstruction therefore is a classical SPECT reconstruction, which does not incorporate correction for the non-homogeneous sensitivity and resolution in the FOV of the camera. A model of the imaging process, based on a Monte Carlo simulation, was included in our second reconstruction method.

3.7.2.1 Gaussian rotator based MLEM

The method of rotating the image matrix according to the detector spin angle to perform the projections in MLEM was chosen as a reference reconstruction method. Two-dimensional Gaussian interpolation was used

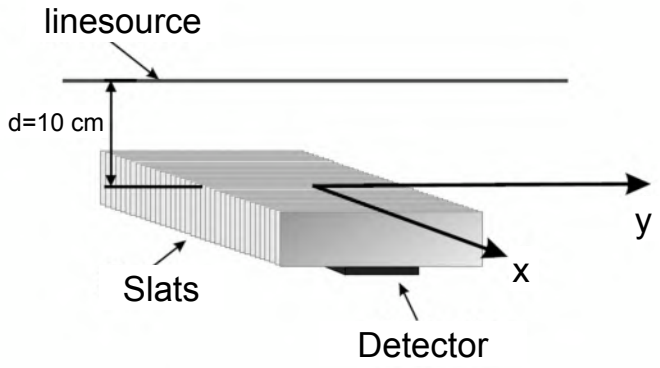

Figure 3.18: Position of the line source for the simulation used for deriving the system matrix.

to do the rotation. The kernel size was 3×3 pixels and the FWHM of the Gaussian was 1 pixel, according to the implementation suggested in [184]. 250 iterations for the 10 measurements resulted in 2500 reconstructed images.

3.7.2.2 Monte Carlo based MLEM

The RS device was modeled in GATE as described in section 3.4.1. The simulation setup of a line source, illustrated in figure 3.18, yielded a partial system matrix, only for source positions y along that line and the detector elements x at rotation angle zero. Translation and rotation of this system matrix to other source positions and toward other detector spin angles respectively, provides knowledge of the complete system matrix. The rotation was performed using nearest neighbor interpolation, since no significant improvement was found using Gaussian interpolation. This can be attributed to the small pixel size (1.8 mm) and the large amount of discrete spin angles. The derivation of the system matrix from the partial system matrix was implemented in the reconstruction and was calculated on the fly on a voxel driven basis, resulting in a fast and accurate execution of the reconstruction.

3.7.3 Contrast and noise calculation

Equation 3.13 shows the contrast recovery coefficient (CRC_l) which was calculated for the 12 different sized lesions in all the images.

$$CRC_l(\%) = \frac{1}{N} \sum_n \frac{\frac{\mu_{l,n}}{\mu_{b,n}}}{C} \times 100 \tag{3.13}$$

In this formula, n represents the realization number with N the total number of realizations. μ_l indicates the reconstructed mean activity in a lesion l and μ_b indicates the reconstructed mean activity in the background. C indicates the activity contrast in the phantom. The noise coefficient (NC) was calculated throughout the 10 realizations as shown as:

$$NC(\%) = \frac{1}{P} \sum_p \frac{\sigma_p}{\mu_p} \times 100. \tag{3.14}$$

σ_p and μ_p represent the standard deviation and the mean of a pixel p calculated over the different realizations. The noise was then averaged over the total number of pixels P in the image.

3.7.4 Results

The CRC was plotted versus the NC for both reconstruction techniques. 23% noise was reached after 45 iterations and after 100 iterations for the Gaussian rotator based (GR-MLEM) and the Monte Carlo based reconstruction (MC-MLEM) technique respectively. At this noise level, the CRC was plotted versus the lesion diameter (figure 3.19). The mean CRC over all lesions was about 9,4% higher using the MC-MLEM method. The second study compares the MC-MLEM method to the CRC obtained with a LEHR parallel hole collimator on a classical system. At 23% noise, the CRC was again plotted versus the lesion size and a mean CRC was found that was 13,1% above the mean CRC obtained with the classical camera (figure 3.20). Further improvement in contrast can be achieved with the RS collimator, especially for the smallest lesions, if we iterate longer. For example, for the 6 mm lesion we can achieve 65% contrast recovery at 35% NC while only a contrast of 45% is obtained using a classical collimator. The noise level will of course increase, but in some cases we could consider to maintain higher contrast for a reasonable NC.

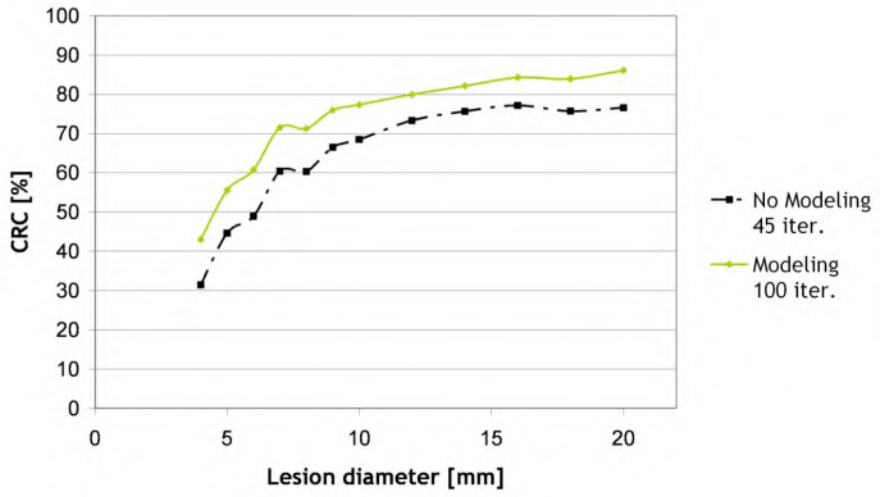

Figure 3.19: Comparison of the reconstruction techniques. Contrast recovery versus lesion size for equal noise level.

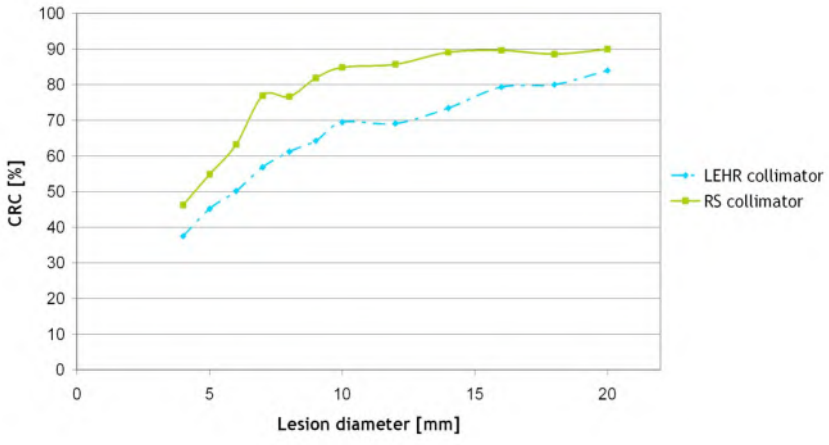

Figure 3.20: Comparison of the two imaging modalities. Contrast recovery versus lesion size is plotted for a matched NL.

3.8 Summary and original contributions

In this chapter, an analytic derivation of the sensitivity and spatial resolution of a rotating slat collimated SPECT camera is presented. To our knowledge, this is the only close field model for this detection geometry so far. We applied the formulas to the specific case of the SOLSTICE prototype. However, the expressions are general and can be applied also for other geometries with for instance larger detector surface or longer slats. A Monte Carlo model of the prototype detector was implemented and compared on the basis of sensitivity and spatial resolution throughout the FOV. Validation of both the calculations and the Monte Carlo model was done by showing excellent agreement with the measurements on the prototype when including a detection efficiency term in the calculations. Accurate knowledge of the sensitivity and spatial resolution allow a comparison to other collimator geometries. Also, modeling these effects in iterative reconstruction can result in improved convergence and better uniformity of the final reconstruction. This was proven in an image quality study with two different image reconstruction techniques, one without and one with system modeling. Also, a comparison with an LEHR system was made. Contributing the improvement in image quality to the rotating slat collimator would however be naive since the systems compared also differed in collimator resolution, detection material and detector surface. Therefore, to make a fair comparison of only type of collimation, chapter 5 will extrapolate the validated Monte Carlo model to a rotating slat collimated detector with equal properties as a parallel hole collimator. This work has been published in two peer reviewed citation indexed A1 journal publications [177, 169].

Chapter 4

Partial field-of-view artifact removal by use of the frequency distance relation

The previous chapter described and validated an analytic description and a Monte Carlo model of the rotating slat collimator in general. Both models were applied to the prototype SOLSTICE detector and good agreement was found with the real system. Furthermore, the importance of modeling the rotating slat system response during reconstruction was addressed.
Before thoroughly investigating image quality with respect to a parallel hole collimator, a problem which is intrinsic to the rotating slat collimator geometry will be investigated. The problem arises from the collimation of planes: a rotating slat collimator also measures activity outside the direct field-of-view. For planar imaging, this is the area described by the detector after a 360◦ spin rotation. This 'partial field-of-view' activity can lead to artifacts in reconstructed images. The purpose of this chapter is to develop a method to remove the contamination, caused by activity outside the direct field-of-view.

4.1 Introduction

The problem of 'partial field-of-view artifacts' in the case of planar imaging with a rotating slat collimator was pointed out in the PhD thesis of Lodge [101]. He showed that 'it is possible for a source to be within the

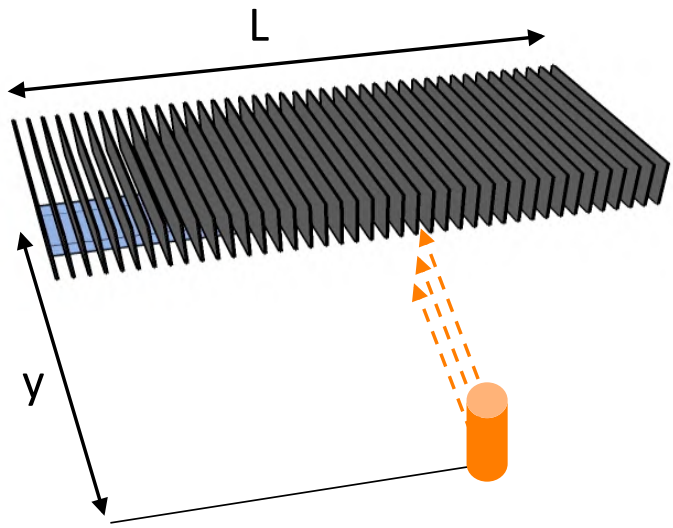

Figure 4.1: When y becomes larger than half the detector length L the source will cause partial FOV activity in the measurement.

field-of-view at some slat orientations but not at others'. In a clinical case, where the brain would be imaged with a slat collimated detector, smaller than the size of the body (which is always the case for a gamma camera), the activity from the bladder will be measured when the slats are in alignment with the camera axis. However, activity from the bladder can not be measured when the slats are perpendicular to the central axis of the scanner. This causes the projections of the bladder to be truncated or, in other words, to be in disagreement with the Orlov condition as described in chapter 2 resulting in truncation artifacts. Lodge investigated the effect of the partial field-of-view (PFOV): although the artifacts were small, they 'create a noisy background, which hinders the detection of cold lesions'. An example of a detector-source setup is illustrated in figure 4.1. When the source is outside the detector's direct FOV (i.e. when $y > L/2$), it will give rise to PFOV activity. A planar rotating slat acquisition of a typical image quality phantom without the presence of PFOV activity will result in plane integral data as depicted in figure 4.2 (a). Also the reconstruction of this dataset is shown. The influence of PFOV activity becomes clear in figure 4.2 (b), where there was a source of PFOV. In the plane integral data, an isolated source outside the direct FOV shows up as a sine wave of which the extremities have been truncated. This truncation leads to artifacts in the reconstructed

image (figure 4.2 (b)). In this chapter we will investigate the influence of PFOV for the prototype SOLSTICE detector and propose a method for reducing the influence of activity outside the direct FOV of the scanner. The proposed method can be applied as a pre-correction technique or as an on-line correction method during iterative reconstruction.

4.2 Frequency distance filtering

4.2.1 The frequency distance relation

In figure 4.3, three points at different distances y from the spin-rotation axis of the scanner are shown. The green point is closest to the detector, the orange point is further away, but still in the direct FOV while the blue point is outside the direct FOV. The two closest points will be seen by the rotating slat collimated detector at every spin angle φ while the third point will not be seen for certain spin angles. This is also reflected in the plane integral data $g(x, \varphi)$ which can be described as:

$$g(x, \varphi) = \int_{-\infty}^{+\infty} s_{\varphi}(x, y) dy, \tag{4.1}$$

where , $s_{\varphi}(x, y)$ is the source density described in the rotated (x, y)-coordinate system (at angle φ with respect to the reference (x_r, y_r)-system). The plane integral data resulting from a rotating slat planar acquisition of the individual point sources is shown in figure 4.4 (a). For the third point, it is clear that truncated data is measured. Figure 4.4 (b) shows the 2D Fourier transform $G(X, \Phi)$ of the corresponding plane integral data $g(x, \varphi)$ in 4.4 (a). An intuitive interpretation of the 2D Fourier transform of the plane integral data is based on this insight: lines with steepness $\frac{d\varphi}{dx}$ in the data translate into lines with steepness $\frac{d\Phi}{dX}$ in Fourier space. By approximating the sine waves by triangle waves, one can easily understand that the sines of figure 4.4 (a) translate into the lines of figure 4.4 (b). Since the steepness of the triangle wave approximations is defined by the distance y of a point source to the center of rotation (CoR), a point at distance y will appear as a line with steepness $y = -\frac{d\Phi}{dX}$ in Fourier space. Mathematically, this insight has been described by Edholm [47] and denoted as the frequency distance relation (FDR). The FDR states that in $g(x, \varphi)$, points at a distance y from the CoR have their main Fourier components on a line in Fourier space defined by $\Phi = -Xy$, where X denotes spatial frequency and Φ is the

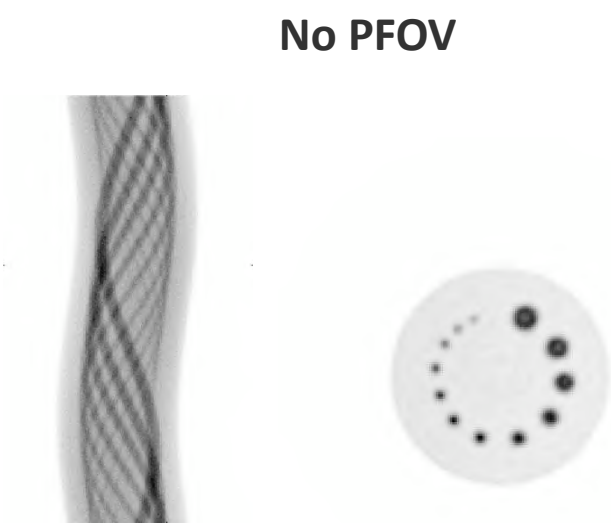

(a)

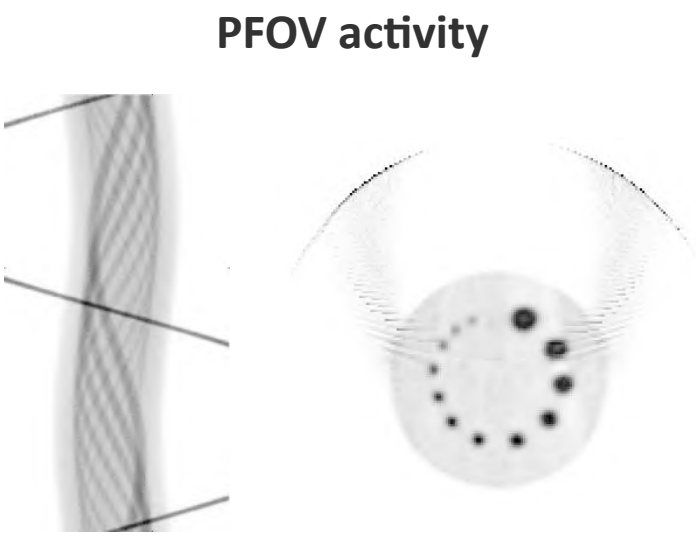

(b)

Figure 4.2: A plane integral dataset and its reconstruction are shown in (a) without PFOV activity and (b) with a source of PFOV activity present.

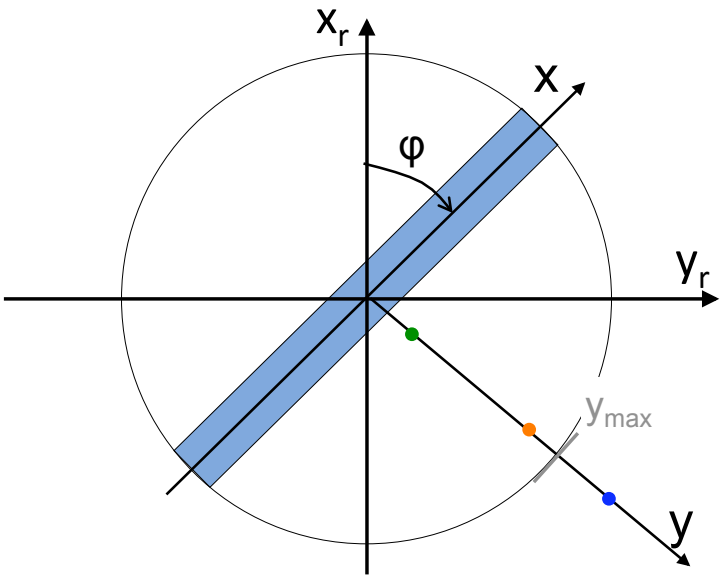

Figure 4.3: The detector, rotated over a spin angle φ with respect to the reference coordinates x_r and y_r. Three points are indicated at difference distances y.

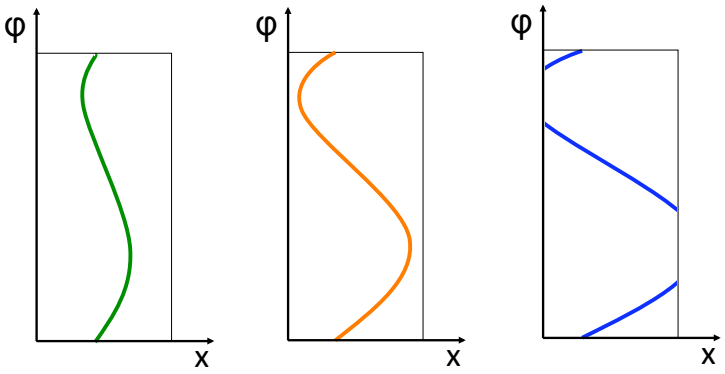

(a)

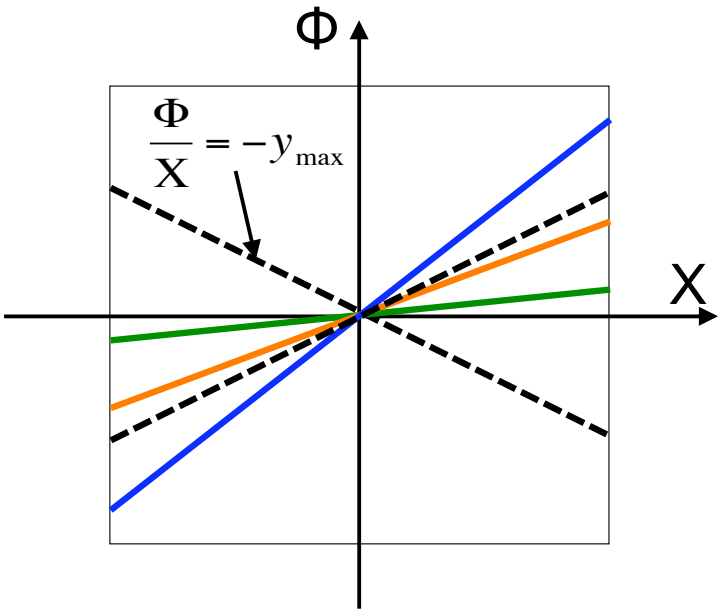

(b)

Figure 4.4: (a) The plane integral data for the three points indicated in 4.3 with (b) their respective Fourier transforms.

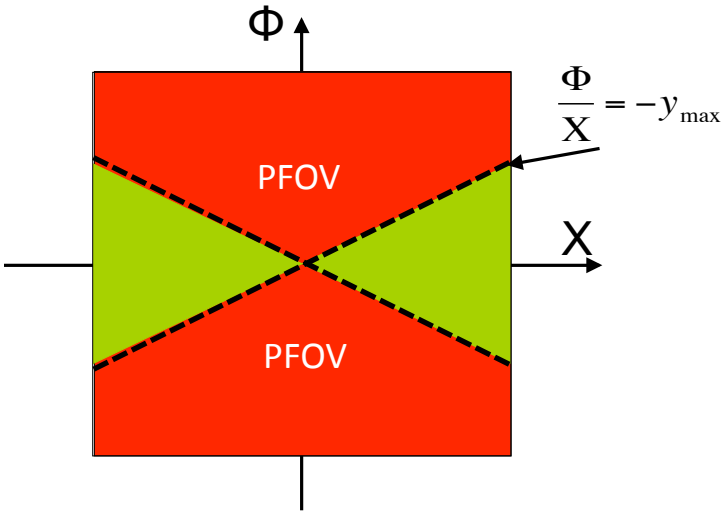

Figure 4.5: The different areas in Fourier space where normal (inside the direct FOV) and partial FOV activity is reflected. By removing the red zone in Fourier space and taking the inverse Fourier transform, the PFOV activity should ideally be removed.

angular frequency. However, this is an idealization since the FDR is only approximate: there will also be some components at lower frequencies. Intuitively, this can be understood by the fact that the sine waves in the data are composed not only of lines with steepness $\frac{d\varphi}{dx}$, but also of lines with smaller steepness. Nevertheless, the FDR has been successfully used for pre-correction of sinogram for the distance dependent resolution of a SPECT scanner [98, 66, 57, 86] and for the restoration of missing data in PET sinograms [77].
The 2D Fourier transform of plane integrals will not have values for which $\Phi > -Xy_{max}$, with $y_{max} = L/2$ when no PFOV activity is present. However, when PFOV activity is present, there will be components for which $\Phi > -Xy_{max}$. This is illustrated in figure 4.5. The basic idea to remove the PFOV activity is to remove those components before taking the inverse Fourier transform. PFOV activity should accordingly be removed from the data. We will indicate this technique by 'frequency-distance filtering' (FDF).

4.2.2 Frequency distance filtering

Two different implementations of the FDF method are proposed which are both based upon constraining the 2D Fourier domain. A similar approach has previously been used by Karp [77] to restore missing data in PET sinograms. For the first method (figure 4.6 (a)), named the pre-filtering method, we will first take the fast Fourier transform (FFT) $G(X,\Phi)$ of the plane integrals $g(x,\varphi)$ which are contaminated by PFOV activity. Based on the frequency distance relation, we will then remove all the components for which $|\Phi| > -Xy_{max}$. This filtering is implemented as multiplication with a filter function $H(X,\Phi)$:

$$G_f(X,\Phi) = H(X,\Phi)G(X,\Phi), \tag{4.2}$$

where $G_f(X,\Phi)$ represents the filtered 2D Fourier transform of the data. H is the filter:

$$H(X,\Phi) = \begin{cases} 0, & \text{if } |\Phi| > -Xy_{max} \\ 1, & \text{elsewhere} \end{cases} \tag{4.3}$$

By taking the inverse 2D Fourier transform (FFT^{-1}) of $G_f(X,\Phi)$, we obtain a filtered plane integral dataset $g_{pf}(x,\varphi)$ which can be reconstructed to a corrected image $\mathbf{s_{pf}}$.
The second method (figure 4.6 (b)) is based on adding a correction term to the forward projection at each iteration of an iterative reconstruction algorithm. By adding the PFOV activity to the forward projection, it is implicitly removed from the image estimate: the update ratio in the iterative reconstruction will converge to unity as the image estimate converges to the uncontaminated image. This technique is often used for scatter correction based on estimation of the scatter sinogram (chapter 2, section 2.5.2.3). Now, we need to obtain an estimate of the plane integral data $g_{fp}(x,\varphi)$ of the contamination only. We can obtain this estimate in a similar way as we obtain a pre-corrected dataset. The only difference with the pre-correction technique is that we zero all elements in Fourier space for which $|\Phi| < -Xy_{max}$ by modifying H to:

$$H(X,\Phi) = \begin{cases} 0, & \text{if } |\Phi| < -Xy_{max} \\ 1, & \text{elsewhere} \end{cases} \tag{4.4}$$

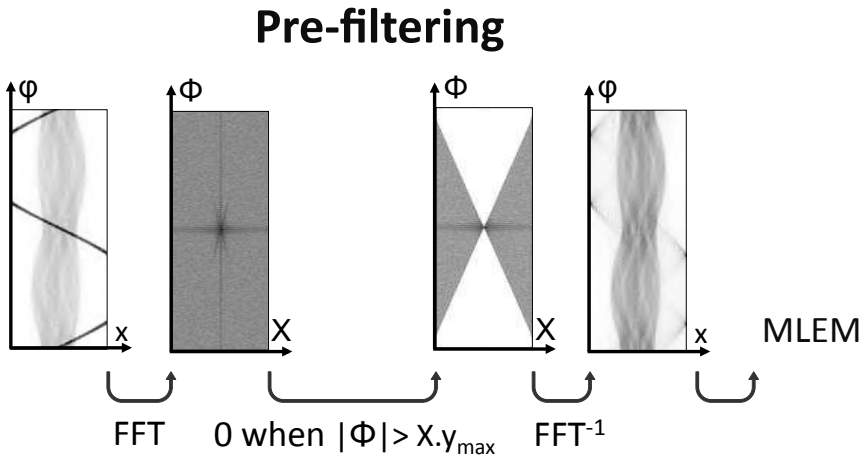

(a)

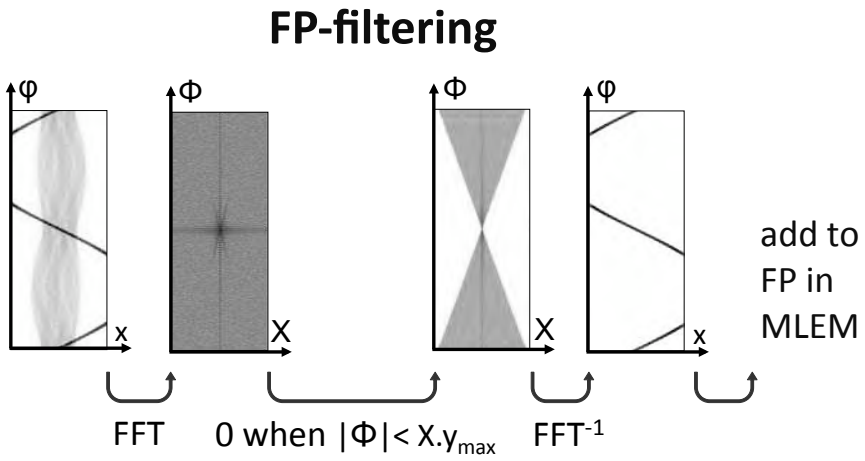

(b)

Figure 4.6: The method for filtering the PFOV activity with (a) the pre-correction method and (b) during forward projection in an iterative reconstruction algorithm.

4.3 Phantom measurements

To investigate the performance of both FDF-techniques, three phantoms were used for measurements inside the direct FOV. Two other sources were used for PFOV measurements. The Hoffman brain phantom slice, the image quality phantom and the bar pattern phantom, used for untruncated data measurements are shown in figure 4.7. They all contained approximately 500 μCi of Tc-99m and were placed centrally in the 345 mm diameter FOV at 10 cm collimator distance for a 20 minutes measurement. The lesions in the image quality phantom ranged from 4 mm to 20 mm while the bars in the bar pattern phantom ranged from 2 mm to 7 mm. For the purpose of PFOV data measurement, a small cylinder (radius = 14 mm, height = 50 mm) and a large box ($80\times200\times50$ mm^3) were filled with approximately 1 mCi of Tc-99m and placed at four different distances d_{FOV} from the FOV (d_{FOV} =100 mm, 200 mm, 300 mm and 400 mm). The acquisitions lasted for 20 minutes. For the acquisition, the detector/collimator pair of the prototype detector was spun 360° around its axis in 512 discrete angles. At each angle, the planar collimation resulted in an array of 192 measurements, yielding a 192 by 512 plane integral dataset. To create datasets, 'contaminated' with truncated data, datasets from the three phantoms are mixed with datasets originating from the PFOV measurements. The plane integral data from the small cylinder at d_{FOV} = 100 mm was therefore added to the data from three phantom measurements within the direct FOV. To investigate the influence of d_{FOV} and the concentration of the activity outside the direct FOV, the datasets from the PFOV measurements from both the cylinder and the box were added to the bar-pattern measurement.
All contaminated datasets were reconstructed to contaminated images $\mathbf{s_c}$ using Monte Carlo based MLEM (chapter 3) which compensates for the non-uniform sensitivity within the FOV of the RS camera. For calculation of the normalized root mean square error (NRMSE):

$$NRMSE = \frac{\sqrt{\frac{\sum_i (s_{c_i} - s_{u_i})^2}{I}}}{mean(\mathbf{s_u})} \times 100\%, \tag{4.5}$$

the data of the three phantoms were also reconstructed without adding PFOV contamination to uncontaminated planar images $\mathbf{s_u}$. Furthermore, the two different FDF techniques were applied for the contaminated datasets, resulting in $\mathbf{s_{pf}}$ and $\mathbf{s_{fp}}$ for the pre-filtering technique and

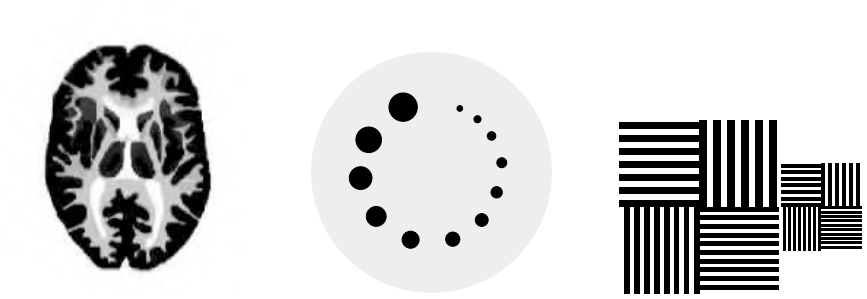

(a) (b) (c)

Figure 4.7: The three different phantoms used in this study. (a) shows the hoffman brain phantom, (b) the image quality phantom and (c) the bar pattern phantom.

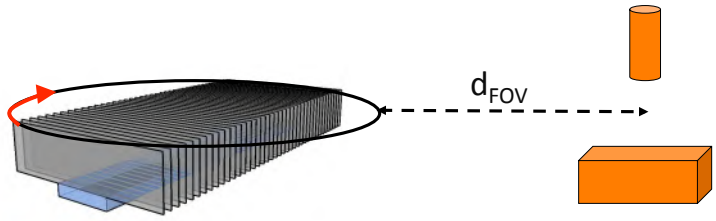

Figure 4.8: The source detector setup for the measurements with PFOV activity at different distances.

the forward projection-filtering respectively. For these images, NRMSE was also calculated.

4.4 Results

4.4.1 Performance of the filtering methods

The images resulting from the uncontaminated brain phantom data $\mathbf{s_u}$, the contaminated data $\mathbf{s_c}$ the pre-filtered data $\mathbf{s_{pf}}$ and the FP-filtered reconstruction $\mathbf{s_{fp}}$ are shown in figure 4.9 (a), (b), (c) and (d) respectively. A profile through these images in drawn in figure 4.9 (e). For the image quality and the bar pattern phantom, images and a profiles are shown in figure 4.10 and figure 4.11 respectively.

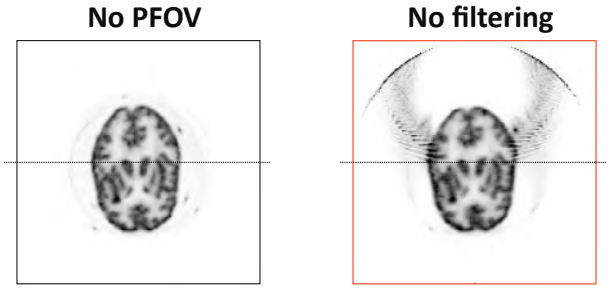

(a)

(b)

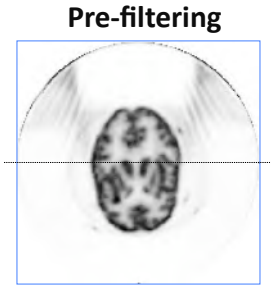

(c)

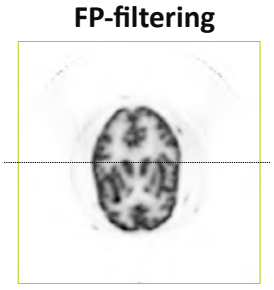

(d)

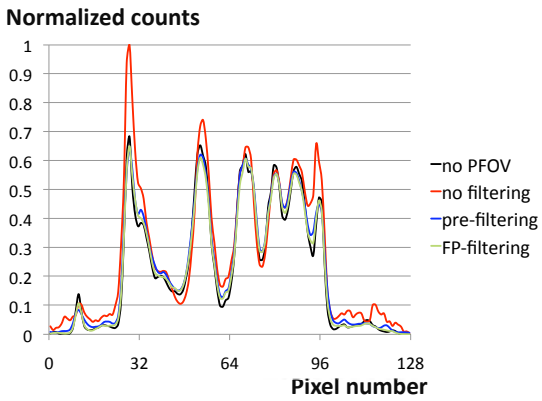

(e)

Figure 4.9: Images of the brain phantom. (a) shows an image of an acquisition without PFOV activity present, (b) shows an image with PFOV activity (small cylinder at 100 mm) present but without corrections, (c) shows a reconstruction from a pre-corrected sinogram and (d) shows an image where the PFOV activity was removed by compensating during reconstruction

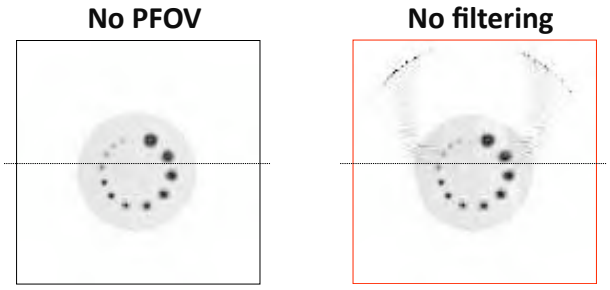

(a)

(b)

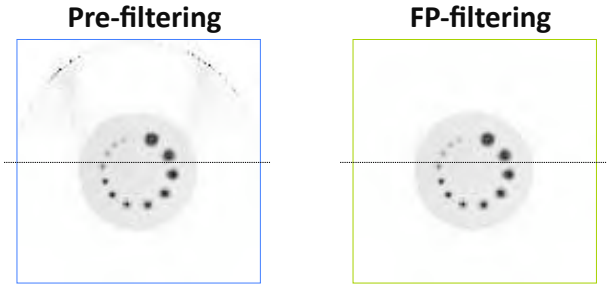

(c) (d)

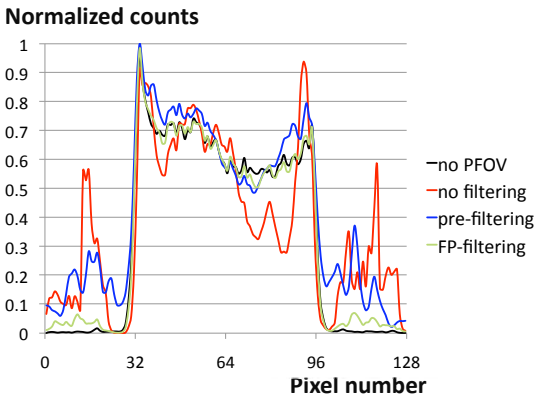

(e)

Figure 4.10: Images of the brain phantom. (a) shows an image of an acquisition without PFOV activity present, (b) shows an image with PFOV activity (small cylinder at 100 mm) present but without corrections, (c) shows a reconstruction from a pre-corrected sinogram and (d) shows an image where the PFOV activity was removed by compensating during reconstruction

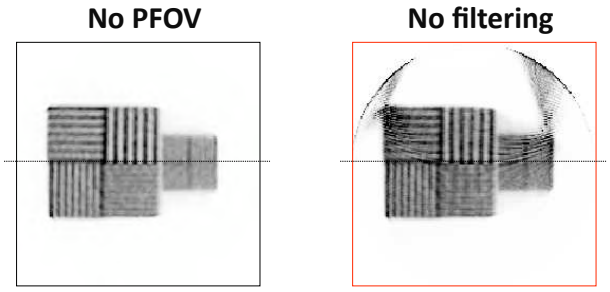

(a)

(b)

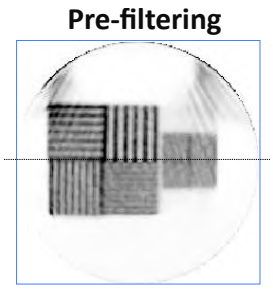

(c)

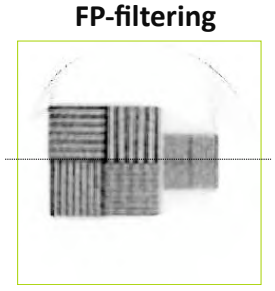

(d)

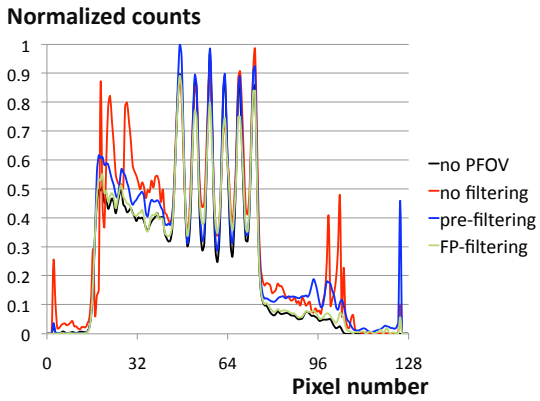

(e)

Figure 4.11: Images of the brain phantom. (a) shows an image of an acquisition without PFOV activity present, (b) shows an image with PFOV activity (small cylinder at 100 mm) present but without corrections, (c) shows a reconstruction from a pre-corrected sinogram and (d) shows an image where the PFOV activity was removed by compensating during reconstruction

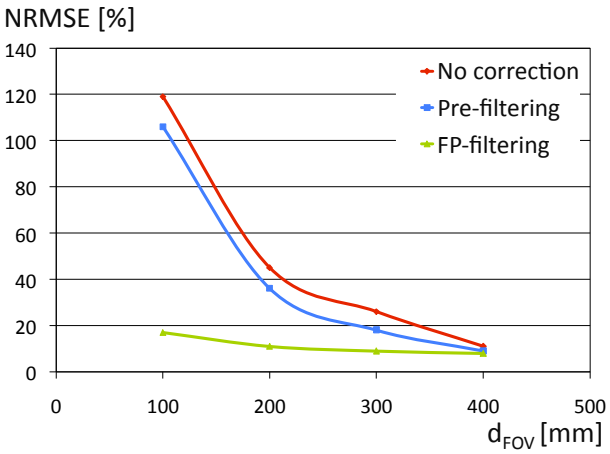

(a)

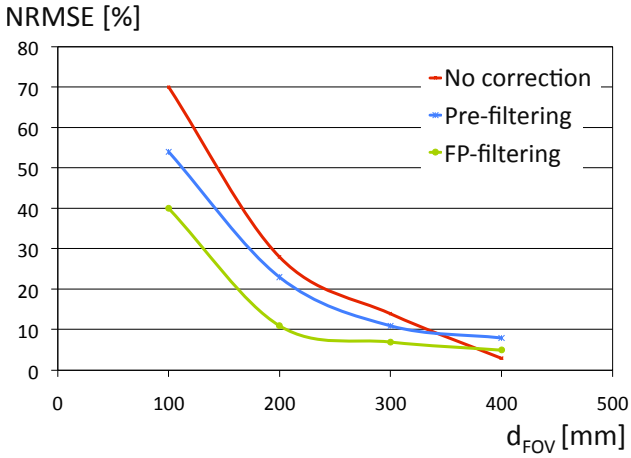

(b)

Figure 4.12: NRMSE for (a) the small PFOV source and (b) the large PFOV source.

From visual inspection and from the profile, the results with the FP-filtering method are the best. When applying no filter, large artifacts appear in the images. They are especially pronounced at the side where the PFOV activity is present. By applying the pre-filtering method, the profiles agree better with the profile without PFOV activity, but the images still show artifacts. The FP-filtering method almost completely cancels out the artifacts and very good agreement of the profiles is found. These findings agree with the NMRSE values, given in table 4.1. While the pre-filtering method only reduces the error by maximally 25%, the FP-filtering reduces the error with maximally 135%. A residual NRMSE of 20%, 13% and 17% is found for the the brain, image quality and bar pattern phantom respectively.
From these results, it is clear that major artifacts are present when a PFOV source is present. Furthermore, pre-filtering the data as described in the methods section still results in a major error. Much better images are obtained when applying the correction during forward projection of an iterative reconstruction algorithm. This is because the compensation is applied at each iteration.

NRMSE(%)	Brain	Image quality	Bar pattern
$\mathbf{s_c}$	155	139	119
$\mathbf{s_{pf}}$	130	114	106
$\mathbf{s_{fp}}$	20	13	17

Table 4.1: NRMSE for the contaminated and filtered reconstructions with respect to the uncontaminated reconstruction.

4.4.2 Influence of the PFOV distance and concentration

The influence of the distance to the direct FOV of the PFOV source was investigated as was the influence of the concentration of activity by using a small and a large volume source with equal activity. In figure 4.12 (a), results are shown for the small source. It is evident that the further the source is moved away from the direct FOV, the less the influence of the PFOV activity will be. At 400 mm, the NRMSE values are almost equal for the three curves shown. It is thus useless to filter the dataset for activity further away than 400 mm. However, in clinical settings, distances larger than 400 mm are not relevant unless there would be different cameras in each others' vicinity.

For the large, less concentrated PFOV source, figure 4.12 (b) shows less influence of the PFOV activity. However, the FP-filtering seems to have more difficulty to remove the contamination caused by this larger source. From approximately 325 mm distance, it is even better not to use any filtering of the dataset, probably because of errors induced by the Fourier transformation. The general trend however remains: the FP-filtering performs best due to the correction at each iteration.

4.5 Summary and original contributions

In this chapter, a method for removing artifacts, caused by the partial field-of-view effect was proposed and investigated. Two similar filtering techniques, one pre-correction technique and one in-reconstruction correction technique were compared. It was shown that the compensation for PFOV during reconstruction performs best. Although, when the sources are larger , the technique has more difficulty to filter out the activity from PFOV sources. For sources further than 400 mm away, no filtering is required. By filtering on the 2D Fourier transform of the different SPECT angle of a tomographic acquisition, one could remove PFOV from tomographic data. However, one could also look at the properties of the 3D Fourier transform of a tomographic acquisition for filtering PFOV sources. This lies beyond the scope of this dissertation but it is an interesting topic for future research.
The work proposed in this chapter has been presented at an international conference [168].

Chapter 5

Comparison of planar image quality with rotating slat and parallel hole collimation

In chapter 3, both an analytic and a Monte Carlo model of the prototype rotating slat collimator were validated. Also, the importance of the incorporation of the model into the reconstruction was pointed out. In this chapter, we will use this Monte Carlo model to compare image quality obtained with a rotating slat (RS) collimator to that obtained with a parallel hole (PH) collimator, using a model for the imaging system during image restoration. Special attention will go out to the shape of the source distribution. Finally, a clinically relevant case is evaluated for both types of collimation.

5.1 Introduction

As pointed out in chapter 2 (section 2.3), the main factor limiting the total spatial resolution of a gamma camera is associated with the design of the collimator. In the case of PH collimation, the collimator spatial resolution can not be optimized without decreasing the system sensitivity. A four-fold decrease in sensitivity would result from 2 times better spatial resolution. Converging beam collimators attempted to overcome this problem, but they all limit the Field Of View (FOV) of the camera

and are thus not suited for whole body imaging. The sensitivity versus resolution trade-off is however less severe in the case of a RS collimator. While collimator resolution remains unaltered, RS sensitivity will only depend to the first order on the gapsize g instead of on g^2 in the case of PH collimation. A factor of two improvement in collimator resolution will thus only result in half of the sensitivity for the RS instead of one-fourth of the sensitivity for a PH collimator. A rotating slat collimator with equal collimator resolution as an LEHR collimator in combination with a 30 cm diameter NaI(Tl) detector results in a factor of 40 higher sensitivity compared to an LEHR parallel hole collimator [190]. How-

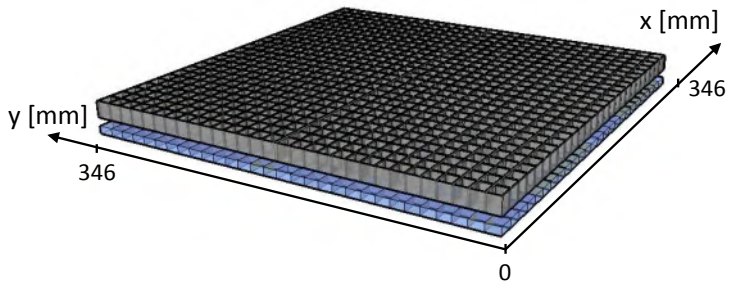

(a)

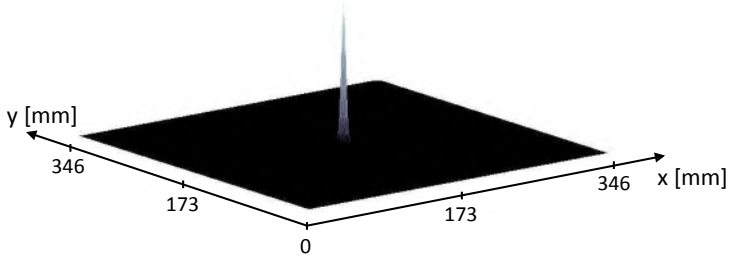

(b)

Figure 5.1: (a) The pixelated detector in combination with a parallel hole collimator and (b) the associated point spread function.

ever, because the spatial support of the point spread function (PSF) of a RS collimator is very large in y-direction (figure 5.2 (b)), it is not possible for a slat collimator to obtain directly interpretable images. This contrasts to PH collimators where direct projection images, being a convolution of the source distribution with the (small) PSF from figure 5.1 (b), are obtained. For obtaining planar images of the radioisotope distribution in an object, a rotating slat collimator needs to spin around

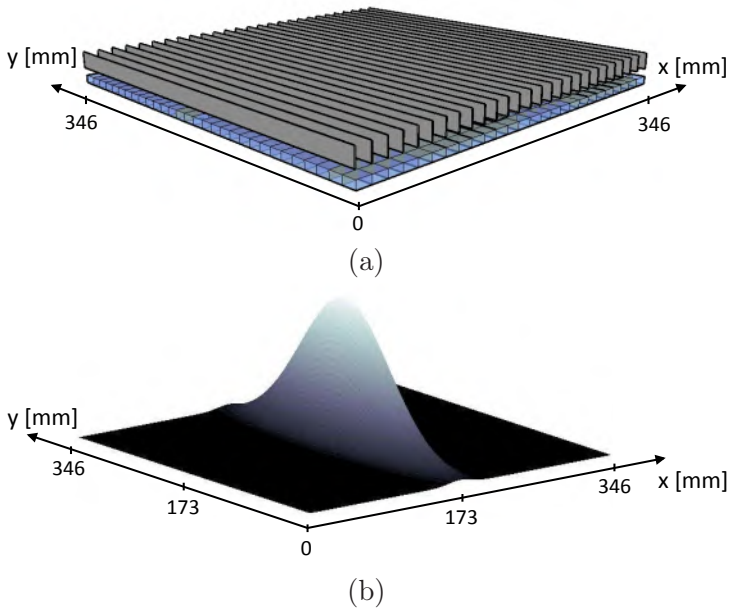

Figure 5.2: (a) The pixelated detector in combination with a rotating slat collimator and (b) the associated point spread function.

its own axis in order to obtain a complete data set [110, 102, 54, 199]. These data can then be reconstructed to projection data using a regular SPECT reconstruction approach with an appropriate system model. Due to the image reconstruction needed for planar RS images and due to the broad PSF in the direction of the slats, noise accumulation will arise in the reconstructed images, compromising the gain in sensitivity. The trade-off between this increased noise accumulation and increased system sensitivity will be investigated in this chapter. Since the sensitivity and noise accumulation depend on the collimator distance and the incidence angle, the shape of the source distribution will be an important factor in this analysis.

The Monte Carlo model of the RS system that will be used is based on a simulation model validated in chapter 3. Since the goal is to compare only the effect of collimation, we match the active detector area with that of the PH collimated system. The strip detector was replaced therefore by a complete detector (figure 5.2 (a)). In order to minimize the pixel crosstalk, a system model that models the system response as close as possible to the real system response will be included in an iterative re-

construction. Also, the PH system (figure 5.1 (a)) was modeled by its PSF, which is used to deconvolve the raw projection images.
By means of simulation studies, the contrast-to-noise for hot and cold spot imaging will be compared for both a RS and a PH system. Next, the influence of the object size and lesion contrast will be investigated by means of the optimal Contrast-to-Noise Ratio (CNR_o). Point Response Functions (PRFs) are derived for the various phantom dimensions. Finally, a realistic simulation setup, modeling a planar bone scan, will demonstrate the visual image quality that can be obtained with the RS collimator.

5.2 Monte Carlo detector models

The Monte Carlo model, validated in chapter 2, was used as a basis to model both the rotating slat and the parallel hole collimated camera. The detector was the same for both systems and was modeled as a pixelated solid state detector consisting of 192×192 individual CdZnTe crystals. The surface of one pixel is 1.8 mm×1.8 mm while its height was set to 5 mm. To make the efficiency of the detector independent of the collimator type, the active area of one pixel is set to be only 1.5 mm×1.5 mm, allowing the collimator to have septa of 0.3 mm thickness. The active area will thus be independent of the collimator type since the area covered by the collimator coincides with the inactive detector area.
The RS collimator was simulated as 193 parallel lead slats of height 40 mm, placed in between two detector pixels rows. The thickness of a slat was set to 0.3 mm while the length was equal to the length of the detector, being 345.6 mm (figure 5.2 (b)). The square PH collimator had the same height and thickness as the RS collimator (40 mm) and was matched to the pixelated detector. This resulted in a parallel hole collimator with square holes of 1.5 mm×1.5 mm (figure 5.1 (a)). The RS collimator/detector pair was rotated around its own axis in 128 discrete steps at a speed of 20 seconds per rotation. The PH collimator/detector pair did not move during acquisition.

5.3 Image reconstruction

5.3.1 Rotating slat reconstruction

The reconstruction of the plane integral data to projection images was performed using the Monte Carlo based MLEM algorithm used in chapter 3. More detail about the algorithm is provided here.
The reconstruction problem of plane integral data to projection images can be described by

$$\mathbf{As} = \mathbf{g}, \tag{5.1}$$

where $\mathbf{g}$ represents a series of M different plane integral projection elements $\mathbf{g} = [g_1, g_2, \ldots, g_M]^T$ and $\mathbf{s} = [s_1, s_2, \ldots, s_N]^T$ represents the projection image to be reconstructed. The system matrix $\mathbf{A} = [a_{ij}]$ with $i = 1, \ldots, N$ and $j = 1, \ldots, M$ represents the probability of measuring a photon originating from projection element i in detection bin j. For our RS system, M equals 24576 since we have 128 (number of spin angles) times 192 projection elements. The individual values assigned to each of these 192 projection elements resulted from summing all the detections along a row of pixels in between two slats (sum in y-direction). We reconstruct the projection image in a 192 by 192 pixel matrix, thus N equals 36864. MLEM takes into account the Poisson nature of the data:

$$\hat{s}_i^{(t+1)} = \frac{\hat{s}_i^t}{\sum_j a_{ij}} \sum_j a_{ij} \frac{g_j}{\sum_i a_{ij} \hat{s}_i^t}. \tag{5.2}$$

Here the ratio of the measured data in one projection element g_j and the forward projection to that projection element $\hat{g}_j^t = \sum_i a_{ij} \hat{s}_i^t$ is back projected. This is repeated and summed over all projection elements before a pixel is updated. Updating all pixels yields a new image estimate (figure 5.3). The system matrix should model the imaging process as accurate as possible. Therefore, Monte Carlo simulations are used, in order to know the source location of each detected photon. Storing the complete system matrix $\mathbf{A}$ for our RS system would require approximately 1,7 Gb of memory assuming two bytes per element. Using a 14 million count simulation in GATE, we derived the PSF for the RS system for a point at 10 cm collimator distance. The mean PSF value was 4500 in a 16 by 192 pixels region of interest (ROI), centered over the PSF resulting in a mean noise smaller than 1,5% in the PSF. Based on translational and rotational system symmetries, the system matrix $\mathbf{A}$, which maps

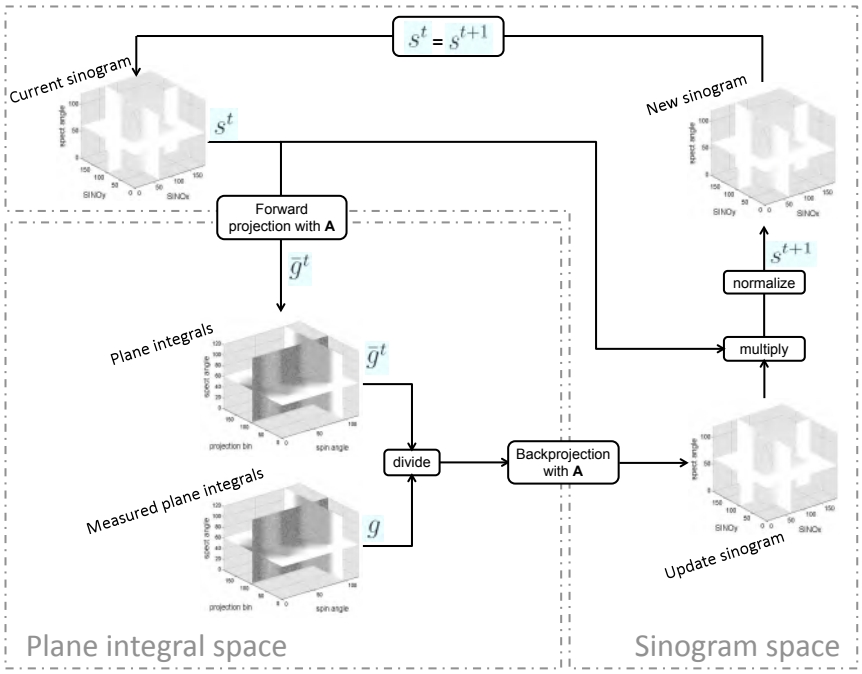

Figure 5.3: Schematic representation of the MLEM algorithm used for reconstruction of plane integral data.

one plane at 10 cm distance to detector space, was calculated on the fly during reconstruction. This procedure only requires storage of the PSF, which has a size of 144 kBytes. For all RS data processed, 400 iterations of this algorithm were reconstructed.

5.3.2 Deconvolution of parallel hole projections

The comparison of PH and RS needs to include the necessary reconstruction for the RS data. Therefore, the PH projection images were deconvolved using the Richardson-Lucy method [138, 105]. The iterative technique for deconvolution is very similar to MLEM and every next iteration is calculated with:

$$\hat{s}_i^{(t+1)} = \hat{s}_i^t \sum_j h_{ij} \frac{p_j}{\sum_i h_{ij} \hat{s}_i^t}, \tag{5.3}$$

where h_{ij} is an element of the PH PSF, s_i is the estimated value at location i, and p_j is the value at pixel location j in the measured projection

image. The PSF was again derived from a 1,6 million count GATE simulation, resulting again in a mean PSF value of 4500 counts per pixel in a 16 by 16 pixels ROI centered over the PSF. By the use of this method we also take into account the resolution of the PH system. A total number of 20 iterations of this algorithm are used to process the PH projections.

5.4 Image quality evaluation study

A contrast-to-noise analysis in images obtained with a classical gamma camera can give an indication of the balance between spatial resolution (related to contrast) and sensitivity (which influences noise). A higher sensitivity, resulting in a poorer resolution, will decrease noise because of the higher number of detected events. However, on the other hand, the contrast will drop, especially for small lesions, because of the larger collimator holes. Decreasing the sensitivity will give increased contrast, but will also increase the noise. Depending on the lesion size under investigation, a collimator can be optimized. For the RS system, the better photon collection efficiency and the noise accumulation during reconstruction will be taken into account in the contrast-to-noise plots. Therefore, such plots can be used to compare image quality of a RS system and a PH system.

5.4.1 Methods

5.4.1.1 Influence of lesion size

To investigate the contrast-to-noise behavior of both collimator types, a planar image quality phantom was simulated (figure 5.4 (a)). The phantom consisted of a warm background (diameter 20 cm), two cold lesions (diameters 23.4 mm and 19.8 mm) and four hot lesions (diameters 16.2 mm, 12.6 mm, 9 mm and 5.4 mm). The activity of the phantom was set to 238 Bq/mm^3 in the background while it was 1904 Bq/mm^3 in the hot lesions to have a hot spot contrast ratio of 8:1. The activity in the cold lesions was zero. The phantom was placed parallel to the detector at 10 cm collimator distance and the simulation time was set to 400 s. Ten realizations of the same simulation setup were obtained both on the PH and the RS collimated system. This allows the study of noise throughout different noisy realizations of the same acquisition. The hot-

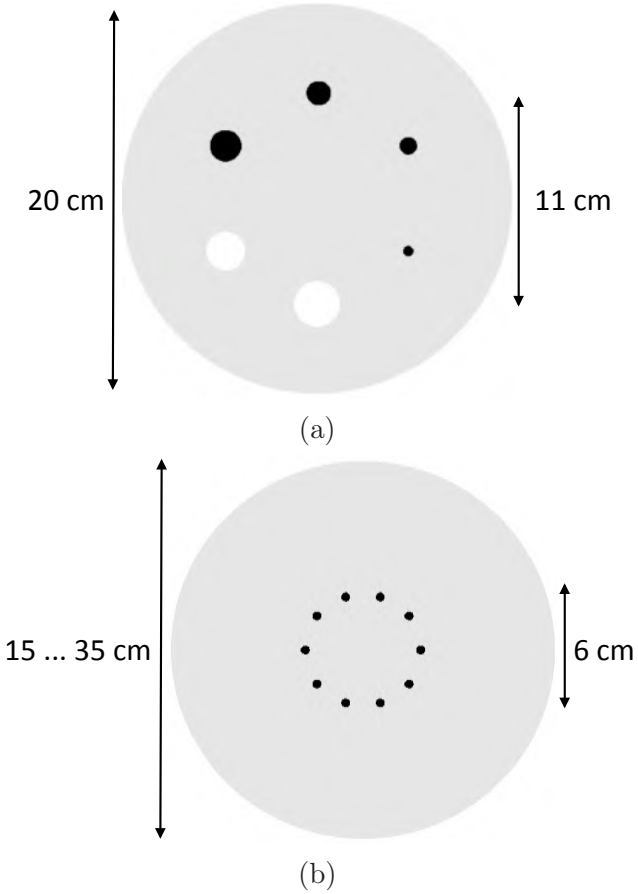

Figure 5.4: (a) The image quality software phantom and (b) the hot spot software phantom used to investigate image quality.

and cold spot contrast recovery were defined to be [80]:

$$CRC(\%) = \frac{\frac{\mu_l - \mu_b}{\mu_b}}{C - 1} \times 100 \tag{5.4}$$

with C being the real contrast in the phantom, in our case $C = 8$ for the hot spots and $C = 0$ for the cold spots. μ_l and μ_b are the mean lesion and background activity, averaged over all realizations. The noise coefficient (%) is calculated as

$$NC(\%) = \frac{\sigma_p}{\mu_p} \times 100. \tag{5.5}$$

Here, σ_p and μ_p respectively are the pixel standard deviation and pixel mean throughout the realizations, averaged over all pixels in a background region of interest.
For every iteration of the RS reconstruction and for every iteration of the PH deconvolution, the CRC was calculated for all lesion sizes. Next, this CRC was plotted in function of the NC, which increases with every iteration. On this contrast-to-noise plot, the optimal Contrast-to-Noise Ratio (CNR_o) was defined as:

$$CNR_o = \frac{CRC_o}{NC_o}. \tag{5.6}$$

Here, CRC_o and NC_o are respectively the contrast recovery and noise level at the iteration where the first derivative of the contrast-to-noise curve reaches a value of 0.5. This figure of merit provides an optimal trade-off between the contrast and the noise. The ratio of $\mathrm{CNR}_{o,RS}$ to $\mathrm{CNR}_{o,PH}$:

$$RCNR = \frac{CNR_{o,RS}}{CNR_{o,PH}}, \tag{5.7}$$

was plotted as a function of lesion size as a measure of image quality improvement of the RS collimator to the PH collimator.
To see the influence of imaging time on the RCNR, the PH simulations were extended to more detections and the RCNR was plotted in function of the relative imaging time (RIT):

$$RIT = \frac{\text{imaging time}_{PH}}{\text{imaging time}_{RS}}. \tag{5.8}$$

5.4.1.2 Object size and contrast dependency

For image reconstruction and restoration, convergence will strongly depend on the shape of the PSF. Due to the large PSF of the RS system in the y-direction, also the surrounding activity has an impact on the convergence speed. To quantify this dependency, the influence of the object size on the PRF, obtained according to Wilson [194], was investigated. The PRF at position r is defined to be:

$$PRF_r = S(f + \delta_r) - S(f). \tag{5.9}$$

Here, f represents the activity distribution and S represent the imaging system, being the combination of the scanning process and the reconstruction or image post-processing. We chose δ to be 100% of the background activity and r in the center of the phantom. The Full Width at

Half Maximum (FWHM) and Full Width at Tenth Maximum (FWTM) of the PRFs, obtained for the RS and the PH collimator was plotted as a function of the iteration number for different phantom background diameters (15 cm, 20 cm, 25 cm, 30 cm and 35 cm).
For a rotating slat collimator, the noise in the images is not only dependent on the speed of convergence but is also propagated due to the large spatial support of the PSF in y-direction. During a measurement, due to the wide PSF, counts (and noise on these counts) are collected from a larger number of points in image space into one detector bin. During reconstruction, the total number of collected counts in that bin will be divided over a number of points in image space. However, the noise will not be divided and every point involved in the backprojection will get the total amount of noise in the projection bin which equals the sum of the individual noise levels in each previously collected point. This results in a noise level which is depending strongly on surrounding activity. This noise accumulation, arising from pixel crosstalk in the RS reconstruction process will increase as the size of the object under investigation increases and as the relative amount of activity increases in the vicinity of the area of interest (e.g. neighboring organs with high uptake). In particular, when a hot spot in a warm background is reconstructed, the convergence of this hot spot will strongly depend on the size of the surrounding warm region and on the lesion-to-background contrast. To investigate this dependency, a hot spot phantom was simulated with 10 mm diameter hot spots in a warm region (figure 5.4 (b)). To see the influence of the object size and contrast, the background diameter was set to 15 cm, 20 cm, 25 cm, 30 cm and 35 cm and 8 different contrast values were assigned to the hot spots (ranging from 2:1 to 16:1). This resulted in 40 simulation setups. 10 realizations of each setup were simulated on both the RS and the PH system and respectively reconstructed and deconvolved. Next, contrast-to-noise plots were generated for each of the 80 sets of images (40 for RS and 40 for PH). From these plots, the CRC_o was calculated and RCNR was plotted as a function of background diameter and contrast.

5.4.2 Results

5.4.2.1 Contrast-to-noise analysis

For all lesions of the phantom of figure 5.4 (a) the contrast-to-noise plots are shown in figure 5.5 and figure 5.6. Figure 5.5 (a) and (b) show the

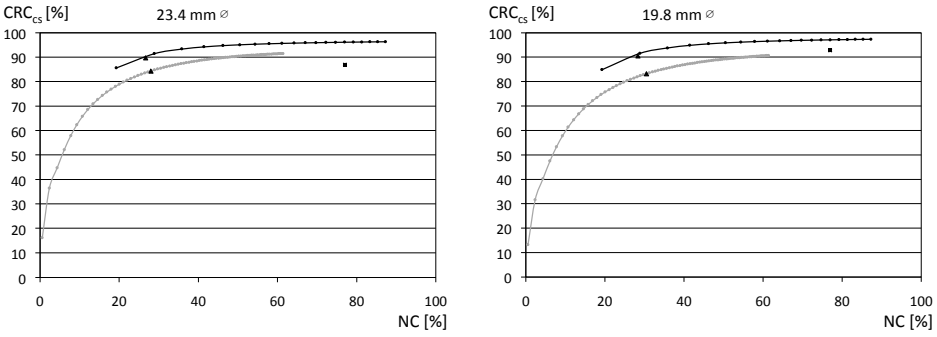

(a) (b)

Figure 5.5: Contrast-to-noise plots for (a) the 23.4 mm and (b) the 19.8 mm cold spot. Results are shown for the RS reconstructions (——), parallel hole collimator deconvolution images (▬▬) and for the original parallel hole collimated projection (■). The point of 50% slope is also shown for each plot (▲)

results for the two cold lesions while figure 5.6 shows the results for the hot spots, starting with the largest one. For comparison, also the (non-deconvolved) original PH projection images were evaluated and are represented as a black square in the plots from figure 5.5 and figure 5.6. It is clear from these plots that cold spot contrast recovery is worse for the RS collimator and the difference is becoming larger as the cold lesion becomes smaller. With the RS collimator, an increased contrast recovery can however be obtained for the hot spots and due to faster convergence, this improvement is larger as the hot lesions become larger. For all the plots, the point of 50% slope was derived. In this point, CNR_o was calculated. In figure 5.7 (a), RCNR is plotted as a function of RIT. From this plot we can derive that we have to measure 3 times longer with the PH collimated system to obtain equal CNR for the smallest hot spot. For the 9 mm hot spot, this would be 6 times longer. For the 12,6 mm or larger lesions, RIT becomes larger than 10. In figure 5.7 (b), RCNR is plotted as a function of lesion diameter for equal imaging time ($RIT = 1$). This ratio equals 0.89 and 0.85 for the 23.4 mm and the 19.8 mm cold spot respectively. For the hot spots, the ratios are 2.88, 2.48, 2.01 and 1.48 for the 16.2 mm, the 12.6 mm , the 9 mm and the 5.4 mm lesion respectively.

In figure 5.8, both a reconstructed RS image and a deconvolved PH image are shown for a NC equal to 20%. It can be seen that the RS image reaches a higher contrast (seen as lower background activity) for

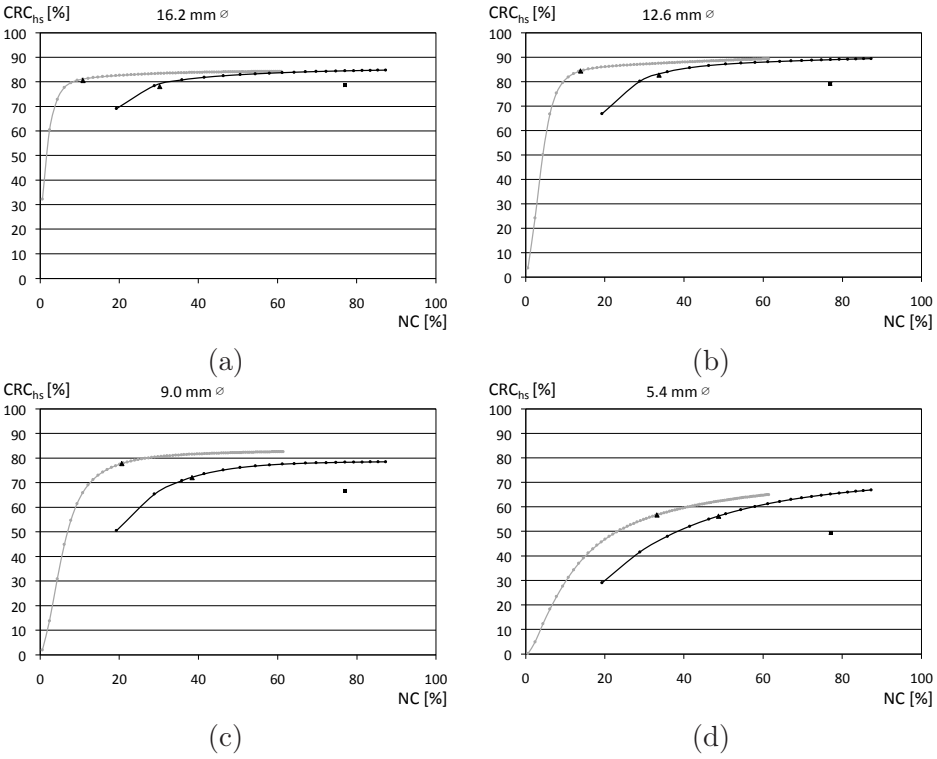

Figure 5.6: Contrast-to-noise plots for (a) the 16.2 mm, (b) the 12.6 mm, (c) the 9 mm and (d) the 5.4 mm hot spot. Results are shown for the RS reconstructions (—), parallel hole collimator deconvolution images (—) and for the original parallel hole collimated projection (■). The point of 50% slope is also shown for each plot (▲)

the hotspots. As the contrast-to-noise plots indicated, the cold spots are more clear in the PH image. For comparison, also the original PH projection is shown with 77% of noise. Here, the excessive noise is deteriorating the image quality. This indicates that, to make a fair comparison with RS images reconstructed with MC-MLEM, the Richardson-Lucy deconvolution is mandatory.

5.4.2.2 Influence of object size and lesion contrast

Figure 5.9 (a) shows the PRF for the RS collimator after 400 iterations and for the PH collimator after 40 iterations, both for the 35 cm background. Figures 5.9 (b) and (c) show the variation of the FWHM and

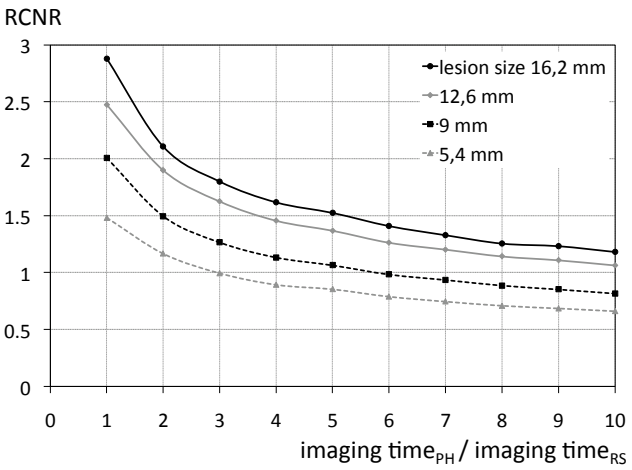

(a)

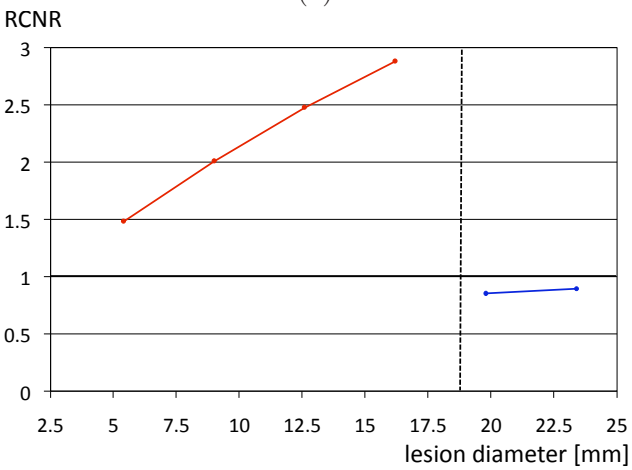

(b)

Figure 5.7: (a) The image quality improvement of the RS system over the PH system expressed as RCNR as a function of the relative imaging time RIT for the four hot spots. (b) RCNR as a function of lesion diameter for equal imaging time (RIT=1).Left are the results for the 4 hot lesions while on the right the results for the two cold lesions are shown.

FWTM respectively for the RS and the PH collimator. In the case of the PRF, which is derived from a very small low contrast ($\delta = 100\%$) lesion (to preserve linearity of the MLEM response), it can be seen that the PH system has a better resolution at the respective points of convergence (figure 5.9 (a)). The situation is however different when con-

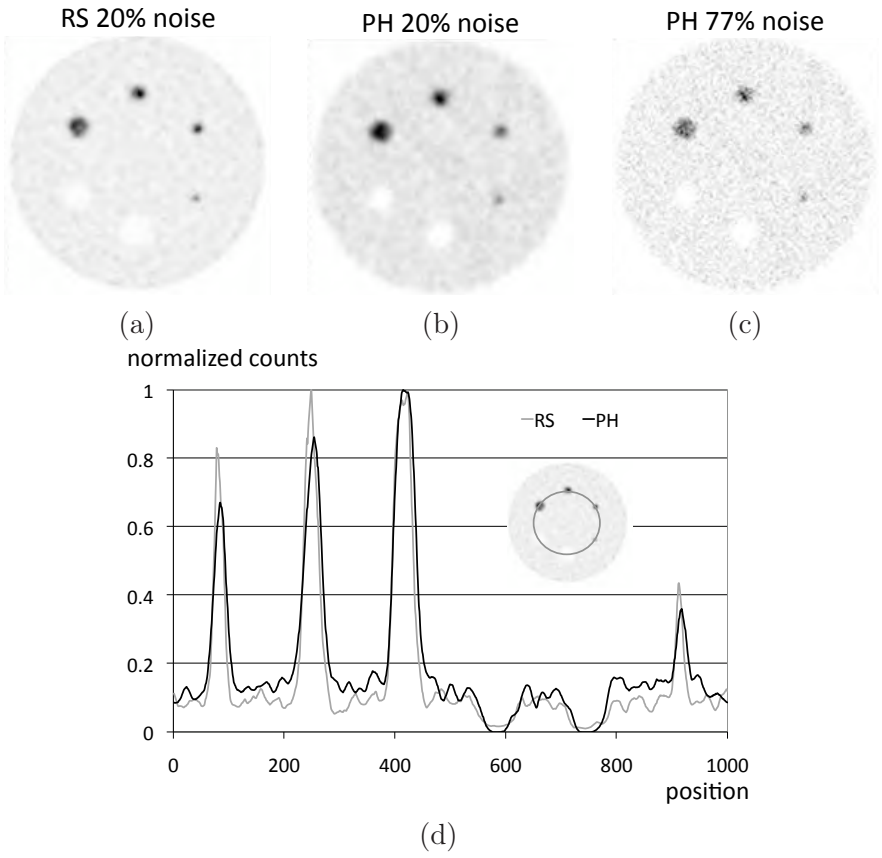

Figure 5.8: (a) RS reconstruction and (b) PH deconvolution images of the image quality phantom for a NC of 20%. (c) The original PH projection image with an NC of 77%. In (d), circular profiles through the lesions of (a) and (b) are plotted in gray and black respectively.

sidering more realistic phantoms with larger lesions and higher contrast. We see no influence of the phantom size for the PH collimator (figure 5.9 (c)). This is because the small PSF makes the convergence independent on the surrounding activity. In figure 5.9 (b) however, we see that the FWHM and FWTM tend to become larger with larger phantom diameter. This can be explained by the slower convergence of the point in a large background. Figure 5.10 (a) and (b) show the variation of respectively $\mathrm{CNR}_{o,PH}$ and $\mathrm{CNR}_{o,RS}$ as a function of contrast for different background dimensions. It can be seen that the influence of background dimensions and lesion contrast is negligible for the PH collimator while

there is a large influence for the RS collimator. The $\mathrm{CNR}_{o,RS}$ is increasing with increasing contrast and is decreasing with increasing background diameter (figure 5.10)(b). From this plot it can be seen that the decrease in image quality as a function of phantom diameter is less pronounced when the diameter becomes larger. This is due to the finite support of the rotating slat PSF in the direction of the slats. As the distance from one point to another becomes larger, the noise crosstalk will decrease, resulting in less influence on image quality for further increasing object size. The RCNR is plotted in figure 5.10 as a function of contrast for varying background dimensions. From this plot, it can be read that only for C=2 and diameters larger than 250 mm, the PH collimator scores better. For C=2 and background diameter equal to 200 mm the image quality defined by the CNR_o is equal for both systems. For the other 37 configurations, the RS collimator performs better with increasing performance for smaller background and higher contrast.
In the next paragraph we propose a clinical setting where image quality is be enhanced by the use of RS collimation.

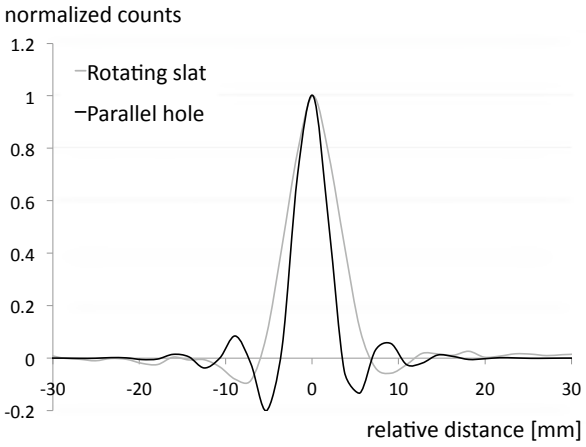

(a)

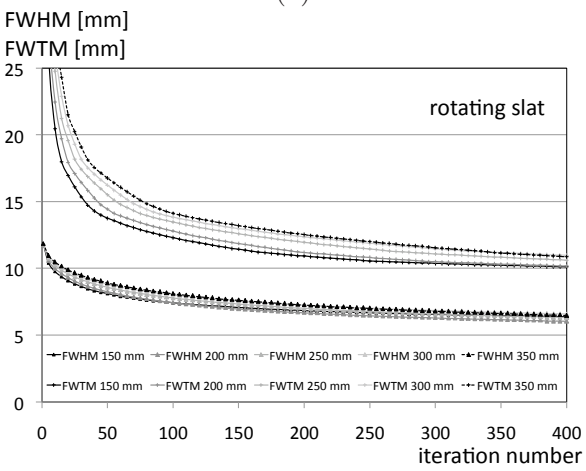

(b))

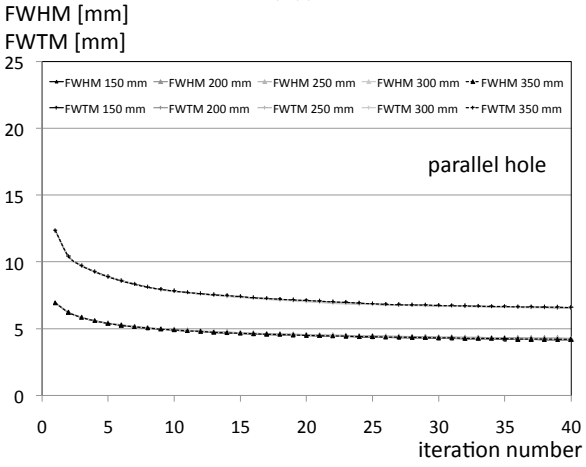

(c)

Figure 5.9: (a) Profiles through the RS and the PH PRF, normalized to the maximum. The FWHM and FWTM as a function of iteration number for (b) the RS collimator and the (c) PH collimator.

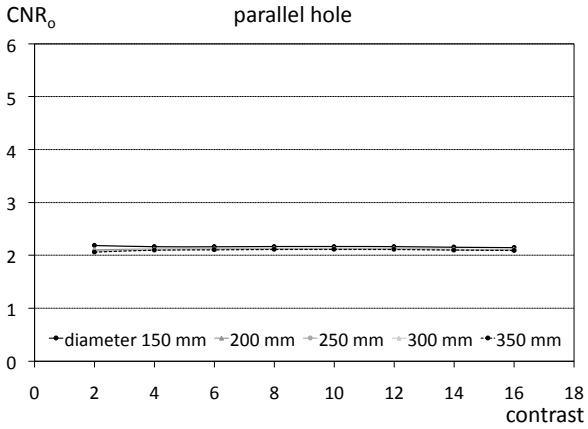

(a)

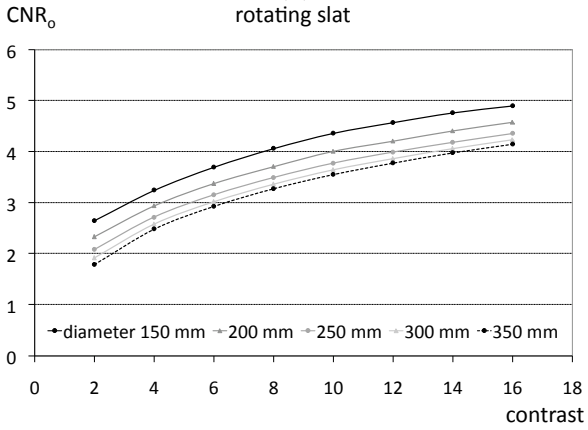

(b)

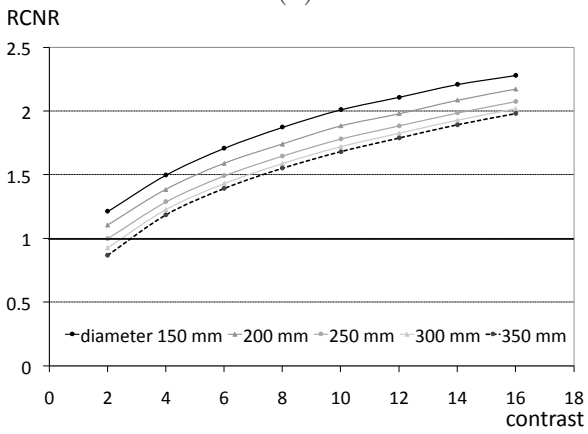

(c)

Figure 5.10: (a) $\mathrm{CNR}_{o,PH}$ and (b) $\mathrm{CNR}_{o,RS}$ as a function of contrast for different background diameters. (c) RCNR as a function of contrast for different background dimensions.

5.5 Case study: planar bone scintigraphy

Bone scintigraphy for studying bone metastases is one of the most common procedures performed in nuclear medicine. Usually, the patient is scanned 2-6 hours after being injected a bolus of 740-925 MBq of technetium-99m-labeled diphosphonates. Most of the diphosphonates will accumulate in the bone (about 30-50%), especially in regions of high osteoblastic activity [104]. Most bone metastases, originating from primary soft tissue tumors (most frequently being tumors from the prostate, lung, breast or kidney), cause osteolysis. The bone will respond to this by reparative activity, involving high osteoblastic activity. In the image, metastases will thus show up as foci of high activity in the skeletal system [65]. A routine clinical study where patients are injected with 740 MBq of Tc^{99m}-MDP for bone scintigraphy was simulated with GATE using the MCAT phantom [157]. Based on literature values of tissue tracer uptake, the activity concentration in the bone was simulated to be 27.14 Bq/mm^3 while the soft tissue had an activity concentration of 1.37 Bq/mm^3 [23]. Three spherical hot lesions with an activity concentration of 271.4 Bq/mm^3, each representing a bone metastasis, were simulated as spheres with a tumor to background ratio of 10:1. The location of the lesions is indicated in figure 5.11. Lesion 1 and 2 lie in the

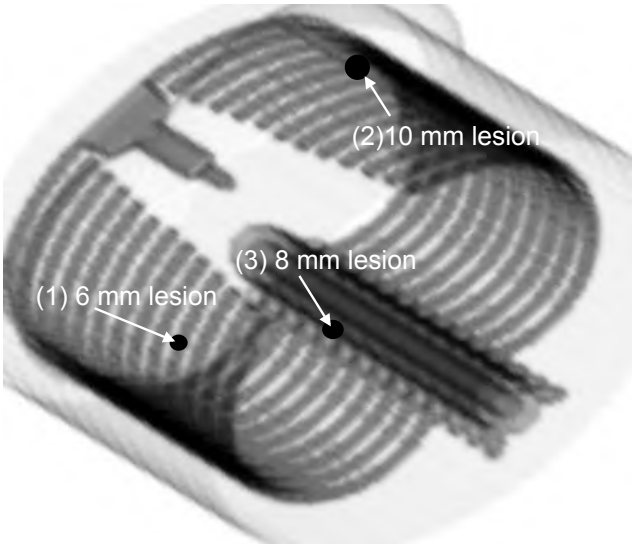

Figure 5.11: The MCAT phantom with indication of the lesion locations.

anterior part of the body and have diameters of 6 mm and 10 mm respectively. Lesion number 3 is a lesion in the spine and has a diameter of 8 mm. The simulation time was set to 800 s to have in ∼1 million counts in both the anterior and posterior view, which is in accordance with the recommendations of the Society of Nuclear Medicine. In the simulation, we included a realistic phantom to simulate the influence of attenuation and scatter. The geometric system response was modeled in the reconstruction and deconvolution by making the assumption that all activity was concentrated in one plane at an average distance of 20 cm from the collimator. No attenuation or scatter correction were performed during reconstruction. As a quantitative measure, the metastasis-to-background ratio (MBR) was calculated. This MBR is calculated as the ratio of the activity in a ROI delineating the metastasis to the activity in the same ROI drawn at the contralateral side in the image. The relative improvement of one collimator to the other is calculated. Figure 5.12 shows the images obtained from the simulation of the Tc^{99m}-MDP scan. All images are displayed with equal background intensity. The PH images were recovered with 4 iterations of the Richardson-Lucy algorithm and the RS images were reconstructed with 220 MLEM iterations. The metastases on the ribs (lesion 1 and 2) are more clear on the anterior views while the spine lesion is better visible on the posterior views. In table 5.1 the MBR can be read for the different collimators and the different metastases. A contrast improvement of 11%, 35% and 8% is obtained with the slat collimator for lesion 1, 2 and 3 respectively. The improvement depends on the size and the location of the metastasis. From the analysis in section 5.4.2.1, one would expect better contrast for a larger lesion. This is reflected in this study if we compare lesion 2 to lesion 1: lesion 2, with larger diameter has a larger contrast improvement. This result would indeed be expected from the study of the CNR_o as a function of lesion size (section 5.4.2.1), but is in fact a combination of both bigger lesion size and a higher contrast. In a projection image, the activity is superimposed with all the activity above and below, resulting in higher contrast when imaging a larger sphere. On the contrary, lesion 3 does not show larger improvement compared to lesion 1. This can be explained by the lower contrast with respect to the spine, where the lesion is located. According to the study of the influence of lesion contrast (section 5.4.2.2), a smaller improvement is expected for lower contrast lesions.

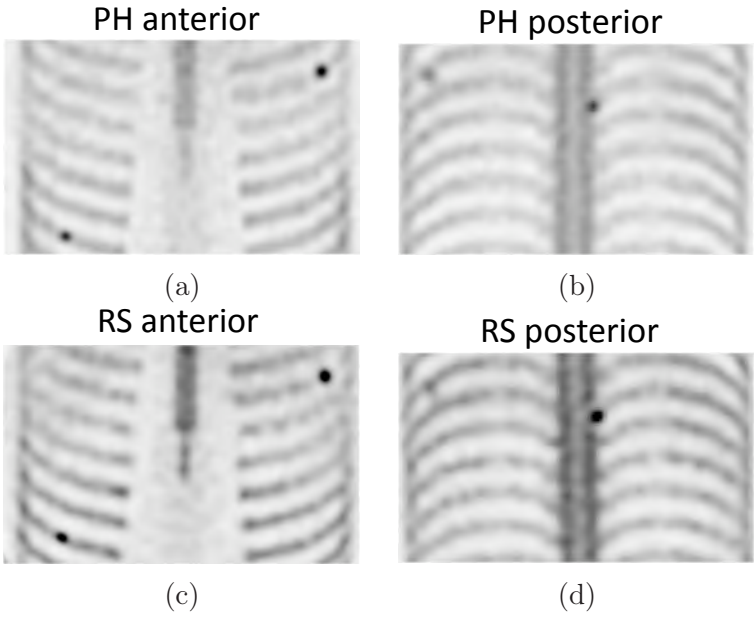

Figure 5.12: (a) and (b) respectively show PH collimated anterior and posterior views. (c) and (d) show the anterior and posterior RS collimated images. Images are displayed at equal background intensity.

5.6 Discussion

In this chapter, the imaging performance of a RS collimator was investigated by comparison with a classical parallel hole collimator. A previous study [102] used Filtered Backprojection (FBP) for the RS reconstruction and compared the signal-to-noise ratio for both a RS and a PH collimator. The conclusion of their work was that comparable image quality could be obtained for both systems. In particular, small hot lesions in a small object were found to benefit from the use of a RS collimator. Our study shows that the impact of using an iterative reconstruction algorithm in combination with an accurate system model moves the trade-off for obtaining better images from small background activity to background activity as large as the FOV. Only for very low input contrast and large background diameters approaching the size of the FOV of the camera, better image quality was found for the PH collimator. Also, in contrast with previous findings, we obtain better image quality for larger lesions, while for FBP, only small lesions seemed to benefit from the use of a RS collimator.

	lesion 1 (6 mm)		lesion2 (10 mm)		lesion 3 (8 mm)	
	PH	**RS**	**PH**	**RS**	**PH**	**RS**
MBR	2.8	3.1	3.4	4.6	2.2	2.4
Improvement		+11%		+35%		+8%

Table 5.1: The MBR and relative improvement of the three metastases measured with the two different collimators.

A difference between PH and RS collimators is that the PSF of a RS system is broad in the direction of the slats, while it is small for a PH collimated system. This broad PSF will spread the noise accumulation through the image reconstruction as discussed earlier. When no modeling would be used (e.g. when using FBP), the noise would accumulate over all the points in the plane seen by a detector element. However, the noise accumulation is reduced to the points under the PSF by applying a system model.
It became clear that even for a planar bone scan, where the activity is distributed over the whole FOV of the camera, better image quality can be obtained by using a RS collimator. The improvement is however subject to the lesion location. While there was an improvement in contrast for spine lesions, the largest improvements were found for lesions located in the ribs.
The analysis of image quality is done for phantoms placed at a fixed distance from the collimator (10 cm). Since the RS system sensitivity decreases when increasing the collimator distance, the image quality of the RS will also decrease. This is especially important in tomography, where the collimator distance is usually larger than in a planar acquisition. Nevertheless, it has recently been shown by Zhou [203] that each detector distance has its own optimal collimator resolution. For instance, at a larger detector distance, a larger aperture would be advisable for the RS collimator with respect to contrast-to-noise. This is not the case for a PH collimator, where a constant aperture is advised. By choosing the optimal aperture at each distance, Zhou [203] found even a better CNR at larger distance for the RS collimator. This approach is however impractical, but one could provide one set of collimators for tomography and one set for planar imaging.
For the tomographic case, an image quality comparison will be made in chapter 7. Previously, image quality of a RS collimator has been investigated by Wang [187], where a blob based 3D RBI-EM algorithm

was used for reconstruction. This comparison however was done for a strip detector. Chapter 7 will present an objective assessment of the tomographic image quality of a rotating slat collimator with respect to a parallel hole collimator.
The figure of merit used is the optimal contrast-to-noise ratio and is based on multiple noisy realizations of the same measurement. This makes the technique practically infeasible when a large number of systems would have to be compared. Other approaches use the Cramér-Rao bound [113] or the Linearized Local Impulse Response (LLIR) for a fixed target resolution [182] have been successfully applied for the design of (multi-)pinhole SPECT systems. Given an accurate model of the imaging system, these techniques enable one to calculate the theoretical trade-off between variance and spatial resolution without the need for multiple realizations. The technique of Vunckx [182] is specific for post-smoothed MLEM images while the technique proposed in Meng [113] is more general in the sense that the trade-off is independent of the reconstruction algorithm and other data processing steps.

5.7 Summary and original contributions

The results obtained in this planar image quality comparison of a RS and a PH collimator show that cold spot imaging is still better with a classical PH collimator. For hot spot imaging, the PH collimator performs slightly better only in the few cases of very low lesion contrast in combination with large background dimensions. Thus, a RS collimator could be a valuable alternative for a PH collimator for 2D imaging, especially for hot spot imaging. This was illustrated by means of a frequently performed planar bone scintigraphy, where an improved contrast was found for all lesions.
The comparison of both collimators in the case of tomographic imaging will be investigated in chapter 7. However, we will first deal with the problem of computationally expensive reconstruction for plane integral data in the next chapter.
The work presented in this chapter resulted in one conference contribution [171] and in a peer reviewed A1 journal publication [173].

Chapter 6

Fast 3D iterative image reconstruction for SPECT with rotating slat collimators

Before investigating the tomographic image quality in chapter 7, this chapter deals with the tomographic reconstruction of 3D Radon data. Compared to normal SPECT reconstruction, iterative reconstruction of plane integral data is computationally very expensive due to the complex forward and backward projection. First, the different methods to reconstruct plane integral data are described whereafter a newly developed method, which aims at both fast computation and fast convergence without loss of image quality, is described. The newly developed method is then compared to existing methods with regard to calculation time, convergence speed and conservation of image quality.

6.1 Introduction

The collection of plane integrals of a 3D activity distribution by spinning the detector around its own axis at each regular SPECT angle can be seen as the 3D Radon transform when ignoring the effects of attenuation, depth dependent blurring and position dependent sensitivity. For image reconstruction, a 3D algorithm which inverts the plane integral

data resulting from the 3D Radon transform is mandatory. For conventional SPECT, there exist different reconstruction approaches for the inversion of 2D Radon data, like analytic reconstruction, algebraic or statistical iterative reconstruction. The same is true for 3D Radon data. A Filtered Back-Projection (FBP) implementation for 3D Radon inversion has been previously developed by Natterer [122], Lodge [103] and by Zeng [197]. An iterative approach has been proposed in the past by Wang [187]. The 3D iterative approach offers better image quality, since it models the Poisson statistics of the data while it can also incorporate the effects of depth dependent blur and position dependent sensitivity into the system matrix. A drawback of the iterative approach is that, for reconstructing an N^3 image ($N \times N \times N$ voxels) from an N^3 plane integral dataset (N bins $\times$ N spin angles $\times$ N SPECT angles), it requires N^5 operations compared to only N^4 operations for conventional SPECT. This makes this approach less attractive for use in clinical practice. Furthermore, due to the non-sparsity of the system matrix (a lot of voxels contribute to 1 projection bin), the fully 3D approach suffers from slow convergence unless a lot of subsets are used [187]. A computationally less demanding alternative (requiring $2 \times N^4$ operations) to the 3D Radon inversion is a 2-step algorithm which first reconstructs the plane integral data to conventional sinograms before reconstructing the 3D object from these sinograms using a classical SPECT reconstruction. This method can be used both for analytical reconstruction and iterative reconstruction. However, for iterative algorithms it is more convenient to just split the system matrix [197]. This approach which is computationally much more attractive however still suffers from slow convergence.

Aiming at an improved convergence rate, we propose a new technique for reconstructing plane integral data based on the integration of two Maximum Likelihood Expectation Maximization (MLEM) iterative reconstruction algorithms. The newly developed method is of the same type as the split matrix approach but differs from it in the sense that the image estimate is calculated from a sinogram estimate, obtained previously in the same iteration. With simulation studies we will compare the newly developed Integrated Split Matrix reconstruction algorithm (ISM-MLEM) to a standard Split Matrix (SM-MLEM) and to a Fully 3D algorithm (F3D-MLEM) on the basis of convergence speed, computational load and contrast-to-noise. Furthermore, since convergence can also be improved by the use of subsets, Ordered Subsets Expectation Maximization (OSEM) implementations of the above three algorithms will be compared. Because of its ability to model the imaging process

very accurately, the fully 3D method will serve as the gold standard throughout this chapter.

6.2 Methods

6.2.1 Image reconstruction

We use three different image reconstruction methods, all based on Maximum Likelihood Expectation Maximization (MLEM). These are denoted as F3D-MLEM, SM-MLEM and ISM-MLEM algorithm. In all reconstructions, 90 SPECT- and 90 spin-angles are used to reconstruct a 96 $\times$ 96 $\times$ 96 volume of 3.6 mm^3 voxels. From these three MLEM algorithms, three OSEM implementations are derived. In the F3D-OSEM and SM-OSEM, we will be able to use more subsets since the convergence is slower. The exact number of desired subsets in both SPECT and spin angles will be derived from the convergence properties of each algorithm. First we will discuss how the system matrices were generated and verify whether they are valid. Next, each of the three reconstruction algorithms will be explained in more detail.

6.2.1.1 System matrices

6.2.1.1.1 System matrices A, B and AB System matrix **A** models the step to go from sinogram to plane integral data (figure 6.1 (a)):

$$\mathbf{As} = \mathbf{g}, \tag{6.1}$$

where $\mathbf{g} = [g_1, g_2, \ldots, g_j, \ldots, g_J]^T$ represents the plane integrals and $\mathbf{s} = [s_1, s_2, \ldots, s_i, \ldots, s_I]^T$ represents the sinogram.
System matrix **B** models the step to go from image to sinogram (figure 6.1 (b)):

$$\mathbf{Bf} = \mathbf{s}, \tag{6.2}$$

where $\mathbf{f} = [f_1, f_2, \ldots, f_k, \ldots, f_K]^T$ represents the 3D source distribution.

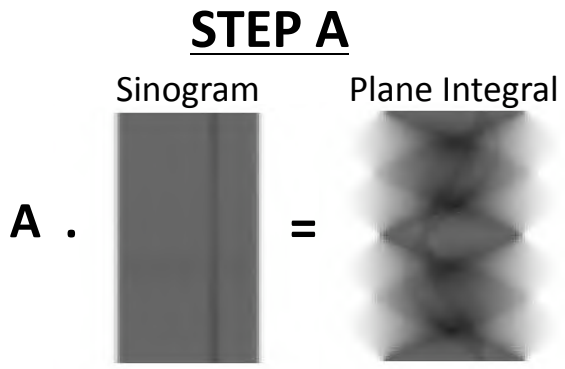

(a)

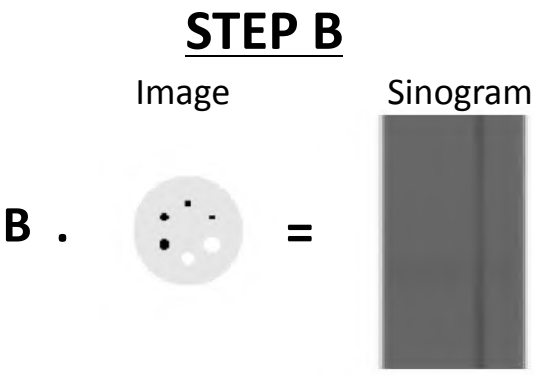

(b)

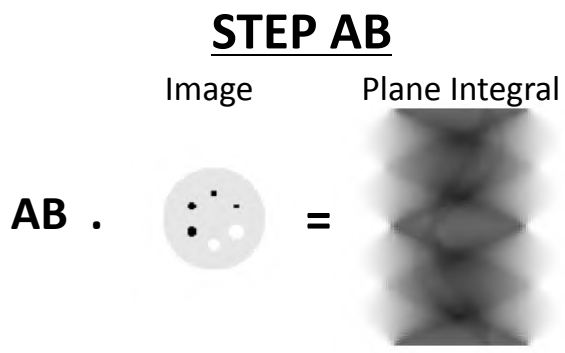

(c)

Figure 6.1: The different steps involved in the reconstruction. (a) System matrix **A** transforms sinograms to plane integrals, (b) system matrix **B** transforms images to sinograms and (c) system matrix **AB** transforms images directly into plane integrals.

Performing the second step in cascade with the first step results in system matrix **AB**. This combined system matrix transforms a 3D image into plane integral data, using a sinogram as an intermediate result (figure 6.1 (c)):

$$\mathbf{ABf} = \mathbf{g} \Longleftrightarrow \mathbf{As} = \mathbf{g}. \tag{6.3}$$

During the first step (step A), we do not have information on the depth of a given voxel in the FOV. Since both resolution and sensitivity are dependent on the depth, we do not include any model in system matrix **A** and modeling is only included in system matrix **B**.
For practical use in an iterative reconstruction, we do not store the complete system matrix **B** but we calculate the system response on-the-fly. After rotating the 3D volume according to the appropriate SPECT angle using a Gaussian rotator [184], we separately apply a model for resolution and a model for sensitivity. Resolution modeling is performed by convolving each parallel projection image of the sinogram with a 2D Gaussian kernel, modeled as a 2 times 1D convolution with the depth dependent kernels of figure 6.2 (b) with Full Width at Half Maximum (FWHM) equal to [177]:

$$FWHM = \frac{g(d+h)}{h}, \tag{6.4}$$

with g the gap between the septa, d the distance to the collimator and h the height of the collimator septa. Figure 6.2 (c) represents the sensitivity in a plane, parallel to the slats of figure 6.2 (a). To apply this sensitivity behavior in **B**, one needs to know the orientation of the slats. Unfortunately, this information is is only available in plane integral data and it is thus not possible to model the complete sensitivity behavior in **B**. The best approximation is to apply the mean sensitivity at a certain depth, which is equal to averaging the weights of figure 6.2 (c) over y. This far field approximation assumes there is no sensitivity variation in a plane parallel to the detector while in y-direction, there is a slight variation of the sensitivity ($\sim \cos^3(\arctan(\frac{y}{d}))$) as can be read from figure 6.2 (c).
The system matrices explained here are presented as a forward projection operator. By transposing them, they are also used as a backward projector in the iterative reconstructions. The system modeling in one forward/backprojector-pairs is thus equivalent.

6.2.1.1.2 System matrix C In the F3D-MLEM, system matrix **C** is used. **C** models the step to go from 3D image directly to plane integral

data and vice versa without intermediate sinograms. This results in a less sparse system matrix compared to **AB** [187]. After rotating the 3D

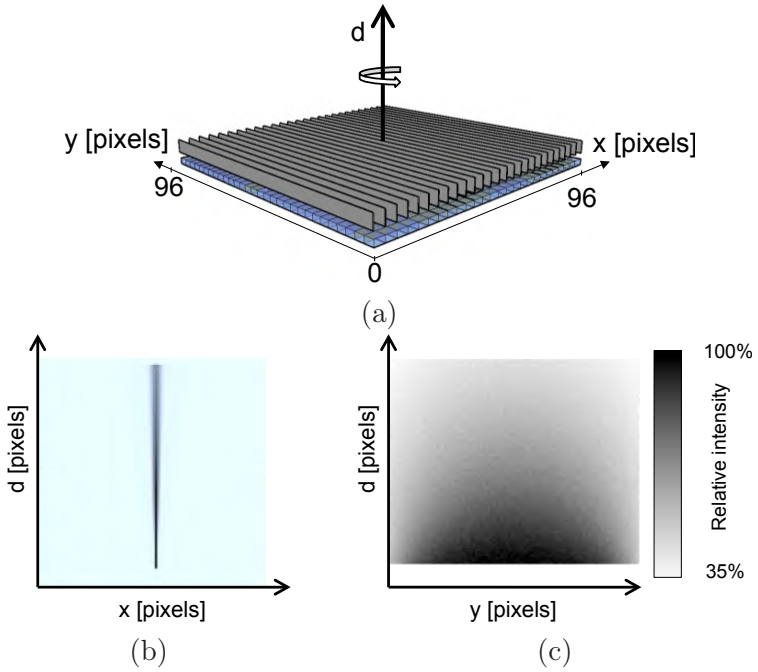

Figure 6.2: (a) The geometry of the rotating slat camera with indication of the different coordinates and the spin rotation. (b) shows the depth dependent convolution kernels which serve to model the resolution while (c) shows the sensitivity variation in a plane of integration.

volume according to the appropriate SPECT and spin angle using the Gaussian rotator, we first model the depth dependent blur by convolving the image with a normalized 1D Gaussian with depth dependent FWHM (figure 6.2 (b)). The convolution is performed in x-direction after the appropriate rotation. Next, the sensitivity is modeled by multiplication of each voxel by the appropriate sensitivity weight (figure 6.2 (c)) which is dependent on the depth and the position y along the slats.

6.2.1.1.3 Validation The accuracy of the system matrices is checked by comparing forward projections g_C and g_{AB} of 3 point sources with respectively system matrix **C** and system matrix **AB** to a high count (30 million) Monte Carlo simulation using GATE. The three point sources were 3.6 mm^3 (one voxel) large and are respectively placed at

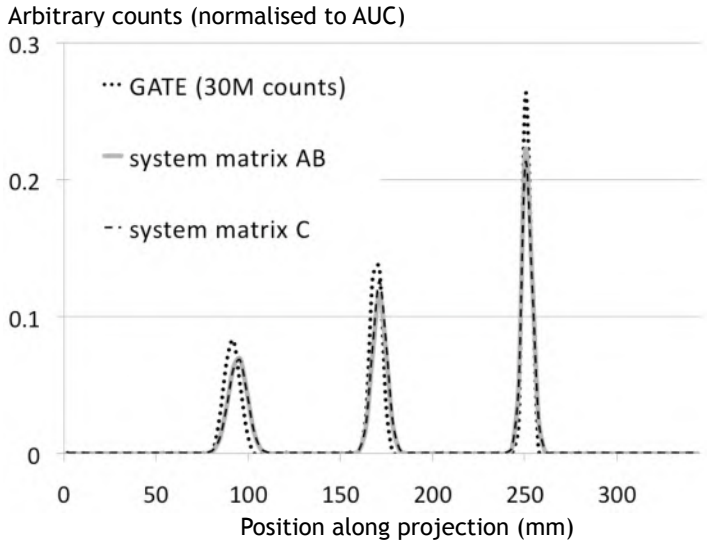

Figure 6.3: Profiles through the different plane integral datasets at SPECT angle 88° and spin angle 88°. The left peak originates from a voxel further away while the right peak originates from a point closer to the detector.

positions (-83, -83, -83), (0, 0, 0) and (83, 83, 83) in the 345.6 mm^3 FOV discretized in a 96^3 voxel grid.
Figure 6.7 (a) shows the camera modeled in GATE. The detector consists of a 192×192 solid state pixel array where each individual pixel measures 1.8 mm by 1.8 mm resulting in a 34.56 cm by 34.56 cm detector. The collimator slats are matched to the detector pixels (in one direction) and the collimator resolution is 5 mm at 10 cm distance to the collimator. The collimator/detector pair is rotated around the central axis of the camera in 90 discrete steps of 4°. At each of these SPECT-angles (figure 6.7 (a)), we rotate the collimator/detector pair around its own axis, again in steps of 4°. This results in 90 discrete spin angles.
The Root Mean Square Error (RMSE) was calculated on the non zero elements of forward projections g_C and g_{AB} as:

$$RMSE = \frac{\sqrt{\frac{\sum_j (g_j - g_{GATE,j})^2}{J}}}{max(g_{GATE})} \times 100\%, \tag{6.5}$$

where g_j represents either g_C or g_{AB}, j represents the non zero projection element, J the total number of non zero elements and g_{GATE} the simulated plane integral dataset. For visual interpretation, line profiles

are plotted through the three different datasets at SPECT angle 88° and spin angle 88°. System matrix **C** shows a better agreement with GATE with a RMSE of 7.0% compared to a RMSE of 17.7% for system matrix **AB**.
The plot of figure 6.3 shows a good agreement of both system matrix projections and the high count GATE simulation. The variation in intensity of the different point projections arises from the 1/r sensitivity behavior of the RS collimator in combination with the depth dependent resolution which blurs more at larger depth.

6.2.1.2 Reconstruction algorithms

6.2.1.2.1 Fully 3D MLEM and OSEM The direct or fully 3D reconstruction uses a system matrix **C** to go immediately from image space to plane integral space and vice versa:

$$\hat{f_k}^{t+1} = \frac{\hat{f_k}^t}{\sum_j C_{kj}} \sum_j C_{kj} \frac{g_j}{\sum_k C_{kj} \hat{f_k}^t}, \tag{6.6}$$

where $\hat{f}_k^t$ is the estimate at iteration t of the image at voxel k. g_j are the observed plane integral data at bin j and C_{jk} is the system matrix element that expresses the probability of having a detection in plane integral projection element j emerging from activity in voxel k. As explained in section 6.2.1.1, apart from the distance dependent resolution degradation, also the position dependent sensitivity [177] was completely modeled in system matrix **C**. The OSEM variant of this algorithm is:

$$\hat{f_k}^{u+1} = \frac{\hat{f_k}^u}{\sum_{j \in S_u} C_{kj}} \sum_{j \in S_u} C_{kj} \frac{g_j}{\sum_k C_{kj} \hat{f_k}^u}, \tag{6.7}$$

with t the sub-iteration number and S_u the u-th subset of the data. One full iteration t is performed after U number of sub-iterations , with U the total number of subsets.

6.2.1.2.2 SM-MLEM and SM-OSEM In the SM-MLEM algorithm, matrix **C** is replaced by system matrix **AB**, leading to:

$$\hat{f_k}^{t+1} = \frac{\hat{f_k}^t}{\sum_i B_{ki} \sum_j A_{ij}} \sum_i B_{ki} \sum_j A_{ij} \frac{g_j}{\sum_i A_{ij} \sum_k B_{ki} \hat{f_k}^t}. \tag{6.8}$$

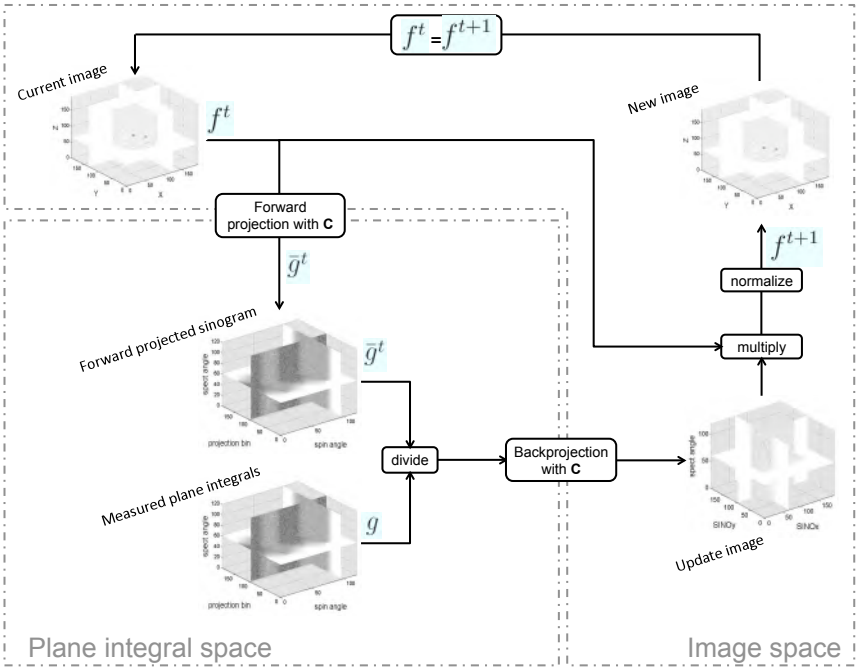

Figure 6.4: Schematic overview of the fully 3D MLEM algorithm to reconstruct tomographic images immediately from plane integrals.

This iterative process is performed by the algorithm: in a first step, an initial image estimate is forward projected with system matrix **B** to a sinogram estimate. Consequently, this sinogram estimate is forward projected using **A** and compared with the measured plane integral data. The resulting plane integral update is projected backward using **A** and immediately projected backward with **B** to image space where it serves as an update image. After updating and normalizing the original image estimate, the next iteration can start (figure 6.5).
In the first part of the system matrix (**B**), which transforms image space to sinogram space, we model the depth dependent sensitivity as the mean sensitivity in a plane parallel to the detector. Furthermore, depth dependent resolution is also modeled in **B**. System matrix **A** involves a mapping from sinogram to plane integral space. At this point, we do not include any sensitivity or resolution modeling.
In the SM-OSEM algorithm every next sub-iteration is calculated as:

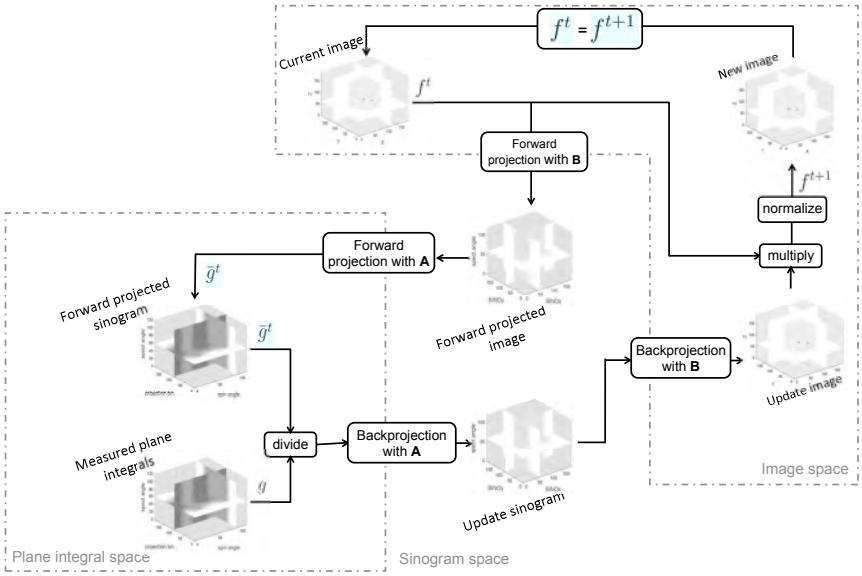

Figure 6.5: Schematic overview of the SM-MLEM algorithm to reconstruct tomographic images from plane integrals by passing through sinogram space.

$$\hat{f}_k^{\,u+1} = \frac{\hat{f}_k^{\,u}}{\sum_{i\in R_u} B_{ki} \sum_{j\in S_u} A_{ij}} \sum_{i\in R_u} B_{ki} \sum_{j\in S_u} A_{ij} \frac{g_j}{\sum_i A_{ij} \sum_k B_{ki} \hat{f}_k^{\,u}} \tag{6.9}$$

with u the sub-iteration number and S_u the u-th subset of the measured data and R_u is the u-th subset of the sinogram data.

6.2.1.2.3 ISM-MLEM Assume an iterative MLEM reconstruction that reconstructs a sinogram given plane integral data $\mathbf{g}$ and a previous sinogram estimate $\hat{\mathbf{s}}^t$:

$$\hat{s_i}^{t+1} = \frac{\hat{s_i}^{\,t}}{\sum_j A_{ij}} \sum_j A_{ij} \frac{g_j}{\bar{g}_j^t}, \tag{6.10}$$

with

$$\bar{g}_j^t = \sum_n A_{nj} \hat{s_n}^{\,t}, \tag{6.11}$$

and where $\hat{s_i}^{\,t}$ is the estimate at iteration t of the sinogram data at bin i, g_j are the observed plane integral data at projection bin j and A_{ij} is the

system matrix that models the step to go from sinogram data to plane integral data. Next, assume a regular SPECT MLEM reconstruction that reconstructs an image given a sinogram $\mathbf{s}$ and a previous image estimate $\hat{\mathbf{f}}^t$:

$$\hat{f_k}^{t+1} = \frac{\hat{f_k}^t}{\sum_i B_{ki}} \sum_i B_{ki} \frac{s_i}{\bar{s}_i^t}, \tag{6.12}$$

with

$$\bar{s}_i^t = \sum_n B_{ni} \hat{f_n}^t, \tag{6.13}$$

where $\hat{f_k}^t$ is the object estimate at iteration t of voxel k and s_i would be the measured sinogram data at bin i.
For integration of both algorithms we make two changes in the above equations, one in equation 6.10 and one in equation 6.12.
In equation 6.10, we replace $\bar{g}_j^t$ by:

$$\bar{g}_j^t = \sum_i A_{ij} \sum_k B_{ki} \hat{f_k}^t, \tag{6.14}$$

according to the denominator in equation 6.8. In equation 6.12 we replace s_i by the outcome of equation 6.10, namely $\hat{s_i}^{t+1}$. This then results in the integrated method which estimates the image from plane integrals $\mathbf{g}$ given a previous sinogram estimate $\hat{\mathbf{s}}^t$ and a previous image estimate $\hat{\mathbf{f}}^t$:

$$\hat{f_k}^{t+1} = \frac{\hat{f_k}^t}{\sum_i B_{ki}} \sum_i B_{ki} \frac{\frac{\hat{s}_i^t}{\sum_j A_{ij}} \sum_j A_{ij} \frac{g_j}{\hat{g}_j^t}}{\bar{s}_i^t}. \tag{6.15}$$

Both $\mathbf{A}$ and $\mathbf{B}$ are exactly the same matrices used in the previous SM-algorithm. The main difference with the previous algorithm is that we first derive an estimate of the sinogram from which we then derive the image estimate. For one iteration loop, this results in a two separate updates where system matrix $\mathbf{A}$ and $\mathbf{B}$ are completely detached. Since both the algorithms of equation 6.10 and 6.12 converge as fast as a conventional SPECT reconstruction, also our ISM method where system matrix $\mathbf{A}$ and $\mathbf{B}$ remain separated, will converge fast. On the contrary, in the SM-MLEM only one update in image space is performed and system matrix $\mathbf{A}$ and $\mathbf{B}$ are multiplied, resulting in a non-sparse system matrix and thus slow convergence [187]. For the OSEM variant of the

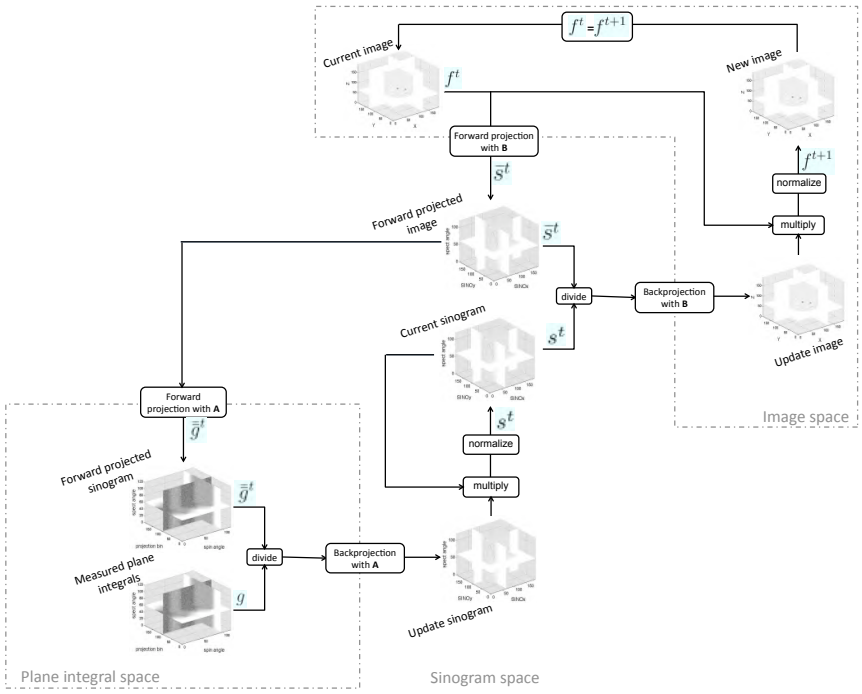

Figure 6.6: Schematic overview of the ISM-MLEM algorithm to reconstruct tomographic images from plane integrals, speeding up the convergence by making an update in sinogram space.

ISM algorithm, subsets can be selected from the sinogram as well as from the plane integrals:

$$\hat{f}_k^{\,u+1} = \frac{\hat{f}_k^{\,u}}{\sum_{i\in R_u} B_{ki}} \sum_{i\in R_u} B_{ki} \frac{\frac{\hat{s}_i^u}{\sum_{j\in S_u} A_{ij}} \sum_{j\in S_u} A_{ij} \frac{g_j}{\bar{g}_j^u}}{\bar{s}_i^u}, \qquad (6.16)$$

with u the sub-iteration number and S_u the u-th subset of the measured plane integral data and R_u is the u-th subset of the sinogram data.

6.2.2 Comparison

The comparison of the three described reconstruction methods is based on convergence speed, computational load and contrast-to-noise. To study the time gain and to prove that the method is converging to a correct reconstruction, we first study convergence of noiseless data.

6.2.2.1 Convergence

Noiseless data are generated with system matrix **C** since it models the acquisition process very accurately. A voxelized (3.6 mm^3 voxels) version of an image quality phantom (Standard Jaszczak Phantom^{TM}), shown in figure 6.7 is used for the forward projection and consists of a warm cylinder (diameter: 186 mm, height 216 mm), containing 4 hot spheres (diameters: 9.9 mm, 12.4 mm, 15.4 mm, 19.8 mm) and two cold spheres (diameters: 24.8 mm and 31.3 mm). The activity concentration ratio in the hot spheres is 8:1. The cold spot activity is zero.
The noiseless data are reconstructed using 3000 iterations for the F3D-MLEM and the SM-MLEM and 1000 iterations for the ISM-MLEM. Plots of contrast recovery versus iteration number are drawn for the largest cold and largest hot lesion to show the convergence of the three reconstruction algorithms. The Contrast Recovery Coefficient (CRC) was defined by equation 5.4.
The CRC, averaged over all 6 lesions, is calculated at 3000 iterations for the F3D-MLEM. This CRC value is then used to find the corresponding number of iterations for both the SM-MLEM and ISM-MLEM reconstructed images. This results in the Iteration number for Equal Contrast (IEC).
The number of subsets used for OSEM is calculated from the number of sub-Iterations for Equal Contrast (sIEC), which is equal to IEC for the respective MLEM reconstructions. Since the number iterations T through all the data is usually 10 to 15 for an OSEM SPECT reconstruction, the number of subsets can be derived by taking the ratio of sIEC and T. We thus pre-impose equal contrast at an equal number of full iterations through the data.
The gain in number of iterations for equal convergence or convergence speedup, referred to as iteration gain (IGain), is calculated with respect to the F3D which is the slowest converging due to the non-sparsity of system matrix **C**:

$$IGain = \frac{\text{(s)IEC for F3D-EM}}{\text{(s)IEC for (I)SM-EM}}, \tag{6.17}$$

6.2.2.2 Computational load

Computational load is expressed in terms of reconstruction Time Per Iteration (TPI) for MLEM and Time Per sub-Iteration (TPsI) for OSEM and in terms of Memory Usage (MU). TPI and TPsI are measured on a

3.0GHz CPU, averaged over 100 iterations or sub-iterations.
For the F3D-MLEM, a higher degree of optimization was implemented by grouping all SPECT-rotated images together before rotating along the spin angle. This reduces the computational load because the interpolation coefficients used for spin rotation only have to be calculated once for all 90 SPECT-rotated images instead of 90 times for the SM-MLEM and ISM-MLEM. However, this comes at the cost of increased memory usage since we have to keep 90 3D images in memory.
The time gain per iteration is calculated as:

$$\text{TGain} = \frac{\text{TP(s)I for F3D-EM}}{\text{TPI for (I)SM-EM}}. \tag{6.18}$$

For speed measurements of the reconstruction algorithms used in this study, we calculated the Total reconstruction Time (TT) as:

$$TT = TPI \times IEC. \tag{6.19}$$

From IGain and TGain we calculate the Total Time Gain (TTG) relative to the F3D reconstruction:

$$TTG = IGain \times TGain. \tag{6.20}$$

6.2.2.3 Contrast-to-noise

The noisy data are generated using GATE Monte Carlo simulations. Figure 6.7 shows the three headed SPECT system that was modeled in GATE and consists of three cameras of figure 6.2 (a). In figure 6.7 (a) the SPECT rotation is illustrated while figure 6.7 (b) shows the additional spin rotation. The image quality phantom (Standard Jaszczak Phantom^{TM}) is simulated with background activity concentration of 0.55 Bq/mm^3, hot sphere activity concentration of 4.4 Bq/mm^3 and cold spot activity of zero. No scatter or attenuation are modeled. The total activity in the phantom was 37.6 MBq and acquisition time is set to 8 minutes. Contrast recovery is defined as in section 6.2.2.1. The noise is calculated according to equation 5.5.

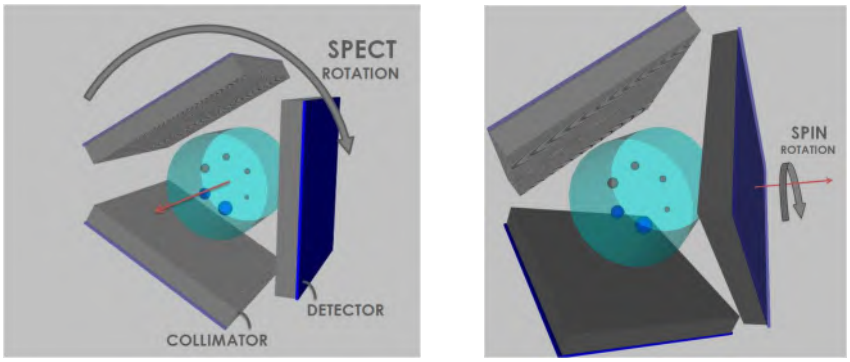

(a) (b)

Figure 6.7: The geometry of the camera and the image quality phantom modeled in GATE. (a) illustrates the SPECT rotation while in (b) the spin rotation is shown.

6.3 Results

6.3.1 Convergence

6.3.1.1 MLEM

The CRC versus iteration number is plotted for the largest cold lesion and the largest hot lesion in figure 6.8 (a) and (b). From these plots, it can be read that the F3D-MLEM and the SM-MLEM converge approximately at the same rate while the ISM-MLEM converges much faster. The CRC at 3000 iterations of the F3D-MLEM, averaged over all lesions, was 71% while the IEC for SM-MLEM and for ISM-MLEM are 2750 and 67 respectively. The ISM-MLEM thus converges 44.8 times faster compared to the F3D-MLEM while SM-MLEM converges only 1.1 times faster. These results indicate that the extra update in sinogram space for ISM-MLEM aids fast convergence. Table 6.1 summarizes these results.

6.3.1.2 OSEM

To obtain the number of subsets, we will pre-impose a fixed number of full iterations T through all the data. When also the number of sub-iterations is fixed, the number of subsets can be calculated as the ratio of the number of sub-iterations and the number of complete iterations T. The choice of number of sub-iterations is based on the IEC for the

MLEM. Since OSEM converges in an equal number of sub-iterations as MLEM does for the number of iterations, sIEC will be equal to IEC for each reconstruction technique. This is true if we at least allow a finite number of full iterations T before convergence is reached. Typically, for parallel hole SPECT, one uses 10 to 15 full OSEM iterations. Here, we arbitrarily fix the total number of iterations T for which convergence has to be reached to 12. From this, the number of subsets for F3D-OSEM is $\frac{3000}{T} = 250$. Rounding this to 270, we use 18 subsets in the SPECT angles and 15 subsets in the spin angles. Analogously, we find 15 subsets in the SPECT angles and 15 subsets in the spin angles for SM-OSEM and 6 subsets for ISM-OSEM, which we will take in the SPECT angles.

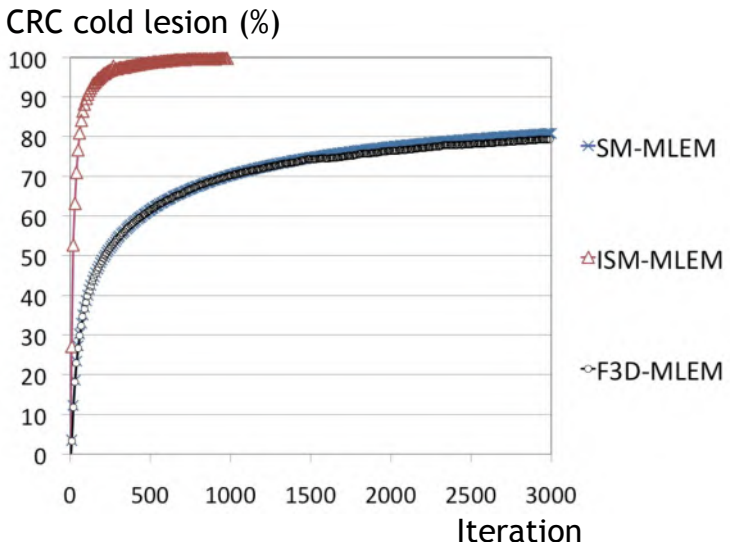

(a)

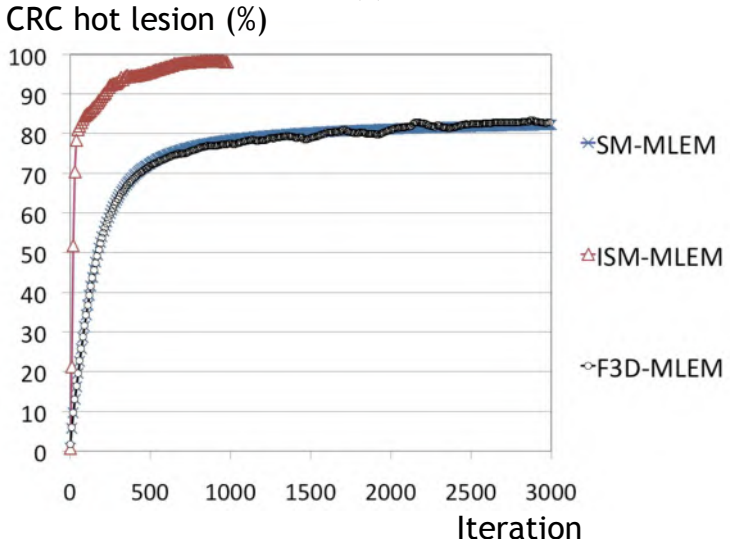

(b)

Figure 6.8: Contrast versus iteration number for (a) the largest cold sphere and (b) the largest hot sphere.

Because we derive sIEC for OSEM from the respective MLEM IEC values, the OSEM variants have similar convergence properties with respect to the number of sub-iterations. In table 6.1 however, small differences between IEC and sIEC can be seen due to the rounding of the number of subsets to a whole number divisor of the number of spin- and SPECT-angles.
In figure 6.9, noiseless image sections of the three reconstruction methods are shown at 3000 iterations for the F3D-MLEM, at 2750 for the SM-MLEM and at 67 iterations for the ISM-MLEM. From these images and from the profiles drawn in figure 6.9 (d), equal convergence can be seen. The CRC, averaged over all 6 lesions in the image is 71% for all images.

	MLEM			OSEM		
	F3D	SM	ISM	F3D	SM	ISM
(s)IEC	3000	2750	67	3240	2700	72
IGain	1	1.1	44.8	1	1.2	45.0

Table 6.1: The number of (sub-)iterations for equal contrast ((s)IEC) and the time gain due to faster convergence rate (IGain) for the three MLEM and three OSEM reconstruction algorithms.

6.3.2 Computational load

The computation time required for one iteration is 849 s, 84 s and 89 s for respectively the F3D-MLEM, SM-MLEM and ISM-MLEM (Table 6.2). This means that by using a split matrix approach, the gain in computation time is about a factor of 10. The overhead of the extra update step in the ISM-MLEM is only 6%. A decrease in memory usage for the split matrix approach of about 21 is found. This is because the F3D-MLEM is highly optimized for computational load. The memory gain factor mainly arises from the fact that before spin rotation, all SPECT angles are grouped in one large array in order to only calculate the rotation once for all SPECT angles. Since OSEM uses a lot less SPECT angles per sub-iteration, also memory consumption goes down. The optimization with respect to simultaneous spin rotation of all SPECT angles is not implemented in the SM and ISM methods since here, no significant speed gain can be obtained. This reduction in MU is therefore not seen in these algorithms.

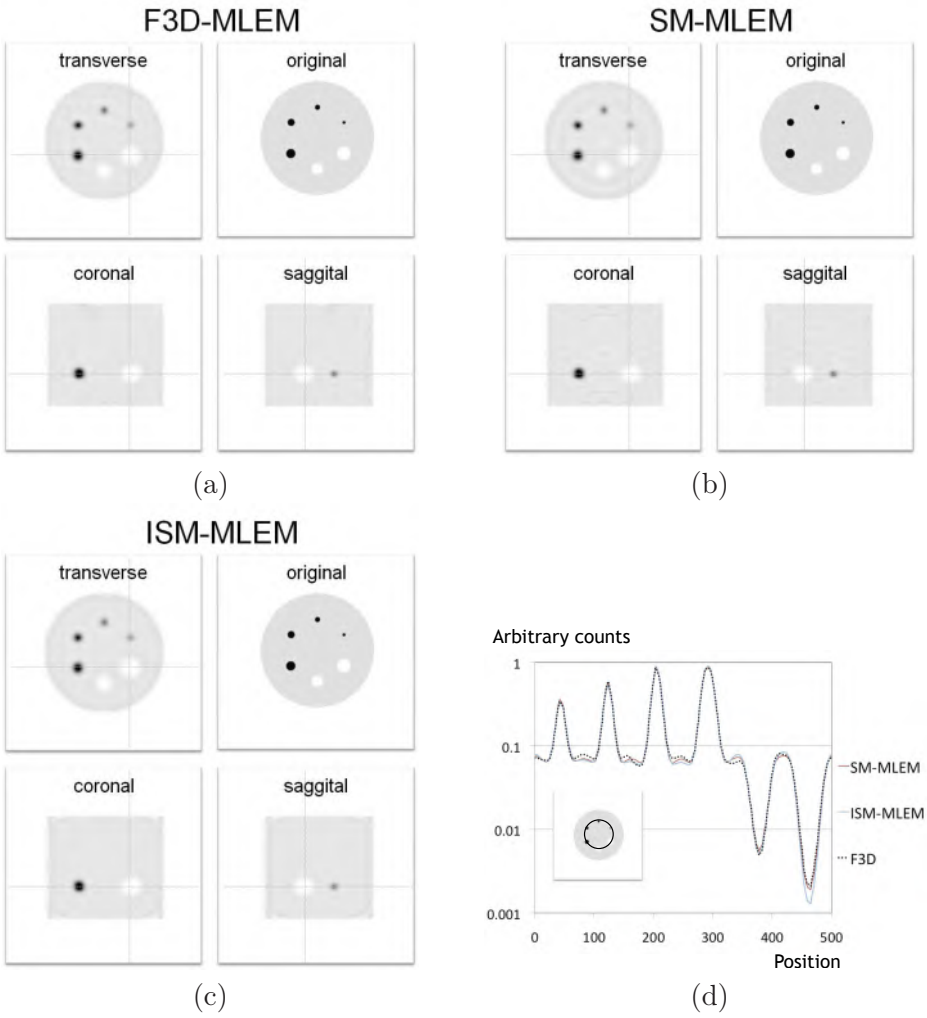

Figure 6.9: Transaxial, coronal and sagittal image sections at 71% mean CRC for (a) the F3D-MLEM (b) SM-MLEM and (c) ISM-MLEM. In (d) a circular profile through all lesions on the transaxial slice is shown for the three methods.

On the other hand, the time required for one sub-iteration for F3D-OSEM (270 subsets), SM-OSEM (225 subsets) and ISM-OSEM (6 subsets) respectively is 11.1 s,10.3 s and 23.4 s. Due to larger number of subset that can be used in the F3D-OSEM and the SM-OSEM, computation times per sub-iteration are shorter compared to the ISM-OSEM with limited number of subsets. However, when using such a large number of subsets for F3D-OSEM and SM-MLEM, the speedup is not linear anymore. This is due to the overhead of steps different from forward and backward projection, which become the speed bottleneck. Results are summarized in table 6.2.

	MLEM			OSEM		
	F3D	SM	ISM	F3D	SM	ISM
TP(s)I [s]	849	84	89	11.1	10.3	23.4
MU [Mb]	790	38	38	71	38	39
TGain	1	10.1	9.5	1	1.1	0.47
IGain	1	1.1	44.8	1	1.2	45.0
TTG	1	11.11	426	1	1.3	21.1
TT	29d11h	2d16h10m	1h39m	9h15m	7h39m	26m

Table 6.2: The computational load expressed in terms of time per iteration (TPI) and memory usage (MU) for all different reconstruction algorithms. The time gain with respect to computational load (TGain) and with respect to convergence (IGain) are also expressed with the F3D-EM as a reference. Next, the total time gain and the total reconstruction time are listed.

6.3.3 Contrast-to-noise

Figure 6.10 (a) and (b) respectively show the contrast-to-noise plot for the largest cold lesion and the largest hot lesion. As can be read from these curves, image quality is very similar for the three different reconstruction methods. This is confirmed by the images shown in figure 6.11. These images are taken at an equal noise level of 30% and correspond with 700 iterations for both F3D-MLEM and SM-MLEM and 40 iterations for ISM-MLEM. The profiles of figure 6.11 (d) show there is almost no difference to be found between the different images. Although not shown, the image quality of the OSEM reconstruction is comparable with the image quality of the MLEM reconstructions.

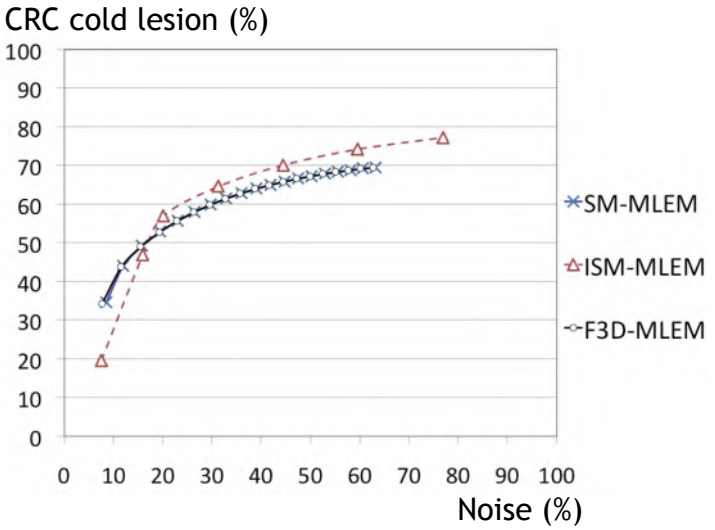

(a)

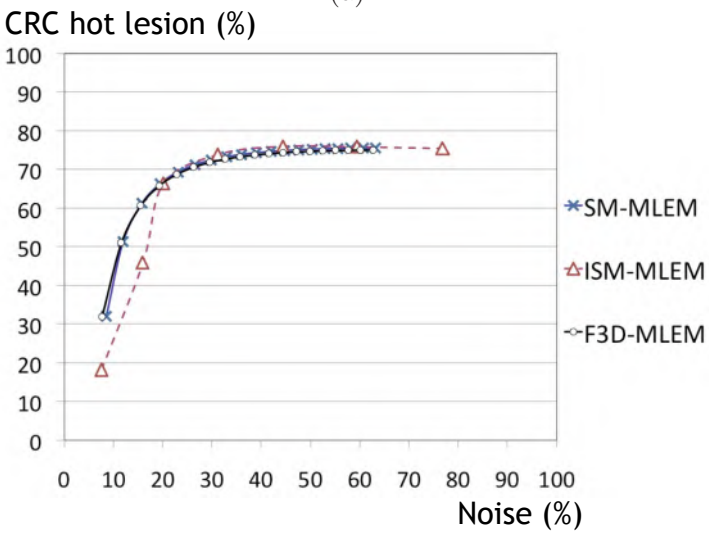

(b)

Figure 6.10: Contrast versus noise for (a) the largest cold sphere and (b) the largest hot sphere.

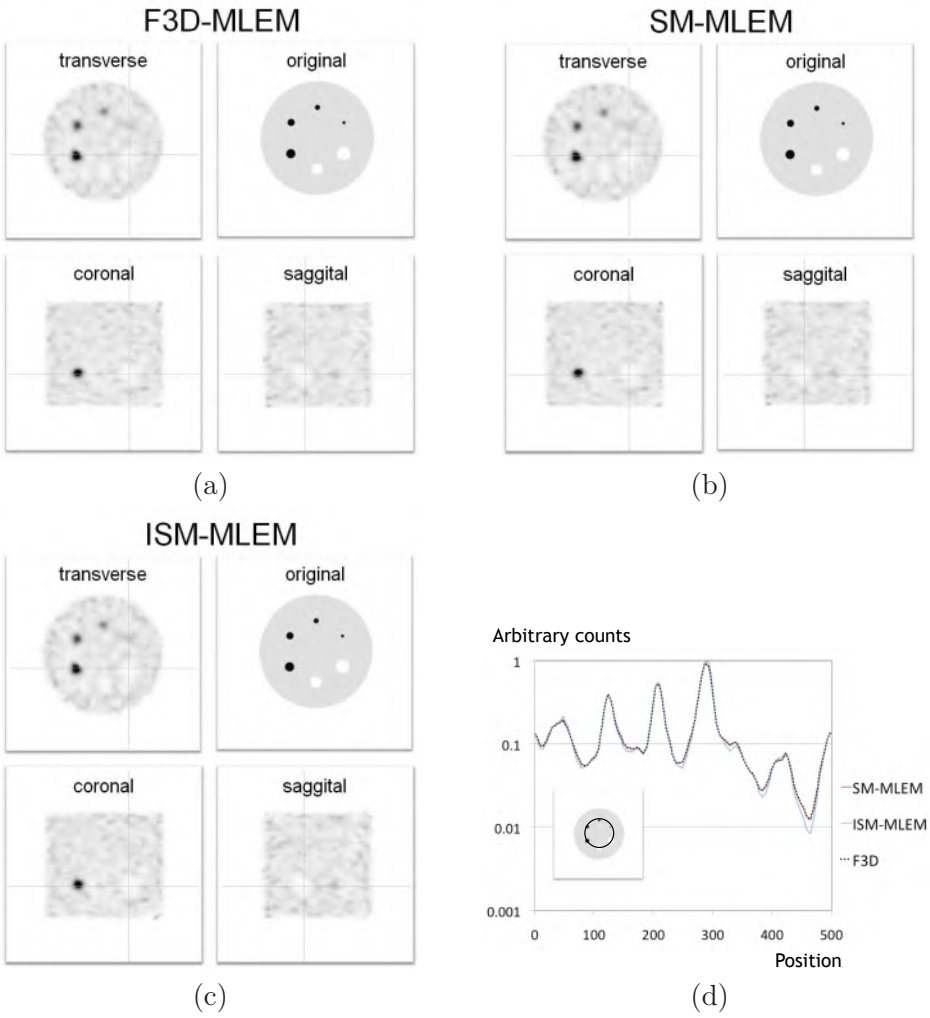

Figure 6.11: Transaxial, coronal and sagittal image sections at 30% noise for (a) the F3D-MLEM (b) SM-MLEM and (c) ISM-MLEM. In (d) a circular profile through all lesions on the transaxial slice is shown for the three methods.

6.4 Discussion

Image reconstructing from plane integral data not only suffers from computational complexity, but also from slow convergence due to the non-sparsity of the system matrix. The first problem can be solved by using a split matrix approach (SM) which reduces computational complexity from N^5 operations to $2 \times N^4$ operations. The problem of slow convergence is however not solved by just splitting the system matrix. The here developed ISM both reduces computational complexity and speeds up convergence and can serve as an attractive alternative to a fully 3D reconstruction. This has been shown by comparing convergence speed and computational load. Convergence of the three algorithms, F3D, SM and ISM, was investigated and we found about 45 times faster convergence compared to a fully 3D and a split matrix approach for both ISM-MLEM and ISM-OSEM. For our ISM-MLEM, computation time per iteration was reduced with about a factor of 10 compared to F3D-MLEM, resulting finally in a total time gain of 38 and 426 compared to respectively SM-MLEM and F3D-MLEM.
For OSEM, convergence is reached in the same number of sub-iterations. Because a larger number of subsets can be used, the calculation time per sub-iteration will be reduced in the case of F3D-OSEM and SM-MLEM. This compromises our very large speed gains found with MLEM. Nevertheless, the shorter calculation time of these algorithms can not fully compensate for the slower convergence. In this work, a final speedup of 18 and 21 was found for our ISM-OSEM compared to respectively SM-OSEM and F3D-OSEM. These speedup factors were found for the number of full iterations T fixed to 12. However, convergence could be further optimized by decreasing this number.
The newly developed algorithm enables us to reconstruct a rotating slat collimated SPECT acquisition within half an hour on a single CPU where we previously would have needed 9 hours for a fully 3D OSEM reconstruction or about 8 hours when using a split matrix OSEM approach.
To investigate whether our new method produces images with image quality similar to that of the gold standard F3D-MLEM, a contrast-to-noise study was performed. This study showed there was almost no difference in image quality to be found. The only difference we found was at low contrast levels. Here the ISM-EM tends to be slightly more noisy. However, in practice, an MLEM or OSEM algorithm is never stopped at these points of low convergence. From around 20% noise, the curves again are in accordance.

6.5 Conclusion and original contributions

When using MLEM, the newly developed method offers a 426 times faster reconstruction than a fully 3D method. However, subsets can be used more efficiently to speedup the F3D method. Even when using OSEM, our method still offers a speed increase of a factor of 21 and enables iterative image reconstruction for rotating slat collimated SPECT within a reasonable period of time without affecting image quality. The work presented here resulted in one conference proceeding [174] and an A1 journal publication [172].

Chapter 7

Comparison of 3D SPECT Imaging with a Rotating Slat Collimator and a Parallel Hole Collimator

7.1 Introduction

To reconstruct plane integral data measured by a rotating slat collimator to 3D images, much more computation time is needed compared to a parallel hole reconstruction. This problem was solved in the previous chapter by the development of a reconstruction method that uses two updates per iteration, one in plane integral space and one in sinogram space. Among different MLEM implementations to reconstruct plane integral data, this newly developed method was found to be the fastest. Furthermore, it maintains image quality. This fast image reconstruction algorithm enables us now to efficiently compare image quality obtained with a rotating slat collimator to that of a parallel hole collimator. Planar RS imaging with Filtered Back-Projection (FBP) reconstruction has previously been studied by Lodge [102]. Their work shows an advantage in signal-to-noise ratio (SNR) over a PH collimator for small activity distributions and enhanced contrast for small hot spots. A comparison of planar image quality in chapter 5 uses accurate system modeling in an iterative reconstruction and indicates improved contrast-to-noise ratios up to a factor 3, even in large objects approaching the size of the

field-of-view (FOV) of the camera [173].
In the tomographic case, FBP reconstructed SPECT images with a RS collimator again confirmed improved noise characteristics for small objects (smaller than 10 cm) and showed improved contrast only for small regions of high tracer uptake [103]. An iterative reconstruction approach found better contrast-to-noise for the RS for both cold and hot lesions [187]. However, in this study a solid state strip detector, investigated in chapter 3 was used and the image quality improvement was not only due to collimation with slats but was also subject to the combined effect of small detector width, better collimator resolution and solid state detector. Moreover, in this comparison, no model for depth dependent detector blurring was used during reconstruction. In this chapter, realistic measurements are simulated and all detector and collimator parameters will be matched in order to make a fair comparison to other collimators. This also implies that an attenuating medium will be present and accurately modeled by GATE. Therefore, we first need to validate whether classical scatter and attenuation correction techniques, discussed in chapter 2 (section 2.5.2.2 and 2.5.2.3), can be applied to plane integral reconstruction. After the development of an appropriate attenuation correction technique for the reconstruction algorithms with split system matrix in general, we will compare image quality to a parallel hole collimator by means of a contrast-to-noise analysis. Next, a realistic Tc-99m-MIBI scan will be simulated on both a SPECT scanner equipped with rotating slat and parallel hole collimators to show the possibilities of slat collimation in clinical practice.

7.2 Scatter and attenuation correction

7.2.1 Scatter correction

Using GATE, a cylindrical phantom filled with Tc-99m, solved in water, was modeled and consequently the datasets are contaminated by scatter. Thanks to the history tracking of the detected events, GATE flags every detection that scattered in the phantom. By binning only these detections in a plane integral dataset, the true scatter distribution g_{TRUE} is known and can be used to compare how well our scatter estimates agree with the real scatter distribution. In order to study the feasibility of a spectral based scatter estimation correction, we looked at the energy spectra of respectively PH collimated data and RS collimated data.

Figure 7.1 (a) and (b) show that the spectral distribution of scattered photons for the RS collimator is not different from the PH collimated scatter distribution. In order to correct for scatter in the data, the Dual Energy Window (DEW) scatter estimation technique [88] can thus be used to correct the data acquired with a rotating slat collimator. The scatter estimate is calculated using the DEW technique as follows:

$$g_{EST} = k\left(g_{SW}\frac{w_{MW}}{w_{SW}}\right), \tag{7.1}$$

with g_{SW} the data measured in the scatter window. The width of our main energy window w_{MW} was chosen 14 keV around 140 keV and w_{SW}, the width of the scatter window was chosen 10 keV and located around 125 keV (figure 7.1). Both energy windows are shown in figure 7.1 where also the estimate of the scatter with the above formula is given for $k = 0.5$. Also the true scatter distribution is plotted and it can be seen from the energy spectrum of the scatters that there is indeed a good agreement between the estimated and the true scattered photons, which were flagged during simulation. For validation, the number of counts, estimated with the DEW technique and the true number of scattered detections were compared for ten realizations of the data using the mean absolute error (MAE). The MAE between estimated and true number of scatters over the different realizations was 0.6%. For comparison, also the MAE for the PH data was calculated resulting in a value of 1.4%. This indicates the DEW scatter correction method is valid for data collected with a RS collimator, although no attempt is made to make a spatial validation at the level of the projections.

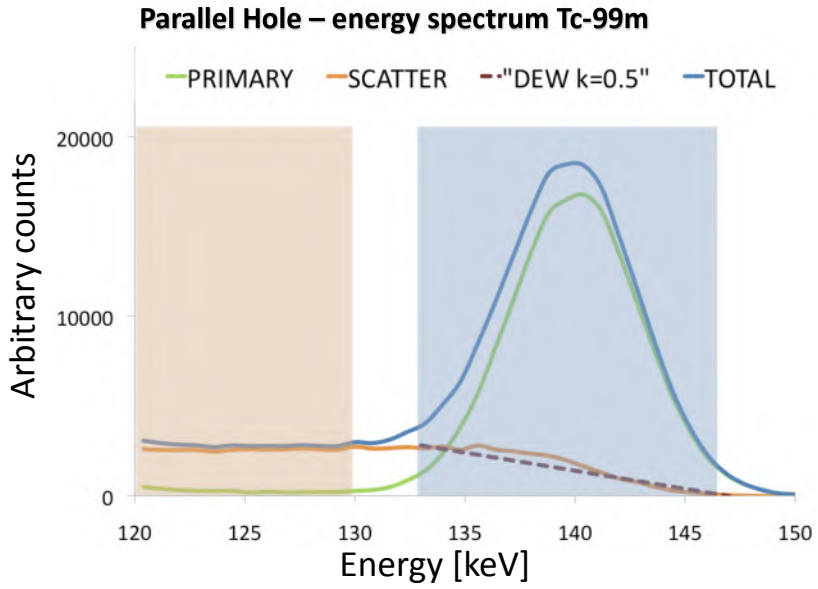

(a)

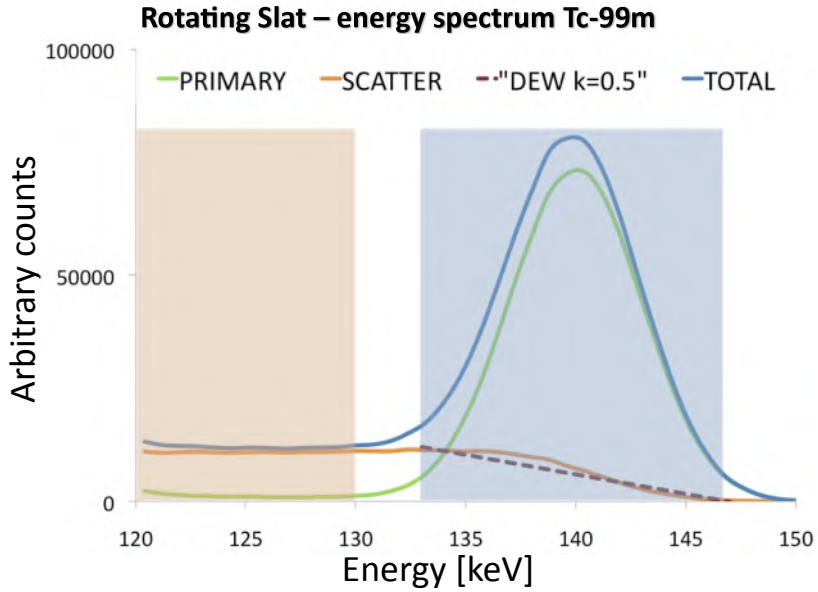

(b)

Figure 7.1: Tc-99m spectrum simulated on (a) a PH collimator and (b) a RS collimator with indication of the scattered photons and the estimated scatter. Also the energy windows used for scatter estimation are drawn.

7.2.2 Attenuation correction

7.2.2.1 Implementation

Since the data are affected by attenuation, we need a method to compensate for the loss of photons at larger depths. An attenuation correction method which fully models the attenuation along each possible ray of projection as used by Zeng et al. [202] is used for the reconstruction of the PH data. However, for RS data, this method is only possible in a fully 3D reconstruction algorithm which directly maps image to the plane integrals using one single system matrix. Since our fast reconstruction method splits the system matrix in two separate ones, the original paths of detection are lost and this method can not be applied. Therefore, we base ourselves on Chang's attenuation correction method [30] which calculates an average attenuation factor at each voxel. However, where Chang calculates the mean attenuation value over all SPECT angles for every voxel, our method will calculate an average attenuation coefficient c over all spin angles ϕ for every voxel (x, y, z) and for every SPECT angle θ:

$$c(x, y, z, \theta) = (\frac{1}{\Phi} \sum_{i=0}^{\Phi} exp(-(\mathrm{M}L)_{\phi_i})^{-1}, \tag{7.2}$$

with $(\mathrm{M}L)_{\phi_i}$ the mean attenuation length product for spin angle ϕ_i. The calculation of $(\mathrm{M}L)_{\phi_i}$ was done by tracing 100 paths connecting the voxel of interest with equidistant points, sampling the detector. In figure 7.2 (a) one of such paths is displayed. The ray tracing, using Siddon's algorithm [146], returned the intersection lengths of these rays with the attenuation image voxels. Sensitivity weighting of the intersection lengths with $\cos^3 \alpha$, with α the incidence angle as defined in figure 7.3 (a), yielded a map of weighted intersection lengths for a certain voxel (figure 7.2 (b)). Finally, multiplication with the μ value of the intersected voxel and averaging over all possible paths resulted in $(\mathrm{M}L)_{\phi_i}$.
Since our system matrix $\mathbf{B}$ rotates (Gaussian rotator) the image according to the appropriate SPECT angle before applying sensitivity and resolution modeling, we can use the factors c to compensate the rotated image for attenuation. In this way, an approximate attenuation compensation is performed in system matrix $\mathbf{B}$, being calculated with every SPECT angle as an average over all spin angles.

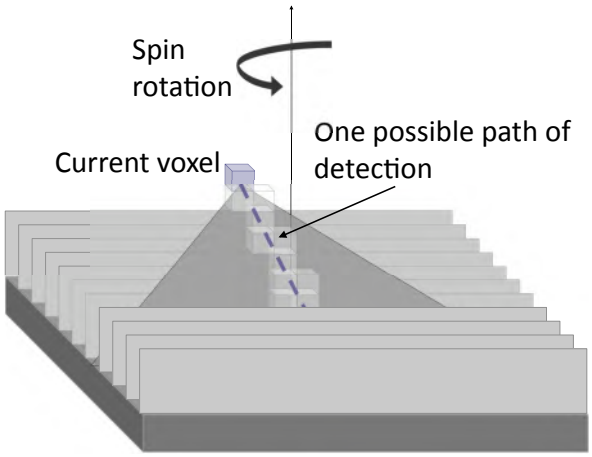

(a)

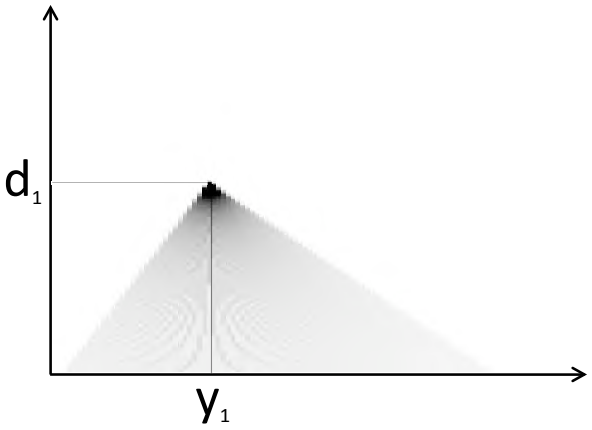

(b)

Figure 7.2: (a) One of the possible paths along attenuation has to be calculated. (b) The sensitivity weighted intersection lengths for all possible paths of detection for one voxel at one spin angle.

7.2.2.2 Validation

GATE was used to validate the correctness of the attenuation values c of our analytic calculation method. Four high count simulations (noise<0.8%) were performed, resulting in four datasets I_d, $I_{d,0}$, I_y and $I_{y,0}$. For the generation of I_d and I_y, line sources aligned with respectively the D and Y axis of the scanner (figure 7.3 (a and (b))) were simulated with a cylindrical water phantom present. The camera was spun over 360 degrees. Binning the recorded data according to the source position resulted in the datasets I_d and I_y. $I_{d,0}$ and $I_{y,0}$ were generated in a similar way with the only difference being the absence of the water cylinder. Since the detector was rotated over all spin angles there exists the following relation between datasets I and I_0:

$$I = I_0 \frac{1}{\Phi} \sum_{i=0}^{\Phi} exp(-(\mathrm{M}L)_{\phi_i})), \tag{7.3}$$

$\frac{I}{I_0}$ should thus be equal to the reciprocal of the attenuation values c. The calculations of c were based on an attenuation map derived from the cylindrical phantom. In figure 7.4 the results are summarized as a line profile through the reciprocal of the calculated attenuation values c (ANALYTIC) for varying d ($y = x = 0$) and for varying y ($d =$ 190 mm and $x = 0$) in figure 7.4 (a) and figure 7.4 (b) respectively. The simulation results (GATE) in figures 7.4 (a) and (b) are the ratio of respectively I_d and $I_{d,0}$ and I_y and $I_{y,0}$. These profiles show very good agreement and suggest the proposed analytic calculation method for the attenuation values is suitable for attenuation compensation during our iterative reconstruction. The difference between both profiles is also plotted (delta) and is small ($< 1\%$) and are due to discretization errors in the calculation method. Transaxial slices through reconstructed images of a uniform cylindrical source are shown in figure 7.5 (a) and (b) in the case of respectively no attenuation correction and attenuation correction with the calculated correction factors c.

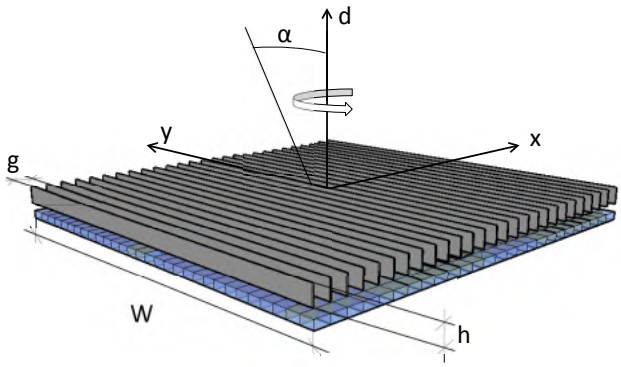

(a)

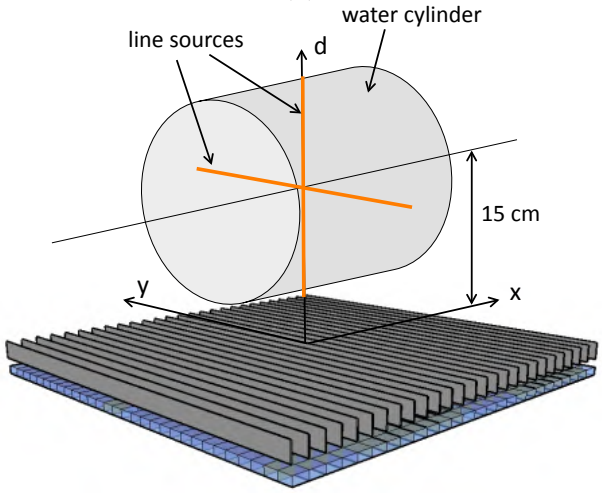

(b)

Figure 7.3: In (a) the geometry of the slat collimator is shown while in (b) the placement of the line sources with respect to the detector and the water cylinder are shown.

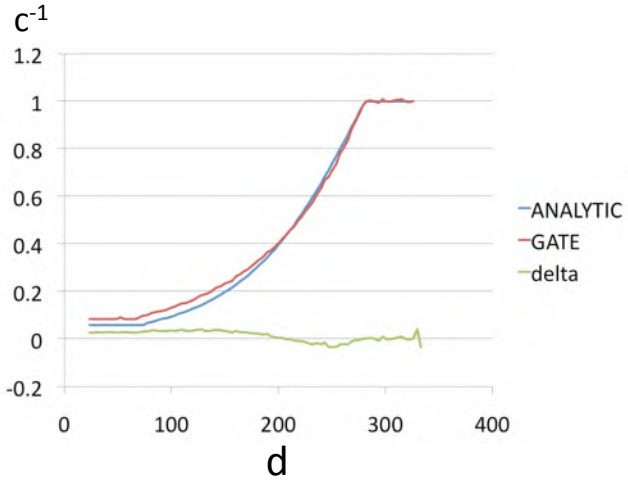

(a)

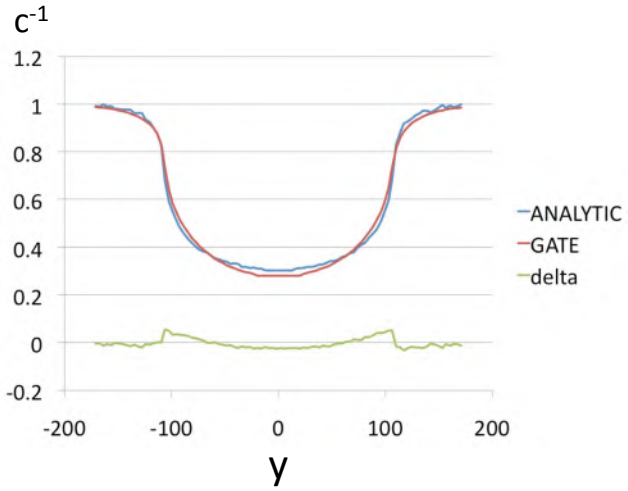

(b)

Figure 7.4: Plot of simulation-based (GATE), calculation-based (ANALYTIC) values for attenuation correction, together with their difference (delta). (a) shows the values along d for $y = x = 0$ and (b) shows the values along y for $x = 0$ and $d = 19$ cm.

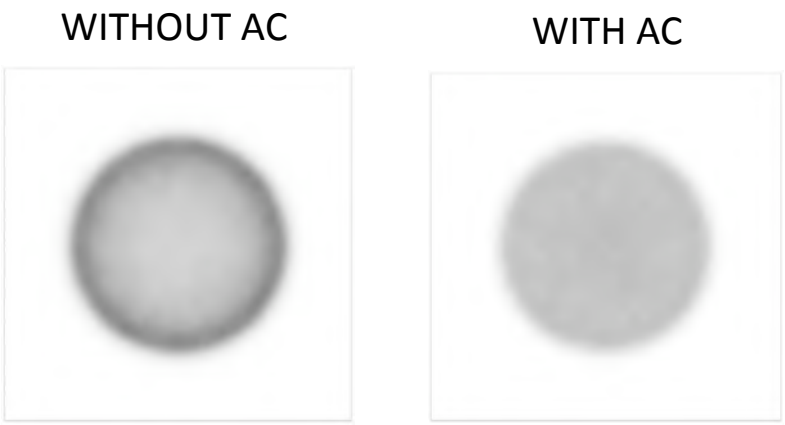

(a) (b)

Figure 7.5: Transaxial slices through reconstruction of uniform cylindrical source. In (a), no attenuation correction was used during reconstruction while in (b) attenuation correction based on attenuation factors c was used.

7.3 Monte Carlo simulations of realistic acquisitions

7.3.1 Image quality phantom

For the purpose of a contrast-to-noise comparison, the image quality phantom (Standard Jaszczak Phantom^{TM}), shown in figure 7.6 is simulated containing 4 hot spheres (diameters: 9.9 mm, 12.4 mm, 15.4 mm, 19.8 mm) and two cold spheres (diameters: 24.8 mm and 31.3 mm). The activity concentration is set in order to have a sphere-to-background activity ratio of 8:1 in the hot spheres. The total activity in the phantom was 370 Mbq. The phantom is simulated to be filled with water with an attenuation coefficient μ of 0.154 cm^{-1} at 140 keV. Figure 7.6 (a) shows the three headed rotating slat camera that was modeled while in figure 7.6 (b) the three headed parallel hole system is shown. Both the PH and the RS camera consist of an identical detector modeled as 192×192 individual pixels of 1.8×1.8 mm. 193 parallel slats of height 40 mm and 0.3 mm thickness model the RS collimator. The PH collimator is implemented as a square hole collimator with height 40 mm and 0.3 mm septal thickness. The hole pitch is 1.8 mm and matches the slat pitch of the RS collimator. The collimator resolution is thus matched for both collimators and is 5 mm at 10 cm collimator distance. The rotation

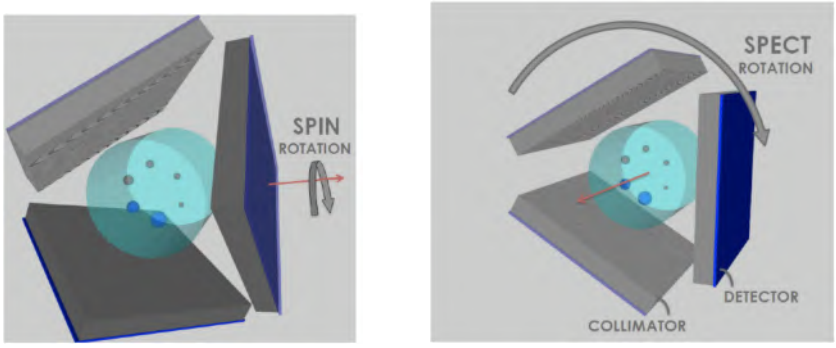

(a) (b)

Figure 7.6: The geometry of the simulated SPECT camera equipped with (a) a RS collimator and (b) a PH collimator. Next to the SPECT rotation, a RS acquisition also needs a spin rotation of each detector.

radius of the detector was 15 cm and the acquisition time was set to 8

minutes. The PH scanner was rotated in 90 discrete steps around the object. At each SPECT angle, the RS detector heads additionally were spun around there own axes also in 90 discrete steps over 360°.

7.3.1.1 Influence of system modeling

The data generated by the Monte Carlo simulation resulted in a one dataset for RS and one for PH. For image reconstruction, we use the algorithm of equation 6.12 derived in chapter 6. After scatter correction according to the DEW technique, validated in paragraph 7.2.1, the data are all reconstructed with attenuation correction as explained in section 7.2.2. In order to investigate the influence of resolution and sensitivity modeling in the system matrix, the two datasets are reconstructed in three different ways: (i) without any modeling, thus using a simple line integral model (no model); (ii) with resolution modeling (RM) and (iii) both with resolution and sensitivity modeling (RSM). Since for a PH collimator the sensitivity is constant over the FOV, reconstruction RM and RSM will produce equal results. Contrast recovery and noise are calculated using equations 5.4 and 5.5 respectively. We evaluated the cold and hot lesion contrast recovery, CRC_c and CRC_h, averaged over respectively the two cold and the four hot lesions at a NC of 25%.

7.3.1.2 Image quality improvement

After investigating the influence of using an accurate system model, transaxial, coronal and sagittal slices through the reconstructed 3D images will be shown for both the PH and RS collimator at equal NC. Also, 1D profiles through the lesions will be drawn. Next, the contrast-to-noise was plotted for all lesions to investigate the contrast-to-noise properties. This will especially be interesting to study the convergence properties. For the PH acquisition, the same simulation as described before is repeated in order to study the difference in imaging time to reach equal contrast-to-noise behavior for both collimators.

7.3.2 Simulation of a realistic Tc99m-MIBI scan

The NCAT software phantom [143] was used to simulate a clinically realistic measurement of a patient injected with Tc-99m-MIBI, used for the assessment of heart perfusion and/or viability. Realistic organ uptake

values which have been published before have been used [71]. Background, lungs, liver and heart-wall respectively were assigned activity concentrations of 0.0075 MBq/ml, 0.0048 MBq/ml, 0.07 MBq/ml and 0.15 MBq/ml. One defect (2.8 ml) was simulated in the left ventricular anterolateral wall with an activity concentration of 0.0075 MBq/ml. Total activity in the NCAT phantom was 490 MBq. The PH and RS scanners were modeled as described in section 7.3.1, with the only difference of rotation radius (23 cm) and acquisition time (810 seconds). The data were binned for PH in 96×96 detector bins for 90 SPECT bins while the RS data were binned in 96 detector bins, 90 SPECT and 90 spin angle bins. The rotation radius was 23 cm. Since the lesion is simulated, we know the exact location of where it should be in the reconstructed images. Therefore, the simulated lesion location is chosen as the lesion ROI (ROI_l). A reference region of interest is chosen in the anteroseptal wall in order to calculate the CRC. Noise is calculated in a background region of interest.

7.4 Results

7.4.1 Image quality phantom

7.4.1.1 Influence of system modeling

The influence of system modeling is evaluated at 25% NL in figure 7.7. In 7.7 (a) the mean CRC for cold and hot lesions is shown for the PH collimated acquisition for reconstruction without modeling (PH no model) and for reconstruction with resolution modeling (PH RM). An increase of 8% with respect to the case without system modeling is found for both cold and hot contrast recovery when applying a depth dependent resolution model. In 7.7 (b) the mean CRC for cold and hot lesions is

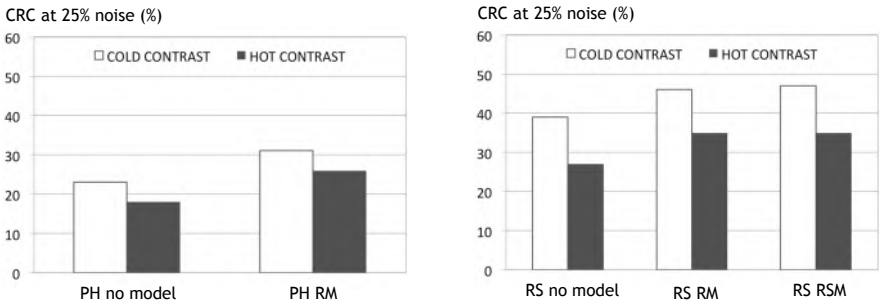

Figure 7.7: Mean cold and hot contrast recovery coefficient at 25% noise for (a) the PH and for (b) the RS reconstruction. Reconstruction without any modeling ('wo model'), with resolution ('RM') and with additional sensitivity modeling ('RSM') are compared.

shown for the RS collimator for reconstruction without modeling (RS no model), for reconstruction with resolution modeling (RS RM) and for reconstruction with both sensitivity and resolution modeling (RS RSM). An increase of 7% and 8% is found for respectively cold and hot contrast recovery when applying a depth dependent resolution model. An additional increased CRC of 1% for cold and hot CRC, is found when sensitivity is additionally modeled. Hot contrast did not increase due to the sensitivity modeling.

7.4.2 Contrast-to-noise

Looking at figure 7.7, for the cases of full system modeling, an increased (+16%) cold CRC can be seen for the RS collimator. Also an increase (+9%) in hot CRC is found for the RS compared to the PH collimator. Figure 7.8 shows the contrast-to-noise plot for the average cold CRC.

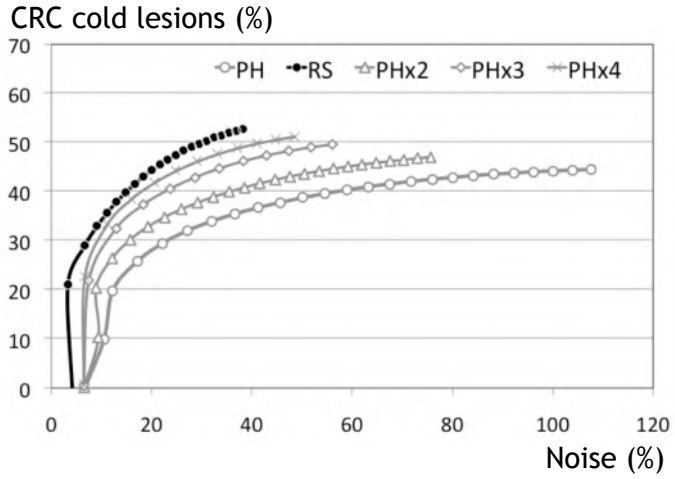

Figure 7.8: Contrast-to-noise averaged over both cold lesions.

The cold lesions show better contrast recovery for RS compared to the PH collimator. To have an idea about the quantitative improvement, the imaging time was increased for the PH collimator. The results for a 2, 3 and 4 times longer PH acquisition are also plotted in figure 7.8. From these plots, it can be seen that, to obtain the same contrast-to-noise, the PH collimator needs more than 5 times longer acquisition time compared to the RS collimator. The average result for the hot lesions is shown in figure 7.9. This plot shows that the RS collimator needs 2 to 3 times less scan time than a PH collimator in order to obtain similar contrast-to-noise characteristics.

7.4.3 Tomographic images

A transverse, coronal and sagittal slice through the images at equal noise (40%) is shown in figure 7.10 (a) and in figure 7.10 (b) for respectively the PH and the RS collimator. It can be seen from the images already

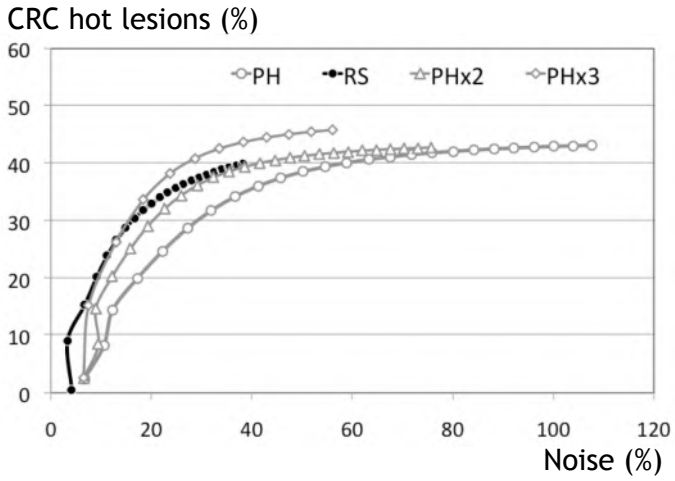

Figure 7.9: Contrast-to-noise averaged over all four hot lesions.

that the RS collimator improves the contrast. The profile drawn through the lesions in figure 7.11 confirms the better contrast recovery with the RS collimator.

7.4.4 Tc-99m-MIBI scan with the NCAT phantom

The contrast-to-noise is calculated for the 2.8 ml heart defect. The ROI of the lesion was exactly aligned with the simulated lesion in the NCAT phantom. Noise was calculated in a ROI in the lungs where the activity was uniform. From figure 7.12, it can be seen that the parallel hole collimator converges to a higher contrast at higher noise levels. However, the RS collimator performs better at noise levels lower than 14%. The better performance of the PH collimator contrasts with the findings for the image quality phantom where we found a more than 4 times better image quality for the cold lesions. To our opinion, this is due to the combination of larger scan radius (23 cm compared to 15 cm for the IQ phantom) and larger object and thus more noise accumulation from surrounding activity. The influence of surrounding activity causes a lot of spill over of activity to the cold lesion in the heart wall. This is illustrated in figure 7.12 for the ideal case of limited source activity. All source activity outside a sphere of radius 110 mm, centered in the FOV was removed from the simulation. It can be seen that the image quality

increases, confirming that the image quality is highly influenced by the object size.

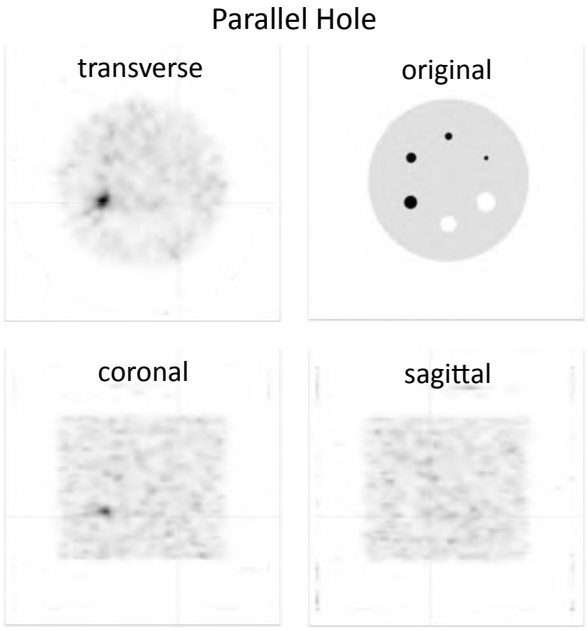

(a)

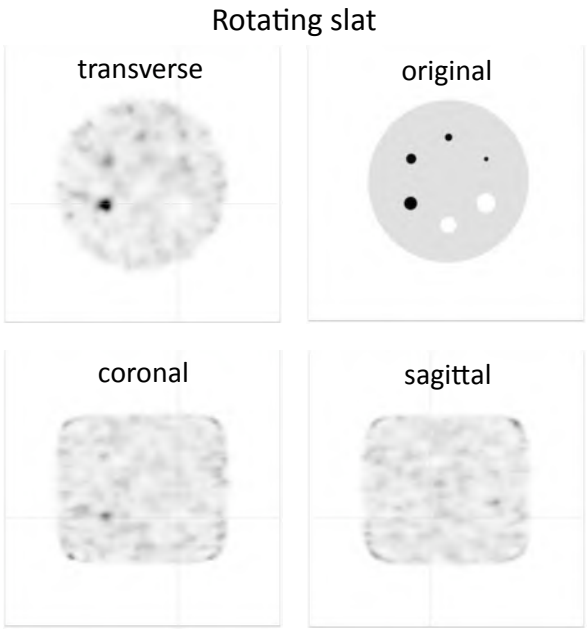

(b)

Figure 7.10: Reconstructed images from the (a) the PH collimator at 10 iterations and (b) from the RS collimator at 10 iterations. Noise is 40%.

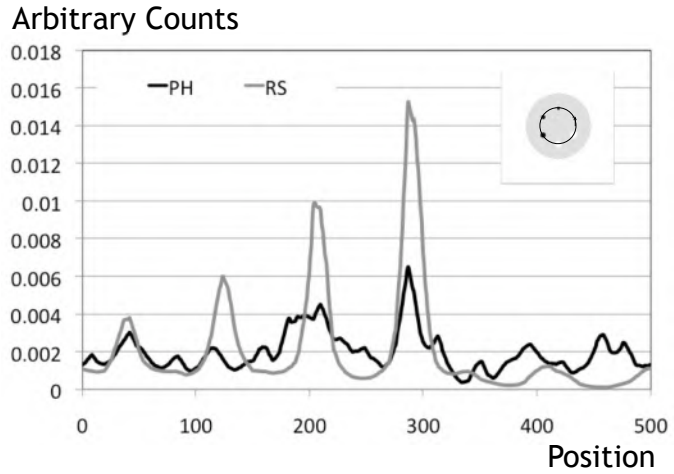

Figure 7.11: Circular profiles through the lesions are drawn, normalized to the total number of counts under the profile. Noise is 40%.

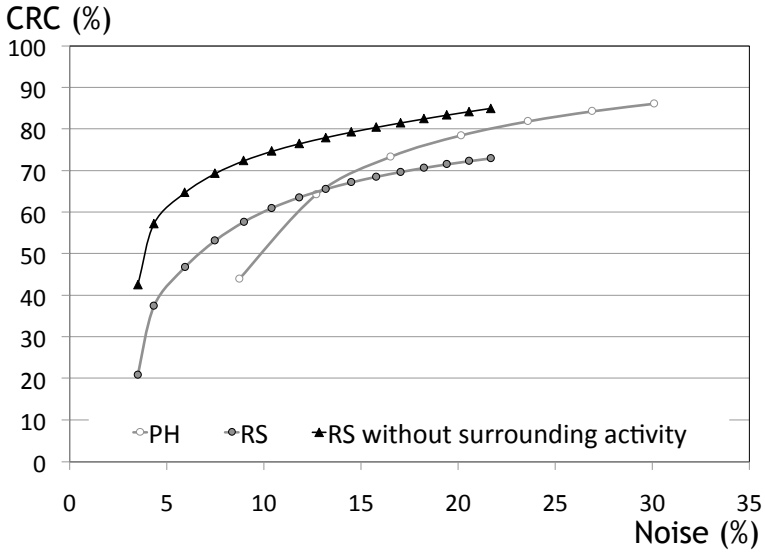

Figure 7.12: Contrast-to-noise for the 2.8 ml heart lesion for the PH collimator and the RS collimator with and without presence of surrounding activity.

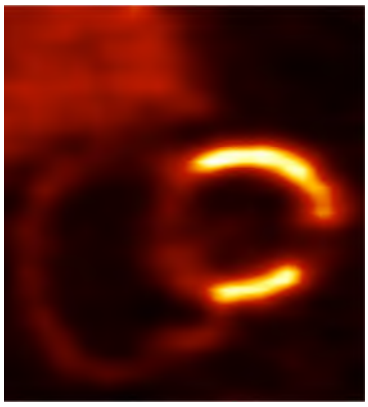

(a)

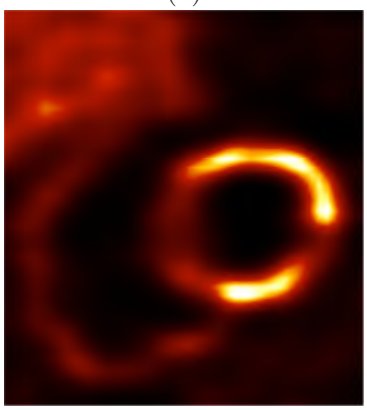

(b)

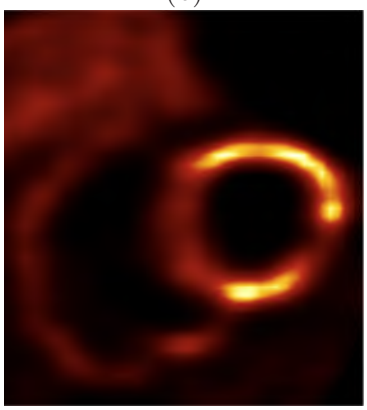

(c)

Figure 7.13: A coronal slice through the heart defect for (a) the PH collimator and (b) and (c) for the RS collimator with and without surrounding activity. The noise in the images is 20%. To reach this noise level, 25 iterations were used for the PH and 20 iterations for the RS collimator.

The fact that the RS collimator still performs slightly worse at higher noise can, to our opinion, be attributed to the larger total amount of surrounding activity compared to the image quality phantom. From the coronal slices through the heart lesion in figure 7.13, the slightly better image quality for the PH collimator can be appreciated. The images are at 20% noise, where a 6% higher contrast is obtained with the PH collimator. Figure 7.13 (c) shows improved lesion visibility compared to figure 7.13 (b) due to the removal of surrounding.

7.5 Discussion

Scatter correction was used and found at least equally accurate compared to DEW scatter correction for PH collimated acquisitions. Furthermore, an analytic method for calculating attenuation factors for every voxel at every SPECT angle was proposed and validated. This enabled us to correct for attenuation in a previously proposed reconstruction method for plane integral data. With these tools available, a realistic Monte Carlo simulation of an image quality phantom could be reconstructed. An investigation of the influence of system modeling shows that both a PH and RS gain image quality when a depth dependent resolution model is used during reconstruction. An increased contrast of about 8% was found for both collimators at 25% noise. An additional model for sensitivity did not significantly increase image quality further for the RS collimator. Also when no modeling is used at all, the RS collimator performs better compared to the PH collimator (16% higher cold contrast and 9% higher contrast at 25% noise). These findings are consistent with the findings of Wang [187]. Based on these findings, one can state that it is not the modeling, but the image reconstruction algorithm itself which is in favor of the RS collimator, most probably due to the statistical model of the noise behavior which is intrinsic to MLEM.
The contrast-to-noise investigation shows that SPECT images obtained with a rotating slat collimator in combination with iterative reconstruction and accurate modeling provide a better contrast-to-noise trade-off compared to images obtained with an equivalent PH collimator. In terms of imaging time, equal average cold contrast-to-noise is found in a more than 4 times shorter scan time for the RS collimated detector. For the contrast-to-noise, averaged over the hot lesions, the results show a 2 to 3 times improvement in terms of acquisition time. This study thus not only shows better hot spot contrast recovery, which was also found by

Lodge [103], but also proves better cold spot contrast recovery, which is consistent with the results obtained by Wang [187]. These results were obtained however with a slat collimated solid-state strip detector, but in that study, no depth dependent resolution was modeled and no attenuation compensation was used. Also, it was unclear whether the improved contrast-to-noise was due to the better solid state detector or due to the slat collimator. This study indicates the improvement is due to the collimator.
The case study of the Tc-99m-MIBI scan with the NCAT phantom shows that in a clinical setting, where a larger scan radius has to be used and where there is more activity throughout the FOV, the RS collimator has more problems to reach better image quality. It is only at lower noise that the RS collimator performs better. Image quality improves when removing surrounding activity from outside a sphere centered in the FOV. This indicates that for clinical imaging, the removal of surrounding activity, for instance by a technique based on the FDF technique proposed in chapter 4 could be very useful. Theoretically, this technique is able to remove activity from outside a centered sphere with radius defined by the extent of the window applied in Fourier space. However, this method has not yet been used in the tomographic case and thus requires further investigation.

7.6 Conclusion and original contributions

In this chapter, an attenuation correction method for the reconstruction of plane integral data was developed in order to study the tomographic image quality with respect to a parallel hole collimator. For a standard image quality phantom, better image quality was obtained. However, in the clinical case of a Tc-99m-MIBI scan of a heart defect, the parallel hole collimator still obtains better images at higher noise levels. At low noise, the RS outperforms the PH collimator. We believe the main factor limiting the performance of a RS collimator in the clinical case of heart defect imaging is due to surrounding activity. A technique based on the removal of partial field-of-view activity proposed in chapter 4 or the local tomography principle, proposed by Zeng, could reduce the influence of surrounding activity.
The results proposed in this chapter were published in a conference proceeding [174].

Chapter 8

Imaging I-123 and I-131with Rotating Slat Collimators

8.1 Introduction

Nuclear medicine studies based on single photon emitters mainly use Tc-99m as a label. Because Tc-99m emits almost 100% of its photons at 140 keV, it is called a pure emitter. This is a likely situation for imaging. Nevertheless, also non-pure emitters are used in nuclear medicine. Non-pure emitters can have emissions at energies above their main (low) energy peak. Also, medium ($<$ 300 keV) and high energy ($<$ 400 keV) emitters are used in combination with respectively medium energy (ME) and high energy (HE) collimators. Here, the imaging performance of a rotating slat (RS) collimator will be investigated for two frequently used isotopes, namely I-123 and I-131 which respectively are representative for low-energy isotopes with high energy emissions and high energy isotopes.

8.1.1 I-123

I-123 is an important isotope to label pharmaceuticals that are taken up by the brain, the myocardium or the thyroid. Besides its main energy peak at 159 keV, I-123 also has higher energy photon emissions. During decay, the total probability for a photon emission at 346 keV, 440 keV, 505 keV, 529 keV or 539 keV adds up to 2.7% (figure 8.1). However,

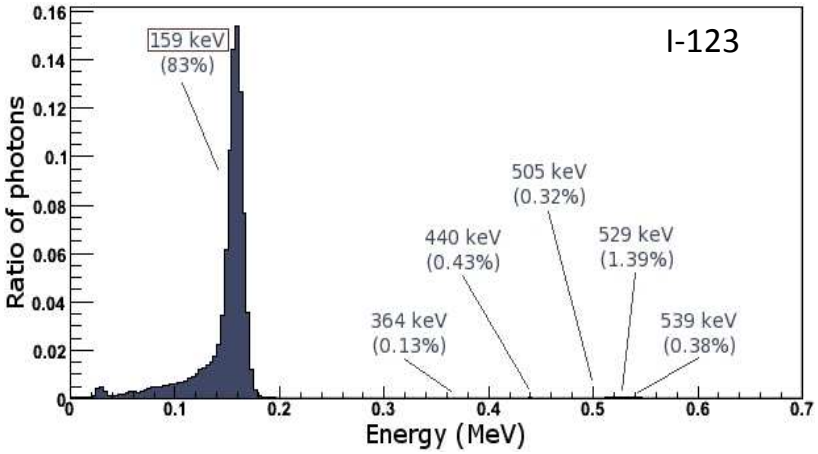

Figure 8.1: A typical I-123 energy spectrum recorded without a collimator present. The emission probability for the different $\gamma-$rays of I-123 is also indicated [134].

since these photons will most likely penetrate the collimator septa, they behave as if there was no collimator. In combination with scatter effects, their probability of detection will be much higher than would be expected from the emission probability and they will compete with the useful photons which have a detection probability of 0.01% on a traditional Parallel Hole (PH) collimated system. It has been shown that the total amount of the HE photons in the photopeak window can add up to 49% to 60% of the detected photons [35, 134]. Different studies show the importance of the choice of collimator and most of them suggest the use of a medium energy collimator [107, 55, 44]. Other solutions involve fanbeam collimators with slightly improved signal-to-noise [35], scatter correction methods [55, 147] or, more recently, modeling of the HE point spread function during iterative reconstruction [34, 150]. However, medium energy collimators result in poor spatial resolution [55, 69], energy window based scatter correction techniques are unable to control the noise [179, 55] and modeling during the reconstruction is computationally expensive. We propose to use a RS collimator for imaging isotopes with high energy emissions. Due to the higher geometric efficiency for the main photopeak, penetration and other contamination from the other photopeaks will be lowered.

8.1.2 I-131

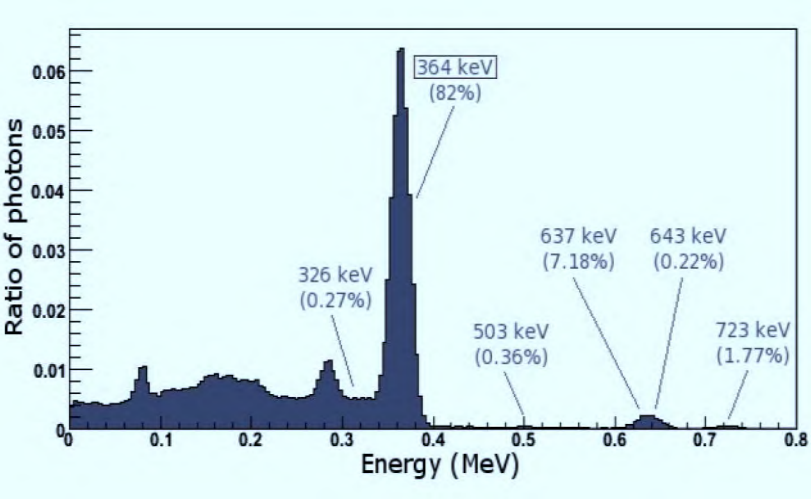

Figure 8.2: The energy spectrum of I-131 recorded without a collimator present. The emission probability for the different $\gamma-$rays is indicated [134].

Because of its β^--decay, I-131 is frequently used during radio-immunotherapy for the treatment of B-cell non-Hodgkin's lymphoma [183, 181]. Next to the emission β^--radiation, I-131 also has decay through gamma-emission. These gammas make imaging possible which in turn aids internal dosimetry of the administered therapeutical agent. Quantification is however difficult because of the higher energy of the photopeak (364 keV) and the multiple higher energy gamma-ray emissions. The most important intensity emissions of I-131 are at 284 (6.1%), 364 (82%), 637 (7.2%), and 723 keV (1.8%) (figure 8.2). The 637 keV and 723 keV higher energy photons are low in intensity but contribute substantially to the data because of their high probability of penetrating the HE collimator. They will thus contaminate the image in a similar way as the high energy emissions do in the case of I-123 imaging. Furthermore, the design of a high-energy collimator has to trade sensitivity or resolution because the septa need to be thicker. For an acceptable sensitivity and resolution, a substantial amount of photons from the main energy peak at 364 keV will still penetrate the septa, introducing an extra source of contamination [42]. Scatter compensation techniques have been derived, based on the measurement of line spread

functions at different depths in a phantom [61]. It has been proposed to use ultra-high-energy (UHE) collimators [41] and more recently, Monte Carlo based scatter correction techniques have been proposed for quantitative imaging of I-131 [40].
For the two isotopes under investigation, we first study the energy spectrum and the relative contribution of HE photons to the photopeak window for both a PH and a RS collimator. To get insight in the mechanisms involved in the detection of a HE photon, the HE contamination will be subdivided into different categories, depending on the interactions taking place before ending up in the main energy window. Also, the shape of the point spread functions (PSFs) will be studied. Finally, the image quality, expressed in contrast-to-noise plots will be investigated for a planar imaging setup.

8.2 Methods

In a real experiment, we can not separate the HE contamination in the main photopeak energy window from degradations arising from collimator scatter, phantom scatter or other physical or geometrical effects deteriorating the image. In order to investigate HE contamination and the different mechanisms behind it, we use Monte Carlo simulations in this study. A model of the AXIS gamma camera (Philips Medical Sys-

Collimator type	Septal thickness (mm)	Height (mm)	Slit/Hole size (mm)
LE-RS	0.18	27	1.4
LE-PH	0.18	27	1.4
HE-RS	0.86	58.4	3.40
HE-PH	0.86	58.4	3.40

Table 8.1: Physical properties of the collimators used in this study.

tems), which was previously validated for GATE [152] was used with a thick crystal (3/4 inch) and Low Energy (LE) collimation for I-123 and HE collimation for I-131. Both the RS and PH variants have equal spatial resolution. Their specifications are summarized in table 8.1. To store the history of each detected photon, the GATE code was modified [36]. The I-123 photon emission was modeled as a main emission peak of 159 keV and high energy emissions with a probability as listed in

table 8.2. This separation makes it possible to attribute the photopeak activity to a certain emission peak after simulation. The I-131 photon emission, which is even more complex, was modeled as listed in table 8.2

I-123	Peak number	Energy (keV)	Emission Probability
Main	1	159	83%
HE	2	346	0.13%
	3	440	0.43%
	4	505	0.32%
	5	529	1.40%
	6	539	0.38%
I-131	**Peak number**	**Energy (keV)**	**Emission Probability**
Main	1	364	81.7%
LE	2	80.2	2.62%
	3	177.2	0.27%
	4	284.3	6.14%
	5	325.8	0.27%
HE	6	503.0	0.36%
	7	637.0	7.17%
	8	642.7	0.22%
	9	722.9	1.77%

Table 8.2: Emission energies and emission probabilities for the simulation of I-123 and I-131

8.2.1 Study of the origin of high-energy contamination

A point source, centered in a 20 cm diameter sphere filled with water, was simulated at 15 cm distance from the collimator for both an RS and a PH collimator (figure 8.3). A total activity of 1 MBq was simulated over a period of 40 minutes. After detection, the photons were categorized in 5 different types of detection (figure 8.4):

1. **geometric**: photons that are detected without any previous interaction.

2. **phantom scatter**: photons that scatter in the water phantom and are then directly detected in the crystal.

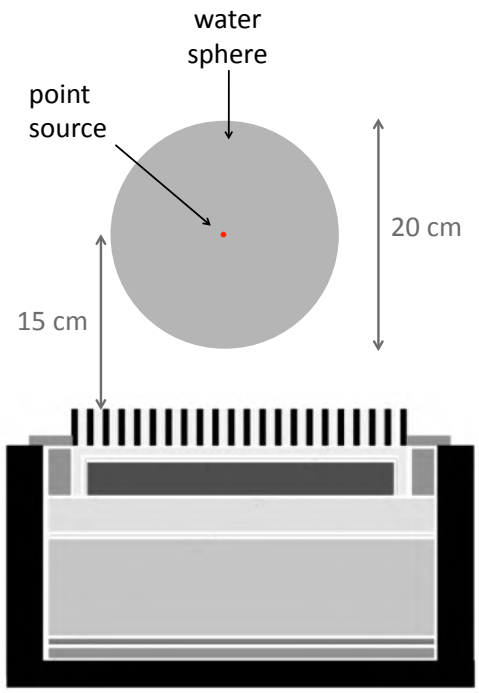

Figure 8.3: The point source phantom and detector setup.

3. **penetration** through the collimator: photons that penetrate the collimator before detection. Most of the HE photons, classified as penetration will undergo Compton scatter in the phantom or in the crystal (or a combination of both) in order to end up in the photopeak window. Nevertheless, they are classified as penetration photons.

4. **collimator scatter**: photons that undergo scatter in the collimator directly before detection, independently of their previous interactions.

5. **backscatter** in the end parts: photons that backscatter in the end parts of the camera, independently of their previous interactions. Most of the HE photons that backscattered, will also first have penetrated the collimator. Nevertheless, they are classified as backscattered.

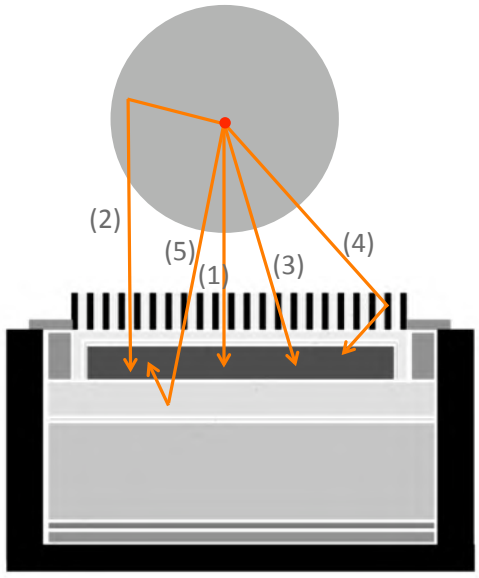

Figure 8.4: The five different classes of detected photons: geometric (1), phantom scatter (2), penetration (3), collimator scatter (4) and backscatter (5).

For the two isotopes under investigation, energy spectra of all the above categories of detected photons are plotted with a detailed view on the content of the 20% photopeak window at 159 keV and 364 keV for respectively I-123 and I-131. Also, all detections in the photopeak were classified according to emission energy and type of detection.

8.2.2 Study of the point spread function

The point spread function was derived for both isotopes and both collimation types. From the PSF, the FWHM and FWTM were calculated. Also, the constituting components of the PSFs are plotted. For the sake of clarity of the plots, phantom scatter and collimator scatter are referred to as 'scatter' while penetrated and backscattered photons are grouped under 'penetration' because almost all backscattered photons will first have penetrated the collimator.

8.2.3 Study of the contrast-to-noise ratio

Quantitative imaging performance was investigated by means of a contrast-to-noise study. For I-123, a planar image quality phantom with hot and cold lesions in a warm background was simulated while for I-131, a 3D image quality phantom was simulated.

8.2.3.1 Planar image quality phantom

The planar phantom consists of a warm background (diameter 25 cm), two cold lesions (diameters 31.8 mm and 25.4 mm) and four hot lesions (diameters 19.1 mm, 15.9 mm, 12.7 mm and 9.5 mm). The activity of the phantom is 119 Bq/mm^3 in the background and 835 Bq/mm^3 in the hot lesions resulting in a hot spot contrast ratio of 8:1. The activity in the cold lesions is zero. The phantom is placed parallel to the detector at 15 cm collimator distance and the simulation time is set to 160 s.

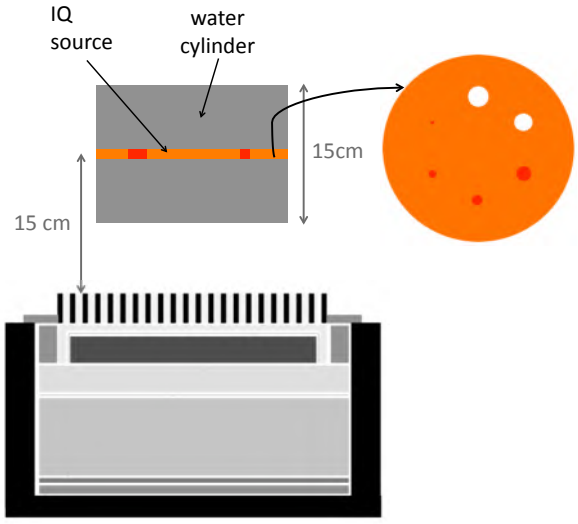

Figure 8.5: The planar image quality phantom and detector setup.

8.2.3.2 3D image quality phantom

The 3D image quality phantom (Standard Jaszczak Phantom^{TM}, figure 8.6) contains 4 hot spheres (diameters: 9.9 mm, 12.4 mm, 15.4 mm,

19.8 mm) and two cold spheres (diameters: 24.8 mm and 31.3 mm). The activity concentration is set in order to have a sphere-to-background activity ratio of 8:1 in the hot spheres. Total activity in the phantom is 37 MBq and the acquisition time is 5 minutes. The phantom is simulated to be filled with water and was centered in a three headed camera (rotation radius of 15 cm).

Figure 8.6: The Standard Jaszczak Phantom^{TM} phantom.

8.2.3.3 Figures of merit

The hot and cold spot contrast recovery were calculated by equation 5.4 while noise is calculated by equation 5.5. The CRC was plotted as a function of noise for every lesion size to compare both imaging systems. The Contrast Recovery Increase (CRI) from the RS system to the PH system is expressed as:

$$CRI(\%) = \frac{CRC_{RS} - CRC_{PH}}{CRC_{PH}} \times 100, \tag{8.1}$$

8.3 Results and discussion

8.3.1 I-123

8.3.1.1 Study of the origin of high-energy contamination

Parallel hole The PH energy spectrum of figure 8.7 (a) shows the most pronounced detection peak around 529 keV. This illustrates that the

small fraction (1.4%) of emitted photons indeed competes with the 83% of emitted 159 keV photons. This is due to the collimator, which only selects the low energy photons and leaves the high energy photons almost unaffected. The observation in figure 8.9 (a) that almost all detected high energy photons have penetrated or backscattered confirms this. From the spectrum of the main energy window (figure 8.8 (a)) it is clear that the **geometric** photons only give rise to small peak above a dominating continuous background, caused by penetration and backscatter. The **backscatter** contribution to the overall spectrum will increase with decreasing energy because most detected backscatter detections have to scatter at large angles to be detected and because of the increasing photoelectric cross section at lower energies. The backscatter spectrum peaks because the photon-energy left after scatter is a nearly continuous function of the scatter angle at large angles. The energy of the backscatter peak E_{bs} is calculated from [85]:

$$E_{bs} = \frac{E_{ref}}{1 + \frac{2E_{ref}}{m_e c^2}}, \tag{8.2}$$

with E_{ref} the incident photon energy and $m_e c^2 = 511\ keV$. For the 529 keV photons, the backscatter peak lies at 172 keV. This can also be read from the backscatter energy spectrum in figure 8.7 (a). The peak is however less pronounced because the spectrum also contains backscatter peaks from the 440 keV, 505 keV and 539 keV emissions, which respectively appear at 161 keV, 170 keV and 173 keV. Since these energies are within the main energy window of I-123, a lot of backscatter contamination will appear. This can be seen in the detailed view of the 20% energy window of figure 8.8(a). Furthermore, backscatter from the 159 keV starts to appear below 159 keV. Together with the blurring of the energy resolution, the result of these superimposed effects leads to a flat backscatter spectrum in the photopeak window.
Photons, directly detected after **penetration** are less pronounced because the high energy photons first have to undergo scatter in the crystal and then escape the crystal in order to end up as a detection in the main energy window. The penetration spectrum has a small peak at 159 keV due to the penetration of the main energy photons. **Phantom scatter** is comparable to Tc-99m imaging and **collimator scatter** is almost not present.
It can be read from figure 8.9(a) that, in the case of a LEHR PH collimator, about 60% of the detected events are due to the HE emissions. The main component of high energy contamination is backscatter, accounting

for 81 % of the HE detections. Penetration of HE photons in combination with either crystal scatter or phantom scatter (or both) accounts for 17% of the HE contamination. The remaining 2% is due to collimator scatter. Furthermore, about half of the photons emitted at 159 keV are also contamination, mainly caused by phantom scatter. Together with the HE contamination this results in only 20% of useful photons in the photopeak window.

Rotating slat For the RS collimator, the spectrum is plotted in figure 8.7(b). Here, the high energy peaks are less much pronounced due to the relative higher number of **geometric** photons from the higher collimator efficiency. The most important contributions to the photopeak energy window are from **phantom scatter** and **backscatter** from the 159 keV emission peak 8.8(b). From the spectra in figures 8.7 (b) and 8.8 (b), it can be seen that **phantom scatter** is comparable to Tc-99m imaging and **collimator scatter** is neglectable.

In figure 8.9 (b), we can read that for the RS collimator, about 48% of the detected counts in the photopeak window are geometric counts. This is mainly the merit of the higher geometrical sensitivity of the rotating slat collimator. Since the HE emissions can be treated as if there were no collimator, the relative proportion of contamination to geometric will decrease. The increased geometrical acceptance of the RS collimator leads to only 7.7% of the detected photons to result from the high energy emissions. The main cause of contamination with the RS collimator is thus from the main energy peak itself. If we only consider the 159 keV emission peak, we see that the same proportion of geometric-to-contamination holds for both collimators (about 50% geometric and about 50% contamination). This indicates that the choice of collimator will not influence the non-HE contamination.

8.3.1.2 Point spread functions

		FWHM (mm)	**FWTM** (mm)
I-123	PH	12.5	53.0
	RS	13.0	28.5

Table 8.3: FWHM and FWTM of the PSFs of I-123 on both a PH and an RS collimator.

The plots of the PSFs for the PH and RS collimator in figure 8.10 (a) and

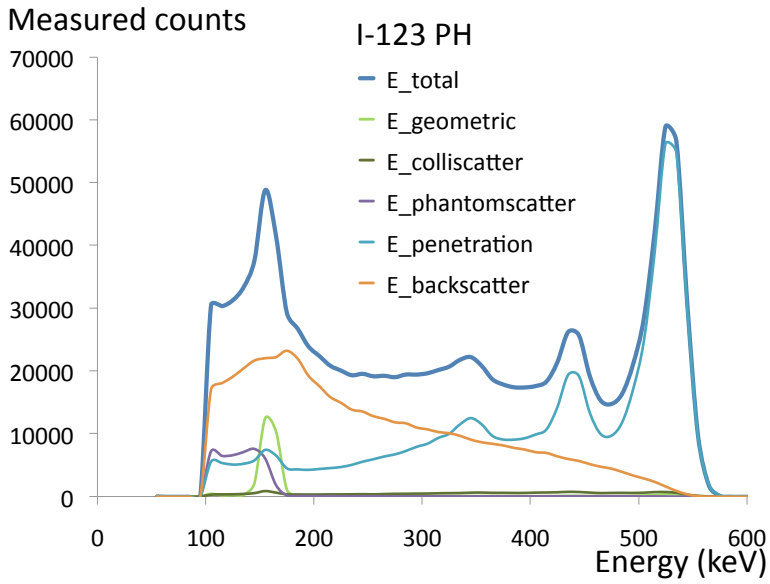

(a)

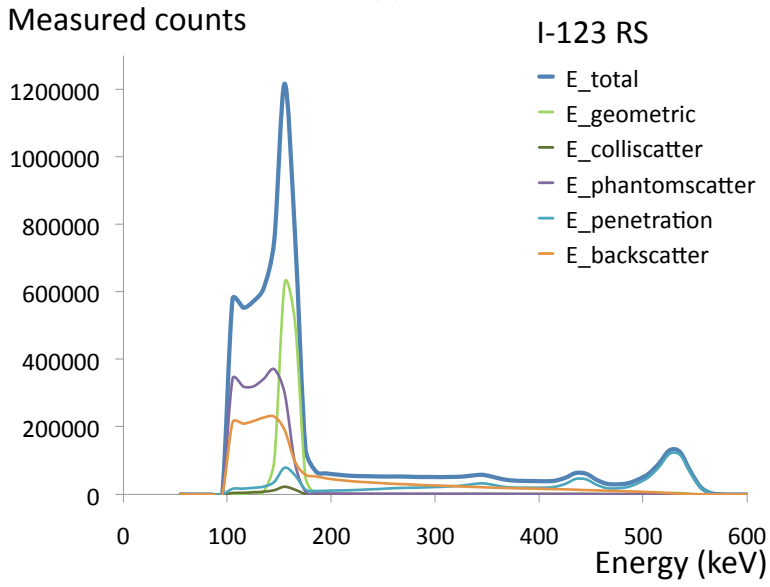

(b)

Figure 8.7: The full energy spectra of I-123 on (a) a LE-PH collimator and (b) a LE-RS collimator.

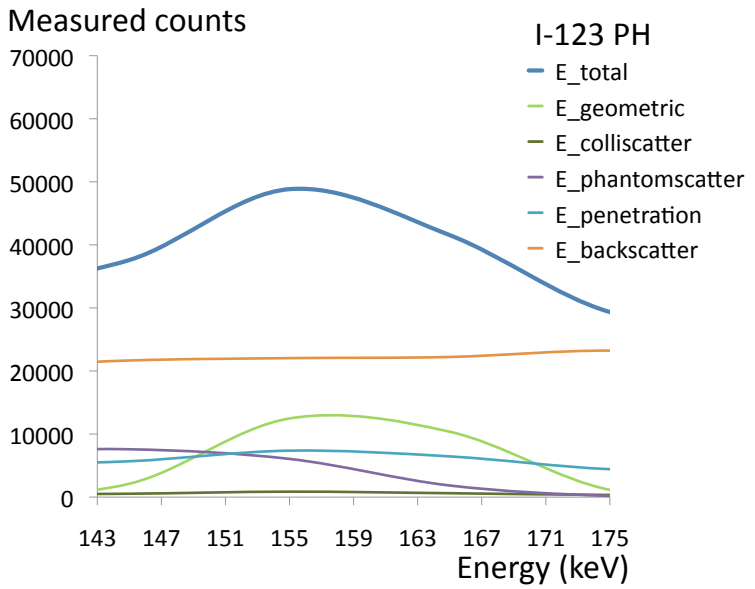

(a)

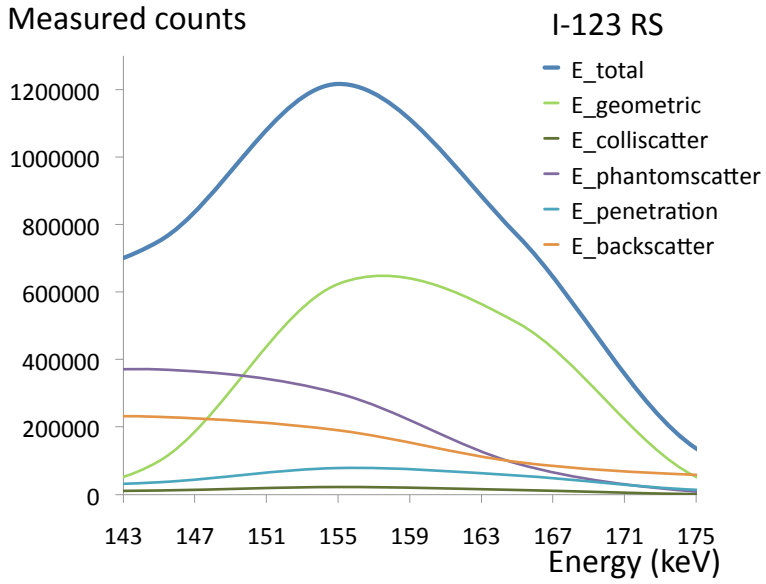

(b)

Figure 8.8: The detailed view of the energy spectra in the photopeak window on (a) a LE-PH collimator and (b) a LE-RS collimator.

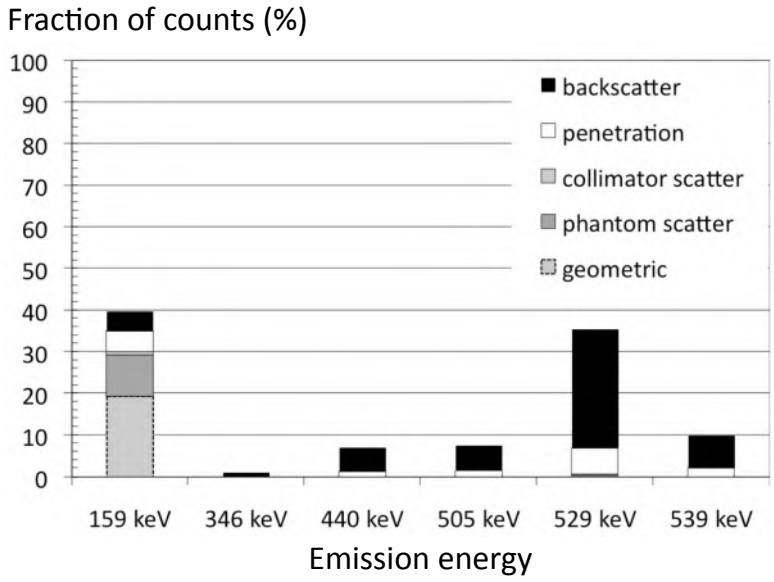

(a)

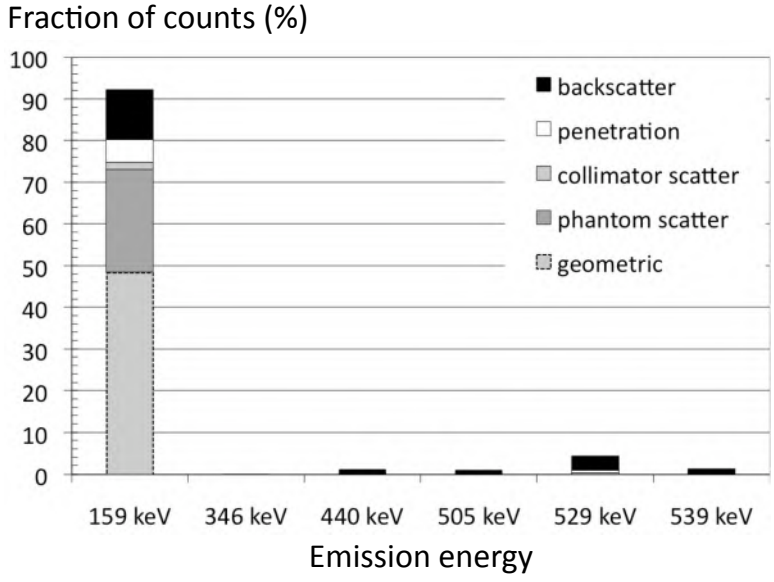

(b)

Figure 8.9: The relative contributions from the different emission energy peaks to the photopeak window of I-123 for the PH (a) and the RS (b) collimator. The probability of emission for every peak is also indicated.

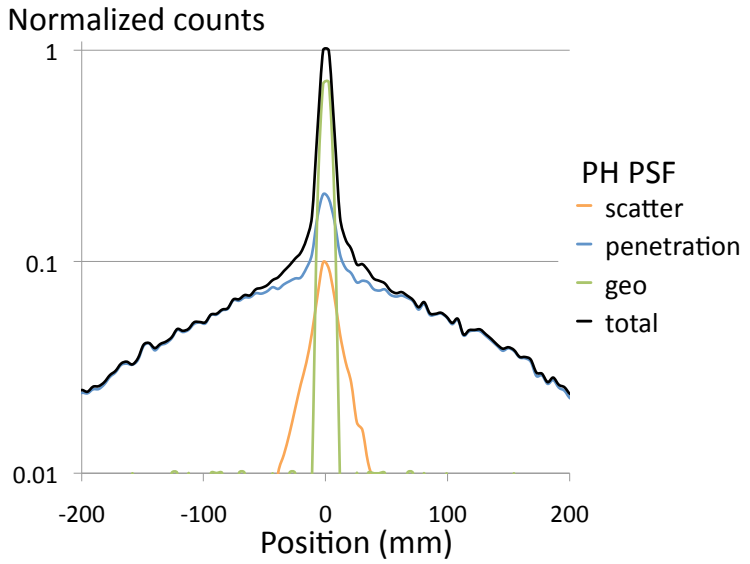

(a)

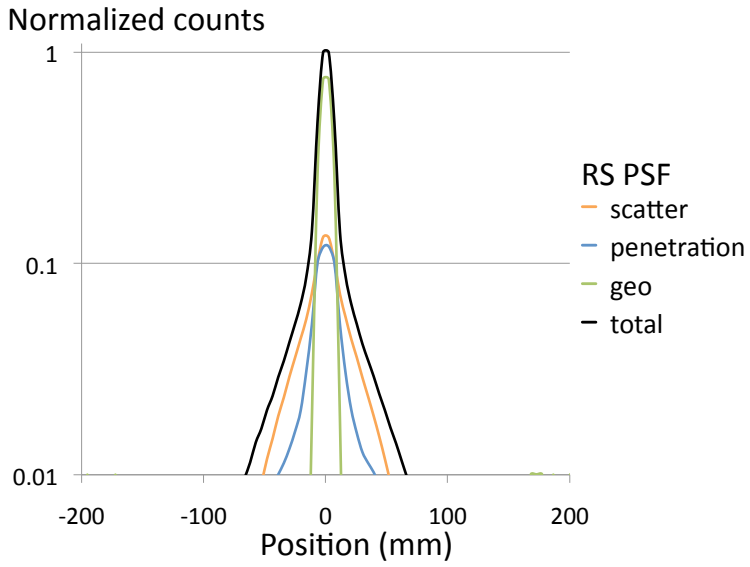

(b)

Figure 8.10: The PSF of all detected photons, geometric, penetrated and scattered photons for (a) the PH collimator and (b) the RS collimator.

(b) show that the effect of high energy contamination also reflects in the spatial response of the system. Especially the influence of the penetrated

photons which arise from HE emissions cause the PH PSF to be worse than the RS PSF. This reflects in the values for FWHM and FWTM which are summarized in table 8.3. While the FWHM is slightly higher for the RS collimator, the FWTM is only half of the PH FWTM. The HE contamination has thus mainly a negative influence on the FWTM. This effect will generate a background with low spatial information. The scatter PSF is approximately the same for both collimators, confirming that the choice of collimator does not influence the spatial distribution of the non-HE contamination.

8.3.1.3 Contrast-to-noise analysis

In figure 8.11(a), contrast-to-noise plots are shown for the average hot spot contrast recovery. Per collimator, there are two curves, one with HE photons present (HE contamination) and one without HE contamination (159 keV photons only). In the case of no contamination, the RS collimator already has a slightly better contrast-to-noise trade-off for hot spot imaging, which was also found for Tc-99m in chapter 5. It can be seen that the influence of HE photon emissions is limited for the RS collimator (both curves overlap) while for the PH collimator, a severe drop of contrast is introduced by the HE contamination. This results in a large contrast difference between both types of collimator compared to the case without HE emissions. The same holds for figure 8.11(b), with the difference that the cold spot imaging is generally not better for a RS collimator in the case of 159 keV emissions only, which is in accordance with the findings in chapter 5 for Tc-99m. With HE emissions present, a contrast drop is observed for the PH collimator. For the RS collimator, the contrast is almost not influenced. Eventually, this results in better contrast for the RS collimator, also for the cold lesions.

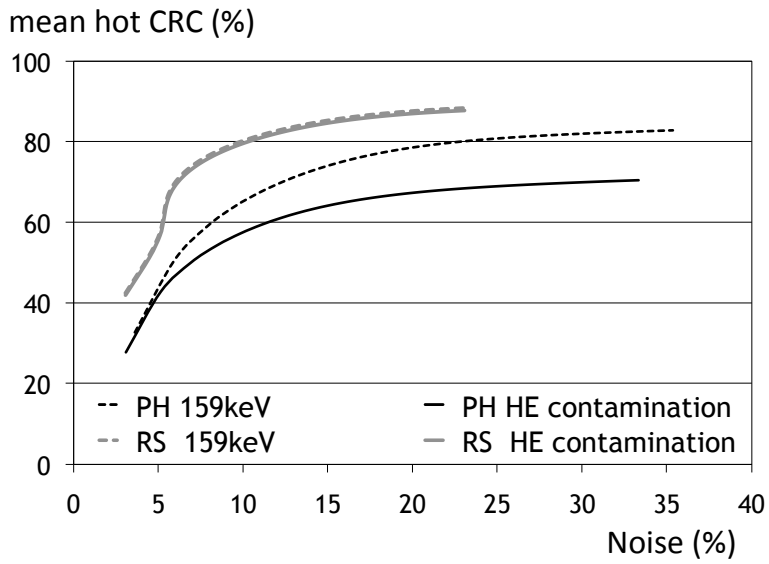

(a)

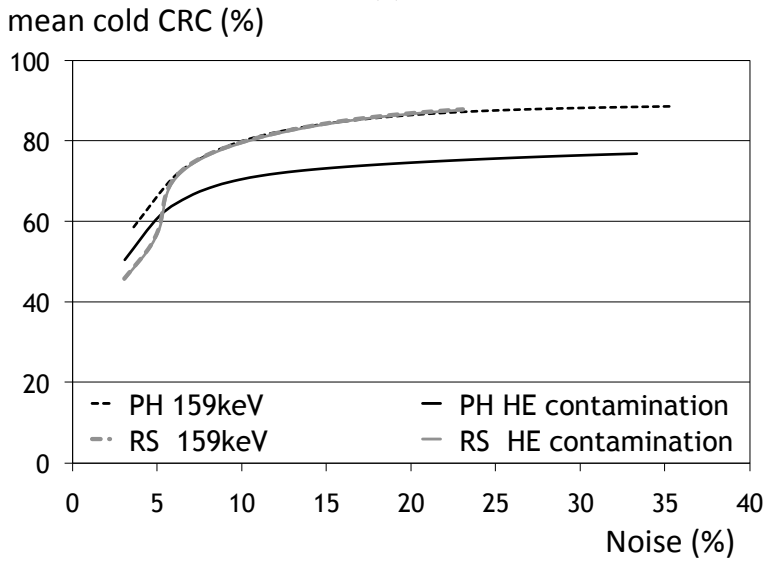

(b)

Figure 8.11: Contrast-to-noise plots for (a) average hot spot contrast and (b) average cold spot contrast for the RS and PH collimator with and without high energy contamination.

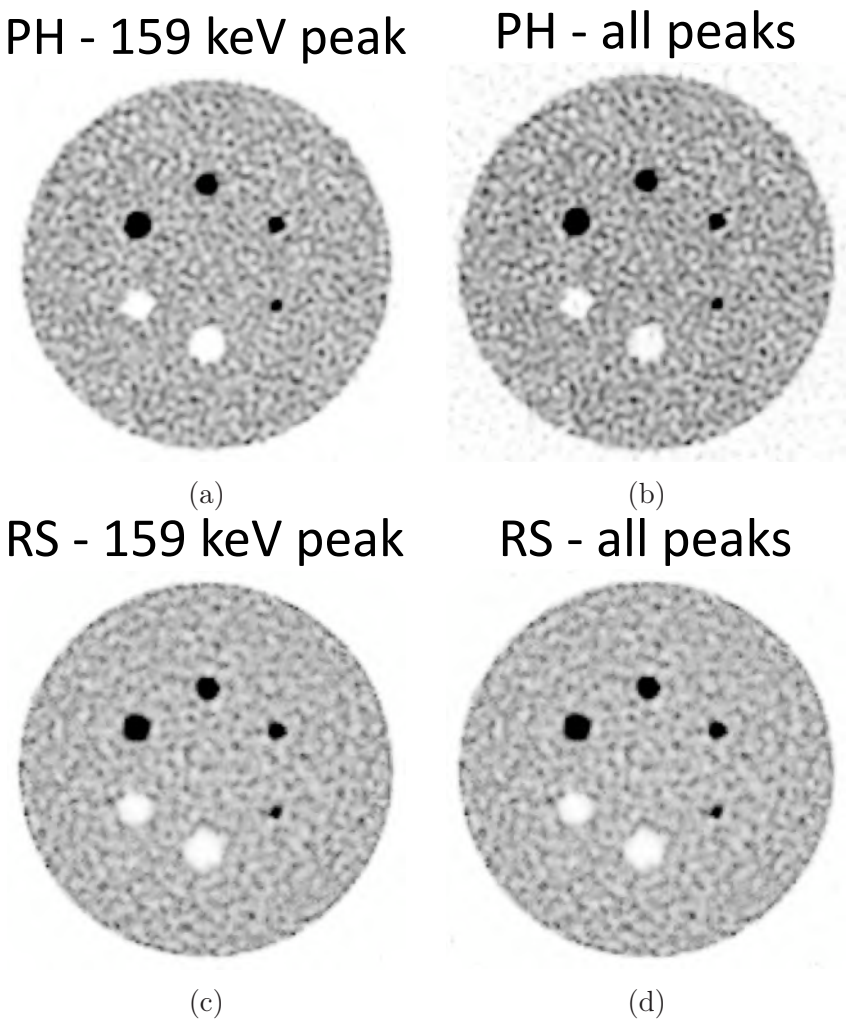

Figure 8.12: Planar images of the PH and RS acquisitions at 20% noise. In (a) and (b) the PH images without and with HE-contamination are shown while in (c) and (d), the RS collimated I-123 images are shown without and with HE-contamination.

From the plots, we derive the CRC at 20% noise. This is a relatively low noise level at which all curves almost reached their maximum contrast. The CRI, calculated at 20% noise, is summarized in table 8.4 for all lesions in the case of only 159 keV emissions and in the case of HE contamination. The difference, which indicates the additional contrast increase compared to non-HE imaging (comparable to Tc-99m imaging), is calculated as $CRI_{HE} - CRI_{159keV}$. From this table we can read that, on average, the RS CRC is 8% higher if there is no contamination. If there is HE contamination this number will increase to 25% and the CRI will always be positive, even for the cold spots. The extra contrast gain of using an RS collimator for I-123 imaging is thus 17% compared to imaging of pure emitters such as Tc-99m.

CRI	**159 keV emission**	**HE emission**	**Difference**
31.8 mm cold spot	+2%	+17%	+15%
25.4 mm cold spot	-1%	+15%	+16%
19.1 mm hot spot	+3%	+20%	+17%
15.9 mm hot spot	+20%	+40%	+20%
12.7 mm hot spot	+16%	+33%	+17%
9.5 mm hot spot	+7%	+24%	+17%
MEAN	+8%	+25%	+17%

Table 8.4: The CRI for all lesions at a noise level of 20%.

The images in figure 8.12 illustrate the better contrast at 20% noise. This shows as a lower background intensity for the RS images. The higher contrast is even more visible in the case where there is contamination present (figures 8.12 (b) and (d)).

8.3.2 I-131

8.3.2.1 Study of the origin of high-energy contamination

Parallel hole The energy spectrum of I-131 on a PH collimator (figure 8.13(a)) shows that the influence of high energy emissions is less pronounced compared to the I-123 spectrum of figure 8.7 (a) due to the thicker septa. Although there is some **backscatter** contamination, unlike the 529 keV backscatter peak of I-123, the backscatter peak of the

637 keV photons of I-131 does not show up in the main energy window. The main factor, influencing the image quality degradation will be due to **penetration** of the 364 keV photons. This can be clearly appreciated in the energy spectrum plot for the main energy window in figure 8.14(a). Besides the penetration, also **phantom scatter** and some **collimator scatter** appear in the main energy window. In the case of a HE-PH collimator (figure 8.15(a)), only about 15% of the detected events are due to the HE emissions. The main component of high energy contamination is penetration from the main energy peak itself (22%). Together with backscatter, collimator and phantom scatter of the main 364 keV photons, the contamination adds up to about 65% in the 20% photopeak energy window. This results in only 35% of geometrically accepted photons.

Rotating slat In the case of RS collimation, the situation is similar (figure 8.13(b)). However, the higher number of **geometric** photons in the main energy window (figure 8.14(b)) will cause the relative influence of the 637 keV **backscatter** to be lower. Also, photon **penetration** from the main energy peak itself will also be suppressed relatively to the higher number of geometrically accepted photons.

In figure 8.15(b), we can read that for the RS collimator, about 51% of the detected counts in the photopeak window are geometric counts. This results in less HE contamination and less penetration from the 364 keV emissions.

8.3.2.2 Point spread functions

		FWHM (mm)	**FWTM** (mm)
I-131	PH	17.0	50.5
	RS	16.3	33.5

Table 8.5: FWHM and FWTM of the PSFs of I-131 on both a PH and an RS collimator.

The plots of the PSFs for the PH and RS collimator in figure 8.16 (a) and (b) again show that the contamination affects the spatial response. The values for FWHM and FWTM are summarized in table 8.5. Both FWHM and FWTM are better for the RS collimator and again, as with I-123, the effect of reduced contamination for the RS is reflected most in the FWTM values. The larger FWHM and FWTM of the PH collimator

are mainly caused by the penetration and backscatter components in the main energy window. The scatter PSF is even more pronounced for the RS collimator.

8.3.2.3 Contrast-to-noise analysis

The contrast-to-noise plots of figure 8.17(a) and (b) respectively show the average hot and average cold contrast recovery as a function of noise. It is clear from these plots that both better hot and better cold contrast can be obtained with a RS collimator. At 25% noise, average cold contrast is 19% higher while average hot contrast is 13% higher. In chapter 7, for the Tc-99m case, we found a larger contrast increase for the cold lesions than for the hot lesions. However, a direct comparison is difficult because of the different collimator that was used in that study (LE versus HE collimator). Therefore, we supposed a perfect collimator which absorbs all photons, no matter their energy. In the case of a perfect collimator, an increased contrast for the RS collimator is found of 22% and 17% for respectively the cold and hot lesions with respect to the PH collimator. This indicates that, in the case of I-131 imaging, the RS collimator is influenced more by the penetration of photons through the collimator. This becomes clear hen looking to table 8.6. For the cold lesions, the relative contrast loss due to using a realistic collimator is 23% and 27% for the RS and PH collimator respectively. For the hot lesions these numbers respectively are 29% and 22%. For the cold lesions, the contrast loss is thus larger for the PH collimator while the opposite is true for the hot lesions. For I-131, there is thus only an additional advantage in using a RS collimator for the cold lesions.
Slices through the tomographic images are displayed in figure 8.18. The better image quality for the RS collimator can clearly be appreciated.

CRC		**perfect**	**realistic**	**relative loss**
cold	RS	48%	37%	23%
	PH	27%	19%	30%
hot	RS	26%	19%	27%
	PH	9%	7%	22%

Table 8.6: Average cold and hot lesion contrast at 25% noise and relative loss of contrast due to the realistic collimator.

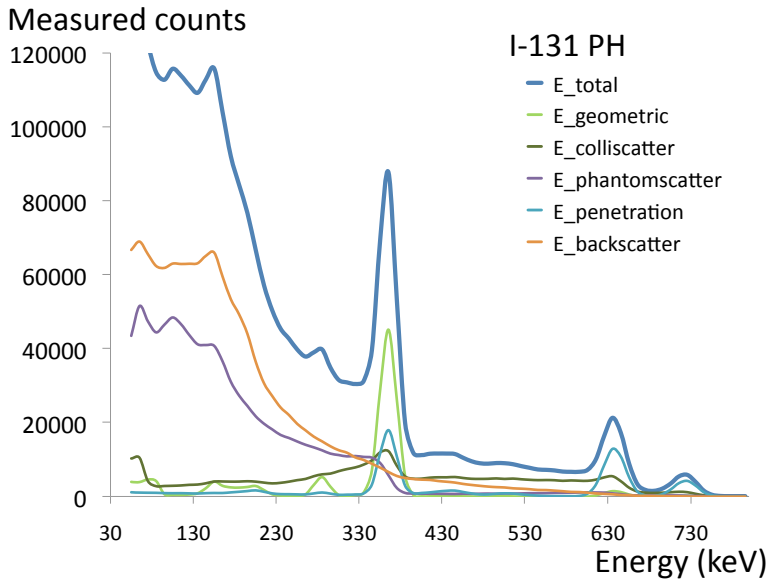

(a)

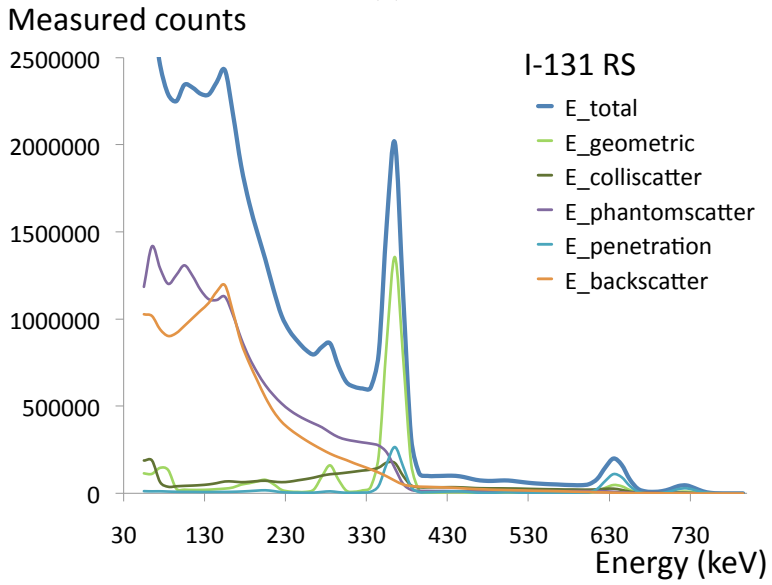

(b)

Figure 8.13: The full energy spectra of I-131 on (a) a LE-PH collimator and (b) a LE-RS collimator.

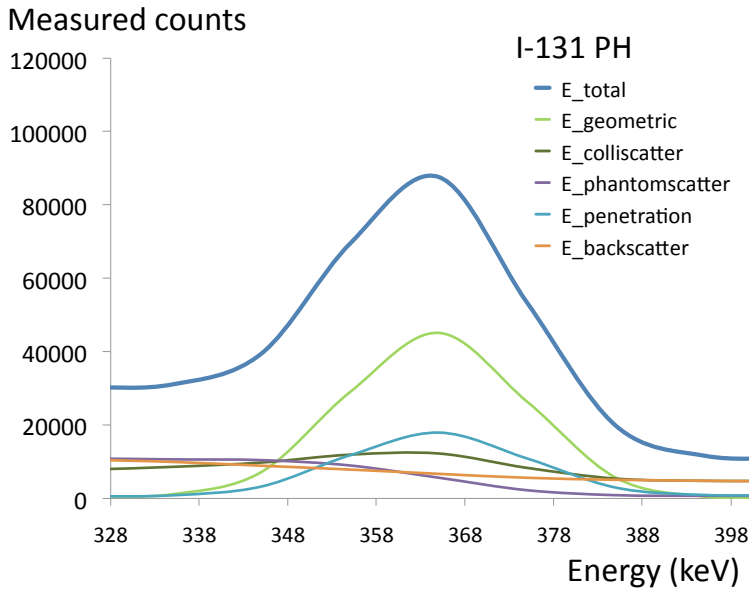

(a)

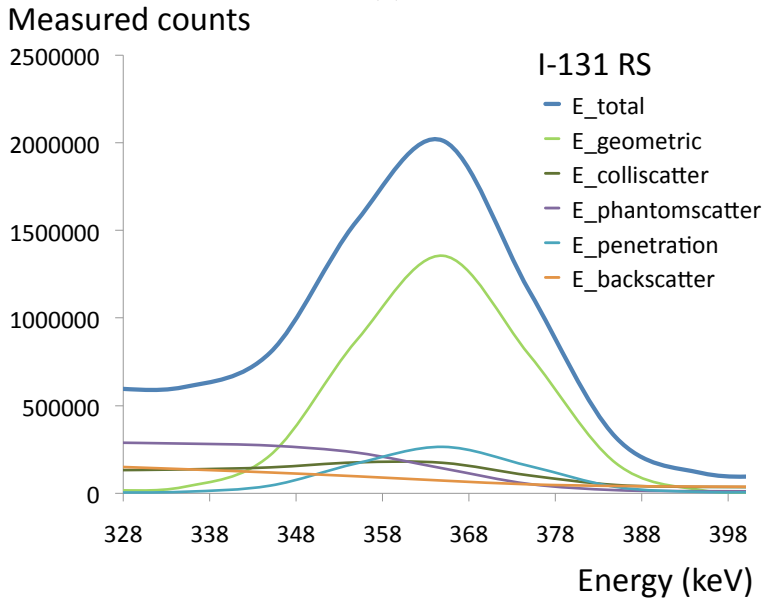

(b)

Figure 8.14: The detailed view of the energy spectra in the photopeak window on (a) a LE-PH collimator and (b) a LE-RS collimator.

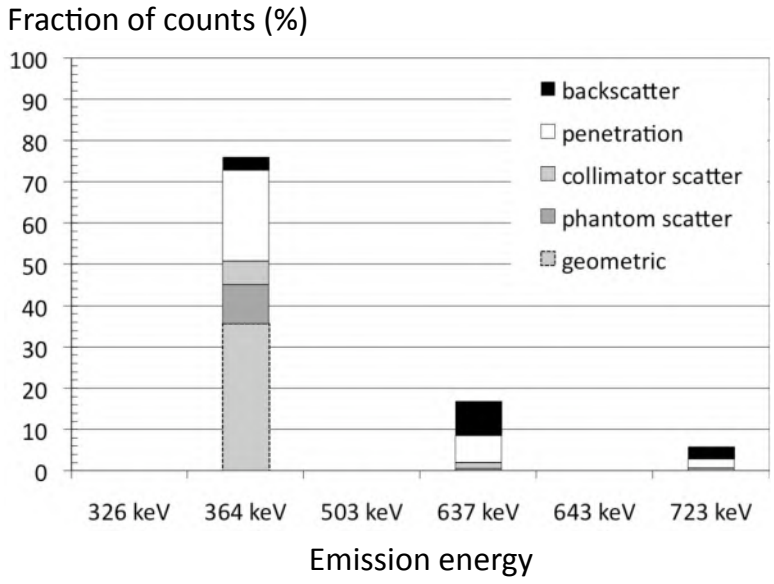

(a)

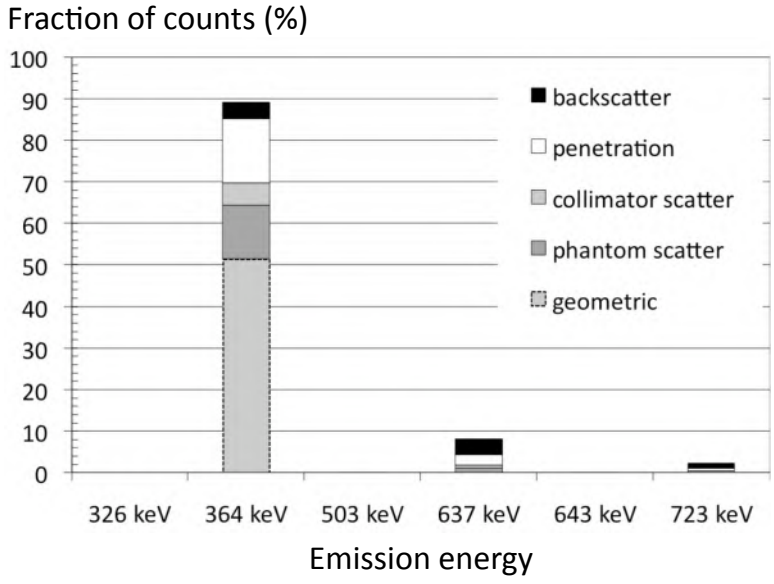

(b)

Figure 8.15: The relative contributions from the different emission energy peaks to the photopeak window for the PH (a) and the RS (b) collimator. The probability of emission for every peak is also indicated.

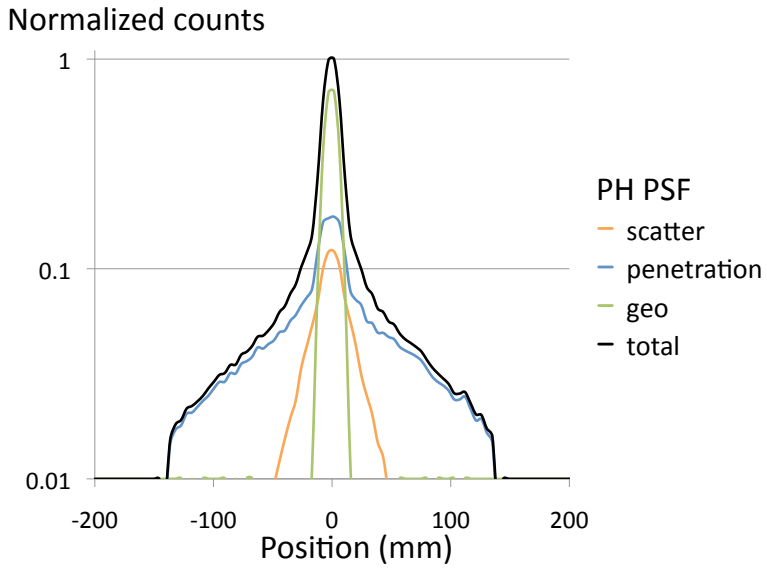

(a)

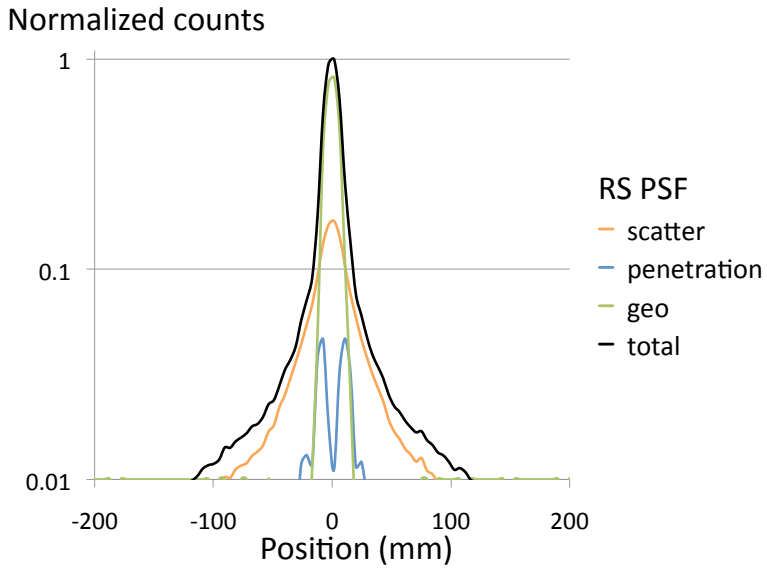

(b)

Figure 8.16: The PSF of all detected photons in the I-131 photopeak energy window. Geometric, penetrated and scattered photons for (a) the PH collimator and (b) the RS collimator.

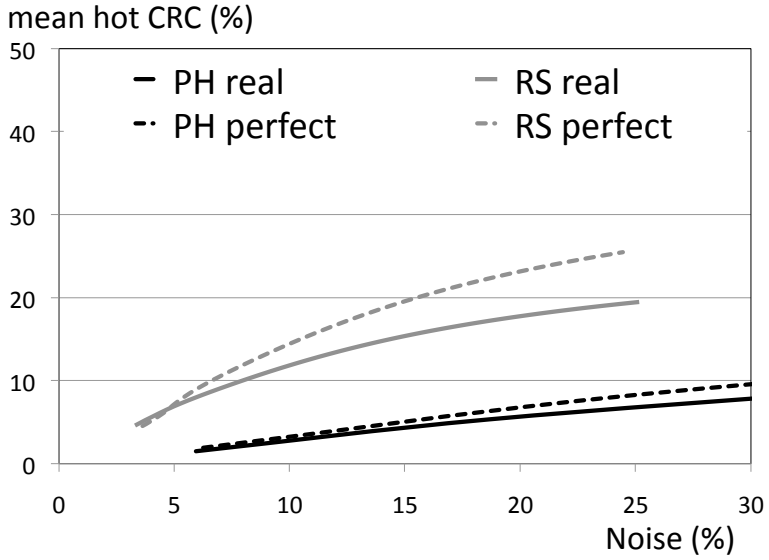

(a)

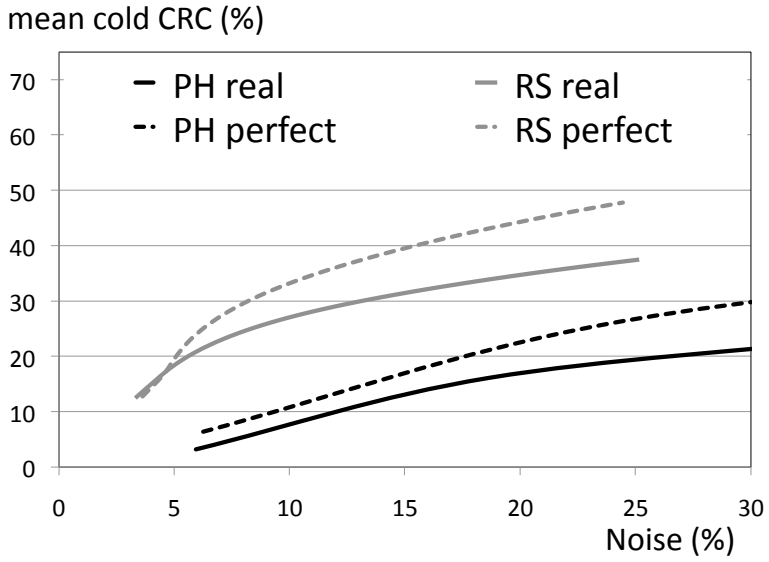

(b)

Figure 8.17: (a) Average cold contrast recovery and (b) average hot contrast recovery.

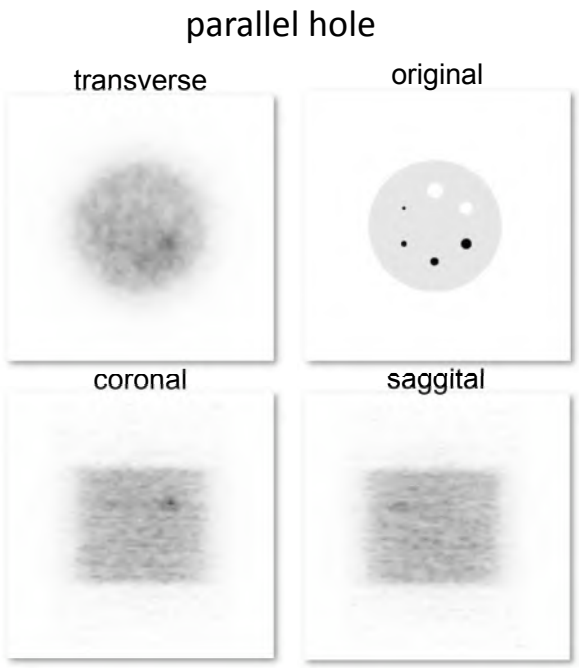

(a)

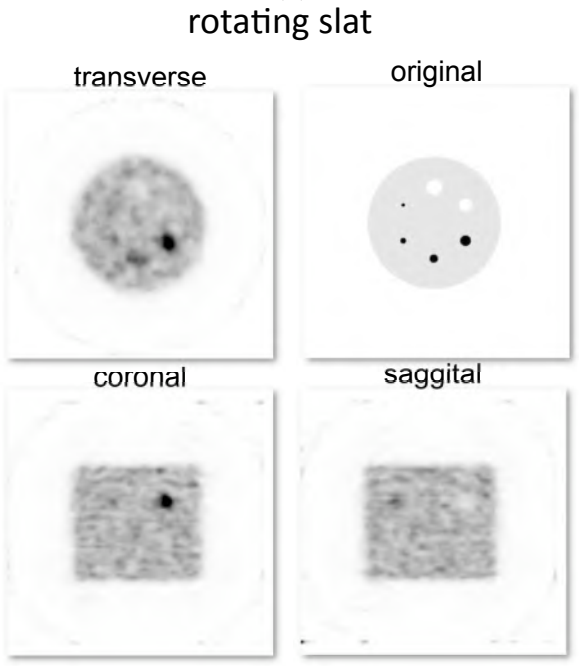

(b)

Figure 8.18: (a) Tomographic image sections for (a) the PH and (b) the RS collimated I-131 image quality acquisition.

8.4 Summary and original contributions

Due to the higher sensitivity for geometric photons of an RS collimator, the relative influence of contamination due to backscatter of HE photons and septal penetration is significantly reduced for isotopes like I-123 and I-131. This leads to improved image quality and better quantification for all isotopes which suffer from HE contamination. The problems related to previous solutions for HE contamination are tackled by the use of an RS collimator since the lower contamination is intrinsic to the design of the collimator. Instead of using a medium energy collimator which stops HE photons, we could thus still use a LEHR RS collimator for I-123 imaging, which maintains the superior spatial resolution. Scatter correction techniques can still be applied for the contamination from the 159 keV peak, but the increased noise due to the HE scatter subtraction will not be present in the case of an RS collimator. Finally, the recent solution of modeling the HE point spread function which is object dependent, becomes less relevant for the case of a RS collimator.

The contrast-to-noise study of chapter 5 which compares RS and PH collimators for Tc-99m planar imaging shows that cold spot contrast recovery is slightly better with a PH collimator if the lesions are small. When the cold lesions become larger, the difference in image quality becomes negligible. The previous study also showed that RS collimators are superior for planar hot spot imaging and that this superiority increases with increasing lesion size, increasing contrast and decreasing background size. These findings are consistent with the I-123 results in this chapter in the case of no HE contamination. The contrast-to-noise analysis of I-123 shows that with HE contamination present, even cold spot contrast of the largest lesion is better with a RS collimator. Furthermore, we see that for I-123, averaged over all lesions, a 25% higher contrast can be recovered compared to a PH collimator case if no corrections are applied. From this number, 8% was already achieved in the case of no contamination due to the better hot spot contrast recovery. The remaining 17% is due to the contrast drop in the PH case when there is emission of HE photons.

For I-131, the case is slightly different because it suffers less from the backscatter of higher energy emissions due to the thicker septa. The main component contributing to contamination arises from penetration of the main energy photons (364 keV). We found that in the case of RS collimation, the relative influence of this penetration is only less for the cold contrast imaging. The contrast of the hot spots was even more

affected in the case of a RS collimator. In chapter 7, the tomographic image quality was compared for Tc-99m. A better hot and cold contrast recovery was found for the image quality phantom. By assuming a perfectly absorbing collimator, we were able to separate the image quality improvement here in a part that can be attributed to the collimator and a part that can be attributed to the different degree of HE-contamination. We found that for cold lesions, there was an additional improvement in image quality due to the lower influence of HE-contamination.
The main conclusion of this chapter is that a RS has an additional advantage regarding image quality for isotopes with high energy emissions, especially if the contamination arises from photons with energies higher than the main emission energy. We believe that other isotopes like In-111 or Tl-201 even like Y-90 could significantly benefit from the use of RS collimation. Also Y-90, where imaging is done through bremsstrahlung measurement, has been investigated by us [159, 135]. The work presented in this chapter resulted in two conference contributions [163, 175].

Chapter 9

General Conclusions

9.1 Summary

In this chapter a summary of the main contributions of the presented work is made.

The purpose of this dissertation was to study the use of rotating slat collimators for SPECT imaging. Our approach consisted of the following steps. First, a detailed investigation of the resolution and sensitivity characteristics was performed. We applied these important system parameters in an iterative reconstruction to investigate the planar image quality compared to a traditional collimator. Before we could study the imaging performance in tomographic case, the problem of complex 3D image reconstruction was tackled. Finally, some interesting applications of the rotating slat collimator were investigated.

Chapter 2 introduces SPECT from a historical point of view. The most important technical characteristics of a gamma camera are explained and an overview of the most essential mechanical collimation techniques is presented. Special attention is paid to collimator optimization and to the choice of the appropriate type of collimation by comparing all classically available collimators. This comparison shows the classical trade-off between spatial resolution and sensitivity of all classical mechanical collimators. Unless field-of-view is sacrificed, both can not be optimized simultaneously. Photon integrating detectors which are clinically used for SPECT are reviewed. Also, some interesting novel detector concept which are still in a research phase are described. An introductory review of iterative image reconstruction techniques is given with special

attention to corrections for different image degrading effects. Finally the usefulness of Monte Carlo simulations in SPECT research, ranging from detector design to Monte Carlo based reconstruction, is discussed.

Chapter 3 studies the basic characteristics, sensitivity and spatial resolution, of a rotating slat collimator. An analytic description of the system is presented with special attention to areas close to the collimator and areas of large photon incidence angle. The error of using a simplified far field model in these areas is calculated. The analytic formulas were then applied to the Solstice prototype detector, purchased from Philips Medical Systems. Concurrently, a Monte Carlo model of this prototype was implemented and compared to the analytic predictions. By measurement of the spatial resolution and sensitivity on the prototype system, both the Monte Carlo and analytic model were validated. Excellent agreement was found between analytic calculations, Monte Carlo simulations and measurements on the system. The presence of an accurate system description is not only important for comparison with other mechanical collimators, it also allows for modeling of the system response in an iterative reconstruction. A phantom measurement with the prototype detector, showing an improved image quality when modeling the system response in the reconstruction, pointed out the need for an available system description.

Chapter 4 proposes and validates a method for the removal of partial field-of-view activity. This source of artifacts is not encountered in parallel hole collimated SPECT. This problem was already reported more than 10 years ago. Here, we propose a method based on the frequency-distance relation to remove the influence of partial field-of-view activity. The method was implemented and verified using measurements on the prototype. In the worst case, we found an improvement of error in the image from 119% to 17%. An interesting future investigation would be to study the 3D Fourier transform of plane integral data to filter out activity in tomographic acquisitions. Furthermore, one could also think of filtering hindering activity within the direct FOV. For instance, when imaging the heart centrally in the FOV, hindering liver activity could be removed with this technique.

In chapter 5, the Monte Carlo model validated in chapter 3, was extrapolated to a detector with the size of a typical gamma camera for the purpose of image quality comparison to a traditional parallel hole collimator. The spatial resolution of the rotating slat and the parallel hole collimator were matched as were the dimensions and materials of the de-

tector and collimator. This was done for the purpose of fair comparison between these two types of collimation. Once the Monte Carlo models were built, image restoration techniques which model the imaging process, were implemented for both collimators. A comparison of the planar image quality that can be obtained with both collimators was performed with the contrast-to-noise ratio as a figure of merit. Since the rotating slat system sensitivity was found to be dependent on the position of the source in the field-of-view of the camera, image quality was investigated with object size, lesion size and contrast as parameters. Point-response functions, indicating the behavior of the system in the case of a local perturbation were also studied. It was found that a rotating slat collimator always performs better than a parallel hole collimator in the case of imaging hot lesions. The improvement in signal-to-noise is more apparent when the lesion size grows, their contrast is higher or when the surrounding sources of activity become smaller. For cold lesions, only a small decreased contrast-to-noise was found. The point-response functions show a larger dependence of the rotating slat collimator resolution on the imaging circumstances. Where the resolution of a parallel hole collimator is almost independent of the surrounding activity, a rotating slat collimator's resolution decreases with increasing object size. A clinically realistic acquisition of a bone scan, which is one of the most frequent planar scans performed on a gamma camera, was simulated and showed an improved lesion visibility when acquiring images with a rotating slat collimator.

Before investigating the tomographic image quality, the problem of computationally intensive and slowly converging three dimensional reconstruction was solved in chapter 6. Reconstructing plane integral data resulting from a rotating slat collimated SPECT acquisition with an iterative reconstruction that fully models the image acquisition physics suffers both from computational complexity and slow convergence. However, it is most accurate and thus serves as a gold standard. One way to speed up reconstruction of rotating slat collimated data is to split the system matrix in a part that models the step to go from image to sinogram and a part that models the step to go from sinogram to plane integral data. This split-matrix approach solves the problem of computational complexity but still suffers from slow convergence. A variation on this split-matrix MLEM image reconstruction algorithm, which uses two update steps per iteration instead of one, is described and investigated. It was found that our newly developed method maintains the computational simplicity of a regular split-matrix reconstruction and speeds

up reconstruction. Furthermore, it maintains image quality. For the MLEM implementation, a speedup of 38 and 426 was found compared to respectively the split matrix approach and the gold standard direct MLEM method. Also, OSEM variants of the reconstruction algorithms were investigated where a speedup of respectively 18 and 2 was found. The newly developed algorithm thus enables us to reconstruct a rotating slat collimated SPECT acquisition within half an hour where we previously would have needed 9 hours for a fully 3D OSEM reconstruction or about 8 hours when using a split matrix OSEM approach. This indicates the importance of speeding up convergence.

Chapter 7 investigated the tomographic image quality of a rotating slat collimator compared to a parallel hole collimator. First, it was investigated whether classical compensation techniques for scatter and attenuation, as described in chapter 2, could also be implemented for a rotating slat collimator. This has lead to the implementation of an approximate attenuation compensation method for a plane integral reconstruction. Once the attenuation compensation method was validated by means of Monte Carlo simulations, a contrast-to-noise study showed a 3 to 4 times better image quality for cold spot imaging and a 2 to 3 times better image quality for hot lesion imaging compared to a parallel hole collimator. Also visually, the improved image quality can be appreciated. Nevertheless, in the clinical setting of heart defect imaging, the improvement in cold contrast, expected from the image quality comparison, was not found. This is due to the surrounding activity and due to the larger scanning radius. An interesting future direction of research would be to investigate if one could cancel-out the influence of surrounding activity by using the technique proposed in chapter 4 or by using the 'local tomography principle', proposed by Zeng.

In chapter 8, two special isotopes which are frequently encountered in nuclear medicine were investigated on a rotating slat collimated system. These isotopes, I-123 and I-131 differ from Tc-99m in the sense that they are not emitting photons at one low emission energy. Where I-123 suffers from high energy emissions which contaminate the main energy window around 159 keV, I-131 suffers from contamination of the main emission peak at 364 keV. Due to the higher sensitivity for geometric photons of an RS collimator, the relative influence of contamination due to backscatter of HE photons and septal penetration is significantly reduced. The contrast-to-noise analysis for planar imaging of I-123 shows that with HE contamination present, even cold spot contrast is better with a RS collimator. On average, a 25% higher contrast can be recov-

ered compared to a PH collimator case if no corrections are applied. The main portion of this improvement (17%) is due to the contrast drop in the PH case when there is emission of HE photons. For I-131, the case is slightly different because it suffers less from the backscatter of higher energy emissions. The main component contributing to contamination arises from penetration of the main energy photons (364 keV). We found that only for cold lesions, there was an additional improvement in image quality due to the lower influence of HE-contamination.

9.2 Final conclusion

A final conclusion of this work is that it is advantageous to use a rotating slat collimator in combination with iterative reconstruction including a system model in the cases of (i) planar hot lesion imaging, even in large objects and low contrast; (ii) In the cases of tomographic hot and cold lesion imaging, when there is limited activity in the neighborhood of the area of interest; (iii) for isotopes with high energy emissions, especially if there is a lot of contamination arising from these high energy emissions.

References

[1] R Accorsi, *High-efficiency, high-resolution SPECT techniques for cardiac imaging*, Proceedings of Science (2006).

[2] R. Accorsi and S. D. Metzler, *Non-diverging analytic expression for the on-axis sensitivity of converging collimators: analytic derivation*, Physics in Medicine and Biology **51** (2006), no. 21, 5675–5696.

[3] ———, *Non-diverging analytic expression for the on-axis sensitivity of converging collimators: experimental verification*, Physics in Medicine and Biology **51** (2006), no. 21, 5697–5705.

[4] R. Accorsi, J. R. Novak, A. S. Ayan, and S. D. Metzler, *Derivation and validation of a sensitivity formula for slit-slat collimation*, IEEE Transactions on Medical Imaging **27** (2008), no. 5, 709–722.

[5] S. Agostinelli *et al.*, *GEANT4 - a simulation toolkit*, Nuclear Instruments and Methods A **506** (2003), 250–303.

[6] H. O. Anger, *A new instrument for mapping gamma-ray emitters*, Biology and medicine quarterly report UCRL, University of California Radiation Laboratory, Berkeley, 1957.

[7] H. O. Anger, *Scintillation camera*, Review of Scientific Instruments **29** (1958), 27–33.

[8] H. O. Anger, *Scintillation camera with multichannel collimators*, Journal of Nuclear Medicine **5** (1964), 515–531.

[9] H. O. Anger and D.H. Davis, *Gamma-ray detection efficiency and image resolution in sodium iodide*, Review of Scientific Instruments **35** (1964), 693–697.

[10] H. O. Anger, M. R. Powell, D. C. van Dyke, L. R. Schaer, R. Fawwaz, and Y. Yano, *Recent applications of the scintillation camera*, Strahlentherapie **65** (1967), 70–93.

[11] K. E. Applegate, L. P. Connolly, R. T. Davis, D. Zurakowski, and S. T. Treves, *A prospective comparison of high-resolution planar, pinhole, and triple-detector SPECT for the detection of renal cortical defects*, Clinical Nuclear Medicine **22** (1997), no. 10, 673–678.

[12] B. Axelsson, P. Msaki, and A. Israelsson, *Subtraction of compton-scattered photons in single-photon emission computerized tomography*, Journal of Nuclear Medicine **25** (1984), no. 4, 490–494.

[13] Y. W. Bahk, S. H. Kim, S. K. Chung, and J. H. Kim, *Dual-head pinhole bone scintigraphy*, Journal of Nuclear Medicine **39** (1998), no. 8, 1444–1448.

[14] F. Beekman and F. van der Have, *The pinhole: gateway to ultra-high-resolution three-dimensional radionuclide imaging*, European Journal of Nuclear Medicine **34** (2007), no. 2, 151–161.

[15] F. J. Beekman, H. W. A. M. de Jong, and S. van Geloven, *Efficient fully 3-D iterative SPECT reconstruction with Monte Carlo-based scatter compensation*, IEEE Transactions on Medical Imaging **21** (2002), no. 8, 867–877.

[16] F.J. Beekman, E.G.J. Eijkman, M.A. Viergever, G.F. Borm, and E.T.P. Slijpen, *Object shape dependent PSF model for SPECT imaging*, IEEE Transactions on Nuclear Science **40** (1993), no. 1, 31–39.

[17] F.J. Beekman, F. van der Have, B. Vastenhouw, A.J.A. van der Linden, P.P. van Rijk, J.P.H Burbach, and M.P. Smidt, *U-SPECT-I: A novel system for submillimeter-resolution tomography with radiolabeled molecules in mice*, Journal of Nuclear Medicine **46** (2005), no. 7, 1194–1200.

[18] J. De Beenhouwer, S. Staelens, S. Vandenberghe, and I. Lemahieu, *Acceleration of GATE SPECT simulations*, Medical Physics **35** (2008), no. 4, 1476–1485.

[19] W. H. Blahd, *Ben cassen and the development of the rectilinear scanner.*, Semin Nucl Med **26** (1996), no. 3, 165–170.

[20] J. E. Bowsher and C. E. Floyd, *Treatment of compton scattering in maximum-likelihood, expectation-maximization reconstructions of SPECT images*, Journal of Nuclear Medicine **32** (1991), no. 6, 1285–1291.

[21] J.E. Bowsher, J.R. Roper, J. Peter, and R.J. Jaszczak, *Pinhole trajectories for SPECT imaging of the breast, axilla, and upper chest*, IEEE Nuclear Science Symposium Conference Record, vol. 4, 2006, pp. 2387–2389.

[22] J.G. Brankov, Y. Yang, and M.N. Wernick, *Tomographic image reconstruction based on a content-adaptive mesh model*, IEEE Transactions on Medical Imaging **23** (2004), no. 2, 202–212.

[23] W. Brenner, K. H. Bohuslavizki, N. Sieweke, S. Tinnemeyer, M. Clausen, and E. Henze, *Quantification of diphosphonate uptake based on conventional bone scanning*, European Journal of Nuclear Medicine **24** (1997), no. 10, 1284–1290.

[24] J. Browne and A. B. de Pierro, *A row-action alternative to the EM algorithm for maximizing likelihood in emission tomography*, IEEE Transactions on Medical Imaging **15** (1996), no. 5, 687–699.

[25] M. H. Buonocore, W. R. Brody, and A. Macovski, *A natural pixel decomposition for two-dimensional image reconstruction.*, IEEE Trans Biomed Eng **28** (1981), no. 2, 69–78.

[26] C.L. Byrne, *Accelerating the EMML algorithm and related iterative algorithms by rescaled block-iterative methods*, IEEE Transactions on Image Processing **7** (1998), no. 1, 100–109.

[27] Z. Cao, G. Bal, R. Accorsi, and P.D. Acton, *Optimal number of pinholes in multi-pinhole SPECT for mouse brain imaging - a simulation study*, Physics in Medicine and Biology **50** (2005), no. 19, 4609–4624.

[28] B. Cassen, L. Curtis, and C.W. Reed, *A sensitive directional gamma-ray detector*, Nucleonics **6** (1950), 78–80.

[29] _____, *Instrumentation for I-131 use in medical studies*, Nucleonics **9** (951), 46–50.

[30] L. Chang, *A method for attenuation correction in radionuclide computed tomography*, IEEE Transactions on Nuclear Science **25** (1978), no. 1, 638–643.

[31] W. Chang, H. Liang, and J. Liu, *Design concepts and potential performance of MarC-SPECT - A high-performance cardiac SPECT system*, Journal of Nuclear Medicine **47** (2006), 190– 191P.

[32] S.R. Cherry, J.A. Sorenson, and M.E. Phelps, *Physics in nuclear medicine*, Philadelphia, PA: Saunders, 2003.

[33] N. H. Clinthorne, W. L. Rogers, L. Shao, and K. F. Koral, *A hybrid of maximum likelihood position computer for scintillation cameras*, IEEE Transactions on Nuclear Science **34** (1997), 97–101.

[34] A. Cot, E. Jane, J. Sempau, C. Falcon, S. Bullich, J. Pavia, F. Calvino, and D. Ros, *Modeling of high-energy contamination in SPECT using Monte Carlo simulations*, IEEE Transactions on Nuclear Science **53** (2006), no. 14, 3125–3136.

[35] A. Cot, J. Sempau, D. Pareto, S. Bullich, J. PavŠa, F. Calvino, and D. Ros, *Study of the point spread function (PSF) for 123I SPECT imaging using Monte Carlo simulation*, Physics in Medicine and Biology **49** (2004), no. 14, 3125–3136.

[36] J. De Beenhouwer, S. Staelens, S. Vandenberghe, J. Verhaeghe, R. Van Holen, E. Rault, and I. Lemahieu, *Physics process level discrimination of detections for GATE: assessment of contamination in SPECT and spurious activity in PET*, Medical Physics **506** (2009), 1053–1060.

[37] H.W.A.M. de Jong, E.T.P. Slijpen, and F.J. Beekman, *Acceleration of Monte Carlo SPECT simulation using convolution-based forced detection*, IEEE Transactions on Nuclear Science **48** (2001), no. 1, 58–64.

[38] G.A. de Vree, A.H. Westra, I. Moody, F. van der Have, K.M. Ligtvoet, and F.J. Beekman, *Photon-counting gamma camera based on an electron-multiplying CCD*, IEEE Transactions on Nuclear Science **52** (2005), no. 3, 580–588.

[39] P. Despres, T. Funk, K.S. Shah, and B.H. Hasegawa, *Monte Carlo simulations of compact gamma cameras based on avalanche photodiodes*, Physics in Medicine and Biology **52** (2007), no. 11, 3057–3074.

[40] Y.K. Dewaraja, M. Ljungberg, and J.A. Fessler, *3-d monte carlo-based scatter compensation in quantitative I-131 SPECT reconstruction*, IEEE Transactions on Nuclear Science **53** (2006), no. 1, 181–188.

[41] Y.K. Dewaraja, M. Ljungberg, and K.F. Koral, *Accuracy of I-131 tumor quantification in radioimmunotherapy using SPECT imaging with an ultra-high-energy collimator: Monte Carlo study*, Journal of Nuclear Medicine **41** (2000), no. 10, 1760–1767.

[42] _____, *Characterization of scatter and penetration using Monte Carlo simulation in I-131 imaging*, Journal of Nuclear Medicine **41** (2000), no. 1, 123–130.

[43] F.P. Difilippo, *Design and performance of a multi-pinhole collimation device for small animal imaging with clinical SPECT and SPECT-CT scanners*, Physics in Medicine and Biology **53** (2008), no. 15, 4185–4201.

[44] A.A. Dobbeleir, A.S. Hambÿe, and P.R. Franken, *Influence of high-energy photons on the spectrum of iodine-123 with low- and medium-energy collimators: consequences for imaging with I-123-labelled compounds in clinical practice*, European Journal of Nuclear Medicine **26** (1999), no. 6, 655–658.

[45] Y. Du, B.M.W. Tsui, and E.C. Frey, *Model-based compensation for quantitative 123I brain SPECT imaging*, Physics in Medicine and Biology **51** (2006), no. 5, 1269–1282.

[46] E. Durand, P. Chaumet-Riffaud, and A. Prigent, *Is it possible to predict renal function in small animals using a multi-pinhole SPECT system?*, European Journal of Nuclear Medicine **34** (2007), no. 4, 606.

[47] P.R. Edholm, R.M. Lewitt, and B. Lindholm, *Novel properties of the fourier decomposition of the sinogram*, Proceedings of the SPIE Medical Imaging conference **671** (1986), 8–18.

[48] G. Entine, R. Luthmann, W. Mauderli, L.T. Fitzgerald, C.M. Williams, and C.H. Tosswill, *Cadmium Telluride gamma camera*, IEEE Transactions on Nuclear Science **26** (1979), no. 1, 552–558.

[49] J.A. Fessler, *Penalized weighted least-squares image reconstruction for positron emission tomography*, IEEE Transactions on Medical Imaging **13** (1994), no. 2, 290–300.

[50] J.A. Fessler, E.P. Ficaro, N.H. Clinthorne, and K. Lange, *Grouped-coordinate ascent algorithms for penalized-likelihood transmission image reconstruction*, IEEE Transactions on Medical Imaging **16** (1997), no. 2, 166–175.

[51] C.E. Floyd, R.J. Jaszczak, and R.E. Coleman, *Inverse Monte Carlo: A unified reconstruction algorithm for SPECT*, IEEE Transactions on Nuclear Science **32** (1985), no. 1, 779–785.

[52] E.C. Frey and B.M.W. Tsui, *A practical method for incorporating scatter in a projector-backprojector for accurate scatter compensation in SPECT*, IEEE Transactions on Nuclear Science **40** (1993), no. 4, 1107–1116.

[53] T. Funk, D.L. Kirch, J.E. Koss, E. Botvinick, and B.H. Hasegawa, *A novel approach to multipinhole SPECT for myocardial perfusion imaging*, Journal of Nuclear Medicine **47** (2006), no. 4, 595–602.

[54] D. Gagnon, G. Zeng, M. Links, J. Griesmer, and F.C. Valentino, *Design considerations for a new solid state gammacamera: SOLSTICE*, Nuclear Science Symposium Conference Record, vol. 2, 2001, pp. 1156–1160.

[55] F. De Geeter, P.R. Franken, M. Defrise, H. Andries, E. Saelens, and A. Bossuyt, *Optimal collimator choice for sequential iodine-123 and technetium-99m imaging*, European Journal of Nuclear Medicine **23** (1996), no. 7, 768–774.

[56] P. Gilbert, *Iterative methods for the three-dimensional reconstruction of an object from projections*, Journal of Theoretical Biology **36** (1972), no. 1, 105–117.

[57] S.J. Glick, B.C. Penney, M.A. King, and C.L. Byrne, *Noniterative compensation for the distance-dependent detector response and photon attenuation in SPECT imaging*, IEEE Transactions on Medical Imaging **13** (1994), no. 2, 363–374.

[58] M. Goitein, *Three-dimensional density reconstruction from a series of two-dimensional projections*, Nuclear Instruments and Methods A **3** (1972), 509–518.

[59] R. Gordon, R. Bender, and G.T. Herman, *Algebraic reconstruction techniques (ART) for three-dimensional electron microscopy and x-ray photography*, Journal of Theoretical Biology **29** (1970), no. 3, 471–481.

[60] R.M. Gray and A. Macovski, *Maximum a posteriori estimation of position in scintillation cameras*, IEEE Transactions on Nuclear Science **NS-23** (1976), 849–852.

[61] A.J. Green, S.E. Dewhurst, R.H. Begent, K.D. Bagshawe, and S.J. Riggs, *Accurate quantification of 131I distribution by gamma camera imaging*, European Journal of Nuclear Medicine **16** (1990), no. 4-6, 361–365.

[62] P. J. Green, *Bayesian reconstructions from emission tomography data using a modified EM algorithm.*, IEEE Transactions on Medical Imaging **9** (1990), no. 1, 84–93.

[63] J. Griesmer, B. Kline, J. Grosholz, K. Parnham, and D. Gagnon, *Performance evaluation of a new CZT detector for nuclear medicine: SOLSTICE*, Nuclear Science Symposium Conference Record, vol. 2, 2001, pp. 1050–1054.

[64] G.T. Gullberg, G.L. Zeng, F.L. Datz, P.E. Christian, C.H. Tung, and H.T. Morgan, *Review of convergent beam tomography in single photon emission computed tomography*, Physics in Medicine and Biology **37** (1992), no. 3, 507–534.

[65] W.D. Hage, A.J. Aboulafia, and D.M. Aboulafia, *Incidence, location, and diagnostic evaluation of metastatic bone disease*, Orthopedic Clinics of North America **31** (2000), no. 4, 515–28.

[66] W.G. Hawkins, P.K. Leichner, and N.C. Yang, *The circular harmonic transform for SPECT reconstruction and boundary conditions on the fourier transform of the sinogram*, IEEE Transactions on Medical Imaging **7** (1988), no. 2, 135–138.

[67] G. T. Herman, A. Lent, and S. W. Rowland, *ART: mathematics and applications. A report on the mathematical foundations and on the applicability to real data of the algebraic reconstruction techniques*, Journal of Theoretical Biology **42** (1973), no. 1, 1–32.

[68] R.H. Huesman, *The effects of a finite number of projection angles and finite lateral sampling of projections on the propagation*

of statistical errors in transverse section reconstruction, Physics in Medicine and Biology **22** (1977), no. 3, 511–521.

[69] Y. Inoue, I. Shirouzu, T. Machida, Y. Yoshizawa, F. Akita, M. Minami, and K. Ohtomo, *Collimator choice in cardiac SPECT with I-123-labeled tracers*, Journal of Nuclear Cardiology **11** (2004), no. 4, 433–439.

[70] R.J. Jaszczak, C.E. Floyd, S.H. Manglos, K.L. Greer, and R.E. Coleman, *Cone beam collimation for single photon emission computed tomography: analysis, simulation, and image reconstruction using filtered backprojection*, Medical Physics **13** (1986), no. 4, 484–489.

[71] R.J. Jaszczak, D.R. Gilland, J.W. McConnick, C. Scarfone, and R.E. Coleman, *The effect of truncation reduction in fan beam transmission for attenuation correction of cardiac SPECT*, IEEE Transactions on Nuclear Science **43** (1996), no. 4, 2255–2262.

[72] J. Joung, R. S. Miyaoka, S. Kohlmyer, and T. K. Lewellen, *Implementation of ML based positioning algorithms for scintillation cameras*, IEEE Transactions on Nuclear Science **47** (2000), 1104–1111.

[73] M.S. Judenhofer, H.F. Wehrl, D.F. Newport, C. Catana, S.B. Siegel, M. Becker, A. Thielscher, M. Kneilling, M.P. Lichy, M. Eichner, K. Klingel, G. Reischl, S. Widmaier, M. RŽcken, R.E. Nutt, H. Machulla, K. Uludag, S.R. Cherry, C.D. Claussen, and B.J. Pichler, *Simultaneous PET-MRI: a new approach for functional and morphological imaging*, Nature Medicine **14** (2008), no. 4, 459–465.

[74] D.J. Kadrmas, E.C. Frey, and B.M.W. Tsui, *Application of reconstruction-based scatter compensation to thallium-201 SPECT: implementations for reduced reconstructed image noise.*, IEEE Transactions on Medical Imaging **17** (1998), no. 3, 325–333.

[75] ———, *Simultaneous technetium-99m/thallium-201 SPECT imaging with model-based compensation for cross-contaminating effects*, Physics in Medicine and Biology **44** (1999), no. 7, 1843–1860.

[76] C. Kamphuis, F.J. Beekman, and B.F. Hutton, *Optimal collimator hole dimensions for half cone-beam brain SPECT*, Proceedings 4th

International Meeting on Fully Three-Dimensional Image Reconstruction in Radiology and Nuclear Medicine (1999), 271–274.

[77] J.S. Karp, G. Muehllehner, and R.M. Lewitt, *Constrained Fourier space method for compensation of missing data in emission computed tomography*, IEEE Transactions on Medical Imaging **7** (1988), no. 1, 21–25.

[78] L. Kaufman, *Maximum likelihood, least squares, and penalized least squares for PET*, IEEE Transactions on Medical Imaging **12** (1993), no. 2, 200–214.

[79] E.L. Keller, *Optimum dimensions of parallel-hole, multi-aperture collimators for gamma-ray cameras*, Journal of Nuclear Medicine **9** (1968), no. 6, 233–235.

[80] R.M. Kessler, J.R. Ellis, and M. Eden, *Analysis of tomographic scan data: limitations imposed by resolution and background*, Journal of Computer Assisted Tomography **8** (1984), 514–22.

[81] J.W. Keyes, J.H. Thrall, and J.E. Carey, *Technical considerations in in vivo thyroid studies*, Seminars in Nuclear Medicine **8** (1978), no. 1, 43–57.

[82] W.I. Keyes, *Correspondence: The fan-beam gamma camera*, Physics in Medicine and Biology **20** (1975), no. 3, 489–493.

[83] H. Kim, L.R. Furenlid, M.J. Crawford, D.W. Wilson, H.B. Barber, T.E. Peterson, W.C.J. Hunter, Z. Liu, J.M. Woolfenden, and H.H. Barrett, *SemiSPECT: a small-animal single-photon emission computed tomography (SPECT) imager based on eight cadmium zinc telluride (CZT) detector arrays*, Medical Physics **33** (2006), no. 2, 465–474.

[84] M.A. King, B.M.W. Tsui, T.S. Pan, S.J. Glick, and E.J. Soares, *Attenuation compensation for cardiac single-photon emission computed tomographic imaging: Part 2. Attenuation compensation algorithms.*, Journal of Nuclear Cardiology **3** (1996), no. 1, 55–64.

[85] G. Knoll, *Radiation detection and measurement*, John Wiley and Sons, New York, USA, 1979.

[86] V. Kohli, M.A. King, S.J. Glick, and T.S. Pan, *Comparison of frequency-distance relationship and Gaussian-diffusion-based methods of compensation for distance-dependent spatial resolution in*

SPECT imaging, Physics in Medicine and Biology **43** (1998), no. 4, 1025–1037.

[87] M. Koole, Y. D'Asseler, S. Vandenberghe, K. Van Laere, J. Versijpt, I. Lemahieu, and R.A. Dierckx, *Modeling of the sensitivity of fan-beam collimation in SPECT imaging*, Proceedings of the 23rd Annual EMBS International Conference (2001), 2375–2378.

[88] K.F. Koral, F.M. Swailem, S. Buchbinder, N.H. Clinthorne, W.L. Rogers, and B.M.W. Tsui, *SPECT dual-energy-window Compton correction: scatter multiplier required for quantification.*, Journal of Nuclear Medicine **31** (1990), no. 1, 90–98.

[89] K.F. Koral, X.Q. Wang, W.L. Rogers, N.H. Clinthorne, and X.H. Wang, *SPECT Compton-scattering correction by analysis of energy spectra*, Journal of Nuclear Medicine **29** (1988), no. 2, 195–202.

[90] C. Lackas, N.U. Schramm, J.W. Hoppin, U. Engeland, A. Wirrwar, and H. Halling, *T-SPECT: A novel imaging technique for small animal research*, IEEE Transactions on Nuclear Science **52** (2005), 181–187.

[91] D.S. Lalush and B.M.W. Tsui, *A fast and stable maximum a posteriori conjugate gradient reconstruction algorithm*, Medical Physics **22** (1995), no. 8, 1273–1284.

[92] D.S. Lalush and M.N. Wernick, *Iterative image reconstruction*, ch. 21, pp. 443–472, San Diego: Academic Press, 2004.

[93] K. Lange, M. Bahn, and R. Little, *A theoretical study of some maximum likelihood algorithms for emission and transmission tomography*, IEEE Transactions on Medical Imaging **6** (1987), no. 2, 106–114.

[94] K. Lange and R. Carson, *EM reconstruction algorithms for emission and transmission tomography*, Journal of Computer Assisted Tomography **8** (1984), no. 2, 306–316.

[95] R. Leahy and C. Byrne, *Recent developments in iterative image reconstruction for PET and SPECT*, IEEE Transactions on Medical Imaging **19** (2000), no. 4, 257–260.

[96] E. Levitan and G.T. Herman, *A maximum a posteriori probability expectation maximization algorithm for image reconstruction in*

emission tomography, IEEE Transactions on Medical Imaging **6** (1987), no. 3, 185–192.

[97] R.M. Lewitt, *Alternatives to voxels for image representation in iterative reconstruction algorithms*, Physics in Medicine and Biology **37** (1992), no. 3, 705–716.

[98] R.M. Lewitt, P.R. Edholm, and W. Xia, *Fourier method for correction of depth-dependent collimator blurring*, Proceedings of the SPIE Medical Imaging conference, vol. 1092, 1989, p. 232.

[99] R.M. Lewitt and S. Matej, *Overview of methods for image reconstruction from projections in emission computed tomography*, Proceedings of the IEEE **91** (2003), no. 10, 1588–1611.

[100] M. Ljungberg and S.E. Strand, *Attenuation and scatter correction in SPECT for sources in a nonhomogeneous object: a Monte Carlo study.*, Journal of Nuclear Medicine **32** (1991), no. 6, 1278–1284.

[101] M.A. Lodge, *A rotating slat collimator for planar and tomographic gamma-camera imaging*, The Joint Department of Physics, The Institute of Cancer Research and The Royal Marsden Hospital Sutton, Surrey, UK, 1996.

[102] M.A. Lodge, D.M. Binnie, M.A. Flower, and S. Webb, *The experimental evaluation of a prototype rotating slat collimator for planar gamma camera imaging*, Physics in Medicine and Biology **40** (1995), no. 3, 427–448.

[103] M.A. Lodge, S. Webb, M.A. Flower, and D.M. Binnie, *A prototype rotating slat collimator for single photon emission computed tomography*, IEEE Transactions on Medical Imaging **15** (1996), no. 4, 500–511.

[104] C. Love, A.S. Din, M.B. Tomas, T.P. Kalapparambath, and C.J. Palestro, *Radionuclide bone imaging: an illustrative review.*, Radiographics **23** (2003), no. 2, 341–358.

[105] L. Lucy, *An iterative technique for the rectification of observed distributions*, The Astronomical Journal **79** (1974), 745–754.

[106] L.R. MacDonald, B.E. Patt, J.S. Iwanczyk, B.M.W. Tsui, Y. Wang, E.C. Frey, D.E. Wessell, P.D. Acton, and H.F. Kung, *Pinhole SPECT of mice using the LumaGEM gamma camera*, IEEE Transactions on Nuclear Science **48** (2001), no. 3, 830–836.

[107] D.J. Macey, G.L. DeNardo, S.J. DeNardo, and H.H. Hines, *Comparison of low- and medium-energy collimators for SPECT imaging with iodine-123-labeled antibodies*, Journal of Nuclear Medicine **27** (1986), no. 9, 1467–1474.

[108] G.E. Mailloux, R. Noumeir, and R. Lemieux, *Deriving the multiplicative algebraic reconstruction algorithm (MART) by the method of convex projection (POCS)*, Proceeding of the IEEE International Conference on Acoustics, Speech, and Signal Processing, vol. 5, 1993, pp. 457–460.

[109] S. Matej and R.M. Lewitt, *Practical considerations for 3-D image reconstruction using spherically symmetric volume elements*, IEEE Transactions on Medical Imaging **15** (1996), no. 1, 68–78.

[110] W. Mauderli, R.W. Luthmann, L.T. Fitzgerald, M.M. Urie, C.M. Williams, C.H. Tosswill, and G. Entine, *A computerized rotating laminar radionuclide camera*, Journal of Nuclear Medicine **20** (1979), no. 4, 341–344.

[111] D.P. McElroy, L.R. MacDonald, F.J. Beekman, Y. Wang, B.E. Patt, J.S. Iwanczyk, B.M.W Tsui, and E.J. Hoffman, *Performance evaluation of A-SPECT: A high resolution desktop pinhole SPECT system for imaging small animals*, IEEE Transactions on Nuclear Science **49** (2002), no. 5, 2139–2147.

[112] D.S. McGregor and H. Hermonb, *Room-temperature compound semiconductor radiation detectors*, Nuclear Instruments and Methods A **395** (1997), 101–124.

[113] L.J. Meng and N.H. Clinthorne, *A modified uniform Cramer-Rao bound for multiple pinhole aperture design*, IEEE Transactions on Medical Imaging **23** (2004), no. 7, 896–902.

[114] C.E. Metz, F.B. Atkins, and R.N. Beck, *The geometric transfer function component for scintillation camera collimators with straight parallel holes*, Physics in Medicine and Biology **25** (1980), no. 6, 1059–1070.

[115] S.D. Metzler, R. Accorsi, J.R. Novak, A.S. Ayan, and R.J. Jaszczak, *On-axis sensitivity and resolution of a slit-slat collimator*, Journal of Nuclear Medicine **47** (2006), no. 11, 1884–1890.

[116] S.D. Metzler, K.L. Greer, and R.J. Jaszczak, *Helical pinhole SPECT for small-animal imaging: A method for addressing sampling completeness*, IEEE Transactions on Nuclear Science **50** (2003), no. 5, 1575–1583.

[117] S.C. Moore, D.J. deVries, B. Nandram, M.F. Kijewski, and S.P. Mueller, *Collimator optimization for lesion detection incorporating prior information about lesion size*, Medical Physics **22** (1995), no. 6, 703–713.

[118] S.C. Moore, M.F. Kijewski, and G. El Fakhri, *Collimator optimization for detection and quantitation tasks: application to gallium-67 imaging*, IEEE Transactions on Medical Imaging **24** (2005), no. 10, 1347–1356.

[119] S.C. Moore, K. Kouris, and I. Cullum, *Collimator design for single photon emission tomography*, European Journal of Nuclear Medicine **19** (1992), no. 2, 138–150.

[120] H. Murayama, I. Ishibashi, H. Uchida, T. Omura, and T. Yamashita, *Depth encoding multicrystal detectors for PET*, IEEE Transactions on Nuclear Science **45** (1998), no. 3, 1152–1157.

[121] S. Nagai, M. Watanabe, H. Shimoi, H. Liu, and Y. Yoshizawa, *A new compact position-sensitive PMT for scintillation detectors*, IEEE Transactions on Nuclear Science **46** (1999), no. 3, 354–358.

[122] F. Natterer and F. Wubbeling, *Inversion of solstice data*, Report (2000).

[123] R. Newell, W. Saunders, and E. Miller, *Multichannel collimators for gamma scanning with scintillation counters*, Nucleonics **10** (1952), 36–40.

[124] J. Nuyts, *Nuclear medicine technology and techniques*, Course at KULeuven (2003).

[125] K. Ogawa, Y. Harata, T. Ichihara, A. Kubo, and S. Hashimoto, *A practical method for position-dependent Compton-scatter correction in single photon emission CT*, IEEE Transactions on Medical Imaging **10** (1991), no. 3, 408–412.

[126] S.S. Orlov, *Theory of three-dimensional image reconstruction: I Conditions for a complete set of projections*, Soviet Physics Crystallography **20** (1976), 429–433.

[127] B. Ostendorf, A. Scherer, A. Wirrwar, J.W. Hoppin, C. Lackas, N.U. Schramm, M. Cohnen, U. Modder, W.B. van den Berg, H.W. Muller, M. Schneider, and L.A.B. Joosten, *High-resolution multipinhole single-photon-emission computed tomography in experimental and human arthritis*, Arthritis and Rheumatism **54** (2006), no. 4, 1096–1104.

[128] D. Pareto, J. Pavía, C. Falcon, I. Juvells, A. Cot, and D. Ros, *Characterisation of fan-beam collimators*, European Journal of Nuclear Medicine **28** (2001), no. 2, 144–149.

[129] M. Park, S.C. Moore, and M.F. Kijewski, *Brain SPECT with short focal-length cone-beam collimation*, Medical Physics **32** (2005), no. 7, 2236–2244.

[130] D.D. Patton, H.H. Barrett, and J.C. Chen, *FASTSPECT: A four-dimensional brain imager*, Journal of Nuclear Medicine **35** (1994), no. 5, P93 Suppl S.

[131] M. E. Phelps, *Pet: the merging of biology and imaging into molecular imaging.*, J Nucl Med **41** (2000), no. 4, 661–681.

[132] A. R. De Pierro, *A modified expectation maximization algorithm for penalized likelihood estimation in emission tomography*, IEEE Transactions on Medical Imaging **14** (1995), no. 1, 132–137.

[133] W.H. Press, S.A. Teukolsky, W.T. Vetterling, and B.P. Flannery, *Numerical recipes in C++: the art of scientific computing, second edition*, Cambridge University Press, 2002.

[134] E. Rault, S. Vandenberghe, Van Holen R., J. De Beenhouwer, S. Staelens, and I. Lemahieu, *Comparison of image quality of different iodine isotopes (I-123, I-124, and I-131)*, Cancer Biotherapy and Radiopharmaceuticals **22** (2007), no. 3, 423–430.

[135] E. Rault, S. Vandenberghe, S. Staelens, R. Van Holen, and I. Lemahieu, *Optimization of Y-90 bremsstrahlung image reconstruction using multiple energy window subsets.*, Journal of Nuclear Medicine, Abstract book 55th SNM annual meeting (New Orleans), vol. 49, 2008, p. 399P.

[136] M.C.M. Rentmeester, F. van der Have, and F.J. Beekman, *Optimizing multi-pinhole SPECT geometries using an analytical model*, Physics in Medicine and Biology **52** (2007), no. 9, 2567–2581.

[137] T.A. Riauka and Z.W. Gortel, *Photon propagation and detection in single-photon emission computed tomography–an analytical approach.*, Medical Physics **21** (1994), no. 8, 1311–1321.

[138] W.H. Richardson, *Bayesian-based iterative method of image restoration*, Journal of the Optical Society of America **62** (1972), 55–59.

[139] W.L. Rogers, N.H. Clinthorne, J. Stamos, K.F. Koral, R. Mayans, J.W. Keyes, J.J. Williams, W.P. Snapp, and G.F. Knoll, *SPRINT: A stationary detector single photon ring tomograph for brain imaging*, IEEE Transactions on Medical Imaging **1** (1982), no. 1, 63–68.

[140] W.L. Rogers, N.H. Clinthorne, J. Stamos, K.F. Koral, R. Mayans, G.F. Knoll, J. Juni, J.W. Keyes, and B.A. Harkness, *Performance evaluation of SPRINT, a single photon ring tomography for brain imaging*, Journal of Nuclear Medicine **25** (1984), no. 9, 1013–1018.

[141] N.U. Schramm, G. Ebel, U. Engeland, T. Schurrat, M. Behe, and T.M. Behr, *High-resolution SPECT using multipinhole collimation*, IEEE Transactions on Nuclear Science **50** (2003), 315–320.

[142] N.U. Schramm, A. Wirrwar, F. Sonnenberg, and H. Halling, *Compact high resolution detector for small animal SPECT*, IEEE Transactions on Nuclear Science **47** (2000), no. 3, 1163–1167.

[143] W.P. Segars, *Development and application of the new dynamic NURBS-based cardiac-torso (NCAT) phantom*, Ph.D. thesis, The University of North Carolina, 2001.

[144] K.S. Shah, R. Farrell, R. Grazioso, R. Myers, and L. Cirignano, *Large-area APDs and monolithic APD arrays*, IEEE Transactions on Nuclear Science **48** (2001), no. 6, 2352–2356.

[145] L.A. Shepp and Y. Vardi, *Maximum likelihood reconstruction for emission tomography.*, IEEE Transactions on Medical Imaging **1** (1982), no. 2, 113–122.

[146] R.L. Siddon, *Fast calculation of the exact radiological path for a three-dimensional CT array.*, Medical Physics **12** (1985), no. 2, 252–255.

[147] A.D. Small, J. Prosser, D.W. Motherwell, G.M. McCurrach, A.M. Fletcher, and W. Martin, *Downscatter correction and choice of*

collimator in 123I imaging, Physics in Medicine and Biology **51** (2006), no. 17, N307–N311.

[148] X. Song, W.P. Segars, Y. Du, B.M.W. Tsui, and E.C. Frey, *Fast modelling of the collimator-detector response in Monte Carlo simulation of SPECT imaging using the angular response function.*, Physics in Medicine and Biology **50** (2005), no. 8, 1791–1804.

[149] A. Spanu, A. Falchi, A. Manca, P. Marongiu, A. Cossu, N. Pisu, F. Chessa, S. Nuvoli, and G. Madeddu, *The usefulness of neck pinhole SPECT as a complementary tool to planar scintigraphy in primary and secondary hyperparathyroidism*, Journal of Nuclear Medicine **45** (2004), no. 1, 40–48.

[150] S. Staelens, T. de Wit, and F. Beekman, *Fast hybrid SPECT simulation including efficient septal penetration modelling (SP-PSF)*, Physics in Medicine and Biology **52** (2007), no. 11, 3027–3043.

[151] S. Staelens, M. Koole, S. Vandenberghe, Y. D'Asseler, I. Lemahieu, and R. Van de Walle, *The geometric transfer function for a slat collimator mounted on a strip detector*, IEEE Transactions on Nuclear Science **52** (2005), no. 3, 708–713.

[152] S. Staelens, D. Strul, G. Santin, S. Vandenberghe, M. Koole, Y. D'Asseler, I. Lemahieu, and R. Van de Walle, *Monte Carlo simulations of a scintillation camera using GATE: validation and application modelling*, Physics in Medicine and Biology **48** (2003), no. 18, 3021–3042.

[153] P.P. Steele, D.L. Kirch, and J.E. Koss, *Comparison of simultaneous dual-isotope multipinhole SPECT with rotational SPECT in a group of patients with coronary artery disease*, Journal of Nuclear Medicine **49** (2008), no. 7, 1080–1089.

[154] C. Tosswill, *Computerized rotating laminar collimation imaging system*, US patent application 646 (granted December 1977) (1977), 917–967.

[155] T. Tsuda, H. Murayama, K. Kitamura, T. Yamaya, E. Yoshida, T. Omura, H. Kawai, N. Inadama, and N. Orita, *A four-layer depth of interaction detector block for small animal PET*, IEEE Transactions on Nuclear Science **51** (2004), no. 5, 2537–2542.

[156] B.M.W. Tsui and G.T. Gullberg, *The geometric transfer function for cone and fan beam collimators*, Physics in Medicine and Biology **35** (1990), 81–93.

[157] B.M.W. Tsui, J.A. Terry, and G.T. Gullberg, *Evaluation of cardiac cone-beam single photon emission computed tomography using observer performance experiments and receiver operating characteristic analysis*, Investigative Radiology **28** (1993), no. 12, 1101–1112.

[158] B.M.W. Tsui, X. Zhao, E.C. Frey, and G.T. Gullberg, *Comparison between ML-EM and WLS-CG algorithms for SPECT image reconstruction*, IEEE Transactions on Nuclear Science **38** (1991), no. 6, 1766–1772.

[159] R. Van Holen, E. Rault, S. Staelens, S. Vandenberghe, and I. Lemahieu, *Bremsstrahlung imaging of yttrium-90 with a rotating slat collimator*, European Journal of Nuclear Medicine, Abstracts from the Annual Congress of the EANM (Munchen), vol. 35, Springer, 10 2008, p. S339.

[160] R. Van Holen, S. Staelens, Y. D'Asseler, I. Lemahieu, and R. Van de Walle, *Nuclear medical imaging with a rotating slat collimator on a solid state detector*, Abstracts of the 5th FTW PhD symposium (Gent), 12 2004.

[161] R. Van Holen, S. Staelens, S. Vandenberghe, Y. D'Asseler, D. Gagnon, and I. Lemahieu, *Simultaneous 99mTc/123I parathyroid imaging with a rotating collimator on a solid state detector : a simulation study.*, European Journal of Nuclear Medicine, Abstracts from the Annual Congress of the EANM **32** (2005), S34.

[162] R. Van Holen, S. Staelens, S. Vandenberghe, Y. D'Asseler, and I. Lemahieu, *Exploiting the characteristics of a prototype rotating slat collimated solid state strip detector: dual isotope imaging.*, Abstract book of the 21st annual symposium of the Belgian Hospital Physicist Association (Gent), 1 2006, p. 120.

[163] R. Van Holen, S. Staelens, S. Vandenberghe, and I. Lemahieu, *Influence of a rotating slat collimator on the quantification of I-131*, Abstract book supplement to the Journal of Nuclear Medicine (New Orleans), vol. 49, 2008, p. 407P.

[164] R. Van Holen, S. Vandenberghe, S. Staelens, Y. D'Asseler, and I. Lemahieu, *Contrast noise behaviour for a rotating slat collimated*

gamma camera., Book of abstracts of the 1st European Conference on Molecular Imaging Technology (Marseille), 5 2006, pp. 20 on CD–rom.

[165] ———, *Improving the resolution of a rotating slat collimated SPECT camera: System behavior considerations.*, Abstracts of the International Conference on Imaging Techniques in Subatomic Physics, Astrophysics, Medicine, Biology and Industry (Stockholm), 6 2006, p. 95.

[166] ———, *Iterative reconstruction of rotating slat collimated gamma camera acquisitions.*, Proceedings of the IEEE/EMBS Benelux symposium, Belgian Day on Biomedical Engineering (Brussel), 12 2006, p. 83.

[167] ———, *Outside field of view activity removal for rotating slat collimated acquisitions using fourier techniques.*, Abstract book supplement to the Journal of Nuclear Medicine **47** (2006), no. 5, 122P.

[168] R. Van Holen, S. Vandenberghe, S. Staelens, Y. D'Asseler, and I. Lemahieu, *Outside field of view activity removal for rotating slat collimated acquisitions using Fourier techniques*, 2006, p. 122P.

[169] R. Van Holen, S. Vandenberghe, S Staelens, Y. D'Asseler, and I. Lemahieu, *Contrast noise behaviour of a rotating slat collimated gamma camera*, Nuclear Instruments and Methods A **571** (2007), 274–277.

[170] R. Van Holen, S. Vandenberghe, S. Staelens, Y. D'Asseler, and I. Lemahieu, *Objective comparison of rotating slat and parallel hole collimation.*, Journal of Nuclear Medicine, Abstract book 54th Society of Nuclear Medicine annual meeting **48** (2007), 435P.

[171] R. Van Holen, S. Vandenberghe, S. Staelens, Y. D'Asseler, and I. Lemahieu, *Objective comparison of rotating slat and parallel hole collimation*, 2007, p. 435P.

[172] R. Van Holen, S. Vandenberghe, S. Staelens, J. De Beenhouwer, and I. Lemahieu, *Fast 3D iterative image reconstruction for SPECT with rotating slat collimators*, Physics in Medicine and Biology **54** (2009), no. 3, 715–729.

[173] R. Van Holen, S. Vandenberghe, S. Staelens, and I. Lemahieu, *Comparing planar image quality of rotating slat and parallel hole*

collimation: influence of system modeling, Physics in Medicine and Biology **53** (2008), no. 7, 1989–2002.

[174] ———, *Comparison of 3D SPECT imaging with a rotating slat collimator and a parallel hole collimator*, IEEE Nuclear Science Symposium Conference Record 2008 (Dresden), 2008, pp. 4592–4597.

[175] R. Van Holen, S. Vandenberghe, S. Staelens, E. Rault, J. De Beenhouwer, and I. Lemahieu, *Reducing high energy contamination in SPECT using a rotating slat collimator*, Book of Abstracts 4th International Conference on Imaging Technologies in Biomedical Sciences (Milos Island), 2007, p. 65.

[176] S. Vandenberghe, Y. D'Asseler, R. Van de Walle, T. Kauppinen, M. Koole, L. Bouwens, K. Van Laere, I. Lemahieu, and R.A. Dierckx, *Iterative reconstruction algorithms in nuclear medicine.*, Computerized Medical Imaging and Graphics **25** (2001), no. 2, 105–111.

[177] S. Vandenberghe, R. Van Holen, S. Staelens, and I. Lemahieu, *System characteristics of SPECT with a slat collimated strip detector*, Physics in Medicine and Biology **51** (2006), no. 2, 391–405.

[178] Stefaan Vandenberghe, Steven Staelens, Charles L Byrne, Edward J Soares, Ignace Lemahieu, and Stephen J Glick, *Reconstruction of 2d pet data with monte carlo generated system matrix for generalized natural pixels.*, Physics in Medicine and Biology **51** (2006), no. 12, 3105–3125.

[179] H.J. Verberne, C. Feenstra, W.M. de Jong, G.A. Somsen, B. van Eck-Smit, and E. Busemann Sokole, *Influence of collimator choice and simulated clinical conditions on 123I-MIBG heart/mediastinum ratios: a phantom study*, European Journal of Nuclear Medicine **32** (2005), no. 9, 1100–1107.

[180] R.A. Vogel, D.L. Kirch, M.T. LeFree, J.O. Rainwater, D.P. Jensen, and P.P. Steele, *Thallium-201 myocardial perfusion scintigraphy: results of standard and multi-pinhole tomographic techniques*, The American Journal of Cardiology **43** (1979), no. 4, 787–793.

[181] J.M. Vose, R.L. Wahl, M. Saleh, A.Z. Rohatiner, S.J. Knox, J.A. Radford, A.D. Zelenetz, G.F. Tidmarsh, R.J. Stagg, and M.S. Kaminski, *Multicenter phase II study of iodine-131 tositumomab*

for chemotherapy-relapsed/refractory low-grade and transformed low-grade B-cell non-Hodgkin's lymphomas, Journal of Clinical Oncology **18** (2000), no. 6, 1316–1323.

[182] K. Vunckx, D. Beque, M. Defrise, and J. Nuyts, *Single and multipinhole collimator design evaluation method for small animal SPECT*, IEEE Transactions on Medical Imaging **27** (2008), no. 1.

[183] R.L. Wahl, K.R. Zasadny, D. MacFarlane, I.R. Francis, C.W. Ross, J. Estes, S. Fisher, D. Regan, S. Kroll, and M.S. Kaminski, *Iodine-131 anti-B1 antibody for B-cell lymphoma: an update on the Michigan Phase I experience*, Journal of Nuclear Medicine **39** (1998), no. 8 Suppl, 21S–27S.

[184] J.W. Wallis and T.R. Miller, *An optimal rotator for iterative reconstruction*, IEEE Transactions on Medical Imaging **16** (1997), no. 1, 118–123.

[185] S.H. Walrand, F. Jamar, M. de Jong, and S. Pauwels, *Evaluation of novel whole-body high-resolution rodent SPECT (Linoview) based on direct acquisition of linogram projections*, Journal of Nuclear Medicine **46** (2005), no. 11, 1872–1880.

[186] S.H. Walrand, L.R. van Elmbt, and S. Pauwels, *Quantitation in SPECT using an effective model of the scattering*, Physics in Medicine and Biology **39** (1994), no. 4, 719–734.

[187] W. Wang, W. Hawkins, and D. Gagnon, *3D RBI-EM reconstruction with spherically-symmetric basis function for SPECT rotating slat collimator*, Physics in Medicine and Biology **49** (2004), no. 11, 2273–2292.

[188] M. Watanabe, T. Omura, H. Kyushima, Y. Hasegawa, and T. Yamashita, *A compact position-sensitive detector for PET*, IEEE Transactions on Nuclear Science **42** (1995), no. 4, 1090–1094.

[189] M. Watanabe, K. Shimizu, T. Omura, M. Takahashi, T. Kosugi, E. Yoshikawa, N. Sato, H. Okada, and T. Yamashita, *A new high-resolution PET scanner dedicated to brain research*, IEEE Transactions on Nuclear Science **49** (2002), no. 3, 634–639.

[190] S. Webb, D. Binnie, M. Flower, and R. Ott, *Monte Carlo modeling of the performace of a rotating slit collimator for improved*

planar gamma camera imaging, Physics in Medicine and Biology **37** (1992), 1095–1108.

[191] S. Webb, M. Flower, and R. Ott, *Geometric efficiency of a rotating slit-collimator for improved planar gamma-camera imaging*, Physics in Medicine and Biology **38** (1993), 627–638.

[192] H. Wieczorek and A. Goedicke, *Analytical model for SPECT detector concepts*, IEEE Transactions on Nuclear Science **53** (2006), no. 3, 1102–1112.

[193] M.B. Williams, A.R. Goode, V. Galbis-Reig, S. Majewski, A.G. Weisenberger, and R. Wojcik, *Performance of a PSPMT based detector for scintimammography*, Physics in Medicine and Biology **45** (2000), no. 3, 781–800.

[194] D.W. Wilson and B.M.W. Tsui, *Spatial resolution properties of FB and ML-EM reconstruction methods*, IEEE Nuclear Science Symposium Conference Record (1993), 1189–93.

[195] A. Wouters, K.M. Simon, and J.G. Hirschberg, *Direct method of decoding multiple images*, Applied Optics **12** (1973), no. 8, 1871.

[196] H. Zaidi, *Relevance of accurate Monte Carlo modeling in nuclear medical imaging*, Medical Physics **26** (1999), no. 4, 574–608.

[197] G.L. Zeng, *Detector blurring and detector sensitivity compensation for a spinning slat collimator*, IEEE Transactions on Nuclear Science **53** (2006), no. 5, 2628–2634.

[198] G.L. Zeng, C. Bai, and G.T. Gullberg, *A projector/backprojector with slice-to-slice blurring for efficient three-dimensional scatter modeling*, IEEE Transactions on Medical Imaging **18** (1999), no. 8, 722–732.

[199] G.L. Zeng, D. Gagnon, C. Matthews, J. Kolthammer, J. Radachy, and W. Hawkins, *Image reconstruction algorithm for a rotating slat collimator*, Medical Physics **29** (2002), no. 7, 1406–1412.

[200] G.L. Zeng, D. Gagnon, F. Natterer, W. Wang, M. Wrinkler, and W. Hawkins, *Local tomography property of residual minimization reconstruction with planar integral data*, IEEE Transactions on Nuclear Science **50** (2003), no. 5.

[201] G.L. Zeng and G.T. Gullberg, *A channelized-hotelling-trace collimator design method based on reconstruction rather than projections*, IEEE Transactions on Nuclear Science **49** (2002), no. 5, 2155–2158.

[202] G.L. Zeng, G.T. Gullberg, B.M.W. Tsui, and J.A. Terry, *Three-dimensional iterative reconstruction algorithms with attenuation and geometric point response correction*, IEEE Transactions on Nuclear Science **38** (1991), no. 2, 693–702.

[203] L. Zhou, M. Defrise, K. Vunckx, and J. Nuyts, *Comparison between parallel hole and rotating slat collimation*, IEEE Nuclear Science Symposium Conference Record NSS '08, 2008, pp. 5530–5539.

Publications author: Journal Papers

[1] R. Van Holen, S. Staelens, and S. Vandenberghe. SPECT imaging of high energy isotopes and isotopes with high energy contaminants with rotating slat collimators. *Submitted to Medical Physics*, 2009.

[2] J. De Beenhouwer, S. Staelens, S. Vandenberghe, J. Verhaeghe, R. Van Holen, E. Rault, and I. Lemahieu. Physics process level discrimination of detections for GATE: assessment of contamination in SPECT and spurious activity in PET. *Medical Physics*, 506:1053–1060, 2009.

[3] R. Van Holen, S. Vandenberghe, S. Staelens, J. De Beenhouwer, and I. Lemahieu. Fast 3D iterative image reconstruction for SPECT with rotating slat collimators. *Physics in Medicine and Biology*, 54(3):715–729, February 2009.

[4] R. Van Holen, S. Vandenberghe, S. Staelens, and I. Lemahieu. Comparing planar image quality of rotating slat and parallel hole collimation: influence of system modeling. *Physics in Medicine and Biology*, 53(7):1989–2002, April 2008.

[5] E. Rault, S. Vandenberghe, R. Van Holen, J. De Beenhouwer, S. Staelens, and I. Lemahieu. Comparison of image quality of different iodine isotopes (I-123, I-124, and I-131). *Cancer Biotherapy and Radiopharmaceuticals*, 22(3):423–430, June 2007.

[6] R. Van Holen, S. Vandenberghe, S Staelens, Y. D'Asseler, and I Lemahieu. Contrast noise behaviour of a rotating slat collimated gamma camera. *Nuclear Instruments and Methods in Physics Research Section A*, 571:274–277, February 2007.

[7] S. Vandenberghe, R. Van Holen, S. Staelens, and I. Lemahieu. System characteristics of SPECT with a slat collimated strip detector. *Physics in Medicine and Biology*, 51(2):391–405, January 2006.

Publications author: Conference Proceedings

[1] R. Van Holen, S. Vandenberghe, S. Staelens, and I. Lemahieu. Comparison of 3D SPECT imaging with a rotating slat collimator and a parallel hole collimator. In *IEEE Nuclear Science Symposium Conference Record 2008*, pages 4592–4597, Dresden, 2008.

[2] J. De Smet, R. Van Holen, S. Staelens, S. Vandenberghe, and I. Lemahieu. Slat collimated multipinhole human brain SPECT. In *IEEE Nuclear Science Symposium Conference Record 2008*, pages 4034–4035, Dresden, 2008.

[3] R. Van Holen, E. Rault, S. Staelens, S. Vandenberghe, and I. Lemahieu. Bremsstrahlung imaging of yttrium-90 with a rotating slat collimator. volume 35, page S339, Munchen, 10 2008. Springer.

[4] R. Van Holen, S. Staelens, S. Vandenberghe, and I. Lemahieu. Influence of a rotating slat collimator on the quantification of I-131. In *Journal of Nuclear Medicine, Abstract book 55th SNM annual meeting*, volume 49, page 407P, New Orleans, 2008.

[5] E. Rault, S. Vandenberghe, S. Staelens, R. Van Holen, and I. Lemahieu. Optimization of Y-90 bremsstrahlung image reconstruction using multiple energy window subsets. In *Journal of Nuclear Medicine, Abstract book 55th SNM annual meeting*, volume 49, page 399P, New Orleans, 2008.

[6] J. De Smet, R. Van Holen, S. Staelens, S. Vandenberghe, and I. Lemahieu. Multipinhole brain SPECT: feasibility study. In *Conference proceedings Liege Image Days 2008: Medical Imaging*, page 1, 2008.

[7] R. Van Holen, S. Vandenberghe, S. Staelens, J. De Beenhouwer, and E. Rault. Reduced effect of high energy contamination in SPECT using a rotating slat collimator. In *Abstracts 8e UGent-FirW doctoraatssymposium*, pages 82–82, Gent, 2007.

[8] R. Van Holen, S. Vandenberghe, S. Staelens, E. Rault, J. De Beenhouwer, and I. Lemahieu. Reduced effect of high energy contamination in SPECT using a rotating slat collimator. In *7th Belgian Day on Biomedical Engineering*, pages 53–53, Brussel, 2007.

[9] R. Van Holen, S. Vandenberghe, S. Staelens, E. Rault, J. De Beenhouwer, and I. Lemahieu. Reducing high energy contamination in SPECT using a rotating slat collimator. In *Book of Abstracts 4th International Conference on Imaging Technologies in Biomedical Sciences*, page 65, Milos Island, 2007.

[10] R. Van Holen, S. Vandenberghe, S. Staelens, Y. D'Asseler, and I. Lemahieu. Objective comparison of rotating slat and parallel hole collimation. *Journal of Nuclear Medicine, Abstract book 54th Society of Nuclear Medicine annual meeting*, 48:435P, 2007.

[11] E. Rault, S. Vandenberghe, R. Van Holen, J. De Beenhouwer, S. Staelens, and I. Lemahieu. Comparison of quantification and image quality for different iodine isotopes (I-123, I-124 and I-131). In *Abstract book of the 22nd Annual BHPA symposium "Physics in Medicine"*, page 20, Liege, 2 2007.

[12] E. Auffray *et al. First results with the clearpet small animal PET scanners.*, pages 149–164. Springer Netherlands, 11 2006.

[13] E. Rault, S. Vandenberghe, R. Van Holen, J. De Beenhouwer, and I. Lemahieu. Comparison of quantification and image degrading factors for different iodine isotopes (I-123, I-124 and I-131). In *Abstracts 7e UGent-FirW doctoraatssymposium*, page 38, Gent, 11 2006.

[14] R. Van Holen, S. Vandenberghe, S. Staelens, Y. D'Asseler, and I. Lemahieu. Iterative reconstruction of rotating slat collimated gamma camera acquisitions. In *Proceedings of the IEEE/EMBS Benelux symposium, Belgian Day on Biomedical Engineering*, page 83, Brussel, 12 2006.

[15] R. Van Holen, S. Vandenberghe, S. Staelens, Y. D'Asseler, and I. Lemahieu. Contrast noise behaviour for a rotating slat collimated

gamma camera. In *Book of abstracts of the 1st European Conference on Molecular Imaging Technology*, pages 20 on CD–rom, Marseille, 5 2006.

[16] E. Rault, S. Vandenberghe, R. Van Holen, J. De Beenhouwer, and I. Lemahieu. Comparison of quantification and image degrading factors with different iodine isotopes. *European Journal of Nuclear Medicine, Abstracts of the annual congress of the EANM*, 33:374, 9 2006.

[17] S. Vandenberghe, R. Van Holen, S. Staelens, Y. D'Asseler, and I. Lemahieu. New technological developments in nuclear medicine. In *Abstract book of the 21st annual symposium of the Belgian Hospital Physicist Association*, pages 41–42, Gent, 1 2006.

[18] R. Van Holen, S. Staelens, S. Vandenberghe, Y. D'Asseler, and I. Lemahieu. Exploiting the characteristics of a prototype rotating slat collimated solid state strip detector: dual isotope imaging. In *Abstract book of the 21st annual symposium of the Belgian Hospital Physicist Association*, page 120, Gent, 1 2006.

[19] R. Van Holen, S. Vandenberghe, S. Staelens, Y. D'Asseler, and I. Lemahieu. Improving the resolution of a rotating slat collimated SPECT camera: System behavior considerations. In *Abstracts of the International Conference on Imaging Techniques in Subatomic Physics, Astrophysics, Medicine, Biology and Industry*, page 95, Stockholm, 6 2006.

[20] R. Van Holen, S. Vandenberghe, S. Staelens, Y. D'Asseler, and I. Lemahieu. Outside field of view activity removal for rotating slat collimated acquisitions using fourier techniques. *Abstract book supplement to the Journal of Nuclear Medicine*, 47(5):122P, 12 2006.

[21] M. Khodaverdi *et al.* High resolution imaging with ClearPET neurofirst animal images. In *2005 Nuclear Science Symposium and Medical Imaging Conference*, pages 1641–1644, San Juan, Puerto Rico, 10 2005.

[22] R. Van Holen, S. Staelens, S. Vandenberghe, Y. D'Asseler, D. Gagnon, and I. Lemahieu. Simultaneous 99mTc/123I parathyroid imaging with a rotating collimator on a solid state detector : a simulation study. *European Journal of Nuclear Medicine, Abstracts from the Annual Congress of the EANM*, 32:S34, 9 2005.

[23] R. Van Holen, S. Staelens, Y. D'Asseler, I. Lemahieu, and R. Van de Walle. Nuclear medical imaging with a rotating slat collimator on a solid state detector. In *Abstracts of the 5th FTW PhD symposium*, Gent, 12 2004.